Utilising the solvation properties of ionic liquids in the size-controlled synthesis and stabilization of metal nanoparticles for catalysis in situ

Paul Campbell

N° d'ordre 212-2010 Année 2010

THESE

Présentée

devant l'**UNIVERSITE CLAUDE BERNARD - LYON 1**
ECOLE DOCTORALE DE CHIMIE
SPECIALITE CHIMIE

Pour l'obtention

du **DIPLOME DE DOCTORAT**
(arrêté du 7 août 2006)

par

PAUL CAMPBELL

UTILISING THE SOLVATION PROPERTIES OF IONIC LIQUIDS IN THE SIZE-CONTROLLED SYNTHESIS AND STABILISATION OF METAL NANOPARTICLES FOR CATALYSIS *IN SITU*

Directeurs de thèse :
Mme. Catherine SANTINI & M. Yves CHAUVIN

présentée et soutenue publiquement le jeudi 28 octobre 2010 devant la commission d'examen :

Jury:
Mme. Anja-Verena MUDRING
M. Agilio PADUA
M. Stéphane DANIELE
M. Bruno CHAUDRET (Président)

Rapporteurs:
M. Christopher HARDACRE
M. Laurent DOUCE

UNIVERSITE CLAUDE BERNARD - LYON 1

Président de l'Université	**M. le Professeur L. Collet**
Vice-président du Conseil Scientifique	M. le Professeur J-F. Mornex
Vice-président du Conseil d'Administration	M. le Professeur G. Annat
Vice-président du Conseil des Etudes et de la Vie Universitaire	M. le Professeur D. Simon
Secrétaire Général	M. G. Gay

COMPOSANTES SANTE

Faculté de Médecine Lyon Est – Claude Bernard	Directeur : M. le Professeur J. Etienne
Faculté de Médecine Lyon Sud – Charles Mérieux	Directeur : M. le Professeur F-N. Gilly
UFR d'Odontologie	Directeur : M. le Professeur D. Bourgeois
Institut des Sciences Pharmaceutiques et Biologiques	Directeur : M. le Professeur F. Locher
Institut des Sciences et Techniques de Réadaptation	Directeur : M. le Professeur Y. Matillon
Département de Biologie Humaine	Directeur : M. le Professeur P. Farge

COMPOSANTES ET DEPARTEMENTS DE SCIENCES ET TECHNOLOGIE

Faculté des Sciences et Technologies	Directeur : M. le Professeur F. Gieres
Département Biologie	Directeur : M. le Professeur C. Gautier
Département Chimie Biochimie	Directeur : Mme le Professeur H. Parrot
Département GEP	Directeur : M. N. Siauve
Département Informatique	Directeur : M. le Professeur S. Akkouche
Département Mathématiques	Directeur : M. le Professeur A. Goldman
Département Mécanique	Directeur : M. le Professeur H. Ben Hadid
Département Physique	Directeur : Mme S. Fleck
Département Sciences de la Terre	Directeur : M. le Professeur P. Hantzpergue
UFR Sciences et Techniques des Activités Physiques et Sportives	Directeur : M. C. Collignon
Observatoire de Lyon	Directeur : M. B. Guiderdoni
Ecole Polytechnique Universitaire de Lyon 1	Directeur : M. le Professeur J. Lieto
Institut Universitaire de Technologie de Lyon 1	Directeur : M. le Professeur C. Coulet
Institut de Science Financière et d'Assurance	Directeur : M. le Professeur J-C. Augros
Institut Universitaire de Formation des Maîtres	Directeur : M R. Bernard

for my brothers and sisters; Sandra, Steven, Ian and Beth

and for my Mum and Dad

Les travaux exposés dans ce mémoire ont été réalisés entre novembre 2007 et octobre 2010 au Laboratoire de Chimie, Catalyse, Polymérisation et Procédés dans l'équipe de Chimie OrganoMétallique de Surface, unité mixte CNRS-CPE Lyon. Je suis reconnaissant envers Monsieur Gérard Pignault, directeur de CPE Lyon, pour m'avoir accueilli dans ses locaux.

Mes remerciements vont tout d'abord à Madame Bernadette Charleux, qui a bien voulu m'accueillir au sein de son laboratoire et Monsieur Jean-Marie Basset, qui m'a chaleureusement accueilli au sein de son équipe.

J'adresse mes plus vifs remerciements à Monsieur Yves Chauvin, Directeur de Recherche honoraire à l'Institut Français du Pétrole, agissant en qualité de co-directeur. En dépit de son éloignement, il a fait preuve d'une grande disponibilité et a été une source constante de conseils et de réflexions. Je lui suis très reconnaissant de sa contribution au développement de ce projet et de m'avoir fait profiter de ses connaissances et de sa grande expérience en chimie.

Je tiens à remercier Madame Catherine Santini, Directeur de Recherche au CNRS, qui a encadré mes travaux de thèse. Je la remercie tout particulièrement pour l'aide et le soutien qu'elle m'a apportés durant ces trois années.

Que Madame Anja-Verena Mudring, Professeur à la Ruhr Universität Bochum, et Messieurs Christopher Hardacre, Directeur de l'école de chimie à la Queen's University Belfast, Laurent Douce, Directeur de Recherche au CNRS, Agílio Pádua, Professeur à l'Université Blaise Pascale Clermont Ferrand, Bruno Chaudret, Directeur de Recherche au CNRS et Stéphane Daniele, Professeur à l'Université Lyon 1, soient vivement remerciés de l'honneur qu'ils m'ont fait en acceptant de juger ce mémoire.

Ce travail a été finance par la Ministère de l'enseignement supérieur et de la recherche et par l'Agence Nationale de la Recherche, projet CALIST (ANR-07-CP2D-02-03). Je remercie tout particulièrement Ajda Podgoršek, Gorka Salas, Margarida Costa Gomes et Karine Philippot, collaborateurs sur ce projet, pour l'aide et les nouvelles idées qu'ils m'ont apportés. Je tiens également à remercier Anne Baudouin, François Bayard, Bernard Fenet, Denis Bouchu, Vincent Collière, et Jacinto Sá pour leurs analyses et leur aide.

Je souhaite également remercier tous les étudiants en stage avec lesquels j'ai eu le grand plaisir de travailler. Je remercie particulièrement Georgina Fraser et Magali Pillot, étudiantes en stage de Master, qui ont contribué de façon significative à l'aboutissement de ces travaux.

Que tous les membres du laboratoire trouvent dans ces quelques lignes l'expression de ma plus profonde gratitude. Je pense en particulier à Jeff, Etienne, Marco, Raphael, Nicolas, Layane et Vickie avec lesquels j'ai vécu ces trois années dans une ambiance qui fut toujours conviviale.

The work presented in this thesis was carried out between November 2007 and October 2010 in the "Laboratoire de Chimie, Catalyse, Polymères et Procédés" in the team "Chimie OrganoMétallique de Surface", CNRS-CPE Lyon. I am grateful Gérard Pignault, director of CPE Lyon, for welcoming me in his institution.

My warm thanks go firstly to Bernadette Charleux, for welcoming me into her laboratory and to Jean-Marie Basset, for his willingness to accept me as part of his team.

I am indebted to Mr. Yves Chauvin, honorary research director at the "Institut Français du Pétrole," acting as my co-supervisor. Despite his distance, he was always available and has been a constant source of thought and advice. I am grateful to him for his contribution in the development of this project and for giving me the opportunity to learn from his great knowledge and experience in chemistry.

It is difficult to overstate my gratitude towards my Ph.D. supervisor, Catherine Santini, CNRS Research Director, without whom, this thesis would not have been possible. With her enthusiasm, her inspiration, and her great efforts to encourage and give sound ideas and advice, these three years have been made tremendously enjoyable.

I also extend my sincere gratitude to Anja-Verena Mudring, Professor at Ruhr Universität Bochum, Christopher Hardacre, Head of the School of Chemistry, Queen's University Belfast, Laurent Douce, CNRS Research Director, Agílio Pádua, Professor at Université Blaise Pascale Clermont Ferrand, Bruno Chaudret, CNRS Research Director and Stéphane Daniele, Professor at Université Lyon 1, for doing me the honour of reviewing this thesis.

This work was funded by the "Ministère de l'enseignement supérieur et de la recherché" and by the "Agence Nationale de la Recherche" under the project CALIST (ANR-07-CP2D-02-03). I would particularly like to thank Ajda Podgoršek, Gorka Salas, Margarida Costa Gomes and Karine Philippot, collaborators on this project, for the help and ideas and fruitful discussion that they provided. I also wish to thank Anne Baudouin, François Bayard, Bernard Fenet, Denis Bouchu, Vincent Collière, and Jacinto Sá for their analyses and help in interpretation.

It has been a great pleasure to work alongside many undergraduate students during these three years and I would especially like to give a mention to Georgina Fraser and Magali Pillot, Master's students, who both made significant contributions to the outcome of this work.

Last but not least, I would like to express my deepest gratitude to my many colleagues for providing a stimulating and fun environment in which to learn and grow. I am above all grateful to Jeff, Etienne, Marco, Raphael, Nicolas, Layane and Vickie for all the emotional support, camaraderie and particularly for the entertainment that they provided.

Abbreviations and acronyms

Units

h: hour min: minute mL: millilitre
g: gram mg: milligram mol: mole
°C: degree Celsius Hz: Hertz K: degree Kelvin
ppm: part per million

Techniques

ESI: ElectroSpray Ionisation Mass Spectrometry
GC: Gas Chromatography
FID: Flame Ionisation Detector
SAXS: Small Angle X-ray Scattering
XRD: X-Ray diffraction
XPS: X-ray photoelectron spectroscopy
NMR: Nuclear Magnetic Resonance
δ: chemical shift *J*: coupling constant
s: singlet, d: doublet, t: triplet, q: quadruplet, quint: quintuplet, sext: sextuplet, m: multiplet
ROESY: Rotational Overhauser Effect SpectroscopY
DOSY: Diffusion Order SpectroscopY
TEM: transition electron microscopy HREM: high resolution electron microscopy

Chemicals

IL: Ionic Liquid
Im: imidazolium
C_1: methyl C_2: ethyl C_4: butyl C_6: hexyl C_8: octyl C_{10}: decyl
$C_{4//}$: but-3-enyl Bz: benzyl
[C_1C_4Im]: 1-butyl-3-methylimidazolium [$C_1C_1C_4$Im]: 1-butyl-2,3-dimethylimidazolium
[OTf]: trifluoromethylsulfonate [NTf_2]: bis-(trifluoromethylsulphonyl)imide
[BF_4]: tetrafluoroborate

COD: 1,5-cyclooctadiene COT: 1,3,5-cyclooctatriene COA: cyclooctane
To: toluene
CYD: 1,3-cyclohexadiene CYE: cyclohexene CYA: Cyclohexane
Lim: (R)-(+)-limonene
Sty: styrene EBn: Ethylbenzene ECHA: ethylcyclohexane

Ru(COD)(COT): (1,5-cycooctadiene)(1,3,5-cyclooctatriene)ruthenium
$Ni(COD)_2$: bis(1,-5(-cyclooctadiene)nickel
NP: nanoparticle

UTILISING THE SOLVATION PROPERTIES OF IONIC LIQUIDS IN THE SIZE-CONTROLLED SYNTHESIS AND STABILISATION OF METAL NANOPARTICLES FOR CATALYSIS *IN SITU*

Imidazolium based ionic liquids (ILs) consist of a continuous 3-D network of ionic channels, coexisting with non polar domains created by the grouping of lipophilic alkyl chains, forming dispersed or continuous microphases. The aim of this work is to use the specific solvation properties of ILs, related to this 3-D organisation, to generate and stabilise *in situ* metal nanoparticles (NPs) of a controlled and predictable size. This approach has found application in fields such as catalysis and microelectronics. The phenomenon of crystal growth of NPs (ruthenium, nickel, tantalum) generated *in situ* in ILs from the decomposition of organometallic complexes under molecular hydrogen, is found not only to be controlled by i) the size of non-polar domains, in which the complexes dissolve, but also by ii) the experimental conditions (temperature, stirring) and iii) the nature of the metal and its precursor complex. The previously unexplained stabilisation mechanism of NPs in ILs is found to depend on the mechanism of formation of NPs, which may lead to the presence of either hydrides or N-heterocyclic carbenes (NHC) at their surface. These have both been evidenced through isotopic labelling experiments analysed by NMR and mass spectrometry. Another advantage of ILs is that they provide an interesting medium for catalytic reactions. Studies on the influence of the IL on the catalytic performance in homogeneous catalysis have highlighted the crucial importance of the physical-chemical parameters of ILs, in particular the viscosity, for which a term must be included in the kinetic rate law. Using these findings, a thorough investigation of the effect of the NP size on catalytic activity and selectivity in hydrogenation in ILs was undertaken, confirming the importance of controlling NP size for catalytic applications.

UTILISATION DES PROPRIETES DE SOLVATATION DES LIQUIDES IONIQUES EN SYNTHESE ET STABILISATION DES NANOPARTICULES METALLIQUES DE TAILLE CONTROLEE POUR LA CATALYSE *IN SITU*

Les liquides ioniques (LIs) à base d'imidazolium présentent une très grande organisation en réseaux 3D et sont constitués de microdomaines polaires et apolaires, dû à la présence des canaux ioniques et le regroupement des chaînes alkyles lipophiles. L'objectif de ce travail est d'utiliser leurs propriétés de solvatation, liées à cette organisation, pour générer et stabiliser *in situ* des nanoparticules métalliques (NPs) d'une taille contrôlée et prévisible. Cette approche a trouvé de nombreuses applications dans des domaines tels que la catalyse et la microélectronique. Le phénomène de croissance cristalline des NPs (ruthénium, nickel et tantale) générées *in situ* lors de la décomposition sous H_2 des complexes organométalliques, est contrôlé i) par la taille des poches apolaires, dans lesquelles le complexe se dissout, ii) par les conditions expérimentales (température, agitation) et iii) par la nature du métal et du complexe précurseur. Le mécanisme de stabilisation des NPs, jusqu'alors mal compris, dépend du mécanisme de formation des NPs, qui pourrait entraîner la présence de ligands hydrures ou carbènes N-hétérocycliques (NHC) à leur surface. Cette présence a été démontrée par marquage isotopique et analysée en RMN ainsi qu'en spectrométrie de masse. Les LIs sont également des milieux intéressants en catalyse. Des études sur l'influence du LI sur l'activité des catalyseurs homogènes ont souligné l'importance cruciale des paramètres physico-chimiques des LIs, et particulièrement de la viscosité, qui intervient ainsi dans la loi cinétique. Enfin, une étude approfondie de l'effet de la taille des NPs sur l'activité catalytique et la sélectivité pour l'hydrogénation, réalisée en milieu LI, a confirmé l'importance du contrôle de la taille des NPs pour les applications catalytiques.

Table of Contents

Intro

Introduction

Introduction

Progress in the comprehension of metallic nanoparticles (NPs) is central due to their great potential in the development of new and innovative materials for applications in areas such as catalysis or microelectronics. Their small sizes, generally reported between 1 and 100 nm, lead to unique physical-chemical properties between the bulk and molecular states, which vary greatly with small changes in NP size. For example, the catalytic properties of NPs are largely determined by the energy of the surface atoms, in turn controlled by the number of neighbouring atoms, dictated by their size, as well as the presence and nature of ligands or supports.[1-3]

Particles less than 10 nm in diameter are particularly interesting in catalysis, due to their high surface to volume ratio, and are also greatly influenced by the aforementioned size-effect. Their preparation by most traditional methods often yields catalysts with broad size distributions. More recent advances in the field have seen the synthesis of NPs with well controlled size (narrow distribution), shapes and composition.[4-6]

NPs are only kinetically stable, the thermodynamically stable state being the bulk metal. Consequently, NPs dissolved freely in solution tend to agglomerate and coalesce. To prevent aggregation, NPs must be stabilised by the use of stabilising agents such as water-soluble polymers, quaternary ammonium salts, surfactants or polyoxoanions, providing electronic and/or steric protection.[4-6]

In this context, ionic liquids (ILs), defined as low temperature molten salts, have emerged as one of the most important and most investigated classes of stabilising agent for the synthesis and stabilisation of metal NPs. My Ph.D. thesis focuses on the overlap of these two prevailing fields of research, studying the synthesis small size controlled NPs (< 5 nm) for use in catalysis *in situ* in ILs.[7]

We can tune the IL moieties and reaction conditions to obtain monodisperse and catalytically active NPs of controlled size.[4, 7-9] This is because imidazolium based ILs exhibit a 3-D organisation in the liquid state due to an extended hydrogen-bond network of ionic channels, coexisting with non-polar domains created by the grouping of lipophilic alkyl chains. Consequently, ILs present specific solvation properties.[10] Polar substrates are preferentially dissolved in polar domains and non-polar compounds in non-polar ones.[11] The non-polar organometallic complex, Ru(COD)(COT), is expected to be concentrated in the non-polar

domains of ILs. Therefore the phenomenon of crystal growth is controlled by the local concentration of Ru(COD)(COT) and consequently limited to the size of the non-polar domains. These play the role of nanoreactors in which the size of ruthenium nanoparticles generated *in situ* can be controlled.[9, 12, 13] As a result, ILs may be used for predictive size-control of RuNPs.

Another major advantage of using ILs is that stabilising additives such as ligands, polymers and supports are not required, meaning that a maximum amount of NP surface is available for the coordination of substrates. However, the reasons behind the stability of NPs dispersed in ILs remain under debate.[14]

After a brief literature survey of the synthesis and catalytic applications of RuNPs in various media (Chapter 1), we go on to investigate the exact stabilisation mechanism of RuNP/IL solutions (Chapter 2). Also, we attempt to generalise the size-controlled NP synthesis of transition metal nanoparticles, by investigating the synthesis of nickel and tantalum NPs in the same media (Chapter 2).

In order to study the catalytic reactivity in ionic liquids, we must have an understanding of how the physical-chemical properties of these media themselves may influence the outcome of a given reaction. For this reason, we carry out a kinetic study of a simple homogeneous hydrogenation reaction (1,3-cyclohexadiene over an Osborn-type cationic Rh catalyst) in different IL media, simultaneously probing the thermophysical properties (viscosity, density, diffusion) and intermolecular interactions of the IL-substrate mixtures. These findings are used to rationalise the differences in reactivity and thus gauge the important parameters to consider when carrying out catalysis in IL media. (Chapter 3)

Finally, using the IL media to synthesise tailor-made RuNPs of distinct sizes, we may investigate the size-effect on catalytic performance (activity, selectivity) in the hydrogenation of several substrates including 1,3-cyclohexadiene, taking into account our findings from Chapter 3 to ensure otherwise identical reaction conditions. (Chapter 4)

References

1. M. Valden, X. Lai and D. W. Goodman, *Science*, 1998, **281**, 1647.
2. A. T. Bell, *Science*, 2003, **299**, 1688 –1691.
3. G. Schmid, *Nanoparticles: From Theory to Application*, Wiley-VCH, Weinheim, 2004.
4. H. Boennemann, K. S. Nagabhushana and in *Metal Nanoclusters in Catalysis and Materials Science: The Issue of Size Control* ed. B. Corain, Schmid, G., Toshima, N., Elsevier B.V, Amsterdam, 2008, pp. 21-48.
5. D. Astruc, *Nanoparticles and Catalysis*, Wiley-VCH, Weinheim, 2008.
6. D. Astruc, F. Lu and J. R. Aranzaes, *Angew. Chem. Int. Ed.*, 2005, **44**, 7852.
7. J. Dupont and J. D. Scholten, *Chem. Soc. Rev.*, 2010, **39**, 1780-1804.
8. J. Dupont, in *Nanoparticles and catalysis*, Wiley-VCH, Weinheim, 2008.
9. T. Gutel, C. C. Santini, K. Philippot, A. Padua, K. Pelzer, B. Chaudret, Y. Chauvin and J.-M. Basset, *J. Mater. Chem.*, 2009, **19**, 3624-3631.
10. A. A. H. Padua, M. F. Costa Gomes and J. N. A. Canongia Lopes, *Acc. Chem. Res.*, 2007, **40**, 1087-1096.
11. J. N. Canongia Lopes, M. F. Costa Gomes and A. A. H. Padua, *J. Phys. Chem. B*, 2006, **110**, 16816-16818.
12. T. Gutel, J. Garcia-Anton, K. Pelzer, K. Philippot, C. C. Santini, Y. Chauvin, B. Chaudret and J.-M. Basset, *J. Mat. Chem.*, 2007, **17**, 3290-3292.
13. P. S. Campbell, C. C. Santini, D. Bouchu, B. Fenet, K. Philippot, B. Chaudret, A. A. H. Padua and Y. Chauvin, *Phys. Chem. Chem. Phys.* 2010, **12**, 4217-4223.
14. R. G. Finke, *Coord. Chem. Rev.*, 2007, **251**, 1075–1100.

Chapter 1

Ruthenium Nanoparticles

Synthesis, Stabilisation & Applications

Chapter 1

Ruthenium Nanoparticles

Synthesis, Stabilisation and Applications

1.1 Introduction

Interest in metal nanoparticles (NPs) is increasing dramatically, as reflected by the ever-growing number of publications. Catalysis is the traditional application of NPs, but they also find application in diverse fields such as photochemistry, electronics, optics or magnetism. In catalysis, progress is constantly being made in the efficiency and selectivity of reactions and recovery and recyclability of the catalytic materials.[1-8]

Usually NP catalysts are prepared from a metal salt, a reducing agent, and a stabiliser and are often supported on an oxide, charcoal, or a zeolite. However, soluble noble metal nanoparticles are also to be considered as an unavoidable family of catalysts, often described as "semi-heterogeneous catalysts", lying at the frontier between homogeneous and heterogeneous chemistry. Besides the polymers and oxides that used to be employed as standard, innovative stabilisers, media, and supports have appeared, such as dendrimers, specific ligands, ionic liquids, surfactants, membranes, carbon nanotubes, and a variety of oxides.[9-14]

As one of the catalytically active noble metals, ruthenium has been widely studied in both homogeneous catalysis, the most well known example being olefin metathesis,[15, 16] and in heterogeneous, for example the partial hydrogenation of benzene to cyclohexene (Asahi process),[17] phenol hydrogenation,[18] or in the synthesis of ammonia from N_2 (Haber-Bosch process).[19, 20]

Over the past couple of decades, much interest has also been devoted towards nanoparticles of ruthenium, even though it is claimed by Galetti *et al.* that the preparation of Ru nanoparticles is more difficult and therefore less-investigated than other noble metals such as Pt or Pd.[18] Their various synthetic routes and catalytic properties are summarised in this chapter.

1.2 Syntheses

1.2.1 RuNPs synthesised directly on supports

The study of RuNPs and their use in catalysis is not a new concept and dates back to the 1980s. Grafting of catalytically active metal complexes onto oxide supports, a technique commonly referred to as surface organometallic chemistry, was becoming a popular area of interest due to the prospect of combining the advantages of heterogeneous and homogeneous catalysis (i.e. obtaining recoverable, reusable catalysts with high activity and selectivity), as well as obtaining new and novel catalysts.[21] This method involves firstly impregnation of the support with a solution (aqueous or organic) of metal precursor, followed by elimination of the solvent and finally thermal treatment, generally under H_2 or vacuum. However, for late transition metals such as ruthenium, after thermal treatment, these surface complexes, e.g. $Ru_3(CO)_{12}$, tend to decompose and agglomerate, forming small oxide-supported RuNPs (1-2 nm on SiO_2, measured by TEM).[22-25] Nonetheless, these supported NPs have been found to display interesting catalytic behaviour, for example in the hydrogenolysis and homologation of olefins.[26, 27]

The use of the organometallic precursor ruthenium(η^4-1,5-cyclooctadiene)(η^6-1,3,5-cyclooctatriene), commonly denoted Ru(COD)(COT), for the formation of RuNPs supported on SiO_2 was first reported Kitajima *et al*. This method rendered very small NPs ~ 1 nm, (measured by H_2 adsorption) smaller than those produced from $RuCl_3$ via the same method.[28] This is thought to be due to the absence of coordinating Cl^-, which would be present in the latter case. Bare RuNPs prepared in this way have been found to coordinate 2 hydride ligands per surface site.[29]

Similarly, RuNPs have been supported on mesoporous silica, firstly by impregnating the support with Ru(COD)(COT) solution in THF and then proceeding to decompose the complex. The size of the NPs obtained varies with the pore size and the impregnation method.[30]

Alumina supports (Al_2O_3) have also been studied and give similar results. For example, impregnation of a precursor (either $RuCl_3$ or $Ru_3(CO)_{12}$) on a K-promoted alumina (added by prior impregnation of the alumina with KOH) followed by reduction at 400 °C under a flow of H_2 produced supported RuNP catalysts. The size distribution and dispersion were found to be superior in the case where $Ru_3(CO)_{12}$ was used as the precursor.[31]

This technique has also been extended to innovative supports such as mesoporous polymers to create new catalytic materials as depicted in Scheme 1. This can be used as a highly recyclable catalyst in the aqueous hydrogenation of olefins and aromatics.[32]

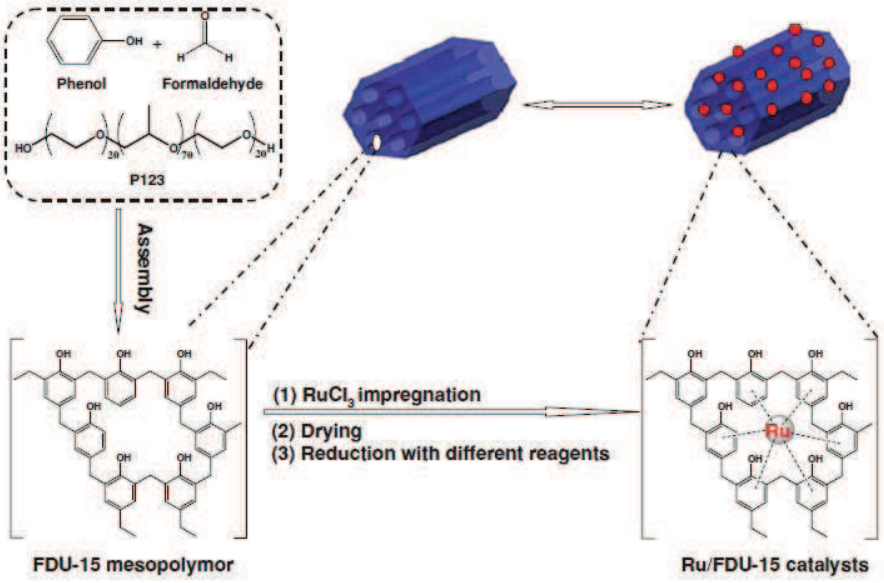

Scheme 1. The synthesis of a RuNP-loaded mesopolymer for catalysis. [32]

Although the direct synthesis of supported NPs in this fashion renders catalytically active supports, due to the absence of ligands and availability of the NP surface, the resulting size and size distribution, a factor which dictates catalytic performance, is difficult to control. For this reason the deposition of ready-synthesised RuNPs onto supports has also received a great deal of interest.

1.2.2 Solvothermal synthesis

The versatile and facile polyol method for the synthesis of nanoparticles involves firstly suspending the metal precursor in a polyol such as ethylene glycol, before bringing the resulting mixture to reflux and awaiting the precipitation of the metallic moieties. The reduction occurs via the simultaneous oxidation of alcohols to aldehydes as shown in Equation (1). The resulting metal NPs can be filtered and dried in air. Using $RuCl_3$ as the metal precursor results in RuNPs with an average diameter of 5 nm.[33]

$$3\ –CH_2OH\ (from\ polyols) + RuCl_3 \rightarrow 3\ -CHO + 2\ Ru(0) + 6\ HCl \qquad (1)$$

The polyol method has been used in the presence of polyvinylpyrrolidone (PVP) to obtain polymer-supported RuNPs by microwave-assisted syntheses.[34-36] The size of the resulting RuNPs may be controlled by the concentration of the precursor, as shown by Somorjai's group using $Ru(acac)_2$ (acac = acetylacetonate) in a microwave-assisted synthesis. TEM images of the size-controlled RuNPs produced are depicted in Figure 1. The PVP-stabilised RuNPs could then be supported on silicon wafers for gas phase catalysis.[37]

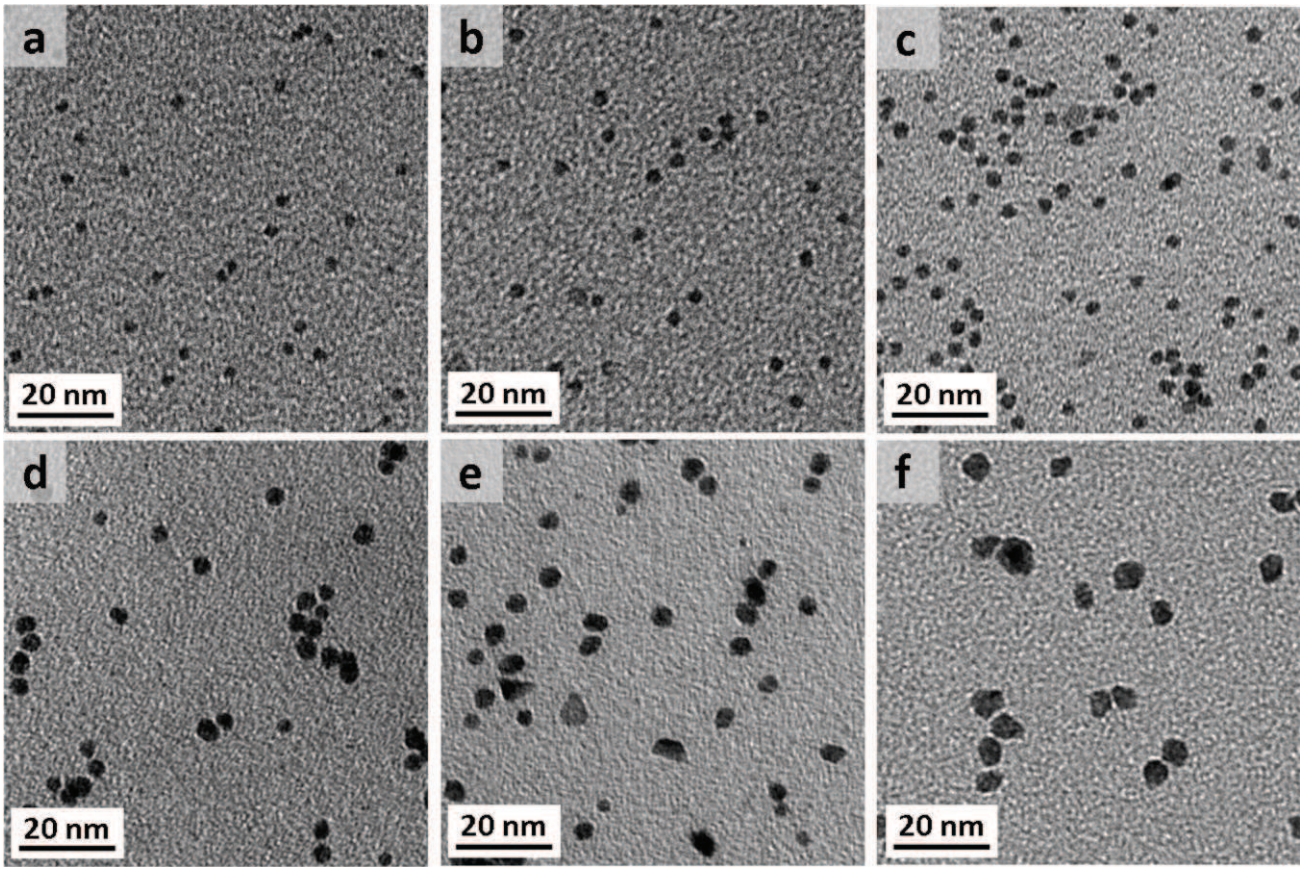

Figure 1. TEM images of Ru NPs: (a) 2.1, (b) 2.8, (c) 3.1, (d) 3.8, (e) 5.0, and (f) 6.0 nm. TEM images were taken using a Philips FEI Tecnai 12 machine, operated at 100 kV.[37]

RuNPs produced via the polyol method, subsequently coated in dodecane thiol and dispersed in toluene, have been found to form supramolecular self-assemblies of anisotropic disc-shaped NPs, the structure varying with the thiol concentration, Figure 2.

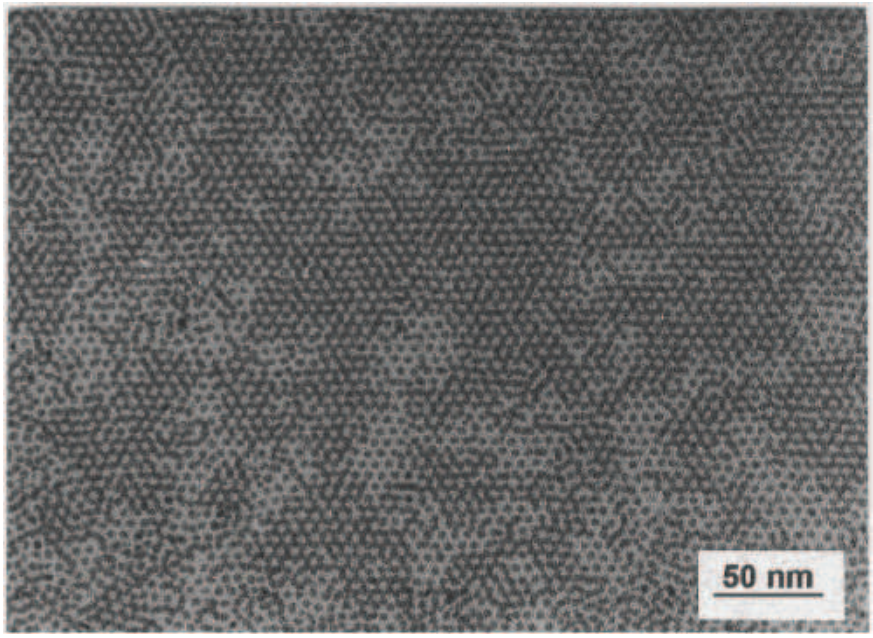

Figure 2. Supramolecular self assemblies of hexagonal RuNP prepared via the polyol method and stabilised with dodecane thiol.[38]

This method has been widely used for subsequent deposition of the NPs onto oxide supports. For example Miyakazi *et al.* prepared RuNPs supported on γ-alumina via the polyol method for use in heterogeneous catalysis. It was found that the best results for size-control were obtained when the γ-alumina was present during the polyol reduction, as this prevented NP agglomeration during the cooling of the polyol mixture. The RuNPs are supported on the alumina by electrostatic forces.[20] Similarly, Xu *et al.* used the polyol method in ethylene glycol to stabilise RuNPs produced *in situ* onto MgO substrates.[39]

Similar to the polyol route, another solvothermal route has been used to produce RuNPs directly from $RuCl_3$ by heating with an anhydrous alchohol, such as methanol. Upon heating Ru(III) may oxidise the methanol to formaldehyde, reduced itself to Ru(0) as shown in Equation (1).[40] The RuNPs produced using this method were found to be between 2 and 10 nm in size and X-ray diffraction analysis indicated the presence of a Ru hcp phase. XPS experiments, however, indicated a slightly oxidised surface, possibly due to coordination of residual chloride.[40]

1.2.3 Colloidal synthesis in organic solvents

Zero-valent organometallic precursors are generally easily decomposed under H_2 atmosphere rapidly producing NPs. The organic by-products can be easily removed without further interaction with the surface of the resulting NPs. For this reason, Chaudret's group has

thoroughly developed the synthesis of RuNPs in organic solvents from the decomposition of the organometallic precursor Ru(COD)(COT), Scheme 2.[12, 41-43]

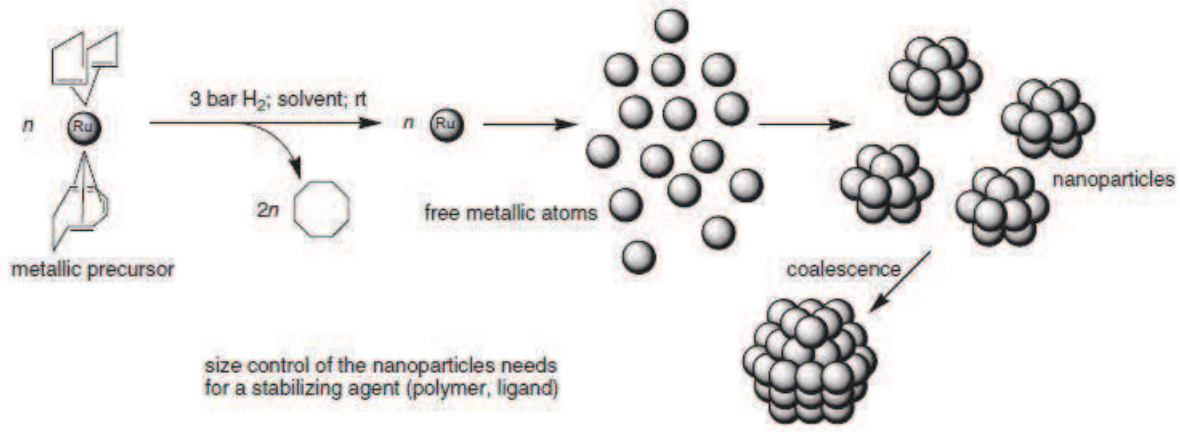

Scheme 2. The synthesis of RuNPs from the decomposition of Ru(COD)(COT) in organic solvents.[12]

In mixtures of methanol/THF of varying composition, this decomposition may take place resulting in RuNPs of sizes varying linearly with MeOH/THF ratio, Figure 3a.[44, 45] These surprising results have been attributed to a colloidal growth mechanism involving micellar type aggregates of MeOH and cyclooctane (resulting from hydrogenation of the ruthenium precursor) acting as nanoreactors in which the size of the RuNPs is constrained, Scheme 3.

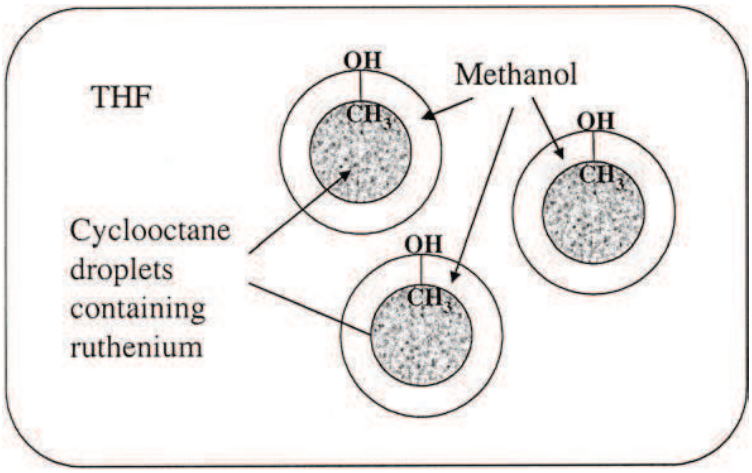

Scheme 3. Hypothesised growth and stabilisation mechanism for RuNPs in THF methanol mixtures.[43]

In a mixture of MeOH/THF 10:90, the size of NPs generated was found to vary inversely with the temperature used during decomposition, Figure 3b. This could be explained by

considering the effect of the temperature on the kinetics of decomposition. At higher T, the decomposition is accelerated and therefore nucleation is rapid leading to a large number of small particles. At low temperature, decomposition is slow and the kinetics of coalescence dominate.[46]

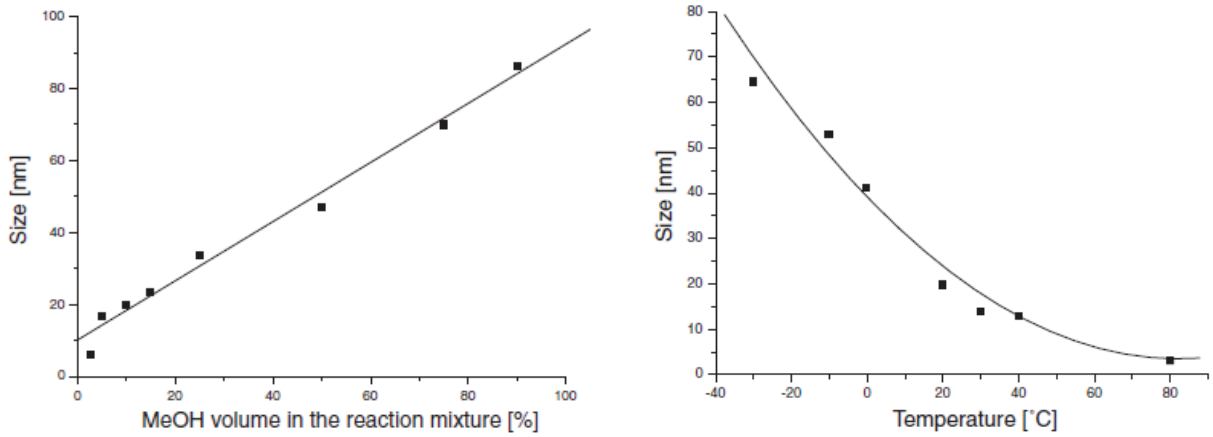

Figure 3. a) variation of RuNP size with MeOH composition (left), **b)** variation of RuNP size with decomposition temperature (right).[44-46]

Through tests of their reactivity towards O_2 and CO, the resulting NPs are shown to be "bare" and therefore have a great surface availability for catalysis. Furthermore, RuNPs produced in such a manner have been supported on porous alumina membranes, Figure 4, and used in the gas phase hydrogenation of butadiene.[44]

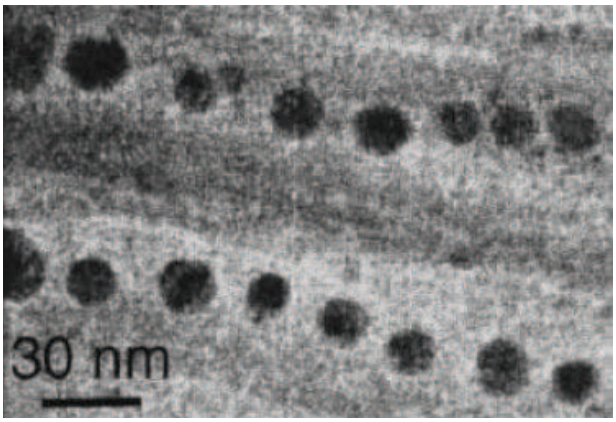

Figure 4. RuNPs produced in MeOH/THF mixtures from the decomposition under H_2 of Ru(COD)(COT), supported in a porous alumina membrane.[44]

This synthesis has also been carried out in the presence of polymeric materials. For example with nitrocellulose in THF, polymer-supported NPs were produced. Here, varying the

ratio of Ru/nitrocellulose was found to control the size of the resulting NPs (2 % - 1.5 nm, 10 % - 2.5 nm).[47]

In the presence of the polymers polyvinylpyrrolidone (PVP) or cellulose acetate (CAC), polymer supported RuNPs of 1.1 nm or 1.7 nm result. High resolution electron microscopy (HREM) images show that these NPs adopt a relaxed hcp structure – a = 2.66 Å, c = 4.36 Å compared to a = 2.7058 Å and c = 4.2811 Å in bulk ruthenium, Figure 5.[48]

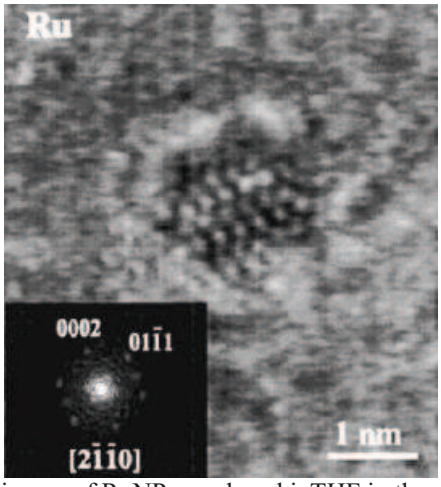

Figure 5. HREM image of RuNPs produced inTHF in the presence of PVP.[48]

Colloidal solutions of RuNPs may also be prepared by using ligands such as amines in THF. Varying the length of the alkyl chain of the amines used, as well as the quantity of amine has been found to produce RuNPs of different sizes and shapes. Elongated RuNPs produced using 0.5 equivalents of hexadecylamine with respect to ruthenium are shown in Figure 6.[48] RuNPs prepared in THF and stabilised with hexadecylamine have been proven by H-D exchange experiments to be covered by surface hydrides, which may provide an additional explanation for their stability.[49]

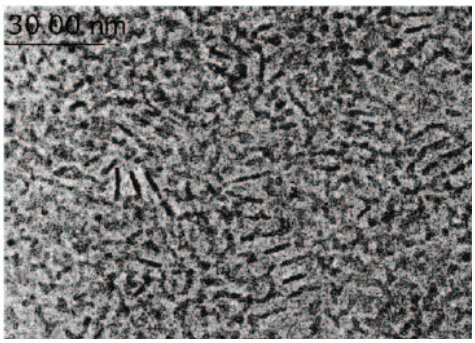

Figure 6. Elongated RuNPs formed in a mixture of THF and hexadecylamine (0.5 equiv.) [48]

A range of thiols has also been studied as potential ligands for the stabilisation of RuNPs in organic solvent. However, agglomeration was noted in this case, possibly related to the dimerisation of thiols to disulphides on the RuNP surface, Equation (2), observed by NMR spectroscopy.[48]

$$2\ C_8H_{17}SH \xrightarrow{Ru} C_8H_{17}SSC_8H_{17} + H_2 \qquad (2)$$

Silanes may also be used to stabilise RuNPs in organic solvent. The grafting of the silane to the NP surface has been observed by solid state NMR spectroscopy.[50]

From an environmentally-friendly point of view, aqueous catalytic processes are a highly interesting concept. Indeed, it has been found that the careful selection of a hydrophilic stabilising ligand in NP synthesis leads to RuNPs which may be redispersed in water for catalysis.[51, 52] An example depicted in Scheme 4 uses 1,3,5-triaza-7-phosphaadamantane, PTA to stabilise water soluble RuNPs.[51]

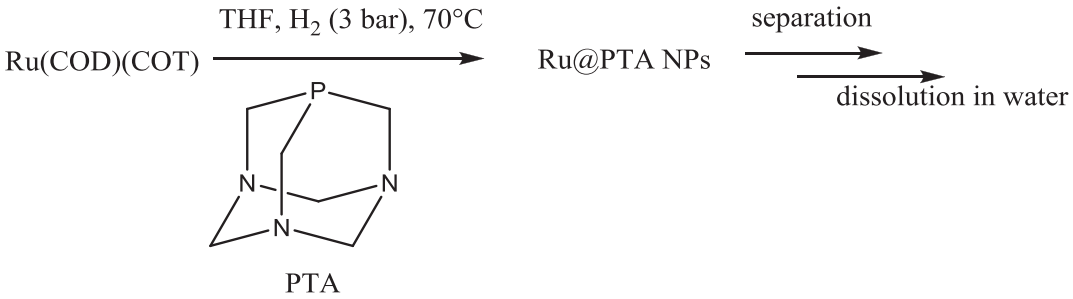

Scheme 4. The synthesis of water soluble RuNPs in THF.

Of course, synthesis of water-soluble RuNPs may also take place *in situ* starting from aqueous solutions of water soluble Ru precursors.

1.2.4 Aqueous Synthesis

For synthesis of NPs in water, non-polar organometallic precursors such as Ru(COD)(COT) are no longer suitable. Instead, metal salts are used, in the case of RuNPs, $RuCl_3$.

Roucoux's group has undertaken much work on the aqueous synthesis of RuNPs from reduction of $RuCl_3$ with $NaBH_4$ in the presence of cyclodextrins (Scheme 5), which stabilise the

resulting NPs by formation of inclusion complexes. The cyclodextrins, which are water-soluble, may also modify the surface of the RuNPs for specific reactivity.[53-55]

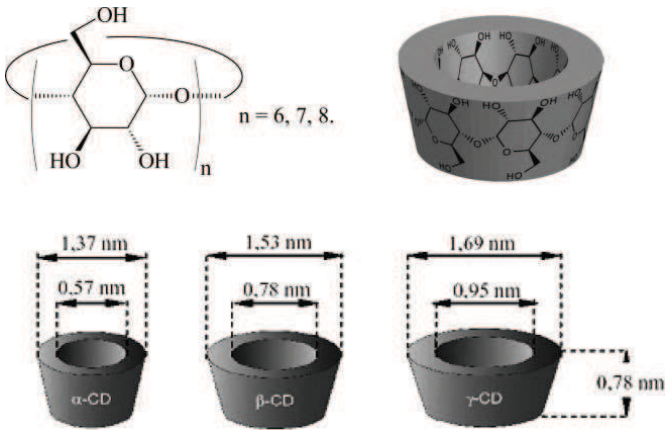

Scheme 5. Schematic representation of α-, β- and γ-cyclodextrins containing 6, 7 and 8 glucopyranose units respectively.[54]

Water-soluble RuNPs have also been achieved using similar experimental conditions but with less complicated ligands such as ethylenediamine,[56, 57] sodium acetate,[58] or even polymers such as poly(4-vinylpyridine).[59] These aqueous media may be used in biphasic catalytic systems for reactions such as hydrogenations, presenting the advantage of easy catalyst recyclability and product separation.[53-55]

The possibility of producing RuNPs that can be dispersed in a variety of media by using amphiphilic ligands has also been explored.[60]

1.2.5 Synthesis in ionic liquids

Due to their specific solvation properties and 3-D structural organisation in the liquid state, ionic liquids are "supramolecular fluids" that can be used as ''entropic drivers'' for the spontaneous, well-defined and extended ordering of nanoscale structures. This includes the synthesis of NPs, which can take place with size-control and in the absence of stabilising additives. The number of publications in this field is increasing exponentially, and these have recently been comprehensively reviewed.[14]

RuNPs were first generated "by accident" in ionic liquids. During an investigation of the catalytic hydrogenation behaviour of RuO_2 in ionic liquids, Hg and CS_2 poisoning tests confirmed that the catalytically active species was in fact colloidal Ru(0). The presence of NPs

was confirmed by TEM, meaning that under mild hydrogenation conditions, RuO_2 was reduced forming a stable suspension of small NPs in the ILs.[61, 62]

Organometallic precursors such as bis(2-methylallyl)(η^4-1,5-cyclooctadiene)ruthenium[63] and Ru(COT)(COD) have also been used as a RuNP precursor in ILs.[62] Ru(COD)(COT), particularly in imidazolium ILs based on the NTf_2 ion, renders interesting results.[64]

Firstly, work undertaken in our laboratory uncovered that, unlike in traditional solvents,[46] decreasing the temperature of decomposition to 0 °C (hence decreasing rate of nucleation) leads to smaller NPs. This could only be explained by considering the organisation of the ionic liquid, which consists of rigid ionic channels and segregated lipophilic domains. The organometallic precursor dissolves preferentially within these lipophilic domains. The size of the resulting RuNP is dictated by the number of available nuclides in the non polar domain after decomposition. At low temperature, diffusion of the precursor and nuclides between these domains is limited, hence the growth of NPs is restricted.

This can be confirmed by observing the effect of stirring on the size distribution. Stirring disrupts the organisation through mechanical forces and increases the diffusion of the precursor and nuclides in solution. The resulting size distributions are therefore broader and the resulting NPs are agglomerated.[64]

Further control of the size of NPs generated in these ionic liquids can be achieved by controlling the size of the non-polar domains by altering the length of the alkyl chains.[65]

Ionic liquids have also been used in combination with supports to synthesise and stabilise RuNPs of a small size. The ionic liquid 1,1,3,3-tetramethylguanadinium (TMG) lactate has been used to immobilise NPs in mesoporous silica (SBA-15). The resulting material was found to exhibit synergistic effects between the RuNPs, the support and the TMG^+, resulting in an active catalyst in arene hydrogenation.[66]

1.2.6 Glossary of RuNP syntheses

Table 1. Non-exhaustive glossary of RuNP syntheses reported in the literature, and sizes obtained.

Precursor	Conditions	Stabiliser/Solvent	Size obtained (nm)	Reference
Ru(COD)(COT)	100-400 °C, H_2 (270 mbar)	SiO_2	0.9-1.0 (depending on decomposition temperature and loading)	28
$RuCl_3$			1.5-5.3 (depending on loading)	
Ru(COD)(COT)	300 °C, H_2 (666 mbar)	SiO_2	2.0 ± 0.3	29
$Ru_3(CO)_{12}$	220 °C, H_2 (1 bar)	SiO_2	1	25
$Ru_3(CO)_{12}$	120 °C, vacuum	SiO_2	1.4	22
$RuCl_3$	400 °C, H_2 (1 bar)	Al_2O_3- KOH	10	31
$Ru_3(CO)_{12}$	400 °C, H_2 (1 bar)		2	
$RuCl_3$	reflux	Ethylene glycol	5	20, 33
$RuCl_3$	150 °C, NaOAc	1,3-propanediol	4	38, 67
$RuCl_3$	reflux	Methanol Ethanol	2 - 10	40
Ru(COD)(COT)	25 °C, H_2 (1 bar)	Nitrocellulose/THF	1.0, 1.5, 2.0 (2, 5, 10 % Ru, resp.)	47
Ru(COD)(COT)	21 °C, H_2 (3 bar)	Methanol/THF	12- >500 (depending on MeOH/THF composition)	44-46
Ru(COD)(COT)	-30 °C, H_2 (3 bar) -10 °C, H_2 (3 bar) 0 °C, H_2 (3 bar) r.t., H_2 (3 bar) 30 °C, H_2 (3 bar) 40 °C, H_2 (3 bar) 80 °C, H_2 (3 bar)	Methanol/THF (10/90)	65 53 41 21 15 13 5	46
Ru(COD)(COT)	20 °C, H_2 (3 bar)	PVP[a]/THF CAC[b]/THF	1.1 1.7	48
Ru(COD)(COT)	20 °C, H_2 (3 bar)	Octylamine/THF Dodecylamine/THF Hexadecylamine/THF	2.3-2.5 1.8-2.3 (elongated shapes) 1.9-2.6 (elongated shapes) (all varying with ligand amount)	48
Ru(COD)(COT)	20 °C, H_2 (3 bar)	Octanethiol/THF Dodecanethiol/THF Hexadecanethiol/THF	2.3-2.5 ~2 1-2 (all varying with ligand amount)	48
Ru(COD)(COT)	20 °C, H_2 (3 bar)	Pure heptanol	3	68
Ru(COD)(COT)	-80 °C-r.t. H_2 (3 bar)	Octylsilane/n-pentane	2.3	50
Ru(COD)(COT)	r.t , H_2 (3 bar)	Mesoporous silica/THF	2-5 (depending on the pore size and impregnation method)	30
Ru(COD)(COT)	r.t., H_2 (3 bar)	N donor chiral ligands/ THF	1.5-2.7 nm (depending on ligand)	69
Ru(COD)(COT)	r.t., H_2 (3 bar)	Heavily fluorinated compounds/ THF	~3 nm grouping into super-structures	70
Ru(COD)(COT)	r.t., H_2 (1 bar)	4-(3-phenylpropyl)-pyridine/ THF	1.3 ± 0.3	71
Ru(COD)(COT)	r.t., H_2 (3 bar)	Diphosphites/THF	1.8-4.0 (depending on nature	72, 73

			of diphosphite)	
Ru(COD)(COT)	45 °C, H_2 (1 bar)	Polyorganophosphazanes/ THF	1.55 ± 0.5	74
Ru(COD)(COT)	70 °C, H_2 (3 bar)	PTA[c]/THF	1.3 ± 0.2	51
Ru(COD)(COT)	25 °C, H_2 (3 bar)	3-APTS[d]/THF	1.7 ± 0.4	75
$RuCl_3$	r.t., $NaBH_4$ (aq)	Dodecylamine/ THF[e]	4.1	76
$RuCl_3$	r.t., $NaBH_4$	methylated cyclodextrins/ H_2O	1 – 2.5	53-55
$RuCl_3$	r.t., $NaBH_4$	Methylenediamine/ H_2O	2.1	56
$RuCl_3$	r.t., $NaBH_4$	NaAcO/ H_2O	2.2 ± 1.0	58, 77
$RuCl_3$	r.t., $NaBH_4$	Poly(4-vinylpyridine)/ H_2O	1-2	59
Ru(COD)(COT)	75 °C, H_2 (4 bar)	C_1C_4Im BF_4 C_1C_4Im PF_6 C_1C_4Im OTf	2.6 ± 0:4 (in 57 nm superstructures)	62
Ru(COD)(COT)	0 °C, H_2 (4 bar) stirred	C_1C_4Im NTf_2	0.9 ± 0.4 (agglomerated in 2-3 nm clusters)	64
	0 °C, H_2 (4 bar) unstirred	C_1C_4Im NTf_2	1.1 ± 0.2	
	25 °C, H_2 (4 bar) stirred	C_1C_4Im NTf_2	2.4 ± 0.3	
Ru(COD)(COT)	0 °C, H_2 (4 bar) unstirred	C_1C_2Im NTf_2	2.3 ± 0.6	65
		C_1C_4Im NTf_2	1.1 ± 0.2	
		C_1C_6Im NTf_2	1.9 ± 0.6	
		C_1C_8Im NTf_2	2.3 ± 0.8	
		$C_1C_{10}Im$ NTf_2	100-150 sponges	
		$C_1C_1C_4Im$ NTf_2	1.8 ± 0.5	
		C_4C_4Im NTf_2	2.0 ± 0.6	
Ru(COD)(2-methylallyl)$_2$	50 °C, H_2 (4 bar)	C_1C_4Im NTf_2	2.1 ± 0.5	63
		C_1C_4Im BF_4	2.9 ± 0.5	
		$C_1C_{10}Im$ NTf_2	2.7 ± 0.5	
		$C_1C_{10}Im$ BF_4	2.1 ± 0.5	78
		$C_1(C_3CN)Im$ NTf_2	2.2 ± 0.5	
RuO_2	75 °C, H_2 (4 bar)	C_1C_4Im PF_6	2:5 ± 0:4	61
		C_1C_4Im OTf	2.0 ± 0:4	
$RuCl_3$	150 °C, H_2 (1 bar)	1,1,3,3,-tetramethyl-guanadinium lactate / SBA-15	2-5	66

[a] polyvinylpyrrolidone. [b] cellulose acetate. [c] 1,3,5-triaza-7-phosphaadamantane. [d] 3-aminopropyltriethoxysilane. [e] NPs formed in a biphasic medium, extracted into organic phase.

1.3 Catalytic properties

As mentioned previously, the major application for metallic NPs is in catalysis. In this section will be discussed several literature examples of catalytic studies performed using RuNPs produced in using different methods.

1.3.1 Nitrogen activation

Nitrogen activation for the synthesis of ammonia is an important catalytic challenge for which the use of RuNPs is reported in the literature.[39, 79] In particular, RuNPs supported on γ-alumina are active in ammonia synthesis.[31] Interestingly, it was observed that those prepared from the impregnation and reduction of $Ru_3(CO)_{12}$ present a better activity than those from $RuCl_3$ as shown in Figure 7, despite using the same preparation conditions. This is claimed to be due to the greater surface available when produced from $Ru_3(CO)_{12}$, emphasising the importance of the precursor complex chosen.[31] Using the polyol method to produce supported RuNPs resulted in an even higher activity, possibly due to the weaker interactions between the NPs and the alumina support.[20]

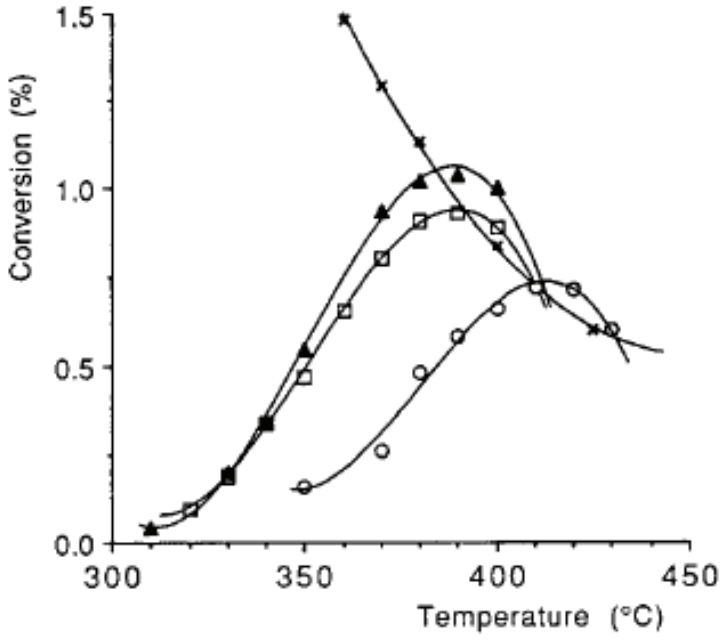

Figure 7. Dihydrogen conversion as a function of reaction temperature (N_2/H_2 = 1:3): (×) equilibrium values; (▲) 4.2% Ru [from $Ru_3(CO)_{12}$, activated under helium up to 673 K]/Al_2O_3-KOH (25.4% K); (□) 4.2% Ru [from $Ru_3(CO)_{12}$, activated under hydrogen up to 673 K]/Al_2O_3-KOH (25.4% K); (○) 5.5% Ru (from $RuC1_3$ activated under hydrogen up to 673 K)/A1203-KOH (25.4% K).[31]

1.3.2 Surface hydrides on RuNPs

One particularity of Ru, as with many noble metal surfaces, is the tendency to adsorb labile hydrides when under H_2 atmosphere.[80, 81] As in many cases the generation of these metallic NPs is performed under H_2, this layer of surface hydrides is probable. Indeed, their presence has been already proven through H-D exchange experiments in colloidal[82] and supported systems.[29]

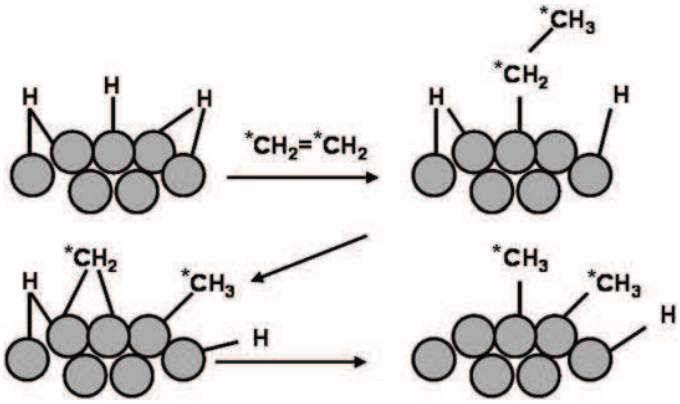

Scheme 6. Ethylene reactivity on RuNP surfaces.[82]

The activity of Ru in hydrogenation is well known and has been used to titrate the number of surface hydrides on RuNPs, both supported,[29] and in colloidal solutions.[82] Scheme 6 illustrates the reactivity of these Ru-H towards ethylene. As well as hydrogenation to give ethane, many different alkyl species can be formed on the metal surface through hydrogenolysis and homologation type processes. Therefore, in order to effectively titrate all surface hydrides, it is important to quantify both the species evolved under ethylene atmosphere and those evolved during subsequent heating under H_2, to account for the surface alkyl species.

1.3.3 Arene hydrogenation

RuNPs are known to be active catalysts in aromatic hydrogenation, and many studies are reported in the literature. Indeed, it is now commonly believed that in the hydrogenation of aromatics, the catalytic species cannot be mono-nuclear, as a metal surface is required in order to activate the π-conjugated system.[83]

A study by Su *et al.* compared the reactivity of RuNPs prepared by thermal reduction and reduction under hydrogen of $RuCl_3$ on various supports (silica and/or carbon). It was consistently found that the RuNPs prepared through thermal reduction were more active, despite often exhibiting larger size distributions. These findings were attributed to the more intensive contact

between the Ru and the carbon of the support, inducing enhanced hydrogen spill-over effects. The nature of the support was found to play a crucial role.[84]

Supported RuNPs have also been found to be effective in the hydrogenation of *N*-heterocycles, but not *S*–heterocycles, unlike tethered Ru(II) catalysts which catalyse effectively both reactions.[25] When supported on polyorganophophazanes, a recyclable catalyst system for the hydrogenation of various olefins, carbonyls and aromatics results. The material may be dissolved in environmentally friendly solvents such as water or alcohols, or used in a heterogeneous manner.[74]

Colloidal solutions of RuNPs in organic solvent have also been tested in the hydrogenation of aromatic substrates such as benzene and quinoline. In the case of benzene, a conversion of 82 % to cyclohexane was obtained after 14 h at 80 °C under 20 bar H_2 ([Sulbstrate]/[Ru] = 500, TON = 311, TOF = 16 h^{-1}).[44, 46, 68]

RuNPs stabilised by cyclodextrins in water have been found to be active in the hydrogenation of substituted aromatics such as styrene and allylbenzene under biphasic conditions with the chemoselectivity controlled by the nature of the cyclodextrin ligand.[53]

When suspended in ILs, RuNPs provide a recyclable system for the biphasic hydrogenation of arenes.[63] The catalytic reaction can be influenced by the nature of the IL. For example, RuNPs stabilised in nitrile-functionalised ILs have been observed to be selective towards the hydrogenation of nitriles but do not hydrogenate arenes.[78] Furthermore, due to the solvation properties of ionic liquids, the possibility of extracting cyclohexene during the hydrogenation of benzene over RuNPs produced *in situ* has been explored. Here the solubility difference of the cyclohexene compared to benzene may be exploited to achieve this.[62]

1.3.4 C=O hydrogenation

The reduction of aldehydes and ketones to alcohols is very easy and mainly performed with hydride reagents. Nonetheless, due to environmental and economical considerations, transition metal compounds are often preferred.[6]

Liu's team has reported the hydrogenation of citronellal to citronellol using a Ru/PVP colloid prepared by reduction with $NaBH_4$. High activity and selectivity for the desired citronellol product was observed, Scheme 7.[85]

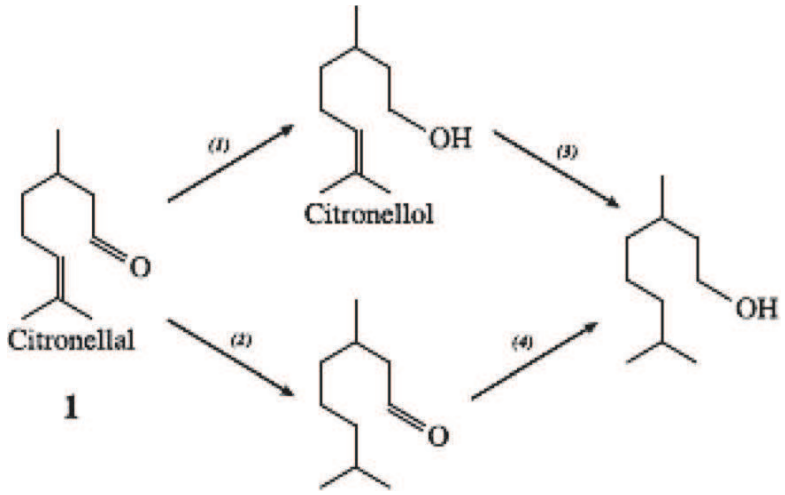

Scheme 7. The hydrogenation of citronellal and the possible products. [85]

RuNPs supported onto polyorganophophazanes in THF have been tested in the hydrogenation of several carbonyl compounds, e.g. cyclohexanone, ethyl acetoacetate, ethyl pyruvate, pyruvic acid and actetophenone. All were quantitatively converted to the corresponding alcohol under mild conditions.[74]

1.3.5 NO_2 hydrogenation

Liu and co-workers have also found PVP-stabilised RuNPs to be chemoselective in the hydrogenation of chloronitrobenzene to chloroaniline. However, the reaction rate is very slow.[86, 87]

1.3.6 Asymmetric hydrogenation

Enantio- and stereo- selectivity is often an important issue in organic synthesis and particularly challenging in NP catalysis. Therefore, attention had been devoted to the use of chiral *N*- or *P*- donor ligands as a potential way to induce enantioselectivity and perform asymmetric hydrogenations. Although asymmetric induction obtained is modest, it reveals the influence of the asymmetric ligand coordinated to the surface. The results obtained for the asymmetric hydrogenation of methylanisoles are depicted in Figure 8.[69]

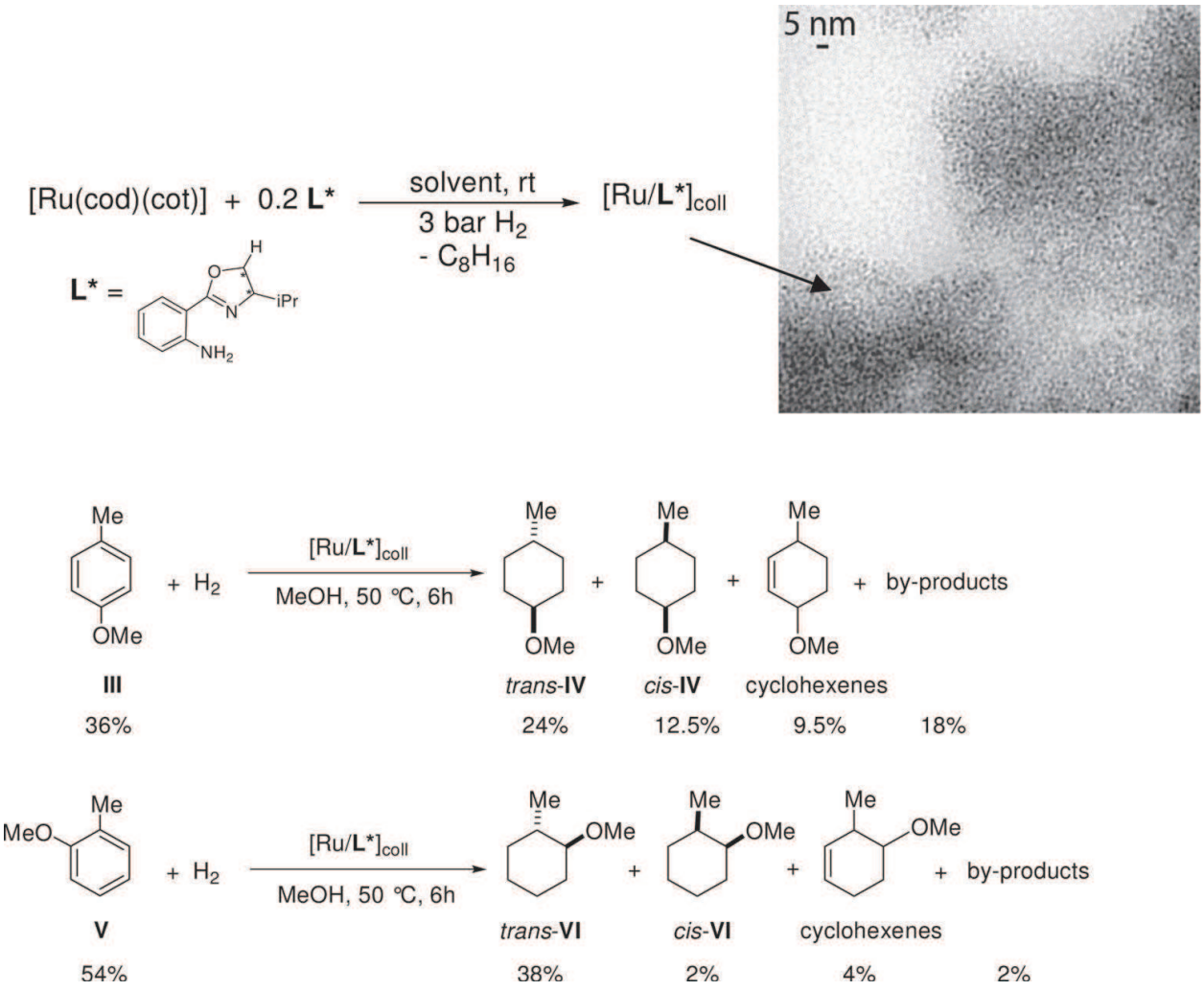

Figure 8. The synthesis of RuNPs in THF with chrial *N*-donor ligand, **L***, the TEM image of the NPs produced and the subsequent performance in the asymmetric hydrogenation of methylanisoles. [69]

The same catalyst systems were found to be active in hydrogen transfer between *iso*-propanol and acetophenone, Scheme 8. The rate of reaction was found to vary with the nature of the chiral *N*-donor ligand, and a moderate enantiomeric excess (10 %) was observed in only few cases.[69]

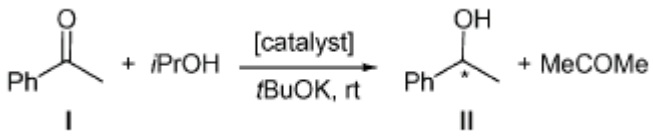

Scheme 8. Hydrogen transfer between *iso*-propanol and acetophenone. [69]

In another example in the literature, diphosphite ligands have been successfully used to stabilise small RuNPs in organic solvent and thus perform diastereoselective hydrogenations of methylanisole,[72, 73] while the use of P(*m*-$C_6H_4SO_3Na)_3$ in combination with a mixture ionic liquids and water has been shown to produce a recyclable and enantio-selective system for hydrogenation.[88] Furthermore, trioctylamine-stabilised RuNPs in a mixture of alcohol and water show a certain stereoselectivity in the hydrogenation of various substituted arenes.[89]

1.3.7 Oxidation

Catalytic oxidation processes, which are of particular interest in industry, may benefit from progress in the field of nanoclusters, but only very few examples of oxidation reactions have been reported in the literature.

One significant result has demonstrated the ability of RuNPs to oxidise cycloalkanes selectively to the corresponding ketones, e.g. cyclooctane to cyclooctanone, Scheme 9. This has been achieved with *tert*-butylhydroperoxide (*t*BHP) in a water/cyclooctane mixture, with very high selectivity.[90, 91]

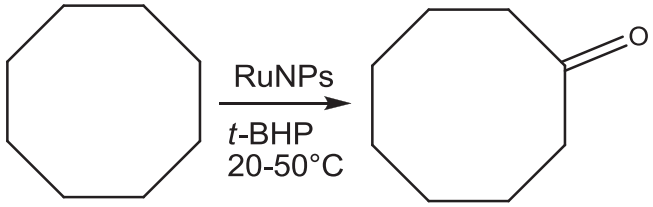

Scheme 9. Oxidation of cyclooctane to cyclooctanone over RuNPs using *t*BHP.[90, 91]

In another catalytic oxidation, RuNPs grafted onto hydroxyapatite have been found to be active in the *cis*-dihydroxylation and oxidative cleavage of alkenes, presenting excellent recyclability.[67]

The oxidation of CO to CO_2 has been achieved quantitatively using RuNPs supported in a porous alumina membrane. A slight difference was noted in activity with particle size, smaller particles being slightly more active.[92] However, this may have been related to the porous material, as when supported on a silicon wafer and stabilised by PVP, the inverse trend in activity with respect to NP size has been observed in the same reaction by Somorjai's group, Figure 9.[37] This last example demonstrates the importance of the size of the NPs in catalysis, as well as how altering the nature of the reaction medium or stabilising support may change entirely the outcome of the reaction under investigation.

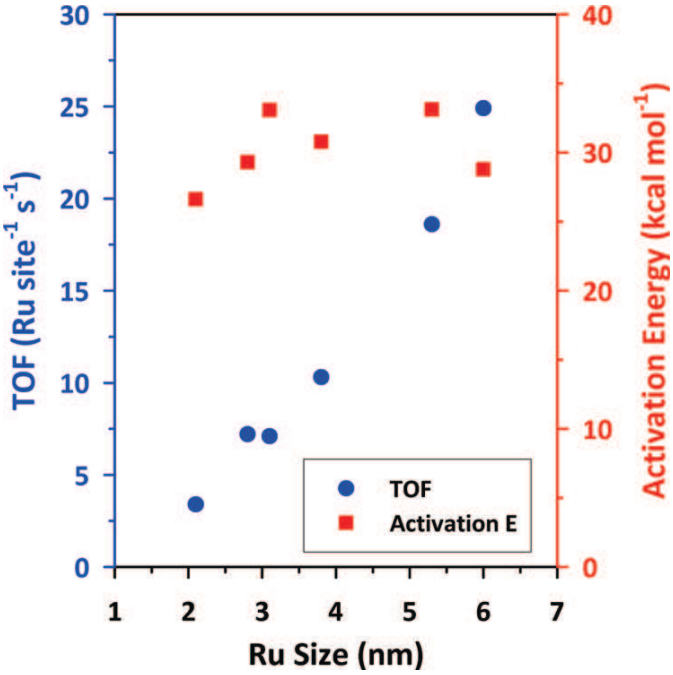

Figure 9. The variation of TOF and activiation energy with RuNP size in the catalytic oxidation of CO, studied by Somorjai's group.[37]

1.3.8 Miscellaneous

1.3.8.1 Cellubiose hydrolysis

Water-dispersed RuNPs have been shown to be active in a one-step hydrolysis of cellobiose to C_6 alcohols, an important reaction in the production of bio-fuels, Scheme 10.[93]

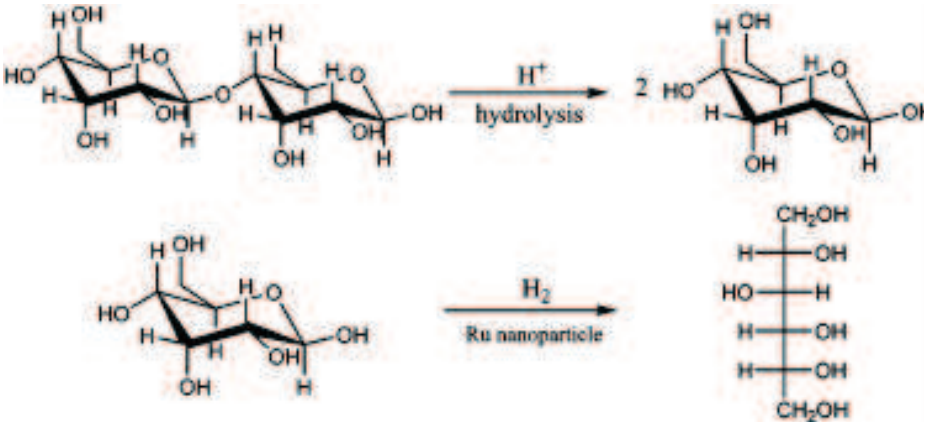

Scheme 10. The single-step conversion of cellobiose to C_6 alcohols using RuNPs.[93]

1.3.8.2 Hydrogen Generation

RuNPs dispersed in water have been found to be active catalysts in the hydrolysis of $NaBH_4$ to produce H_2, Equation (3). This is a safe way of producing H_2 due to the non-flammability of the surrounding environment.[77]

$$NaBH_4 + 2H_2O \xrightarrow{RuNPs} NaBO_2 + 4H_2 \quad (3)$$

Very recently, RuNPs coordinated by silane ligands have been found to be highly active and reusable as catalysts for the dehydrogenation of dimethylamine–borane, which could be an interesting prospect in solid hydrogen storage materials.[75]

1.3.8.3 Synthesis of novel functional materials

RuNPs have been found to be active and efficient catalysts for growth of single-walled carbon nanotubes (SWNTs), an increasingly important material in fields such as microelectronics. This occurs via a chemical vapour deposition (CVD) process.[81] RuNPs dispersed in hybrid nanomaterial are also reported as attractive materials for catalytic filters in gas sensors.[94]

1.4 Conclusion

As we can see, there has already been a great deal of work reported in the literature regarding the synthesis and catalytic applications of RuNPs. The catalytic properties of these NPs are highly dependent on their surface properties and their size. The ability to predict and control the size of the NPs produced is therefore of the utmost importance. Also, producing NPs free of ligands and other surface contaminants can only be advantageous in catalysis. In this respect, the ionic liquid route, which has been shown to produce RuNPs of a controlled size without necessitating stabilising ligands or supports, seems promising. However, in this case little is known about the stabilisation mechanism – is the surface really ligand and contaminant free? This is the first question answered in this thesis, in Chapter 2. Following this we look at the possibility of extending the potential of ionic liquids to the controlled growth and stabilisation of other catalytically active metals, namely nickel and tantalum, also in Chapter 2.

Ionic liquids are also reported as interesting media for catalysis, so performing catalysis with NPs produced *in situ* is a very intriguing prospect. However, first we must discern how the properties ionic liquid itself effect the outcome of the catalytic process. This question is answered in Chapter 3 by performing a model homogeneous catalytic reaction, namely the hydrogenation of 1,3-cyclohexadiene using an ionic Osborn-type rhodium catalyst, in different IL media.

Finally, in Chapter 4, we perform the hydrogenation of several substrates using RuNPs generated *in situ*, with precise size-control, and confirm the substantial influence that nanoparticle size can have on the catalytic performance.

1.5 References

1. G. Schmid, ed., *Nanoparticles: From Theory to Application*, Wiley-VCH, Weinheim, 2004.
2. H. Bönnemann and K. S. Nagabhushana, in *Surface and Nanomolecular Catalysis*, ed. R. M. Richards, CRC Press, Boca Raton, 2006, pp. 63-94.
3. D. Astruc, F. Lu and J. R. Aranzaes, *Angew. Chem. Int. Ed.*, 2005, **44**, 7852.
4. D. Astruc, ed., *Nanoparticles and Catalysis*, Wiley-VCH, Wienheim, 2007.
5. A. Roucoux, J. Schulz and H. Patin, *Chem. Rev.*, 2002, **102**, 3757-3778.
6. A. Roucoux, A. Nowicki and K. Philippot, in *Nanoparticles and Catalysis*, ed. D. Astruc, Wiley-VCH, Weinheim, 2007, pp. 349-390.
7. A. Roucoux and K. Philippot, in *Handbook of Homogeneous Hydrogenation*, eds. J. G. de Vries and C. J. Elsevier, Wiley-VCH Weinheim, 2007, pp. 217-256.
8. G. A. Somorjai and J. Y. Park, *Top. Catal.*, 2008, **49**, 126-135.
9. H. Bönnemann and K. S. Nagabhushana, in *Encyclopedia of Nanoscience and Nanotechnology*, ed. H. S. Nalwa, American Scientific Publishers, Stevenson Ranch, CA, 2004, pp. 777-813.
10. H. Bönnemann and K. S. Nagabhushana, in *Metal Nanoclusters in Catalysis and Materials Science: The Issue of Size-control*, eds. B. Corain, G. Schmid and N. Toshima, Elsevier, Amsterdam, 2007, pp. 21-48.
11. B. Chaudret, *Top. Organomet. Chem.*, 2005, **16**, 233-259.
12. B. Chaudret and K. Philippot, *Oil & Gas Science and Technology-Revue De L Institut Francais Du Petrole*, 2007, **62**, 799-817.
13. C. Amiens and B. Chaudret, *Mod. Phys. Lett. B*, 2007, **21**, 1133-1141.
14. J. Dupont and J. D. Scholten, *Chem. Soc. Rev.*, 2010, **39**, 1780-1804.
15. C. Bruneau and P. H. Dixneuf, eds., *Ruthenium Catalysts and Fine Chemistry*, Springer, Berlin/ Heidelberg, 2004.
16. G. C. Vougioukalakis and R. H. Grubbs, *Chem. Rev.*, **110**, 1746-1787.
17. H. Nagahara, M. Ono, M. Konishi and Y. Fukuoka, *Appl. Surf. Sci.*, 1997, **121**, 448-451.
18. A. M. R. Galletti, S. Antonetti, S. Giaiacopi, O. Piccolo and A. M. Venzia, *Top. Catal.*, 2009, **52**, 1065.

19. R. Schlögl, *Angew. Chem. Int. Ed.*, 2003, **42**, 2004-2008.
20. A. Miyazaki, L. Balint, K. Aika and Y. Nakano, *J. Catal.*, 2001, **204**, 364-371.
21. J. M. Basset and A. Choplin, *J. Mol. Catal.*, 1983, **21**, 95-108.
22. A. Theolier, A. Choplin, L. D'Ornelas and J. M. Basset, *Polyhedron*, 1983, **2**, 119-121.
23. V. L. Kuznetsov, A. T. Bell and Y. I. Yermakov, *J. Catal.*, 1980, **1980**, 374-389.
24. A. Zecchina, E. Guglielminotti, A. Bossi and M. Camia, *J. Catal.*, 1982, **74**, 225-239.
25. C. Bianchini, V. Dal Santo, A. Meli, S. Moneti, M. Moreno, W. Oberhauser, R. Psaro, L. Sordelli and F. Vizza, *J. Catal.*, 2003, **213**, 47-62.
26. M. Leconte, A. Theolier, D. Rojas and J. M. Basset, *J. Am. Chem. Soc.*, 1984, **106**.
27. E. Rodriguez, M. Leconte, J.-M. Basset, K. Tanaka and K.-I. Tanaka, *J. Am. Chem. Soc.*, 1988, **110**, 275-278.
28. N. Kitajima, A. Kono, W. Ueda, Y. Moro-oka and T. Ikawa, *J. Chem. Soc., Chem. Commun.*, 1986, 674-675.
29. R. Berthoud, P. Delichere, D. Gajan, W. Lukens, K. Pelzer, J. M. Basset, J. P. Candy and C. Coperet, *J. Catal.*, 2008, **260**, 387-391.
30. V. Hulea, D. Brunel, A. Galarneau, K. Philippot, B. Chaudret, P. J. Kooyman and F. Fajula, *Microporous Mesoporous Mater.*, 2005, **79**, 185-194.
31. P. Moggi, G. Albanesi, G. Predieri and G. Spoto, *Appl. Catal., A*, 1995, **123**, 145-159.
32. L. Y. Song, X. H. Li, H. N. Wang, H. H. Wu and P. Wu, *Catal. Lett.*, 2009, **133**, 63-69.
33. L. K. Kurihara, G. M. Chow and P. E. Schoen, *Nanostruc. Mater.*, 1995, **5**, 607-613.
34. R. Harpeness, Z. Peng, X. S. Liu, V. G. Pol, Y. Koltypin and A. Gedanken, *J. Colloid Interface Sci.*, 2005, **287**, 678-684.
35. M. Zawadzki and J. Okal, *Mater. Res. Bull.*, 2008, **43**, 3111-3121.
36. X. P. Yan, H. F. Liu and K. Y. Liew, *J. Mater. Chem.*, 2001, **11**, 3387-3391.
37. S. H. Joo, J. Y. Park, J. R. Renzas, D. R. Butcher, W. Huang and G. A. Somorjai, *Nano Lett.*, 2010, **10**, 2709-2713.
38. G. Viau, R. Brayner, L. Poul, N. Chakroune, E. Lacaze, F. Fievet-Vincent and F. Fievet, *Chem. Mater.*, 2003, **15**, 486-494.
39. Q. C. Xu, J. D. Lin, X. Z. Fu and D. W. Liao, *Catal. Commun.*, 2008, **9**, 1214-1218.
40. S. Gao, J. Zhang, Y. F. Zhu and C. M. Che, *New J. Chem.*, 2000, **24**, 739-740.
41. B. Chaudret, *C.R. Phys.*, 2005, **6**, 117-131.

42. B. Chaudret, *Actual. Chim.*, 2005, 33-43.
43. K. Philippot and B. Chaudret, *C.R. Chim.*, 2003, **6**, 1019-1034.
44. K. Pelzer, K. Philippot, B. Chaudret, W. Meyer-Zaika and G. Schmid, *Z. Anorg. Allg. Chem.*, 2003, **629**, 1217-1222.
45. O. Vidoni, K. Philippot, C. Amiens, B. Chaudret, O. Balmes, J.-O. Malm, J.-O. Bovin, F. Senocq and M. J. Casanove, *Angew. Chem. Int. Ed.*, 1999, **38**, 3736-3738.
46. K. Pelzer, O. Vidoni, K. Philippot, B. Chaudret and V. Colliere, *Adv. Funct. Mater.*, 2003, **13**, 118-126.
47. A. Duteil, R. Queau, B. Chaudret, R. Mazel, C. Roucau and J. S. Bradley, *Chem. Mater.*, 1993, **5**, 341-347.
48. C. Pan, K. Pelzer, K. Philippot, B. Chaudret, F. Dassenoy, P. Lecante and M. J. Casanove, *J. Am. Chem. Soc.*, 2001, **123**, 7584-7593.
49. T. Pery, K. Pelzer, G. Buntkowsky, K. Philippot, H. H. Limbach and B. Chaudret, *ChemPhysChem*, 2005, **6**, 605-607.
50. K. Pelzer, B. Laleu, F. Lefebvre, K. Philippot, B. Chaudret, J. P. Candy and J. M. Basset, *Chem. Mater.*, 2004, **16**, 4937-4941.
51. P.-J. Debouttiere, V. Martinez, K. Philippot and B. Chaudret, *Dalton Trans.*, 2009, 10172-10174.
52. N. Mejias, A. Serra-Muns, R. Pleixats, A. Shafir and M. Tristany, *Dalton Trans.*, 2009, 7748-7755.
53. A. Nowicki, Y. Zhang, B. Leger, J. P. Rolland, H. Bricout, E. Monflier and A. Roucoux, *Chem. Commun.*, 2006, 296-298.
54. A. Denicourt-Nowicki, A. Ponchel, E. Monflier and A. Roucoux, *Dalton Trans.*, 2007, 5714-5719.
55. C. Hubert, A. Denicourt-Nowicki, A. Roucoux, D. Landy, B. Leger, G. Crowyn and E. Monflier, *Chem. Commun.*, 2009, 1228-1230.
56. J. Y. Lee, J. Yang, T. C. Deivaraj and H. P. Too, *J. Colloid Interface Sci.*, 2003, **268**, 77-80.
57. J. Yang, J. Y. Lee, T. C. Deivaraj and H. P. Too, *J. Colloid Interface Sci.*, 2004, **271**, 308-312.
58. J. Yang, T. C. Deivaraj, H. P. Too and J. Y. Lee, *Langmuir*, 2004, **20**, 4241-4245.

59. R. A. Sanchez-Delgado, N. Machalaba and N. Ng-A-Qui, *Catal. Commun.*, 2007, **8**, 2115-2118.
60. T. Tsukatani and H. Fujihara, *Langmuir*, 2005, **21**, 12093-12095.
61. L. M. Rossi, G. Machado, P. F. P. Fichtner, S. R. Teixeira and J. Dupont, *Catal. Lett.*, 2004, **92**, 149-155.
62. E. T. Silveira, A. P. Umpierre, L. M. Rossi, G. Machado, J. Morais, G. V. Soares, I. J. R. Baumvol, S. R. Teixeira, P. F. P. Fichtner and J. Dupont, *Chem.--Eur. J.*, 2004, **10**, 3734-3740.
63. M. H. G. Prechtl, M. Scariot, J. D. Scholten, G. Machado, S. R. Teixeira and J. Dupont, *Inorg. Chem.*, 2008, **47**, 8995-9001.
64. T. Gutel, J. Garcia-Anton, K. Pelzer, K. Philippot, C. C. Santini, Y. Chauvin, B. Chaudret and J.-M. Basset, *J. Mater. Chem.*, 2007, **17**, 3290-3292.
65. T. Gutel, C. C. Santini, K. Philippot, A. Padua, K. Pelzer, B. Chaudret, Y. Chauvin and J.-M. Basset, *J. Mater. Chem.*, 2009, **19**, 3624-3631.
66. J. Huang, T. Jiang, B. Han, W. Wu, Z. Liu, Z. Xie and J. Zhang, *Catal. Lett.*, 2005, **103**, 59-62.
67. C. M. Ho, W. Y. Yu and C. M. Che, *Angew. Chem. Int. Ed.*, 2004, **43**, 3303-3307.
68. K. Pelzer, K. Philippot and B. Chaudret, *Z. Phys. Chem.*, 2003, **217**, 1539-1547.
69. S. Jansat, D. Picurelli, K. Pelzer, K. Philippot, M. Gomez, G. Muller, P. Lecante and B. Chaudret, *New J. Chem.*, 2006, **30**, 115-122.
70. M. Tristany, B. Chaudret, P. Dieudonne, Y. Guari, P. Lecante, V. Matsura, M. Moreno-Manas, K. Philippot and R. Pleixats, *Adv. Funct. Mater.*, 2006, **16**, 2008-2015.
71. I. Favier, S. Massou, E. Teuma, K. Philippot, B. Chaudret and M. Gomez, *Chem. Commun.*, 2008, 3296-3298.
72. A. Gual, M. R. Axet, K. Philippot, B. Chaudret, A. Denicourt-Nowicki, A. Roucoux, S. Castillon and C. Claver, *Chem. Commun.*, 2008, 2759-2761.
73. A. Gual, C. Godard, K. Philippot, B. Chaudret, A. Denicourt-Nowicki, A. Roucoux, S. Castillon and C. Claver, *ChemSusChem*, 2009, **2**, 769-779.
74. A. Spitaleri, P. Pertici, N. Scalera, G. Vitulli, M. Hoang, T. W. Turney and M. Gleria, *Inorg. Chim. Act.*, 2003, **352**, 61-71.

75. M. Zahmakiran, M. Tristany, K. Philippot, K. Fajerwerg, S. Oezkar and B. Chaudret, *Chem. Commun.*, 2010, **46**, 2938-2940.
76. J. Yang, J. Y. Lee, T. C. Deivaraj and H. P. Too, *Colloids Surf., A*, 2004, **240**, 131-134.
77. S. Ozkar and M. Zahmakiran, *J. Alloys Compd.*, 2005, **404**, 728-731.
78. M. H. G. Prechtl, J. D. Scholten and J. Dupont, *J. Mol. Catal. A: Chem.*, 2009, **313**, 74-78.
79. Q. C. Xu, J. D. Lin, J. Li, X. Z. Fu, Y. Liang and D. W. Liao, *Catal. Commun.*, 2007, **8**, 1881-1885.
80. J. R. Anderson, ed., *Structure of metallic Catalysts*, Academic Press, London, 1975.
81. J. Okal, *Catal. Commun.*, 2010, **11**, 508-512.
82. J. Garcia-Anton, M. R. Axet, S. Jansat, K. Philippot, B. Chaudret, T. Pery, G. Buntkowsky and H. H. Limbach, *Angew. Chem. Int. Ed.*, 2008, **47**, 2074-2078.
83. C. M. Hagen, G. Vieille-Petit, G. Laurenczy, G. Suss-Fink and R. G. Finke, *Organometallics*, 2005, **24**, 1819-1831.
84. F. Su, L. Lv, F. Y. Lee, T. Liu, A. I. Cooper and X. S. Zhao, *J. Am. Chem. Soc.*, 2007, **129**, 14213-14223.
85. W. Yu, H. Liu, M. Liu and Z. Liu, *J. Colloid Interface Sci.*, 1998, **208**, 439.
86. M. Liu, W. Yu and H. Liu, *J. Mol. Catal.*, 1999, **243**, 120.
87. M. Liu, W. Yu, H. Liu and J. Zheng, *J. Colloid Interface Sci.*, 1999, **214**, 231.
88. J. Wang, J. Feng, R. Qin, H. Fu, M. Yuan, H. Chen and X. Li, *Tetrahedron: Asymmetry*, 2007, **18**, 1643-1647.
89. F. Fache, S. Lehuede and M. Lemaire, *Tetrahedron Lett.*, 1995, **36**, 885.
90. F. Launay and H. Patin, *New J. Chem.*, 1997, **21**, 247.
91. F. Launay, A. Roucoux and H. Patin, *Tetrahedron Lett.*, 1998, **39**, 1353.
92. H. P. Kormann, G. Schmid, K. Pelzer, K. Philippot and B. Chaudret, *Z. Anorg. Allg. Chem.*, 2004, **630**, 1913-1918.
93. N. Yan, C. Zhao, C. Luo, P. J. Dyson, H. Liu and Y. Kou, *J. Am. Chem. Soc.*, 2006, **128**, 8714-8715.
94. V. Matsura, Y. Guari, C. Reye, R. J. P. Corriu, M. Tristany, S. Jansat, K. Philippot, A. Maisonnat and B. Chaudret, *Adv. Funct. Mater.*, 2009, **19**, 3781-3787.

II

Chapter 2

Generation and Stabilisation of Transition Metal Nanoparticles in Imidazolium-Based Ionic Liquids

Chapter 2

Generation and Stabilisation of Transition Metal Nanoparticles in Imidazolium-Based Ionic Liquids

2.1 Introduction

During the last decade, the use of ionic liquids (ILs) has become a very popular route for the generation of transition metal nanoparticles (NPs).[1] The main advantage over traditional solvents is that IL media are able to stabilise NPs in the absence of further additives such as ligands, inhibiting metal coalescence to the bulk.[2] For catalytic applications this is good news, as the surface of the resultant NPs is ligand-free and therefore completely available for the coordination of substrates. However, the question of *precisely how* ILs stabilise transition metal NPs remains under debate.

Very little data is available in the literature to explain this phenomenon, and much is speculative.[3] Many describe *"electrosteric stabilisation"* whereby an electrostatic double layer of anions and cations surround the electropositive NP surface.[4, 5] These NP-IL aggregates are therefore separated by electrostatic repulsion, Derjaugin–Landau–Verwey–Overbeek-type forces (DLVO), Scheme 1.[3, 6-8] A small angle X-ray scattering (SAXS) study of various ILs in the presence and absence of IrNPs has provided evidence to suggest the ordering of the ions around the NP surface, corroborating the DLVO model.[9]

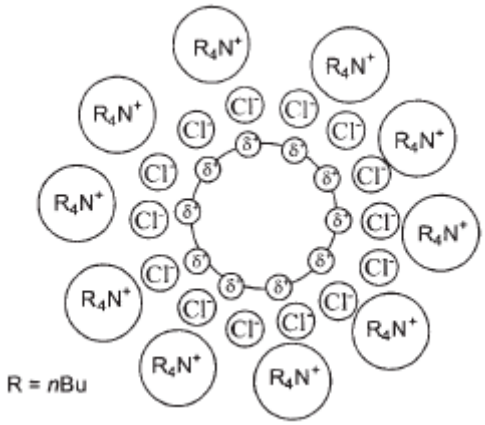

Scheme 1. An electrosterically stabilised nanoparticle in tetrabutyl ammonium chloride.[10]

Surface enhanced Raman spectroscopy (SERS) has been used to probe the interactions between an imidazolium based IL and the surface of AuNPs generated *in situ*, providing evidence for a planar interaction between the imidazolium ring and the NP surface, but very little interaction between the anion and the NP.[11] This is clearly contradictory to the much discussed DLVO model. Furthermore, the coordination of the IL moieties to the NP surface could be

envisaged. Indeed, this has been evidenced for IrNPs synthesised by reduction of an ionic organometallic complex in the ionic liquid $[C_1C_4Im][BF_4]$. Subsequent treatment of the mixture under deuterium, followed by ^2H NMR analysis showed that hydrogen-deuterium exchange had occurred on the imidazolium ring, Figure 1. This was used to evidence the formation of labile N-heterocyclic (NHC) ligands, namely imidazolylidene, however given the acidic nature of the C_2-H of the imidazolium ring this exchange would be facile and therefore the conclusion seems speculative.[12, 13]

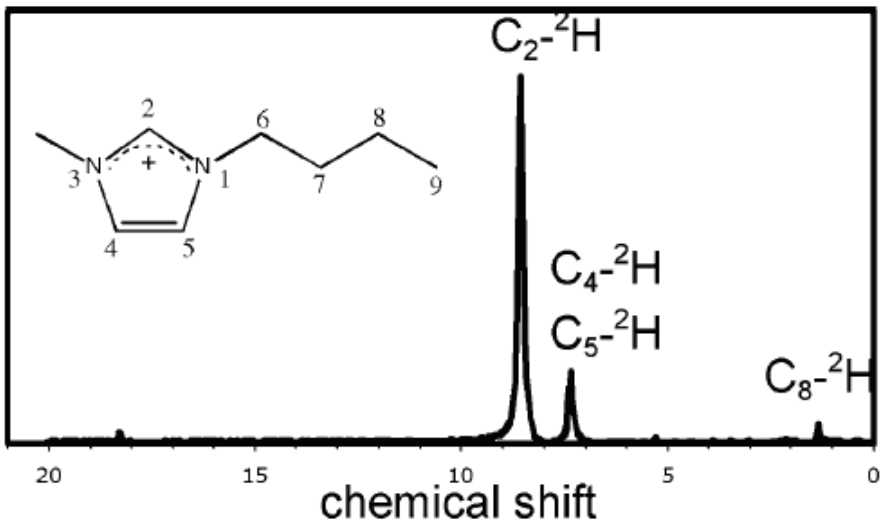

Figure 1. ^2H NMR spectrum of $[C_1C_4Im]^+$ after treatment under D_2 in the presence of IrNPs.[12, 13]

If these literary observations are believed, it seems that the stabilisation of NPs is a complex issue, dependent on the nature of both the metal and the IL in question, not to mention the synthetic route. To the best of our knowledge, no stabilisation mechanism has been proposed for RuNPs in ILs to date. Consequently, in this chapter we investigate and discuss the stabilisation mechanism for RuNPs in imidazolium ILs. Following this, the possibility of generalising our findings to other transition metals is explored.

2.2 The stabilisation of ruthenium nanoparticles in ionic liquids

ILs, particularly those based on imidazolium, can be thought of as *"supramolecular fluids"*, since in the liquid state they display a high degree of self-organisation. In these media, ionic channels, formed by extended hydrogen-bond networks between the anions and cation headgroups, coexist with non-polar *"pockets"*, created by the grouping of lipophilic alkyl side chains, illustrated in Scheme 2.[14-17]

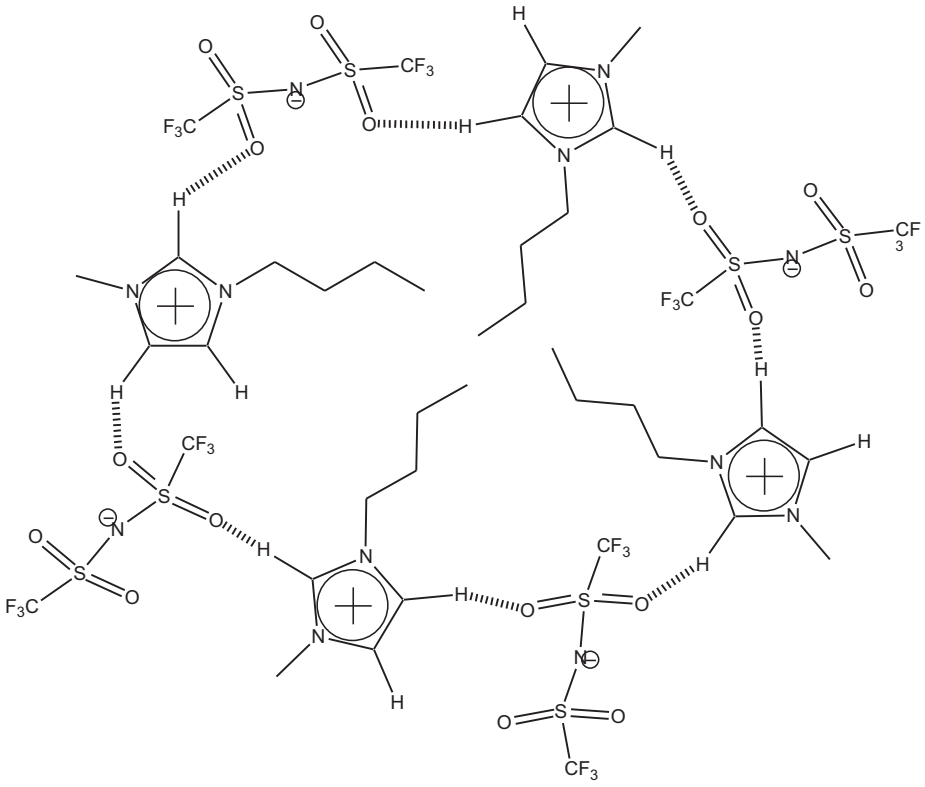

Scheme 2. Representation of intermolecular organisation in $[C_1C_4Im][NTf_2]$ in the liquid state: ionic channel linked through H-bonds and consequent aggregation of alkyl chains.

This structural organisation of ILs can be used as an entropic driver for the spontaneous self-assembly of nanoscale structures with long-range order.[18] For this purpose, ILs have already been used as media for the synthesis of some zeolite-related, microporous aluminophosphates or ordered mesoporous materials in which ILs have served both as solvents and as structure-directing agents.[19]

This segregation of polar and non-polar domains in imidazolium-based ILs dictates their interactions with given solutes. Polar or ionic species, e.g. water, will preferentially dissolve in

the polar regions, whereas non-polar lipophilic compounds, e.g. hexane, will be concentrated in the non-polar pockets.[20]

The synthesis of RuNPs by direct reduction RuO_2 is reported, however this leads to the presence of an oxide surface and/or strongly coordinating water ligands, which are difficult to remove.[21] The decomposition of (η^4-1,5-cyclooctadiene)(η^6-1,3,5-cyclooctatriene)ruthenium(0), Ru(COD)(COT), by hydrogen is a well known route to obtaining RuNPs, in both organic,[22, 23] and ionic liquid media, Scheme 3.[24-26] The main advantage of this halogen-free synthesis is that the only side product, cyclooctane, is easily removed under vacuum. This organometallic complex is non-polar and therefore when dissolved in an ionic liquid is concentrated in the aforementioned non-polar pockets. This principle has already been exploited in our laboratory in the size-controlled synthesis of RuNPs from Ru(COD)(COT) in various imidazolium ILs (1-alkyl-3-methylimidazolium bis(trifluoromethylsulphonyl)imide $[C_1C_nIm][NTf_2]$, n = 2, 4, 6, 8, 10).[26] The local concentration of organometallic precursor, therefore number of Ru atoms, is controlled by the size of these non-polar pockets, which in turn is dictated by the length of the alkyl side chain. As a result, after decomposition under molecular hydrogen the resulting RuNPs are small, with narrow size distributions. Their mean diameter varies with the length of the imidazolium alkyl side chain, as seen in Figure 2. It is worth nothing that for both short (n = 2) and long (n = 10) alkyl chains, size control is not achieved, due to lack of domain segregation for the former and interconnection of the non-polar pockets for the latter.

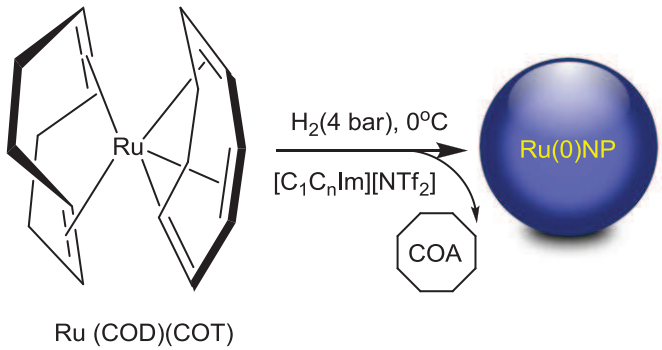

Scheme 3. The synthesis of RuNPs from the decomposition under H_2 of Ru(COD)(COT) in ILs

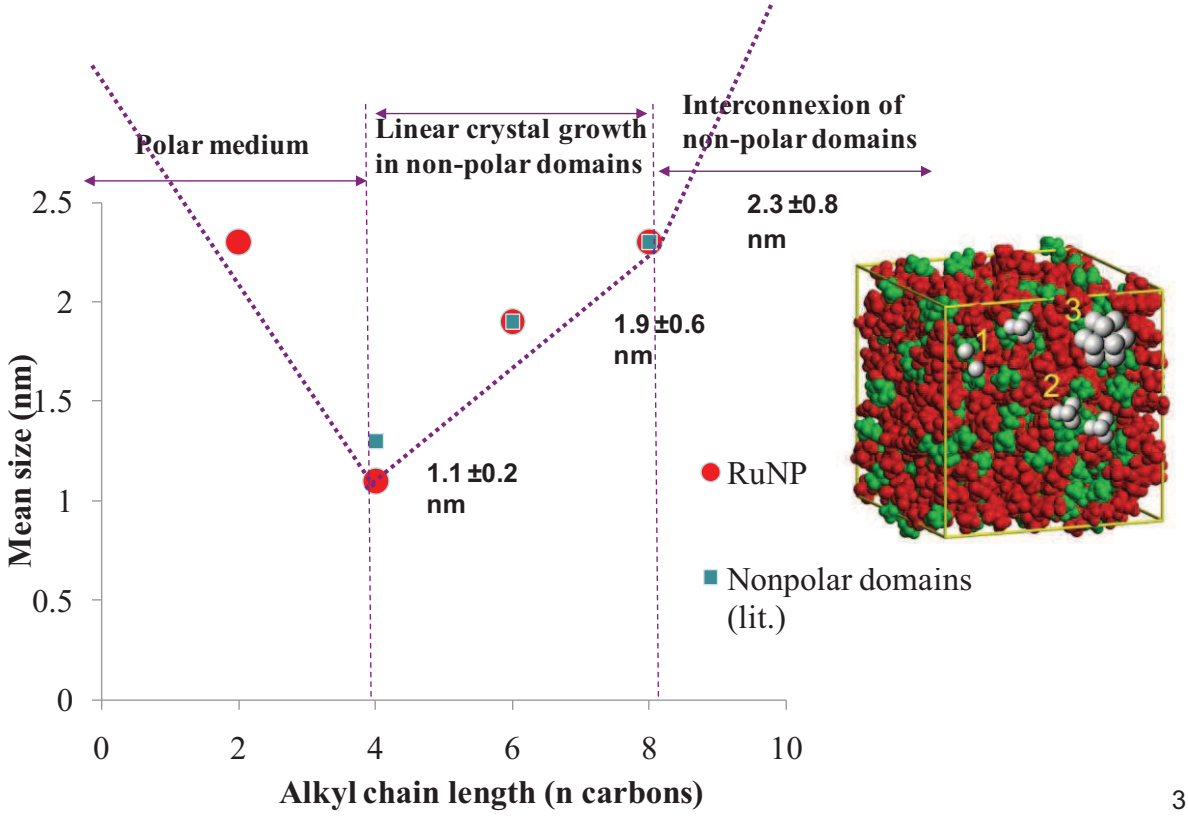

Figure 2. Graph to show the variation in RuNP size with repect to imidazlolium side alkyl chain length. (circles)[26] Also plotted, experimentally measured mean diameter of non-polar domains with respect to alkyl chain length. (squares) [15]

The RuNP/IL solutions obtained via this method remain stable indefinitely under inert atmosphere and ambient conditions, with no coalescence or precipitation observed. Given the apparent absence of ligands, the reason behind this stability is unknown.

When carried out at low temperatures (0 °C) in the absence of stirring in 1-butyl-3-methylimidazolium bis(trifluorosulphonyl)imide, $[C_1C_4Im][NTf_2]$, this procedure consistently yields the smallest small NPs with the narrowest size distribution (mean size: 1.1 ± 0.2 nm calculated from TEM images realised *in situ*).[25] These conditions have been replicated throughout this work, to obtain fresh IL-stabilised colloidal solutions, on which NMR and mass spectroscopy experiments have been performed, to determine the key points in their stabilisation.

2.2.1 *In situ* evidence of surface hydrides

The presence of surface hydrides has already been reported on RuNPs in organic solvents.[23, 27-29] Furthermore, in heterogeneous catalysis, it is well-known that under hydrogen atmosphere, the surface of late transition metals is covered by hydrides.[30-32] In ILs, is such

coverage still possible? Given the current and general stabilisation theory concerning NPs in ILs, (strong interaction between the NPs and anion or cation, DLVO model),[6, 33] the formation of surface hydrides could be inhibited. Surface hydrides on NPs in ILs have to the best of our knowledge never been reported or envisaged.

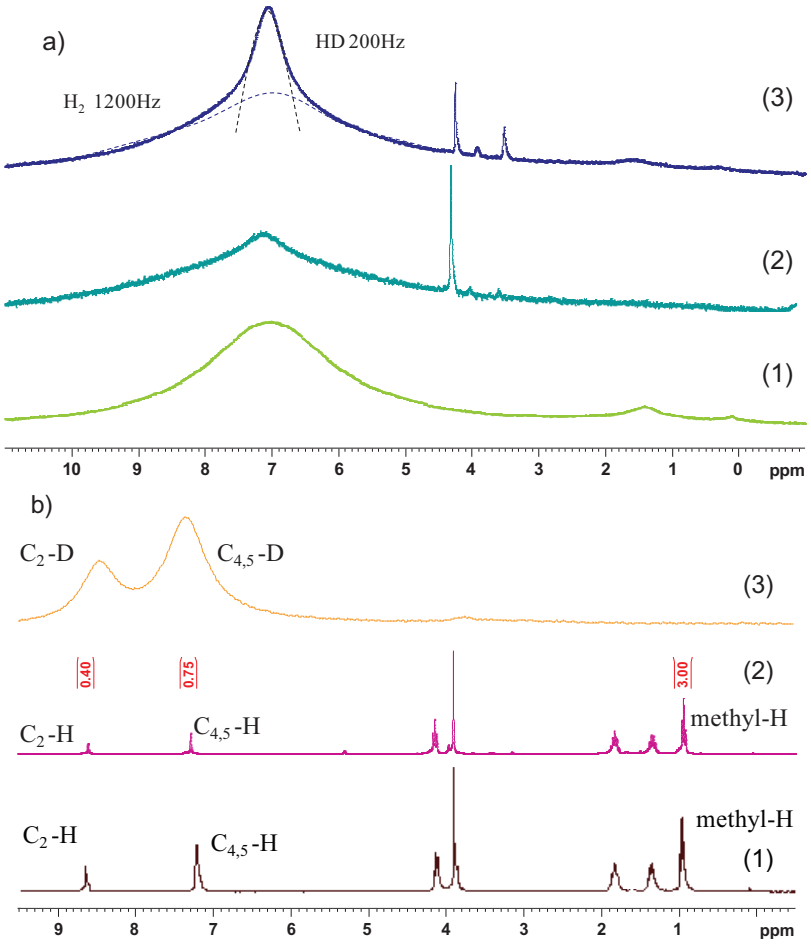

Figure 3a) ^{1}H NMR of gas phase (1) pure H_2, (2) gas phase after 1 hour dynamic vacuum and 1 day under deuterium, (3) gas phase after 4 hours dynamic vacuum and 4 days stirring under deuterium; **b)** (1) ^{1}H NMR spectrum of IL after NP formation under H_2 and evacuation of H_2 and cyclooctane, (2) ^{1}H and (3) ^{2}H NMR spectra of the reaction medium after addition of D_2.

2.2.1.1 H/D exchange by gas phase ^{1}H NMR spectroscopy

Due to the low solubility of H_2 in ILs,[34] the remaining H_2 dissolved after decomposition of Ru(COD)(COD) is totally removed under high vacuum. A solution of freshly prepared RuNPs in $[C_1C_4Im][NTf_2]$ (IL_1) was thus first treated under dynamic vacuum (10^{-5} mbar, 1 h or 4 h) and then stirred under deuterium (1 bar at 25 °C, 1 day or 4 days). The gas phase was then expanded

into an airtight Young NMR tube. The ^{1}H NMR spectrum obtained exhibited a broad peak, ($w_{½}$ = 1200 Hz) corresponding to H_2, superimposed with a finer peak ($w_{½}$ = 200 Hz) corresponding to HD, the intensity increasing with reaction time, Figure 3a. This is in agreement with previous findings in the literatue for RuNPs in organic solvents,[28] or supported on oxides,[31, 32] and allows us to assign the HD desorption as resulting from deuterium activation on RuNPs and recombination with bound H atoms, as observed on metal surfaces, Scheme 4.

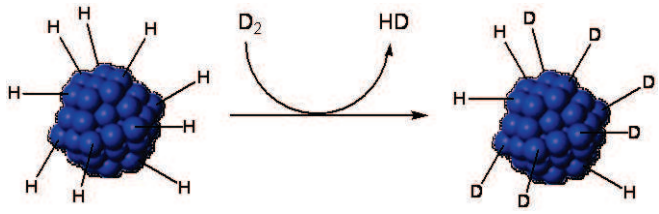

Scheme 4. H-D exchange on the RuNP surface.

The fact that there is ~ 60 % H/D exchange on positions 2, 4 and 5 of the imidazolium ring, as shown by ^{1}H and ^{2}H NMR spectra of the IL, Figure 3b, could suggest that the HD formed is due to this exchange and not from putative surface hydrides. However, when the ionic liquid is treated under D_2 in the absence of RuNPs, no H/D exchange is observed. The observed H/D exchange must inevitably involve RuNP surface. To prove the presence of these surface hydrides, further experiments have been performed characteristic of metal surface reactivity, such as hydrogenation, as detailed in the following section.

2.2.1.2 Reaction with ethylene

The reaction of alkenes with PVP- (polyvinylpyrrolidone-) and ligand-stabilised RuNPs has recently been used to quantify the surface hydrides.[29] A similar approach was transposed to a solution of RuNPs in IL_1. In the following discussion, the RuNPs were generated in 2mL of IL_1 from 86 µmol of Ru(COD)(COT). Given that the dispersion of NPs, (*D*, i.e the ratio surface atoms N_s per total number of atoms N_t, $D = N_s/N_t$), is correlated to their size,[30, 35, 36] we could estimate that for RuNPs of 1.1 nm the dispersion is 83 %, corresponding for 86 µmol of Ru(COD)(COT) to $N_S \approx 71$ µmol of Ru surface atoms. This IL_1-stablised RuNP solution was flushed overnight with argon to remove dissolved hydrogen. Then the solution was stirred under an ethylene atmosphere (105.5 mbar) at 25°C. After 24 h of reaction the system reached equilibrium, i.e. the pressure remained constant. In the gas phase, analysed by GC, 11 ± 1 µmol of ethane and 0.1 µmol of iso-butane were found, corresponding to at least 22 ± 1 µmol of

surface hydride: ($C_2H_4 + H_2 \rightarrow C_2H_6$). Note that butenes (*trans*- and 1-) were also observed (0.2 μmol), however no hydrogen would be consumed in their formation. In summary, IL_1-stabilised RuNPs reacted with ethylene at room temperature to give ethane (hydrogenation) and surface-bound alkyl species (homologation).[37, 38]

To quantify the total amount of surface-bound alkyl species, the gas phase was evacuated and substituted by H_2 (120 mbar) and the medium was heated at 100 °C for 12 h. In the gas phase, methane (4.6 μmol), ethane (8.2 μmol), propane (2.7 μmol), n-butane (1.0 μmol) and n-pentane (0.1 μmol) were detected, corresponding to at least a further 16 μmol of hydrides. Knowing the total amount of surface Ru atoms available (65 μmol) and the number of surface hydrides consumed in all the hydrogenation reactions (38 μmol) it is possible to calculate the ratio of hydrides per surface Ru atom: c.a. 0.6 H /Ru_S.* The combination of these results provides substantial evidence for the existence of surface hydrides on the IL_1-stabilised RuNPs, although the level of error in the quantitative results means that it is difficult to establish accurately the quantity. The amount of H adsorbed on PVP- and ligand- stabilised RuNPs in organic solvent is reported between 1.1-1.3 H/Ru_S,[28]and between 1 and 2 H/Ru_S for RuNPs supported on oxides.[31, 32] Note that if the IL_1-stabilised solutions of RuNP were treated under high vacuum (10^{-6} mbar) overnight at room temperature, instead of being flushed with argon to remove the dissolved H_2, ethylene conversion is negligible. This suggests that the surface hydrides on RuNPs are labile and almost completely desorbed under high vacuum.[39-41]

Indeed, hydrides bound to metal surfaces are known to be labile and the dissociation of H_2 adsorbed onto a metal surface is reversible: $M + H_2 \leftrightarrow MH_2 \leftrightarrow 2\ M–H$. In the case of Ru, about 2/3 of the total amount of surface hydrides are reversibly bound. These H species correspond to more weakly adsorbed hydrogen on the surface, which is easily removed by treating the sample under vacuum at 25 °C.[31, 32].This explains why the hydrogenation of ethylene (in the absence of hydrogen) does not occur over NPs previously treated under high dynamic vacuum (10^{-5} mbar) for an extended period (12 h), as very few surface hydrides remain.[39-41] It is nevertheless very interesting that the presence of hydrides on ruthenium particles in ionic liquids is confirmed, since this is in agreement with the presence of these nanoparticles in uncharged lipophilic domains.

* For calculations see experimental section 2.5.6

2.2.2 Stabilising effect of the surface hydrides

In order to ascertain the stabilising effect of hydrogen, two aliquots of the RuNP/IL_1 solution were taken and stirred at 100 °C for a period of 24 h, either under H_2 or under Ar (1 bar). The resulting solutions were analysed by TEM. For the aliquot heated under H_2, the mean size of the RuNPs increased to 1.4 ± 0.7 nm, and for the aliquot heated under argon, the mean size increases to 2.2 ± 0.8 nm. This difference in size increase with the gas atmosphere demonstrates the inferior stability of the particles when heated under argon compared to under H_2. In addition, when the RuNP/IL_1 solution was treated under high vacuum (10^{-6} mbar) overnight at room temperature, the TEM images show an increase in size from 1.1 ± 0.2 nm to 1.7 ± 0.4 nm, Figure 4. From these results, it appears that there is less coalescence of the RuNPs when heated under H_2 at 100 °C than under argon at the same temperature. This may be explained by the elimination of the hydrogen atoms reversibly bound to the metal surface, which is made likely by heating under an inert atmosphere or treatment under high vacuum. In conclusion, the presence of surface Ru–H stabilises the RuNPs. The results of these stability experiments are also consistent with the lability of the hydrides which can be desorbed from the nanoparticles *in vacuo* or at 100 °C.

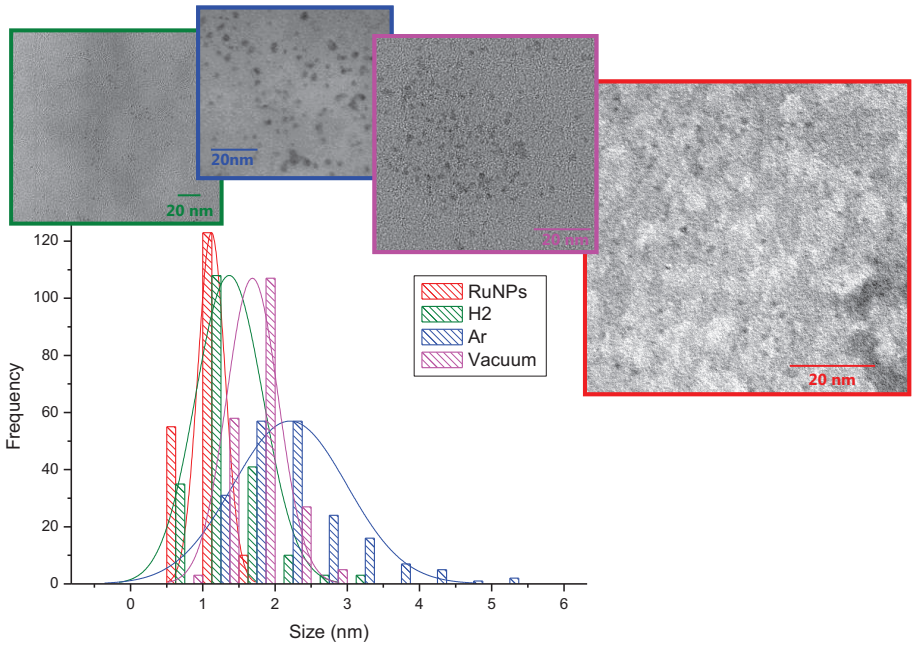

Figure 4. TEM images captured *in situ* in ionic liquids and comparative size histograms of RuNPs/[C_1C_4Im][NTf_2] (1.1 ± 0.2 nm) heated to 100 °C for 24h under H_2, under Ar and kept under dynamic vacuum (10^{-5} mbar) for 24 h at 25 °C.

In further tests, samples of these NP solutions were stirred under pure CO or pure O_2 atmosphere (1 bar) during a period of 24 h. It was seen that under O_2 the NPs underwent slight coalescence, growing to a size of 1.5 ± 0.4 nm, and those resulting from stirring under CO exhibited an interesting bimodal size distribution centred at 1.3 and 1.8 nm, Figure 5. It is worth noting that the number of RuNPs smaller than 1 nm increases probably due to the formation of ruthenium carbonyl clusters. Due to the low concentration of RuNPs in solution, ν(CO) for coordinated CO was not observed by IR spectroscopy. In comparison with H_2, O_2 and CO appear to have a destabilising effect, inducing slight agglomeration.

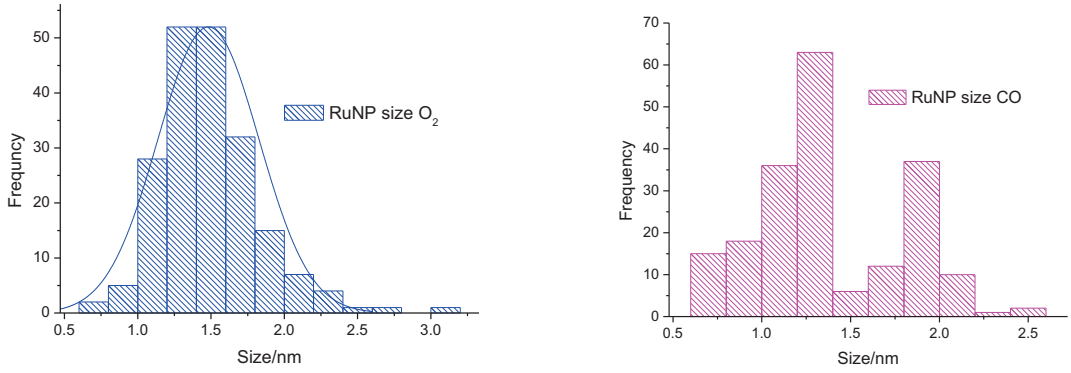

Figure 5. Size distribution histograms of RuNPs formed in IL_1 after treatment under dry O_2 (left) and CO (right).

2.2.3 Evidence for close proximity between the RuNP surface and the alkyl chains

The fact that in $[C_1C_nIm][NTf_2]$, the non-polar domains control the local concentration of Ru(COD)(COT) and consequently the size of RuNPs generated *in situ*, could allow us to consider them as nanoreactors in which the phenomenon of crystal growth occurs.[26] If the RuNPs are indeed encapsulated in these non-polar pockets, it would be expected that the side alkyl groups of the ILs be in close proximity or even in interaction with the RuNP surface.

To demonstrate this, the RuNPs were synthesised under deuterium instead of hydrogen (following otherwise identical reaction conditions), since an H-D exchange on the side group of the IL would prove the existence of the NPs in these domains. In the case of IL_1, ^{2}H NMR spectra show us that, as expected, deuteration occurs at all positions on the imidazolium ring due to the relatively high acidity of these protons. Furthermore, one small peak is apparent at ~1.5 ppm, which may correspond to deuteration at position C_8, i.e. the penultimate carbon of the butyl chain, however this is not irrefutable. The intensities of the peaks in the ^{1}H NMR spectrum

were reduced by roughly 30 % at positions C_2, C_4 and C_5, but no significant reduction in intensity was noted for any of the alkyl peaks. ESI mass spectra indicate the formation of mono-, di-, tri- and a trace amount of tetra-deuterated species. This is in agreement with the higher reactivity of the hydrogen bound to the imidazolium ring than to the alkyl side chain. Note that, in contrast to findings for IrNPs, [5] where the deuteration was found mainly at position C_2, for RuNPs deuterium incorporation occurs equally at positions C_2, C_4 and C_5 on the imidazolium ring.

This experiment was then carried out in ILs with unsaturated functional side groups: 1-(but-3-enyl)-3-methylimidazolium bis(trifluorosulphonyl)imide $[C_1C_{4//}Im][NTf_2]$, IL_2 and 1-benzyl-3-methylimidazolium bis(trifluorosulphonyl)imide $[C_1BzIm][NTf_2]$, IL_3. These functionalised side groups are more susceptible to H-D exchange.

2.2.3.1 $[C_1C_{4//}Im][NTf_2]$, IL_2:

TEM images of nanoparticles synthesised in IL_2 under deuterium at 0°C show that the nanoparticle size distribution is similar to that of RuNPs synthesised in IL_1. This result provides supplementary evidence to suggest that the size is dictated by the length of the alkyl chain and that the RuNPs are formed in the non-polar domains of the ILs, Figure 6.

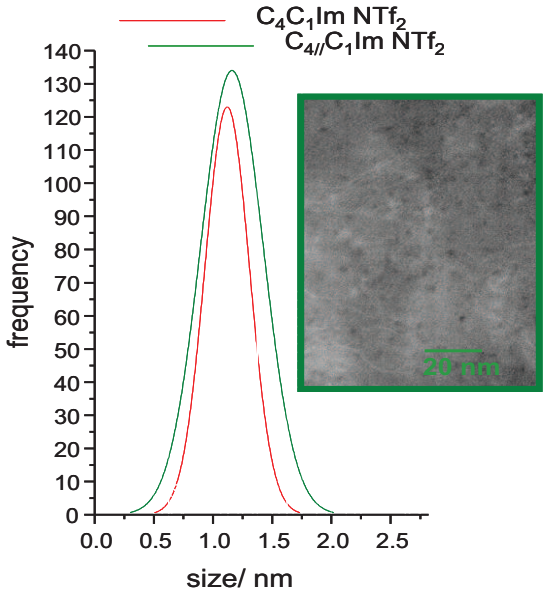

Figure 6. Comparative size distribution curves for RuNPs synthesised in IL_1 and IL_2 and TEM image captured *in situ* IL for RuNPs synthesised in IL_2

For IL_2, ^2H NMR spectra show that deuteration takes place at positions C_8 and C_9, i.e. the olefinic positions, as well as at position C_2. Surprisingly, isotopic exchange is observed neither at

positions C_4 and C_5 of the imidazolium ring, nor at positions C_6 and C_{10}. Instead, and more interestingly, a new set of peaks appears at high field, corresponding to a deuterated butyl group due to the deuteration and reduction of the C_8=C_9 double bond, Figure 7. Further heating of this solution under deuterium at 50 °C for 12 h led to a pronounced growth of all peaks already deuterated, but no deuteration at other positions. The intensities of the peaks in the ^{1}H NMR spectrum of IL_2 after reaction are reduced significantly at positions C_2, C_8 and C_9 indicating that 24 % of the ionic liquid had undergone at least one H-D exchange and NMR and ESI mass spectra indicate that around a further 15 % had been reduced to a deuterated butyl species corresponding to a TON of ~16 with respect to Ru_s at 0 °C.[†] Also, besides the peaks due to IL_1 (labelled * in Figure 8), new peaks appeared (labelled ° in Figure 8) in the C_{sp2} and C_{sp3} regions, corresponding to IL_{2isom} in which there had been an isomerisation of the butenyl chain, Scheme 5.

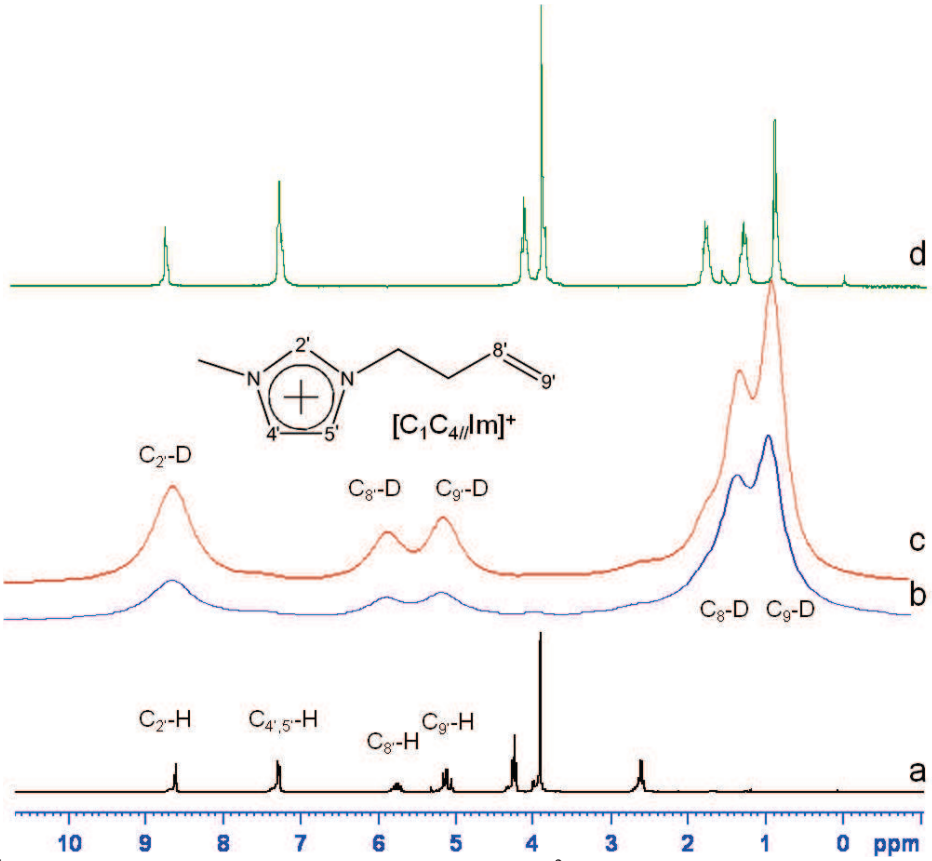

Figure 7 a) ^{1}H NMR spectrum of $[C_1C_{4//}Im][NTf_2]$, neat IL_2; **b**) ^{2}H NMR spectrum of IL_2 after RuNP formation at 0°C under deuterium; **c**) ^{2}H NMR spectrum of IL_2 after RuNP formation at 50 C under deuterium; **d**) ^{1}H NMR spectrum of $[C_1C_4Im][NTf_2]$, neat.

[†] ESI mass spectra and calculations of TON are given in the experimental section 2.5

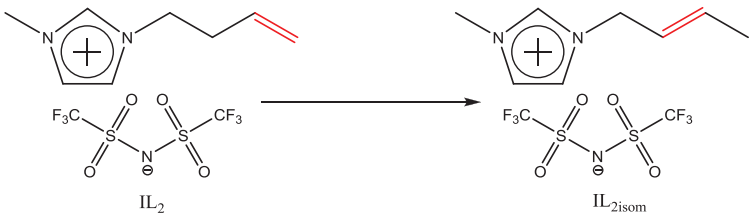

Scheme 5 Isomerisation of IL_2

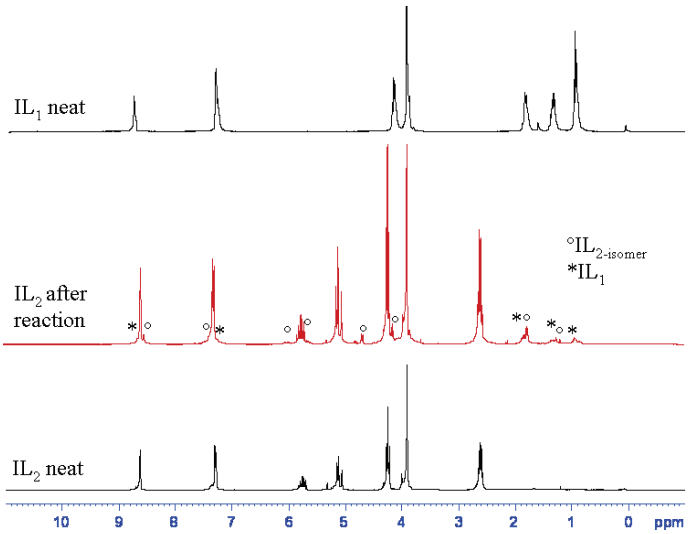

Figure 8. ^{1}H NMR spectra of neat IL_2; IL_2 after RuNP formation at 0 °C under deuterium; neat IL_1.

2.2.3.2 [C_1BzIm][NTf_2], IL_3:

The TEM images of RuNPs synthesised in IL_3 under deuterium at 0 °C showed a size distribution centred at 3.2 ± 0.7 nm. The larger size is expected due to the higher degree of 3-dimensional supramolecular organisation of ILs with the side chain substituted by an aryl group, provoking π-π and π-cation interations.[42]

In the ^{2}H NMR spectra of IL_3 after reaction, deuterium incorporation at position C_2, and positions C_4 and C_5 of the imidazolium ring and/or the aromatic positions is observed. Also a new set of aliphatic peaks appears at high field centred at 1.4 ppm corresponding to a reduced methylenecyclohexyl group, Figure 9. The intensities of the peaks in the ^{1}H NMR spectrum of IL_3 after reaction are reduced at positions C_2, C_4 and C_5 but even more significantly at the aromatic positions, where peak intensity is reduced by 35 %. Indeed, from ^{1}H NMR and electrospray ionisation (ESI) mass spectra, it appears that around 60 % of the ionic liquid undergoes at least one H-D exchange, around 30 % of which is transformed into the deuterated methylenecyclohexyl $CH_2C_6D_xH_{11-x}$ form, with a corresponding TON of ~64 with respect to

Ru_s.[‡] Further heating of this solution under deuterium at 50 °C for 12 h led to a pronounced growth of all peaks mentioned in the ^2H NMR spectrum.

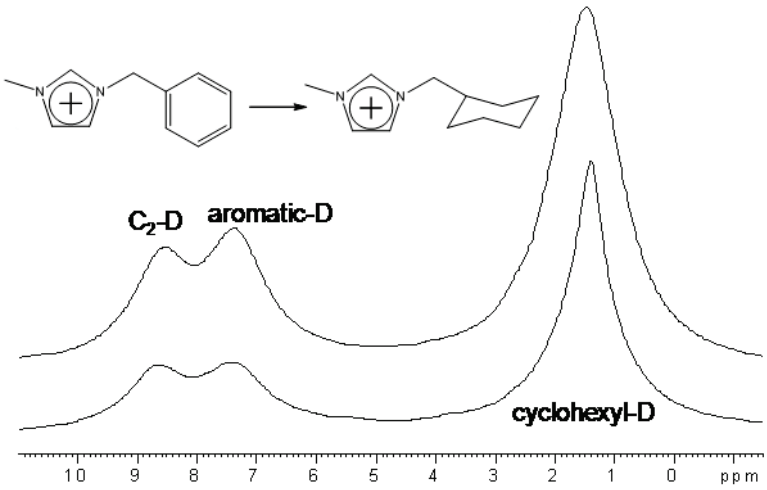

Figure 9. ^2H NMR spectra of $[C_1BzIm][NTf_2]$, IL_3, after RuNP formation at 0 °C under deuterium (lower) and after a further 12 h of heating to 50 °C under deuterium (upper).

The hydrogenation of an aryl substituent, which does not occur with any molecular ruthenium complexes derived from Ru(COD)(COT), must occur on the nanoparticle surface.[43] This observed reduction therefore clearly demonstrates the proximity between the aryl groups of the ILs and the RuNP surface.

During the formation of RuNPs under deuterium in both IL_2 and IL_3, the side groups of the imidazolium rings are saturated with deuterium. In neither case is the C_2 position the primary site for H–D exchange, in contrast to literature results.[13] Furthermore, in the case of IL_2, no exchange is observed at positions C_4 and C_5. Note that no exchange occurs at either position C_6 or C_{10} in either IL. These results indicate that the side chains of the imidazolium are situated in close proximity of the RuNP surface, where activation of deuterium and C-H occurs.

2.2.4 Role of the continuous 3-D network of ionic channels in the isolation of RuNPs

Addition of coordinating substrates, such as water, solvate the rigid ionic channels of the IL through the formation of strong hydrogen bonds with the anions and also weaker hydrogen bonds between the H bound to the C_2 of the cation.[20, 44, 45] Solvation of this ionic network alters the structure of the ionic liquid causing aggregation of the non-polar domains.[46-49] The following question arises: what happens to the RuNPs if the structure of the IL is disrupted?

[‡] ESI mass spectra and calculations of TON are given in the experimental section 2.5

When, under argon atmosphere, an amount of water is added to a stable RuNP/IL suspension, TEM images show agglomeration of the NPs after treatment, Figure 10, supporting the fact that the RuNPs are originally isolated within nonpolar pockets by this network. It is clear that before coalescing, NPs must agglomerate, so preventing agglomeration has an indirect influence on stability.

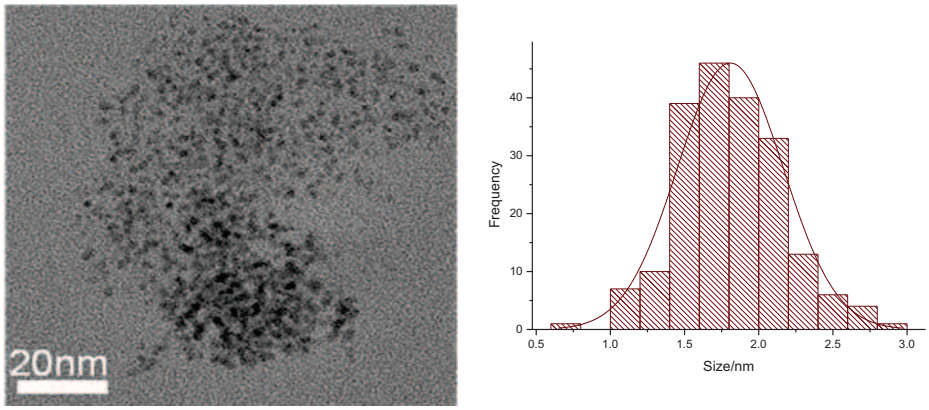

Figure 10. TEM image of RuNPs in IL_1 after treatment with water and resultant size distribution histogram.

2.2.5 The effect of water

As the destructive nature of water on the IL structure and the hydrophobic properties of the RuNPs formed *in situ* in ionic liquids has been demonstrated, this gives rise to the question of what happens when RuNPs are formed in an IL in the presence of water.

Ionic liquids based on the [NTf_2] anion are hydrophobic due to the perfluorinated nature of this anion and therefore immiscible in water. The maximum solubility of water in [C_1C_4Im][NTf_2] is reported as 26 % molar at ambient temperature (299 K). Two different tests were performed:

1) Firstly, a solution of Ru(COD)(COT) in IL_1 was prepared, then an amount of pure heavy water (D_2O) (3% molar, 30% molar or large excess of water) was added to destroy the structure of the ionic liquid before decomposition of Ru(COD)(COT) under H_2 (4 bars) at 0 °C.
2) Secondly, IL-heavy water mixtures were prepared (3% molar, 30% molar or an excess of water), into which was dissolved Ru(COD)(COT) before decomposition under H_2 (4 bars) at 0 °C.

In neither case did the presence of water provoke the decomposition or oxidation of Ru(COD)(COT), which may be indicative of the segregation of the Ru(COD)(COT) and water

by their solvation in different domains of the ionic liquid. TEM images of the NPs obtained are shown in Figure 11.

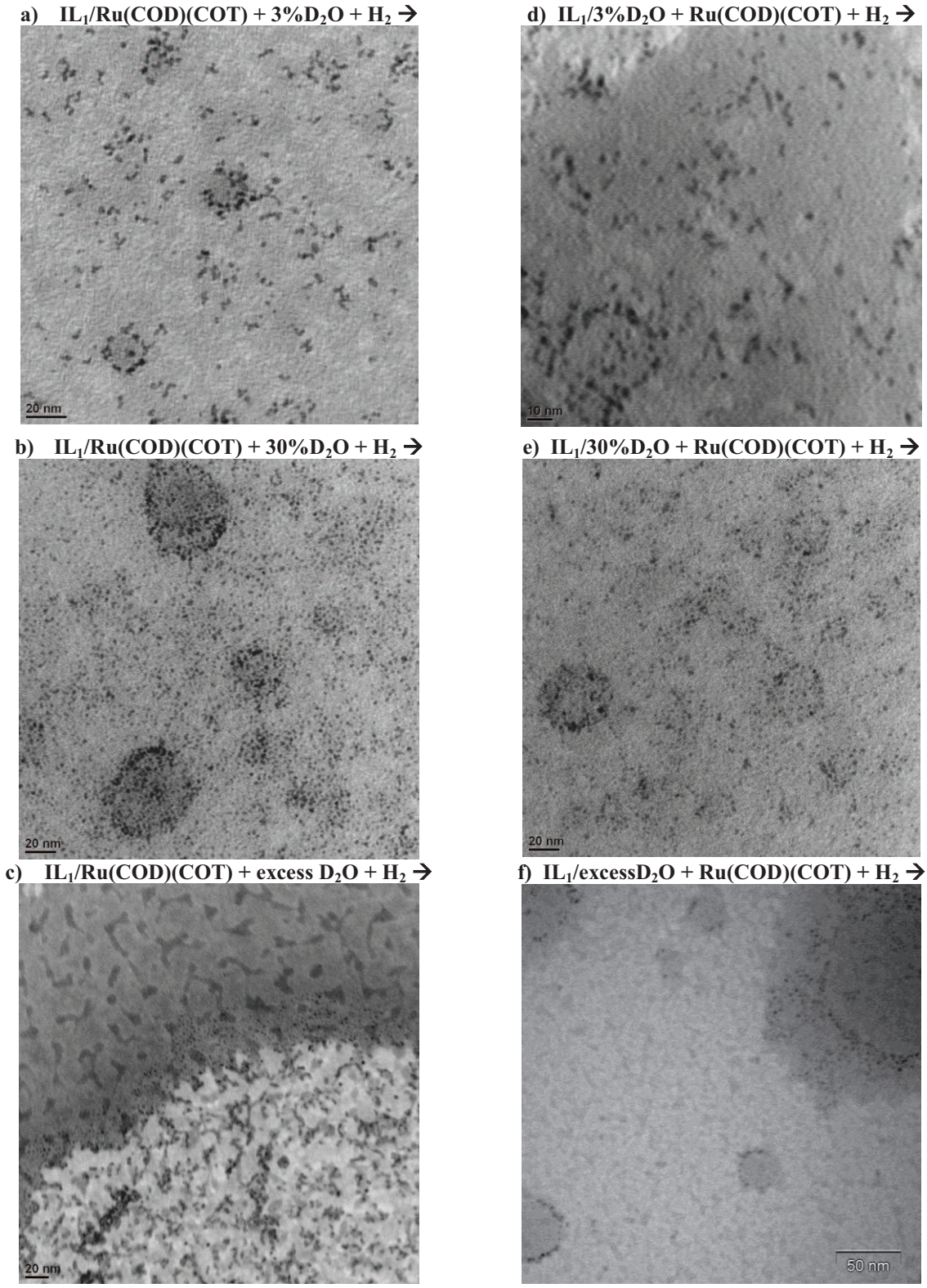

Figure 11. TEM images of solutions of RuNPs synthesised in ILs in the presence of water.

As can be seen in the TEM images in Figure 11 the presence of water has a significant impact on the organisation of the resultant NPs. For the solutions prepared with water below the limit of solubility, whether the water be added before or after the Ru(COD)(COT) the same pattern is observed. For 3 % water (molar), RuNPs of around 2 nm group in circular aggregates of around 20-30 nm in diameter (a and d in Figure 11), and for 30 % water RuNPs also of around 2 nm, group in larger circular aggregates of 30-50 nm (b and e in Figure 11). NPs formed from the dissolution of Ru(COD)(COT) into water-saturated IL_1 before decomposition exhibit the same type of agglomeration of NP, here the diameter of the circular aggregates varying from between 30 and 150 nm (f in Figure 11). This findings support the idea of "water-pools" in wet ILs i.e. micellar-type aggregates of water, as through diffusion measurements water has found to not be completely miscible on the microscale.[47] In this case, RuNPs appear to decorate the water-IL interface, known as the "Pickering effect".[50]

In the final case, when excess water was added to the preformed solution of Ru(COD)(COT) in IL_1 and the subsequent mixture exposed H_2 for NP generation, clear phase separation is apparent from the TEM image, with the NPs uniquely in the IL phase,[§] and again concentrated at the IL-water interface.

2.2.6 Conclusion

The phenomenon of crystal growth of RuNPs generated *in situ* from Ru(COD)(COT), in imidazolium-based ILs is found to be controlled by the size of non-polar domains created by the grouping of lipophilic alkyl chains. Close proximity of the RuNPs to the non polar R group of the cation is evidenced by *in situ* labelling experiments (deuteration and reduction), thus corroborating the hypothesis that RuNPs are surrounded by these non-polar pockets. Addition of water, destroying the ionic network, induces agglomeration of the RuNPs, supporting the fact that the RuNPs are originally isolated within non-polar pockets by the 3-D network of ionic channels. Furthermore, the presence of surface hydrides and their role in the stabilisation of the nanoparticles is demonstrated. Finally, the RuNPs are shown to be hydrophobic.

As already mentioned, literary results give conflicting views on the mechanism for the growth and stabilisation of transition metal nanoparticles in ionic liquids, leading to the conclusion that this could depend on the nature of the metal, its precursor complex, the synthetic

[§] Given the relative volatility of water with respect to the IL, we assume the light regions correspond to water, which under the electron beam and UHV conditions will evaporate.

route and/or the ionic liquid used. We have already demonstrated the growth, size control and stabilisation mechanism of RuNPs from the decomposition under H_2 of the zero-valent organometallic ruthenium compound Ru(COD)(COT) in imidazolium ionic liquids.

This leads to the question of whether the same would be true of NPs generated in the same way from an analogous organometallic compound of another metal. For this reason, in this chapter we investigate the possibility of generalising these findings to the generation of nickel nanoparticles, NiNPs, as the organometallic complex bis(1,5-cyclooctadiene)nickel, $Ni(COD)_2$, analogous to Ru(COD)(COT), is commercially available.

Furthermore, as zero-valent ogranometallic complexes are often difficult to come by, particularly those of the early transition metals, it may be interesting to look at the reductive decomposition of alkyl-metals. Therefore, the generation of tantalum nanoparticles, TaNPs from decomposition in IL media of the well-known Schrock complex, tris(neopentyl)(neopentylidene)tantalum, is also investigated in this chapter.

2.3 Synthesis and stabilisation of nickel nanoparticles in ionic liquids

Nickel is one of the most abundant and therefore least costly of the catalytically active late transition metals – 17 USD/kg (nickel) vs. 5340 USD/kg (ruthenium) – so presents a clear economic advantage if its catalytic potential is exploited. Furthermore, bulk nickel being ferromagnetic, magnetic nanomaterials often exhibit interesting optical and photoelectronic properties,[51] as well as being superparamegnetic. Their magnetic properties vary with size, shape and composition and therefore magnetic measurements are often used as complementary characterisation.

NiNPs have been prepared by the reduction of organometallic precursors such as nickel tetracarbonyl ($Ni(CO)_4$), bis-(cyclopentadienyl) nickel, ($Ni(C_5H_5)_2$), bis-(acetylacetate) nickel ($Ni(acac)_2$),[52] and bis-(1,5-cyclooctadiene)nickel ($Ni(COD)_2$,[53-57] in different stabilising media. For the purpose of our work $Ni(COD)_2$ is chosen due firstly to its zero-valence and also to the fact that the by-products of decomposition are light hydrocarbons that are easily removed under vacuum and will not react with the surface of the NiNPs, unlike any halide or carbonyl precursor. Furthermore, this complex is analogous to Ru(COD)(COT), facilitating the comparison of results.

The aim of this section is to (1) determine whether, as for RuNPs, the size control of NiNPs generated *in situ* in ILs may be achieved through use of the intrinsic 3-D structure, and (2) determine the stabilisation factors of the resultant NiNPs.

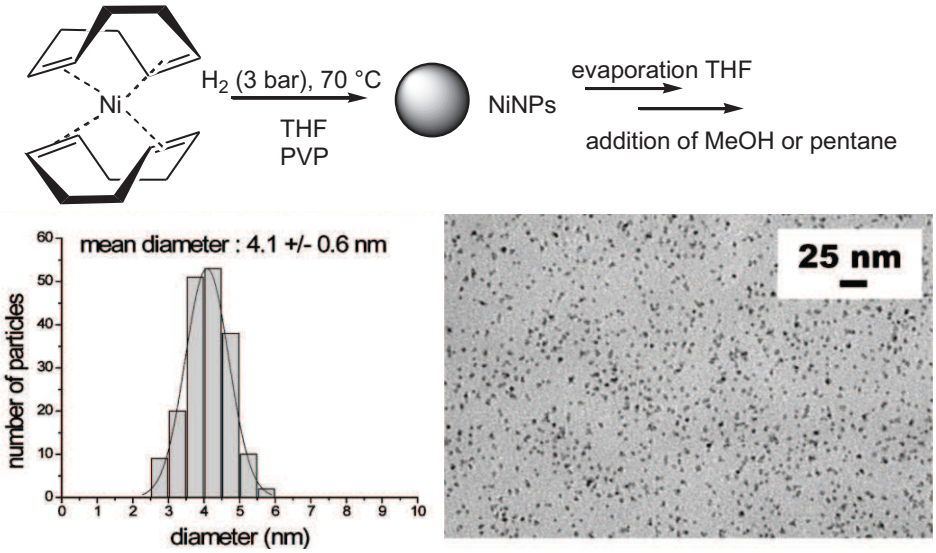

Figure 12. Typical synthesis of PVP-stabilised NiNPs dispersed in organic solvent (Chaudret's method). TEM image of PVP-stabilised NiNPs dispersed in MeOH and subsequent size distribution histogram.[53]

$Ni(COD)_2$, when decomposed under hydrogen in organic solvents such as THF in the presence of hexadecylamine (HDA) as the stabiliser ligand or polyvinylpyrrolidone (PVP) as polymer support,[53, 54] produces NiNPs of a face centred cubic structure with a size distribution centred around 4 – 5 nm, as found by Chaudret's group. Cyclooctane is produced as a side product. These NPs may be removed from the media by evaporation of the solvent and homogenised by redispersion into other solvents, such as methanol or pentane, as seen in Figure 12. The NiNPs display a magnetisation value comparable to that of bulk Ni, although the magnetic behaviour may be altered by adding more coordinating substrates to the medium, e.g. CO.[53, 54]

Clearly research into NiNPs is well advanced, however the challenge remains to generate sizes of less than 4 nm, which have not yet been successfully prepared from organometallic precursors. To our knowledge the smallest recorded NiNPs are 2.5 nm, prepared by means of laser electrodispersion techniques.[58]

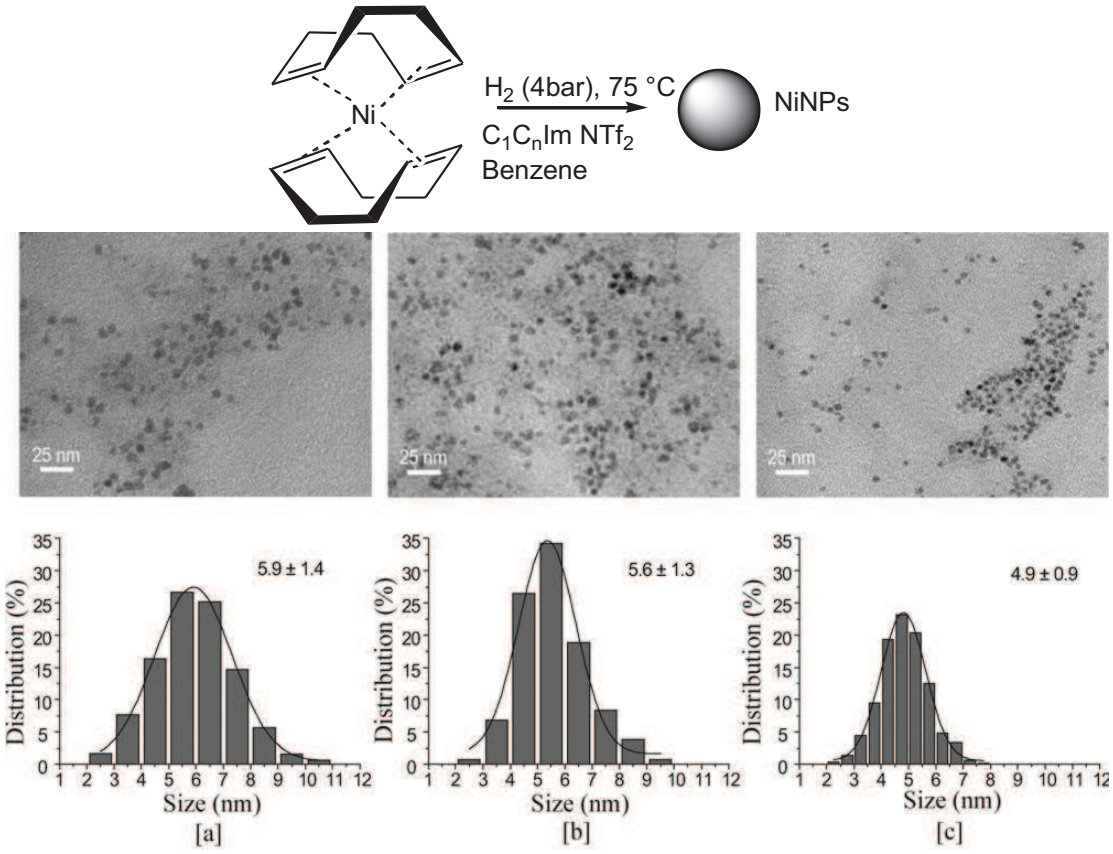

Figure 13 TEM micrographs and respective histograms showing the size-distribution of Ni nanoparticles prepared and dispersed in $[C_1C_4Im][NTf_2]$ [a], $[C_1C_8Im][NTf_2]$ [b], $[C_1C_{10}Im][NTf_2]$ [c].[56, 59]

Dupont *et al.* have already reported the preparation of NiNPs from $Ni(COD)_2$ in imidazolium based ILs in order to control the size of the NiNPs by varying the length of the imidazolium alkyl substituent.[56, 59] Here, the size of the NPs formed was found not to vary greatly on changing the nature of the ionic liquid employed, i.e the alkyl side chain length, and in contrast to previous findings from our group for RuNPs,[26] the average size of NiNPs was found to vary inversely with alkyl chain length, Figure 13. However, it is worth noting that a substantial amount of benzene was used to aid the dissolution of $Ni(COD)_2$ (6 mL of benzene for 2 mL of IL) and although effort was made to remove the volatiles before decomposition, we cannot be sure of the complete removal of benzene and therefore the media in which the decomposition actually occurred. Furthermore, the Ni-NiO core-shell particles produced bring into question the purity of the solvents used. Therefore, the results are not comparable with the work in our laboratory, where pure neat ILs are used as the solvent.

2.3.1 Size-controlled synthesis of NiNPs

The synthesis of nickel nanoparticles, NiNPs, from the decomposition of *bis*-(1,5-cyclooctadiene) nickel ($Ni(COD)_2$), under molecular hydrogen (4 bars) at 0 °C or 25 °C, was attempted firstly in the following imidazolium based ionic liquids (ILs); $[C_1C_nIm][NTf_2]$, with n = 2, 4, 6, 8, 10, varying the length of the alkyl chain in order to investigate the effect on the size of the resulting NiNPs.

2.3.1.1 Decomposition in $[C_1C_6Im][NTf_2]$, $[C_1C_8Im][NTf_2]$ and $[C_1C_{10}Im][NTf_2]$

Firstly, $Ni(COD)_2$ (50 mg, 0.14 mmol) was stirred into the ionic liquid (10 mL) until a light yellow solution resulted (14 mmol L^{-1} in each case). For all three ILs, the solutions were exposed to H_2 (4 bar) at 0 °C or 25 °C producing after 3 days black suspensions of NiNPs, Scheme 6, except in the case of $[C_1C_6Im][NTf_2]$ at 0 °C, where the reaction proceeded very slowly, and the starting product was still present with the NPs. The resulting volatiles were removed *in vacuo*, trapped and characterised by ^1H and ^{13}C NMR spectroscopy. The spectra obtained showed the predominance of cyclooctane, with a small amount of remnant 1,5-COD and even a trace amount of its isomer 1,3-COD. We may conclude that in this case the decomposition occurs mainly via the hydrogenation of 1,5-COD, and the small amount unchanged ligand may undergo isomerisation in the presence of Ni-H.

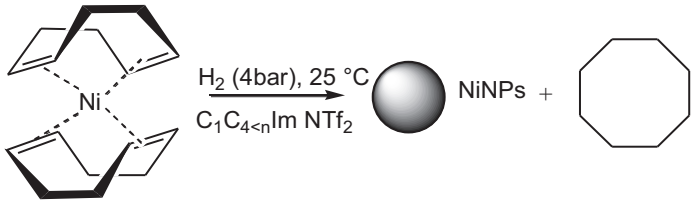

Scheme 6. Decomposition of Ni(COD) under H_2 – Route to obtain NiNPs

2.3.1.2 Effect of temperature

In $[C_1C_8Im][NTf_2]$ and $[C_1C_{10}Im][NTf_2]$ the NiNPs formed at 0 °C are smaller than those generated at 25 °C, Figure 14.

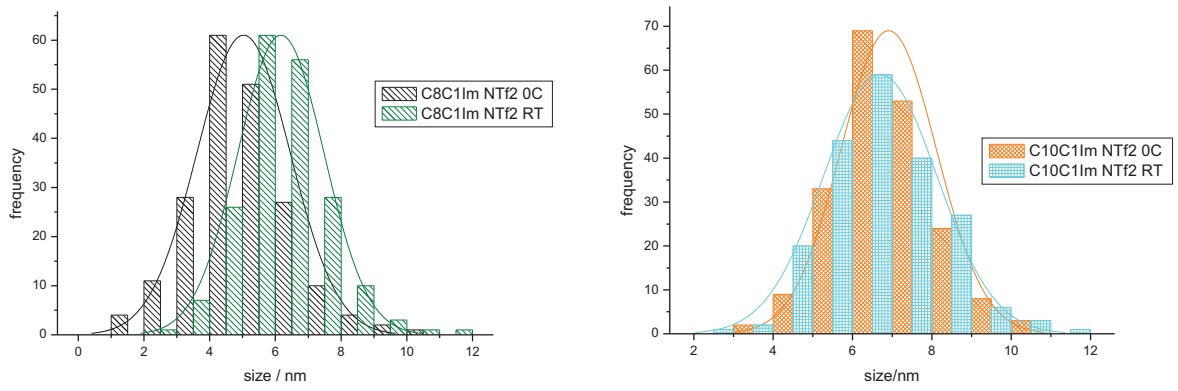

Figure 14. Size distribution histrograms of NiNPs synthesized in $[C_1C_8Im][NTf_2]$ (left),and $[C_1C_{10}Im][NTf_2]$(right), under 4 bars of H_2 in various at 0 °C and at 25 °C

Even if the variation of H_2 solubility as a function of the temperature is still under discussion, the ILs are more viscous at 0 °C than at 25 °C, thus the H_2 diffusion and its solubility expected to be lower. Consequently, by working at 0 °C without stirring, the conditions disfavoured hydrogen solubility and diffusion. This is different to that described by Aiken *et al.*, who observed in similar conditions in organic solvent, the formation of irregular and aggregated clusters.[60] Moreover, in organic media, increasing temperature is often leads to a decrease in NP size, due to the kinetics of the NP growth process.[61, 62] Consequently, the differences observed in ILs could once again be rationalised on the basis of their degree of self-organisation.[25]

2.3.1.3 Influence of the length of the alkyl side chains

When realised at the same temperature in different ILs $[C_1C_6Im][NTf_2]$, $[C_1C_8Im][NTf_2]$, and $[C_1C_{10}Im][NTf_2]$ the decomposition of $Ni(COD)_2$ resulted in different sized NPs as can be seen in the histograms presented in Figure 15.

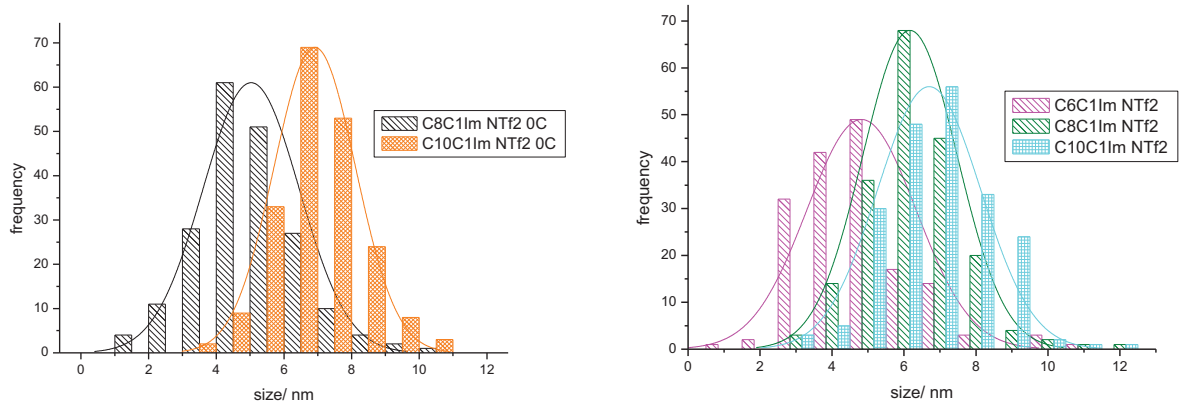

Figure 15. Size distribution histograms of NiNPs size synthesised under 4 bars of H_2, at 0° and 25°C without stirring in different ILs.

At room temperature, the observed mean diameter increases with the side alkyl chain length: in $[C_1C_6Im][NTf_2]$, (5 ± 2 nm), in $[C_1C_8Im][NTf_2]$ (6 ± 2 nm). and in $[C_1C_{10}Im][NTf_2]$, (7 ± 2 nm). It was noted that a "mirror" appeared on the bottom of the glass auto-clave during the reaction in $[C_1C_{10}Im][NTf_2]$ at 25°C corresponding to the deposition of bulk metallic nickel.

2.3.1.4 Comparison with RuNPs

The synthesis of NiNPs under H_2 in these ILs, was seen to give similar trends to RuNPs, i.e. mean size of resultant NPs increasing with both increasing temperature and increasing alkyl chain length. In the case of RuNPs, when n = 10 we observe the formation of large “sponge-like superstructures” with a size of 100–150 nm containing small aggregated particles. This phenomenon could result from a diffusive process of RuNPs between the different non-polar domains due to the chain length. For NiNPs, this phenomenon is not observed, although at 25 °C in the same IL, the deposition of a metallic mirror as well as the formation of NiNPs was recorded.

Unlike RuNPs generated *in situ* the sizes of NiNP obtained were large, and with a relatively broad size distribution. Indeed, the NiNPs obtained are too large to be correlated to the measured size of the non-polar domains. The fact that they cannot be contained within these

domains may explain their gradual agglomeration and precipitation, observed in each case between 5 and 10 days after formation, and storage under inert atmosphere.

These differences between RuNPs and NiNPs could be related to a different mechanism involved in generation. The complex Ru(COD)(COT) reacts readily with H_2.[63] Consequently, its decomposition under H_2 rapidly affords nuclides which subsequently coalescence to generate small RuNPs of controlled size.

On the other hand, a higher energy barrier is involved in its decomposition of $Ni(COD)_2$. Consequently, the formation of nuclides is slow. Few nickel nuclides therefore coexist with a great deal of $Ni(COD)_2$. The nuclides induce the decomposition of $Ni(COD)_2$ meaning that the growth process in this case is much faster than the nucleation and therefore fewer larger NPs are formed with less control, as illustrated in Scheme 7.

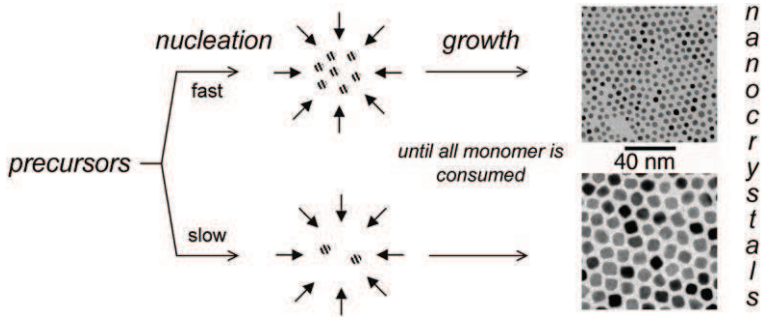

Scheme 7. The kinetics of nucleation and growth in the formation of nanoparticles.[64]

Similarly to RuNPs, when a solution of freshly prepared NiNPs was treated under ethylene, in the absence of H_2, ethane was detected in the atmosphere, indicating the presence of hydrides on the nickel surface.[30, 65] However, unlike RuNPs when heated and stirred under an atmosphere of H_2, NiNPs undergo rapid coalescence and precipitation. Recently, it has been reported that the size of NiNPs formed by "dewetting" of Ni metal film drastically increases with increasing H_2 pressure. By analogy with Raney nickel, this result has been related by the authors to the formation of a surface hydride leading to a modification of the surface free energy.[66]

2.3.2 Spontaneous decomposition on solvation

In the absence of hydrogen, in **neat** $[C_1C_2Im][NTf_2]$ and $[C_1C_4Im][NTf_2]$ at room temperature, and in $[C_1C_6Im][NTf_2]$ at 40 °C, spontaneous decomposition of $Ni(COD)_2$ occurred on dissolution. TEM was performed on the resulting black solutions and revealed in each case a mixture of NiNPs (< 10 nm) and sponge-like agglomerates of larger particles, Figure 16. It can be seen from the TEM image that these sponge-like structures clearly consist of individual

particles. This is completely different from Dupont's work,[56] emphasising the important role that a co-solvent such as benzene plays in the medium.

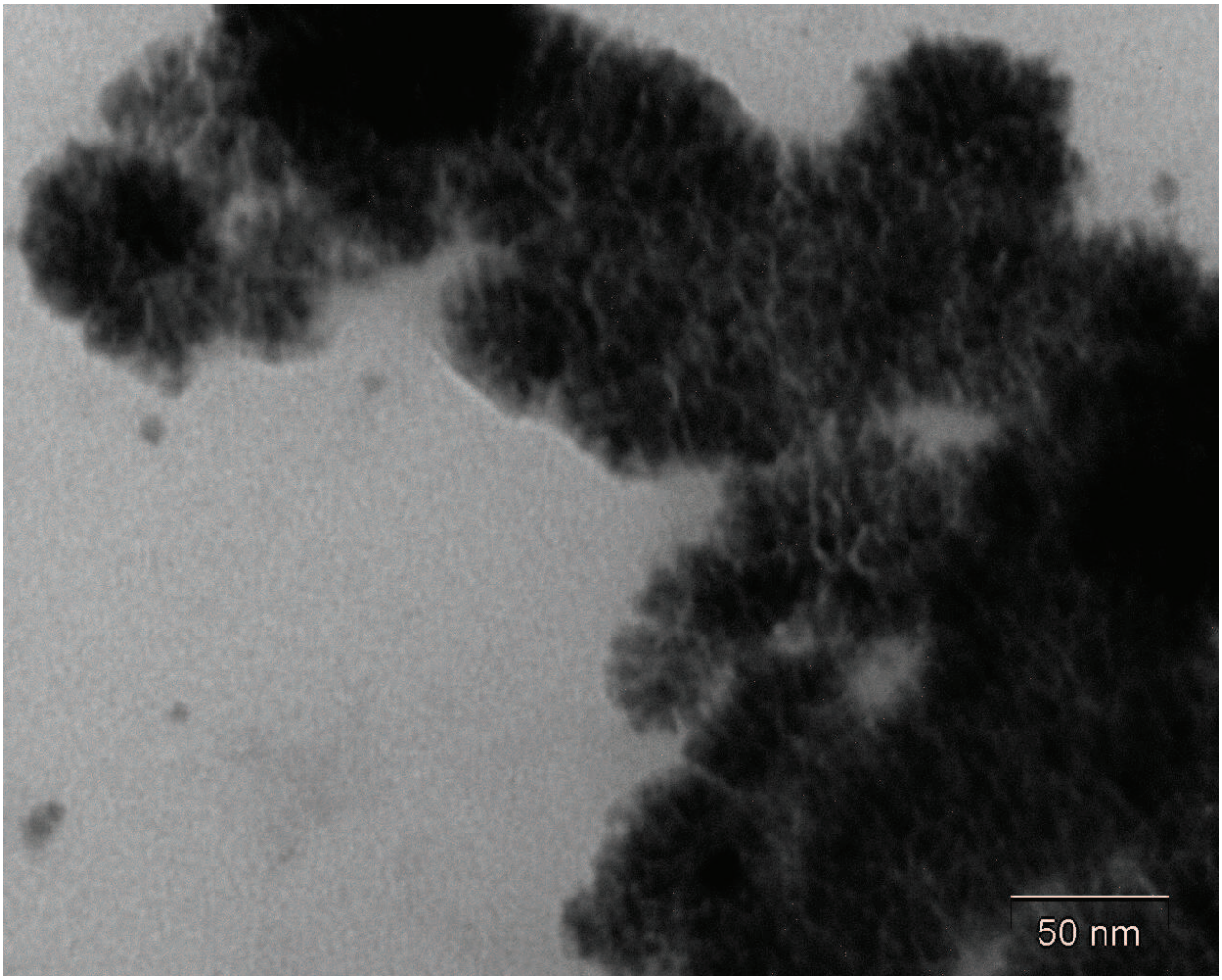

Figure 16. Sponge-like agglomerates of NiNPs formed by autodecomposition of $Ni(COD)_2$ in $[C_1C_4Im][NTf_2]$

Note that ^1H NMR spectroscopy and gas chromatography performed on the resulting solution showed **only a trace** of cyclooctane COA, resulting from the hydrogenation 1,5-COD, the by-product of decomposition reported in the literature.[53] Instead, the presence of both 1,5-cyclooctadiene and its isomer 1,3-cyclooctadiene (1,3-COD) was detected by both gas chromatography and ^1H and ^{13}C NMR spectroscopy. 1,3-COD must be a result of 1,5-COD isomerisation, which could only take place at a metal centre in the presence of [Ni]-H bond, Scheme 8.

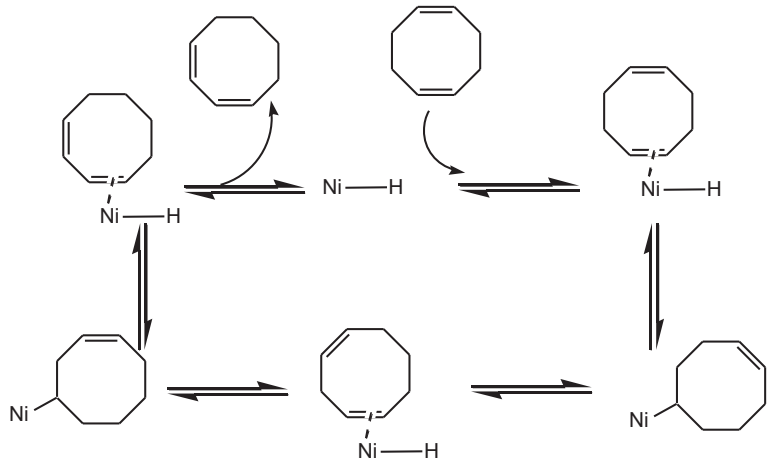

Scheme 8. Mechanism for the isomeration of COD necessitating a Ni-H

With RuNPs, the presence of surface hydrides has been proven by hydrogenation of ethylene without the addition of H_2 by a solution of RuNPs in IL, as shown in Scheme 9.[67] We repeated this experiment for the NiNP solutions formed by autodecomposition of $Ni(COD)_2$ in the media.

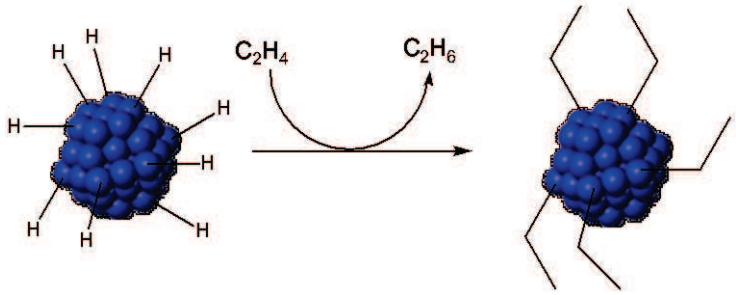

Scheme 9. Hydrogenation of ethylene over RuNPs without addition of H_2, - evidence for surface hydrides.

After treatment under ethylene atmosphere (4 bars, 100 °C, 24 h) no ethane was detected by GC as a result of ethylene hydrogenation, however significant amounts of butenes and hexenes were detected, probably a result of oligomerisation of the ethylene.

The formation of an ethyl substituted IL $[C_1C_2C_4Im][NTf_2]$ was also observed by NMR spectroscopies; ^1H shown in Figure 17, COSY, HETCOR and DOSY; and confirmed by electrospray mass spectrometry, where cations at m/z = 139 and 167 were observed with similar abundances, corresponding to $[C_1C_4Im]^+$ and $[C_1C_2C_4Im]^+$, respectively. Note that a small amount of the cation $[C_1C_4C_4Im]^+$ was also observed by mass spectrometry, m/z = 195, probably a result of oligomerisation of ethylene to 1-butene before reaction with the imidazolium cycle.

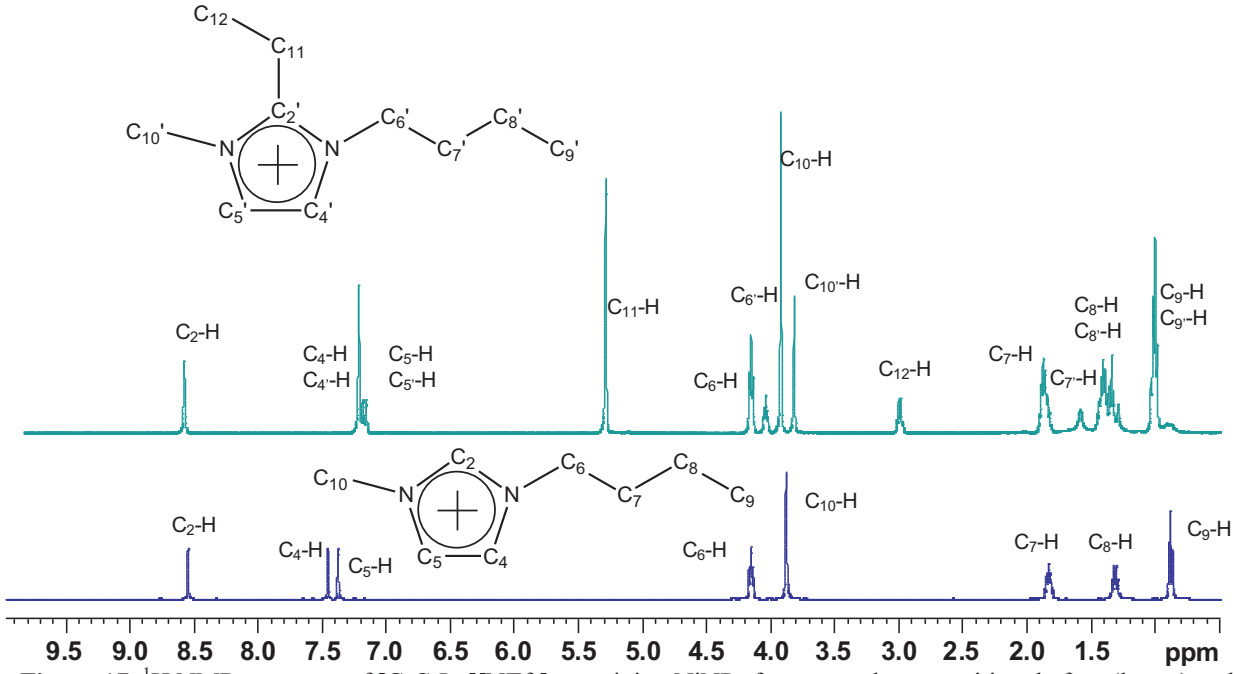

Figure 17. ^{1}H NMR spectrum of $[C_1C_4Im][NTf_2]$ containing NiNPs from auto-decomposition, before (lower) and after (upper) treatment under ethylene.

The evidence gathered suggests that the observed decomposition could be due to the cleavage of the very acidic C_2-H bond and the consequent *in situ* generation of a nitrogen heterocyclic carbene (NHC), as already reported in the case of Ir NP preparation in ILs[3, 5, 13] and with homogeneous complexes of Ni[68], Pd,[69, 70] and of Rh and Ir.[71]

Cavell *et al.* have proposed a scheme for the possible catalytic cycle for the imidazolium/alkene coupling reaction where the organometallic starting material they studied was $Ni(OAc)_2$.[72] The same phenomenon has also been observed in work by Lecocq *et al*. who were investigating the oligomerisation behaviour of Ni in imidazolium ionic liquids.[68]

At this point it is impossible to determine whether the observed reactions (isomerisation of 1,5-COD and formation of $C_1C_2C_4ImNTf_2$) occur on molecular or colloidal species. However, these results do prove that the cleavage of the C_2-H bond does occur during the spontaneous decomposition on dissolution. The proposed mechanism of the reaction of imidazolium salts with low valent M^0 (M = Pd and Ni) hypothesises the formation of a molecular carbene-M-H species,[73, 74] as also proposed in the catalytic cycle for oligomerisation and formation of trialkylimidazolium species in Scheme 10.

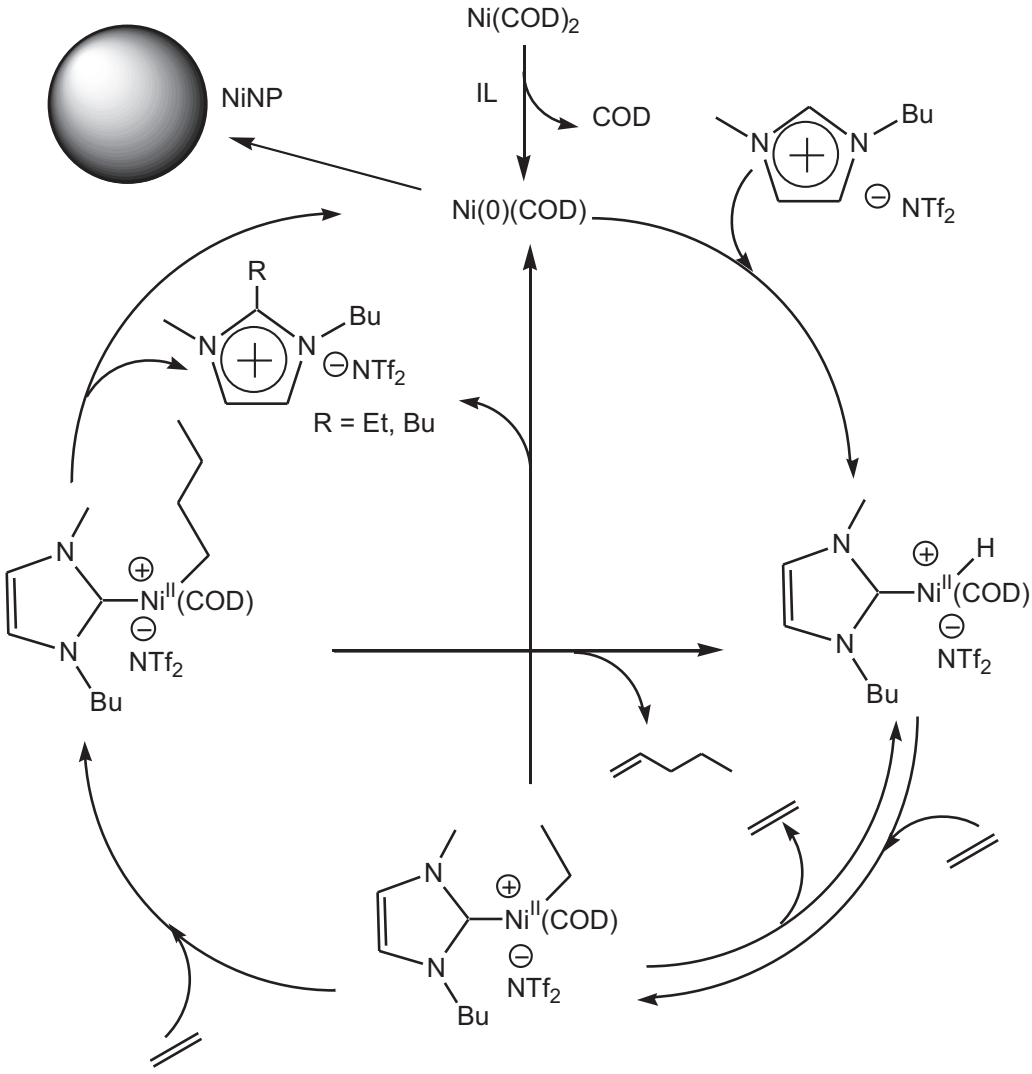

Scheme 10. The proposed catalytic cycle for oligomerisation of ethylene and formation of trialkylimidazolium species.

The presence of bis(imidazolylidene)nickel complexes $[(NHC)_2NiH]^+$ was also detected by mass spectrometry, implying that a molecular intermediate is in fact present as proposed. This may be as a transient species and could be the active species for the abovementioned reactions. Similar *bis*-carbene iodide nickel complexes have already been prepared in imidazolium ILs and isolated by Wasserscheid's group.[72] These were indeed found to be active in the dimerisation of butene carried out in ILs, although no production of NiNPs was noted here, perhaps due to the presence of the strongly coordinating iodides.

2.3.3 Avoiding carbene formation

Although the exact mechanism remains unclear, from our investigations it is certain that the spontaneous decomposition of $Ni(COD)_2$ on dissolution into the ionic liquids with short alkyl

chains, involves attack on the acidic C_2-H. This may be inhibited in the longer chain ionic liquids due to the greater distance between the imidazolium ring and the non-polar domains, where $Ni(COD)_2$ will dissolve preferentially. If we are to achieve the generation of small size-controlled NiNPs, we must find a way of inhibiting this auto-decomposition in imidazolium ILs with short chains. Several strategies were attempted in order to circumvent the problem.

Firstly, $[C_1C_1C_4Im][NTf_2]$ which does not contain the most acidic C_2–H proton was used as the solvent. Surprisingly, the $Ni(COD)_2$ still decomposed on stirring, but this time afforded well dispersed NiNPs (7 ± 2 nm), Figure 18. This can only be explained by attack on the two less acidic protons C_4-H,C_5-H of the imidazolium ring and generation of transitory non-classical NHC ligands.[75]

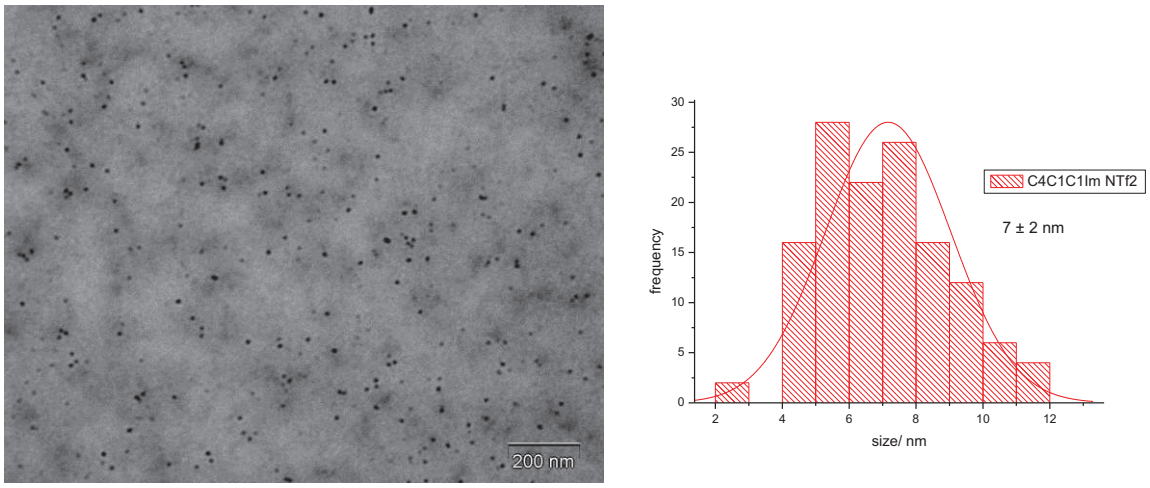

Figure 18. TEM image of NiNPs formed by autodecomposition of $Ni(COD)_2$ in $[C_1C_1C_4Im][NTf_2]$ and size distribution histogram.

Another possible solution to this spontaneous decomposition is to increase the strength of the H-bond between C_2-H on the cation and the anion. The more strongly co-ordinating anion BF_4^- was selected, yielding important results. The formation of NiNPs in $[C_1C_4Im][BF_4]$ occurred not spontaneously, but very slowly at 25 °C **only** under 4 bars of H_2. The solution had turned entirely black after 5 days. Analysis by TEM revealed well dispersed small NiNPs of 2.8 ±0.9 nm, Figure 19.

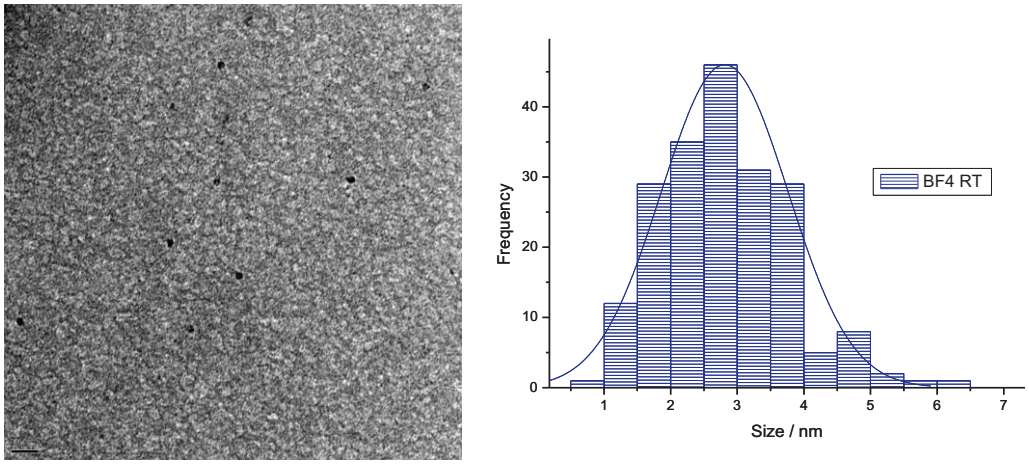

Figure 19. TEM image of NiNPs formed by decomposition of $Ni(COD)_2$ under H_2 (4 bars at 25 °C) in $[C_1C_4Im][BF_4]$ and size distribution histogram.

2.3.4 Conclusion

The synthesis of NiNPs from $Ni(COD)_2$ under H_2 (4 bar) has been carried out in various imidazolium based ionic liquids at 0 °C and 25 °C. Imidazolium cations substituted with longer chains $[C_1C_6Im][NTf_2]$, $[C_1C_8Im][NTf_2]$ and $[C_1C_{10}Im][NTf_2]$, the IL media were found to offer fairly good media for the preparation and stabilisation of nickel nanoparticles. NiNP size increased with increasing chain-length and in this way we were able to control NiNP size. Additionally, upon decreasing the reaction temperature to 0 °C, we were able to produce smaller NiNPs than those produced in the same IL media at 25 °C. The presence of surface hydrides on on these NiNPs as on RuNPs has been evidenced by hydrogenation of ethylene in the absence of hydrogen. The resulting NiNPs in these ILs were found to be larger than RuNPs produced in the same media. This can be largely attributed to differences in the nucleation and growth processes for the two metals.

Unexpectedly, spontaneous decomposition of $Ni(COD)_2$ occurred without the addition of hydrogen for imidazolium ILs with short alkyl chains; $[C_1C_2Im][NTf_2]$. $[C_1C_4Im][NTf_2]$ and $[C_1C_1C_4Im][NTf_2]$. In $[C_1C_2Im][NTf_2]$ and $[C_1C_4Im][NTf_2]$, TEM micrographs showed NiNPs of fairly large diameter were formed as well as sponge-like super agglomerates. In $[C_1C_1C_4Im][NTf_2]$ well dispersed NiNPs are formed. In these cases, an explanation concerning the activation of the acidic protons on the imidazolium ring and the consequent nitrogen heterocyclic carbene formation leading to rapid decomposition of the complex, has been proposed, Scheme 11.

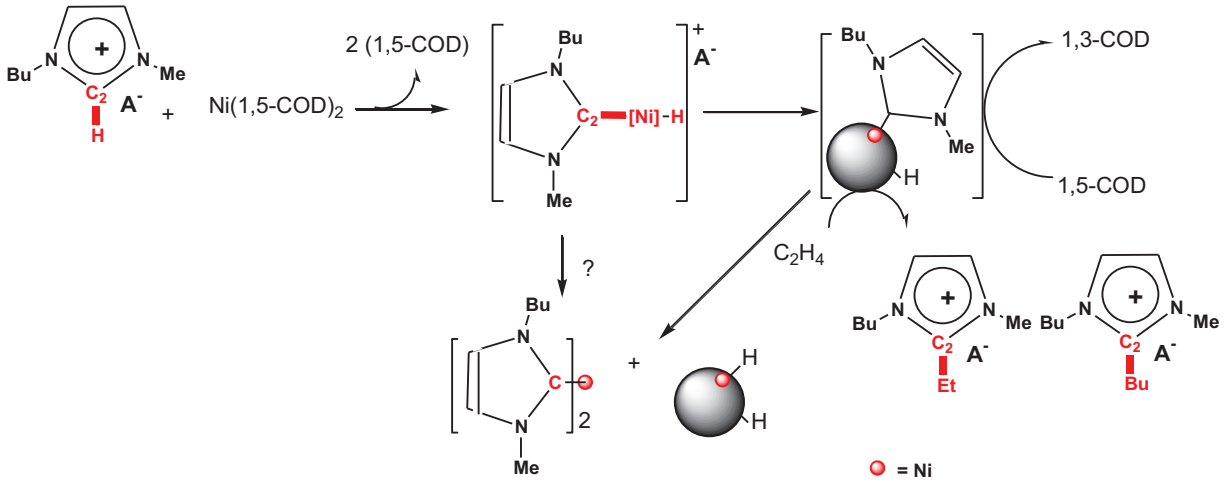

Scheme 11. Reactions occuring during the autodecomposition of $Ni(COD)_2$ in imidazolium ionic liquids.

On changing the anion of the IL to the more strongly co-ordinating tetrafluoroborate $[C_1C_4Im][BF_4]$, the acidic protons of the imidazolium ring were protected, and more controlled NiNP formation took place, only in the presence of hydrogen. This medium was therefore successfully used to synthesise NiNPs smaller than 4 nm in diameter.

This work provides a novel route to NiNP synthesis and offers the possibility of NiNPs in ILs as a medium for catalysis.

2.4 Tantalum nanoparticles

To meet the constant challenge of miniaturisation in the microelectronics industry, traditional methodologies must be replaced by new innovative pathways to produce nano-objects. In particular, oxophilic metals of groups 4 to 6 are of great interest due to their various applications, e.g. as conducting contacts between active devices,[76] or as barriers to the diffusion of metals such as Cu.[77] These metals could be used as thin layers but also as nanoparticles, NPs, thus exhibiting further interesting properties that increase their appeal, such as quantum effects and heightened reactivity.[78] Recently, the potential of NP suspensions in ILs for use in electronic applications has been revealed.[79, 80]Among metals of group 4 to 6, tantalum is currently of large importance with 79% of the world's annual production being used in electronics.[81]

Note that of the early transition metals, only chromium, molybdenum and tungsten NPs in ILs are reported in literature. They are obtained by by thermal or photolytic decomposition under argon of mononuclear metal carbonyl precursors $M(CO)_6$ (M = Cr, Mo, W).[82]

The number of publications describing the synthesis of Ta(0)NPs, is limited. Due to high melting and boiling points, Ta(0)NPs are difficult to prepare by conventional physical methods. For example, the preparation of Ta(0)NPs by a hydrogen rich plasma (water used as the plasmatic medium as it dissociates under the effect of an electric arc) led to a mixture of Ta(0)NPs and TaO NPs.[83] Studies by XRD indicate that the TaO NPs present a hexagonal phase with interplanar distances of 0.31 and 0.39 nm depending on the face under study (100 and 001 respectively). The Ta(0)NPs however, have a face centred cubic structure much like bulk Ta metal. Their average size was estimated to be 10 nm and interplanar distances of the (110) face were measured as being 0.24 nm.[84]

Chemical methods are rarely used. They involve the reduction of $TaCl_5$ or K_2TaF_7 at high temperature or in liquid ammonia in the presence of sodium.[85, 86] Such techniques result in Ta particles of sizes ranging between 1 – 100 μm. More recently, Ta(0)NPs supported on silica have been described. The reaction of pentabenzyl tantalum, $Ta(CH_2C_6H_5)_5$, with the silica surface, results in the formation of surface complex(es) that under hydrogen atmosphere at 573 K and 723 K, lead to the formation of Ta(0)NPs on SiO_2 Scheme 12.[87] Such Ta(0)NPs, of mean size ≈ 1 nm, contain Ta-Ta bond lengths of ≈2.93 Å (determined by EXAFS) and Ta-O-Si bond lengths of 1.9 Å. The latter would suggest that the Ta(0)NPs are chemically bonded to the

surface. The question of the oxidation state of these surface Ta(0)NPs remains unanswered, having not yet obtained XPS data.

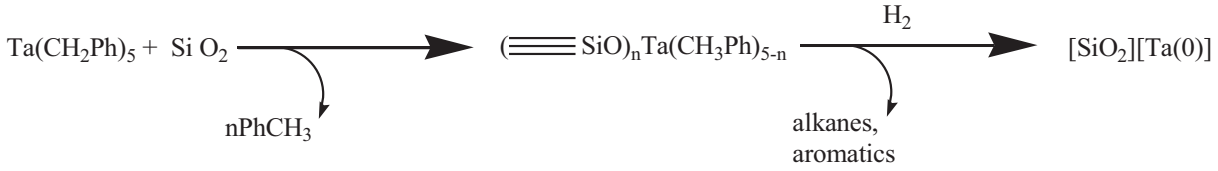

Scheme 12. The synthesis of silica supported TaNPs[87]

Although ILs are known to be good media for the synthesis and stabilisation of NPs, few papers regarding oxophilic metals are available.[82] To our knowledge, no Ta(0)NPs have yet been synthesised in ionic liquid media, although several examples of the electroreduction of tantalum halides are reported leading to electroplated Ta on Pt electrodes, without reduction of the ionic liquids.[88-90] Here, a thin layer of halides is present at the surface, outlining the consequences and importance of the chosen starting complex.

As previously discussed; in both organic and IL media, it has been widely reported that treatment of group VIII organometallics under H_2 leads to zero-valent transition metal NPs at moderate temperature. The alkanes produced are inert towards the surface of the $M^{(0)}$NPs and easily eliminated under vacuum.[25, 91, 92] In the case of the oxophilic group early transition metals, such a strategy is not evident as zero oxidation state complexes are few and far between. For this reason, as for the preparation of supported TaNPs on silica,[87] we propose the use of an organometallic precursor of Ta(V) as a source of Ta(0)NPs, namely tris(neopentyl)neopentylidene tantalum(V), $Np_3Ta{=}CHCMe_3$, **1**, whose synthesis is well documented.[93]

2.4.1 Synthesis in pure $[C_1C_4Im][NTf_2]$

The synthesis of Ta(0)NPs in 1-butyl-3-methylimidazolium bis(trifluomethylsulphonyl)-imide, $[C_1C_4Im][NTf_2]$ from $Np_3Ta{=}CHCMe_3$, **1**, was performed as follows. **1** (25 mg, $5.4.10^{-5}$ mol) was dissolved in pure dried $[C_1C_4Im][NTf_2]$ (5 mL) by vigorous stirring under argon. The mixture was transferred into a Fischer-Porter bottle via a canula, which was then charged with 4 bars of H_2 during a period of 72 h at 25 °C. This afforded a black suspension which was stable several days under argon at 25 °C. Analysis of the gas phase after reaction by gas chromatography showed the presence of only neopentane. The Ta(0)NPs produced were analysed by transmission electron microscopy, TEM, from which a size distribution histogram (in number) was constructed (Figure. 20) giving a mean size of 5 ± 3 nm (c.a. 70 % of NPs).

However, the NPs were not monodisperse as larger species of up to ~ 18 nm were also detected (c.a. 30 % of NPs larger than 10 nm).

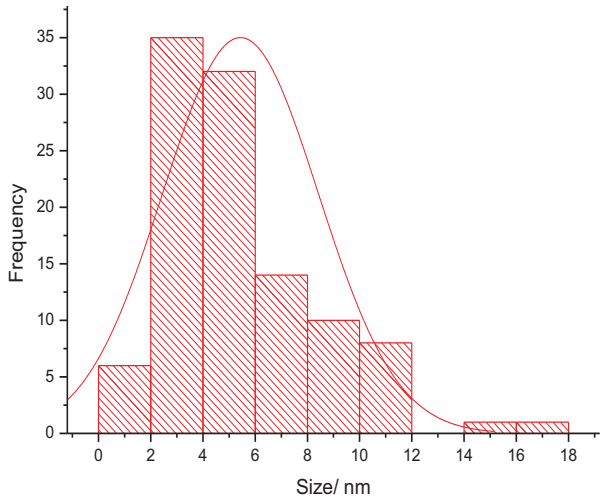

Figure 20. Size distribution histogram for TaNPs formed in $[C_1C_4Im][NTf_2]$

2.4.2 Addition of a co-solvent

During the dissolution of **1** into $[C_1C_4Im][NTf_2]$, a problem of solubility was noted, despite an extensive stirring period, probably the cause of the production of larger NPs outside of the normal distribution. In the literature several groups have overcome such a problem by addition of a co-solvent to aid the dissolution of the organometallic complex into the ionic liquid.[56,57] Therefore in subsequent experiments, **1** was first dissolved in toluene or in pentane before addition to $[C_1C_4Im][NTf_2]$. Before proceeding, it was first ascertained that a simple organic solution of **1** did not lead to NPs under pressure of H_2 without the IL present. A ratio of organic solvent to $[C_1C_4Im][NTf_2]$ was used such that a maximum amount of **1** would dissolve, and demixing would not occur, i.e. n-pentane/IL = 2 % and toluene/IL = 36 % (weight percentages). **1** is highly soluble in n-pentane which is inactive towards the NP surface and therefore easily eliminated. However, pentane is poorly soluble in $[C_1C_4Im][NTf_2]$. **1** is less soluble in toluene but toluene was chosen due to its relatively high solubility in $[C_1C_4Im][NTf_2]$. Once prepared, these solutions were treated under H_2 as before, and the NP solutions produced were analysed by TEM, and the size distribution histograms constructed, Figure 21. The resulting NP sizes are tabulated below, Table 1.

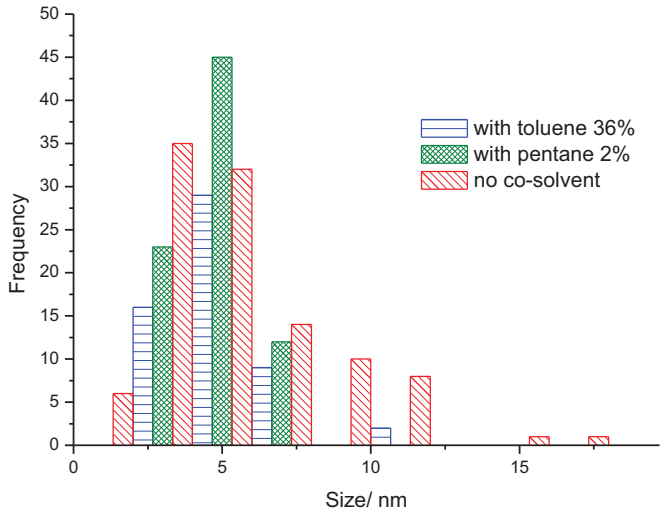

Figure 21. Superimposed size distribution histograms for TaNPs produced in $[C_1C_4Im][NTf_2]$ neat and in the presence of co-solvents, pentane (2 % wt) and toluene (36 % wt).

Table 1. Resulting sizes of TaNPs, produced in different media under H_2 (4 bars) and 25 °C

Ionic Liquid	Co-solvent	Mean size NPs (nm)
$C_1C_4Im\ NTf_2$	none	5 ± 3 (70%) (<10 (30%))
$C_1C_4Im\ NTf_2$	toluene (36% wt)	5 ± 3
$C_1C_4Im\ NTf_2$	n-pentane (2% wt)	5 ± 1

Due to the structured nature of ionic liquids, previously determined by molecular dynamics simulations, non-polar substrates are contained within non-polar pockets of the IL, created by the alkyl chains causing a swelling of these pockets.[16] It has also been reported that these domains are responsible for the size control of certain NPs generated in ILs.[26] It is evident that increasing the size of these domains by addition of a non-polar solvent increases the solubility of **1** in $[C_1C_4Im][NTf_2]$, and thus the size distribution is largely monodisperse. This is especially clear for the addition of a small amount of pentane, Figure 21.

However, the NP mean size remains large with respect to RuNPs generated in $[C_1C_4Im][NTf_2]$, in the absence of solvent. As the addition of a non-polar solvent causes a swelling of these domains, the larger size of Ta(0)NPs compared to RuNPs may be explained, although it could be due to a different growth and stabilisation mechanism, as observed in the case of nickel.

2.4.3 Increasing the chain length

In imidazolium ILs, for a given anion, the solubility of a nonpolar substrate increases upon increasing the length of the alkyl chain.[94] Consequently, another means of increasing the solubility of **1** would to be to increase the length of the alkyl chain on the imidazolium of the IL. A second approach was therefore employed involving the use of the hexyl- substituted ionic liquid $[C_1C_6Im][NTf_2]$. Here, **1** was fully dissolved into pure dried $[C_1C_6Im][NTf_2]$ without co-solvent and the decomposition proceeded as previously described. In this medium smaller NPs were produced, 3 ± 1 nm, with a narrower size distribution, Figure 22. The decrease in size compared to $[C_1C_4Im][NTf_2]$, is contradictory to observations for RuNPs.[26] This could be explained by the decreased polarity of this medium and much enhanced solubility of the precursor. Indeed, in the generation RuNPs we observe a similar phenomenon when changing from $[C_1C_2Im][NTf_2]$ to $[C_1C_4Im][NTf_2]$ attributed to the higher polarity of the former.[26]

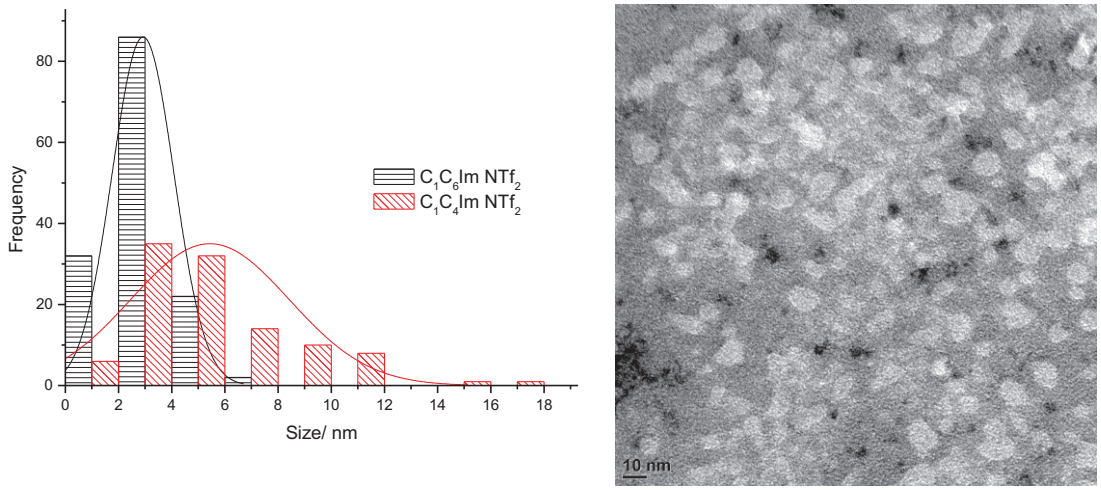

Figure 22. Comparative size distribution histograms of TaNPs produced in $[C_1C_4Im][NTf_2]$ and $[C_1C_6Im][NTf_2]$ and TEM image of those formed in the latter.

2.4.4 High resolution electron microscopy of TaNPs

A sample of TaNPs produced in $[C_1C_4Im][NTf_2]$ has also been analysed by high resolution electron microscopy, HREM, in the absence of air. From the images obtained, interplanar distances within the nanoparticles were found to be of 2.2Å corresponding to the (110) face of bulk fcc crystalline tantalum metal, Figure 23.[84] This provides significant evidence to suggest the particles generated are of tantalum in its zero oxidation state and not oxidised forms. Given the high oxophilicity of Ta metal however, these NPs must be kept under an inert

atmosphere to remain zero-valent. The NP suspensions produced were not stable and decanted over time. This presents the possibility of facile extraction of the NPs produced for use in other media.

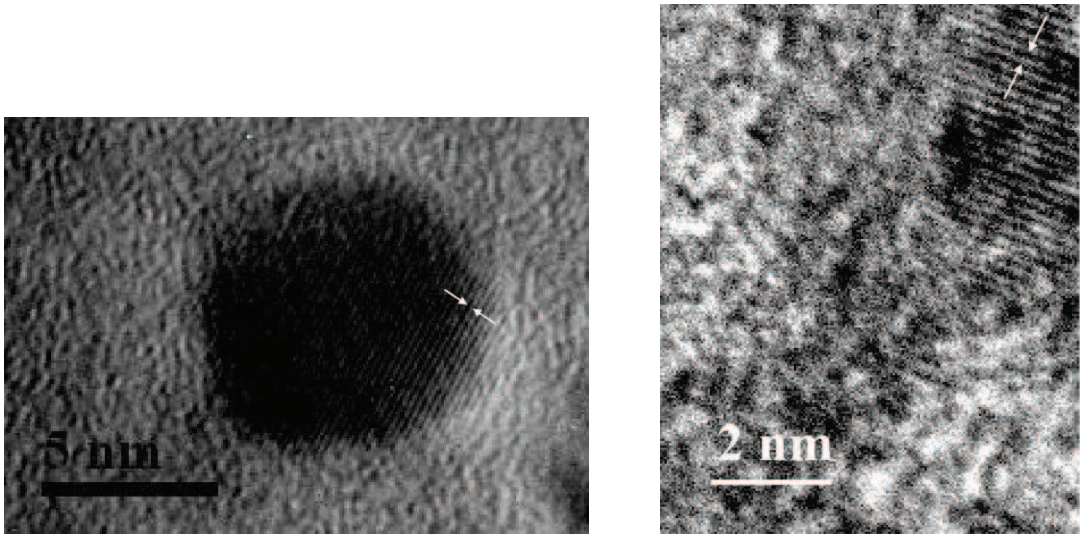

Figure 23. HREM images of crystalline TaNPs produced in $[C_1C_4Im][NTf_2]$. Interplanar distances indicated by the arrows are of 2.2 Å.

2.4.5 Conclusion

In conclusion, we have demonstrated that small monodisperse and zero-valent tantalum nanoparticles, Ta(0)NPs, may be generated under mild conditions, by decomposition of the organometallic complex tris(neopentyl)neopentylidene tantalum(V), under H_2 in imidazolium derived ionic liquids. The control of the size and the factors of stabilisation of these NPs in ionic liquids are currently under investigation. This method has opened up the possibility of facile access to other oxophilic metal nanoparticles, which we are currently studying, and could be of great potential interest in the drive for smaller and more efficient electronic devices.

2.5 Experimental Section

2.5.1 Materials and Methods

All operations were performed in the strict absence of oxygen and water under a purified argon atmosphere using glovebox (Jacomex or MBraun) or vacuum-line techniques.

Ionic Liquid syntheses

The synthesis of $[C_1C_4Im][NTf_2]$ is reported below. All other syntheses imidazolium ionic liquids $[C_1C_6Im][NTf_2]$, $[C_1C_8Im][NTf_2]$, $[C_1C_{10}Im][NTf_2]$, $[C_1C_{4//}Im][NTf_2]$, $[C_1BzIm][NTf_2]$, were synthesised in the same way, as reported.[69]

1-butyl-3-methylimidazolium chloride [C_1C_4Im][Cl] 1-chlorobutane (106 mL, 1.01 mol) was added to freshly distilled 1-methylimidazole (50 mL, 0.63 mol). The mixture was stirred for 48 h at 65 °C. The hot solution was then transferred dropwise via a canula into toluene (200mL) at 0 °C under vigorous mechanical stirring. The white precipitate formed was then filtered and washed repeatedly with toluene (3 × 200 mL) and dried over night *in vacuo* giving a white powder (95.6 g, 87 %). ^{1}H-NMR (CD_2Cl_2): δ (ppm) : 11.05 (s, 1H, C_2H) ; 7.33 (d, 1H, C_4H) ; 7.28 (d, 1H, C_5H) ; 4.31 (t, 2H, NCH_2) ; 4.07 (s, 3H, NCH_3) ; 1.90 (qt, 2H, $CH_2CH_2CH_2$) ; 1.41 (st, 2H, $CH_2CH_2CH_3$) ; 0.96 (t, 3H, CH_2CH_3) ; ^{13}C{^{1}H}-NMR (CD_2Cl_2) : δ (ppm) : 138.3 (C_2H) ; 122.3 (C_4H) ; 119.8 (C_5H) ; 50.1 (NCH_2) ; 36.8 (NCH_3) ; 32.5 ($CH_2CH_2CH_2$) ; 19.8 ($CH_2CH_2CH_3$) ; 13.6 (CH_2CH_3)

1-butyl-3-methylimidazolium bis(trifluoromethylsulphonyl)imide [C_1C_4Im][NTf_2] A solution of lithium bis(trifluorosulphonylimide) [$LiNTf_2$] (50 g, 0.17 mol) in water (50 mL) was added to a solution of BMICl (30.4 g, 0.17 mol) in water (100 mL). The solution was stirred for 2 h at room temperature, then dichloromethane (50 mL) was added and the mixture transferred to a separating funnel. The lower phase was collected and washed repeatedly with water (8 × 100 mL) until no chloride traces remained in the washings (tested with silver nitrate solution). The ionic liquid in dichloromethane was purified through a short alumina column and the solvent removed *in vacuo* giving a colourless viscous liquid. ^{1}H-NMR (CD_2Cl_2): δ (ppm) : 8.73 (s, 1H, C_2H) ; 7.28 (d, 1H, C_4H) ; 7.24 (d, 1H, C_5H) ; 4.15 (t, 2H, NCH_2) ; 3.90 (s, 3H, NCH_3) ; 1.83 (qt, 2H, $CH_2CH_2CH_2$) ; 1.32 (st, 2H, $CH_2CH_2CH_3$) ; 0.94 (t, 3H, CH_2CH_3) ; ^{13}C{^{1}H}-NMR (CD_2Cl_2) : δ (ppm) : 134.3 (C_2H) ; 124.3 (C_4H) ; 122.4 (C_5H) ; 118.2 (CF_3) ; 50.3 (NCH_2) ; 37.1 (NCH_3) ; 33.2 ($CH_2CH_2CH_2$) ; 19.8 ($CH_2CH_2CH_3$) ; 13.5 (CH_2CH_3)

1-Methylimidazole (> 99 %) was purchased from Aldrich and distilled prior to use. Chlorobutane, benzyl chloride and 4-chlorobut-1-ene (> 99 %, Aldrich) were used without further purification. Bis(trifluoromethanesuflonyl)imide lithium salt (> 99 %, Solvionic) was used without further purification.

Organometallic complexes

(η^4-1,5-cyclooctadiene)(η^6-1,3,5-cyclooctatriene)ruthenium(0) Ru(COD)(COT) was synthesised as reported.[95] Degassed cycloocta-1,5-diene (60 mL, 0.49 mol) filtered over alumina and zinc dust (10.0 g) were added to a solution of $RuC1_3.3H_2O$ (3.6 g, 13.7 mmol) in distilled degassed methanol (50 mL). The mixture was heated under reflux with magnetic stirring for 6 h and then filtered, washing the solid residue with dry degassed toluene. The resulting brown solution was evaporated *in vacuo* until the residue was completely dry. Extraction with n-pentane (2 mL) gave a red solution which was filtered through a column of alumina (20 cm), resulting in a yellow solution. The volume of the solvent was reduced to ca. 5 mL *in vacuo* and the yellow solution was cooled to - 78 °C to give, in 6 h, yellow crystals of Ru(COD)(COT) (1.7 g, 43 %), m.p. 92 - 94 °C. ^{1}H-NMR (C_6D_6) δ (ppm) : 4.78 (dd, 2 H), 5.22 (m, 2 H), 6.21 (m, 2 H), 7.08 (m, 4 H), 7.78 (m, 8 H), 8.36 (m, 2 H), 9.10 (m, 2 H).

Bis(η^4-1,5-cyclooctadiene)nickel(0), $Ni(COD)_2$, (Strem > 99 %) was used as recieved.

Tris(neopentyl)(neopentylidene)tantalum(V), Ta Schrock, was prepared according to the literature procedure. [93] A 1.56 M solution of NpMgCl in diethylether (100 mL) was added drop-wise over 0.5 h to a stirred suspension of $TaCl_5$ (6.0 g, 16 mmol) in 150 mL of diethylether at room temperature. Any solid $TaC1_5$ rapidly dissolved as the reaction proceeded through stages characterized by greenish-yellow, yellow, and finally, orange-brown colours. The final solution contained some magnesium chloride, which was removed by filtration over celite. All solvent was removed *in vacuo* and the residue sublimed in two stages at 90 °C and ~ 10^{-8} bar to give 1.7 g (22 %) of deep orange crystals on the probe. ^{1}H-NMR (C_6D_6) δ (ppm): 8.09 (s, 1H) , 8.57 (s, 9H), 8.85 (s, 27H), 9.16 (s, 6H)

Nanoparticles

Ruthenium In a typical synthesis, Ru(COD)(COT) (66 mg, 0.21 mmol) was stirred virorously into the dry degassed ionic liquid (5 mL). The resulting bright yellow suspension was then transferred via canula to a Fischer-Porter bottle, in a thermostatic bath (0° C or 25° C), which was pressurised under pure H_2 or D_2 (4 bars) over 3 days (0° C) or 18 h (25° C). The

volatiles (cyclooctane) were subsequently removed under reduced pressure and the resultant black solution was stored under inert (Ar) atmosphere in the glovebox.

Nickel – decomposition under H_2. The same procedure as above was applied to $Ni(COD)_2$ (50 mg, 0.14 mmol) in ionic liquid $[C_1C_{n>4}Im][NTf_2]$ (10 mL).

Nickel – decomposition on dissolution. $Ni(COD)_2$ (50 mg, 0.14 mmol) was stirred into ionic liquid $[C_1C_{n\leq4}Im][NTf_2]$ (10 mL) producing a pale yellow solution at 25 °C. After 1 h the solution had turned green and after a further hour the solution a black solution resulted.

Tantalum. Ta Schrock (25 mg, 5.4×10^{-5} mol) was dissolved in the ionic liquid (10 mL) or ionic liquid-organic solvent mixture (dry, degassed toluene or pentane). The resulting orange solution was canulated into a Fischer-Porter bottle, which was pressurised under 4 bars of H_2 at 25 °C during 4 days. A black solution resulted, which was stored in a glove box under argon.

2.5.2 NMR Spectroscopy

Solution NMR spectra were recorded on Bruker Avance 300 MHz spectrometer for ^1H and ^{13}C. DRX 500MHz for ^2H. Gas phase ^1H NMR spectra were obtained on a Bruker DRX 500 instrument at 298 K (nominal) with a resonance frequency at 500 130 MHz.

2.5.3 Mass spectrometry

Mass spectra were acquired on a ThermoFinnigan LCQ Advantage ion trap instrument, detecting positive (+) an negative (–) ions in the ESI mode. Samples (1 to 10 µg/mL in acetonitrile) were infused directly into the source (5 $\mu L.min^{-1}$) using a syringe pump. The following source parameters were applied: spray voltage 3.0–3.5 kV, nitrogen sheath gas flow 5–20 arbitrary units. The heated capillary was held at 200°C. MS spectra were obtained by applying a relative collision energy of 25 to 40% of the instrumental maximum.

1) ESI^+ mass spectrum for $[C_1C_{4//}Im][NTf_2]$ after deuterium incorporation.

$[C_1C_{4//}Im][NTf_2]$:

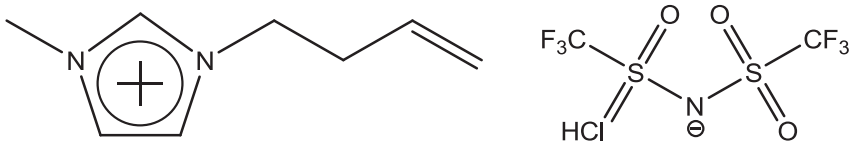

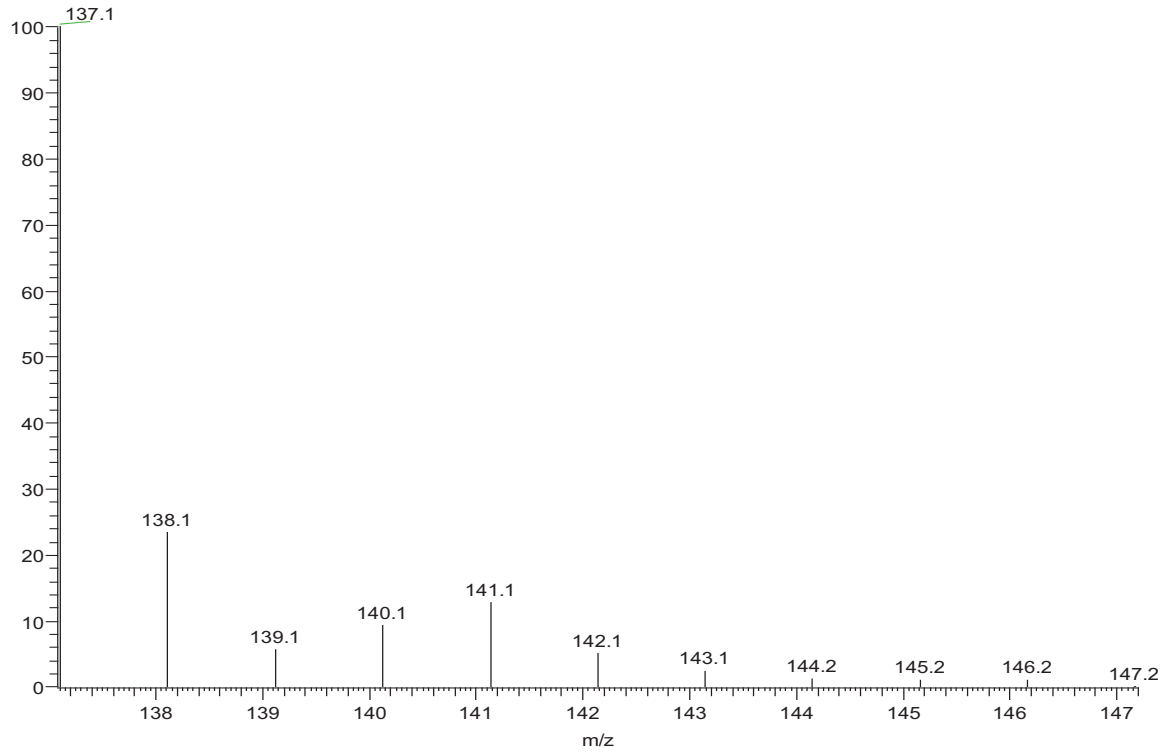

Relative peak intensities from the above spectrum

2) ESI^+ mass spectrum for $[C_1BzIm][NTf_2]$ after deuterium incorporation

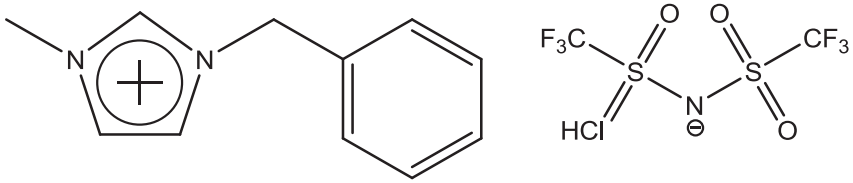

$[C_1BzIm][NTf_2]$:

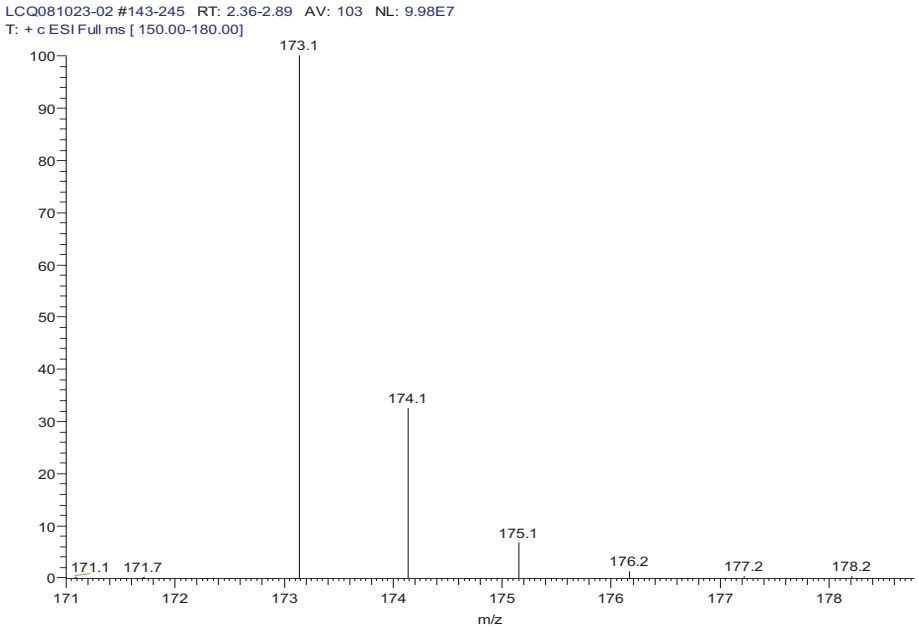

ESI$^+$ spectrum – deuterated methylenecyclohexyl region

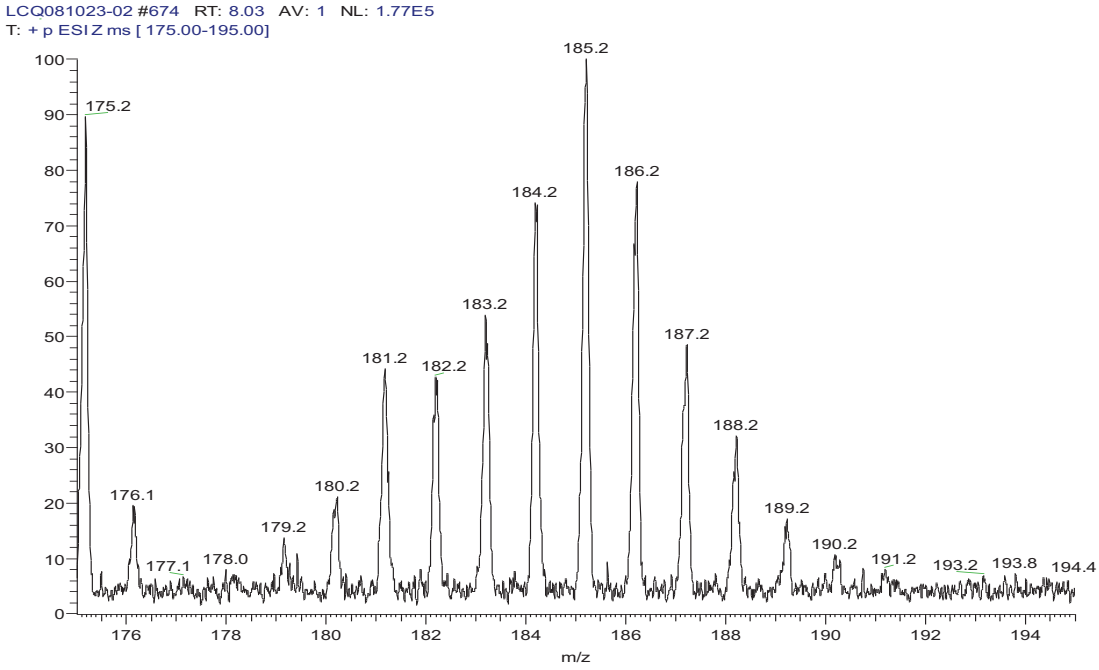

2.5.4 Transition Electron Microscopy

Samples for TEM observations were prepared by placing a thin film of the nanoparticles dispersed in ionic liquids on a copper grid coated with holey carbon film. The size distribution histograms of the metal particles were constructed from the measurement of roughly 200 particles, assuming spherical shape.

The transmission electronic microscopy (TEM) experiments were performed directly in the IL media. A thin film of RuNP solution in IL was deposited on a carbon film supported by a copper grid. Conventional TEM micrographs were obtained at the "Centre Technologique des Microstructures", UCBL1, Villeurbanne, France, using a Philips 120 CX electron microscope. The acceleration voltage was 120 kV. Size distribution histograms were constructed from the measurement of at least 200 different nanoparticles assuming a near spherical shape and random orientation.

2.5.5 GC analyses

The products were quantitatively analysed by gas chromatography on a P6890 chromatograph equipped with a flame ionisation detector (FID) and an Al_2O_3/KCl column (L) 50 m, φint) 0.32 mm, film thickness) 5 μm). The injector and detector temperature was 230° C, and the injection volume was 1 μL. The temperature was fixed at 190° C.

2.5.6 Hydrogenation of Ethylene by RuNPs in the IL

A 2 mL sample of the RuNP solution in the IL was introduced under argon into a Schlenk of known volume. The sample was treated under flow of argon for 18 h. The argon atmosphere was replaced with a known pressure of ethylene using a vacuum line and the system was stirred. A decrease of the internal pressure was observed, and the composition of the gas phase was monitored by gas chromatography. After 12 h, the atmosphere was replaced by a H_2 atmosphere and the system was heated and stirred for 12 h. The composition of the gas phase was again monitored by gas chromatography.

Ethylene Hydrogenation Calculations

$pV = nRT$

$V_{reactor} = 125.8\ cm^3 = 1.258 \times 10^{-4}\ m^3$

$p_r = 129\ mbar = 1.2 \times 10^4\ Pa$

$R = 8.314\ m^3\ Pa\ K^{-1}\ mol^{-1}$

$T = 298\ K$

$n = (1.29 \times 10^4 \times 1.258 \times 10^{-4}) / (8.314 \times 298)$ m^3 Pa m^{-3} Pa^{-1} K mol K^{-1} =

6.54×10^{-5} mol ethylene introduced

GC calibration results: $2.3 \times 10^{-12} \times A$ = no. moles of C

300µL injections = 3×10^{-7} m^3

Table 2. GC results following treatment under ethylene

Species	*Ret time/ mins*	*Peak Area*	*No. Moles of C*	*No. of Moles (in 300 µL)*	*No. of Moles (in reactor)*
ethane	4.816	2.31×10^4	5.3×10^{-8}	2.7×10^{-8}	1.1×10^{-5}
ethylene	5.094	6.57×10^4	1.5×10^{-7}	7.6×10^{-8}	3.2×10^{-5}
isobutane	8.322	367	8.4×10^{-10}	2.1×10^{-10}	8.8×10^{-8}
butenes	10.5	805	1.9×10^{-9}	4.6×10^{-10}	1.9×10^{-7}

$C_2H_4 + H_2 \rightarrow C_2H_6$:

1 mole ethane produced = 1 mole H_2 consumed, i.e. 2 moles of surface hydrides

$2C_2H_4 + H_2 \rightarrow C_4H_{10}$:

1 mole isobutane produced = 1 mole H_2 consumed, i.e. 2 moles of surface hydrides

$2C_2H_4 \rightarrow C_2H_8$

1 mole butene produced = No H_2 consumed

Table 3. GC results following treatment under H_2 liberating surface alkyls

Species	*Ret time/ mins*	*Peak Area*	*No. Moles of C*	*No. of Moles (in 300 µL)*	*No. of Moles (in reactor)*
methane	4.501	4.79×10^3	1.1×10^{-8}	1.1×10^{-8}	4.6×10^{-6}
ethane	4.826	1.69×10^4	3.9×10^{-8}	1.9×10^{-8}	8.1×10^{-6}
n-propane	5.871	8.47×10^3	1.9×10^{-8}	6.5×10^{-9}	2.7×10^{-6}
n-butane	8.753	4.04×10^3	9.2×10^{-9}	2.3×10^{-9}	9.7×10^{-7}
n-pentane	12.434	463	1.1×10^{-9}	2.1×10^{-10}	8.9×10^{-8}

½ C_2H_4 + ½ $H_2 \rightarrow$ -CH_3

1 mole methyl produced = ½ mole H_2 consumed, i.e. 1 mole of surface hydrides

C_2H_4 + ½ $H_2 \rightarrow$ -C_2H_5

1 mole ethyl produced = ½ mole H_2 consumed, i.e. 1 mole of surface hydrides

1½ C_2H_4 + ½ $H_2 \rightarrow$ -C_3H_7

1 mole propyl produced = ½ mole H_2 consumed, i.e. 1 mole of surface hydrides

$2C_2H_4$ + ½ H_2 → -C_4H_9

1 mole butyl produced = ½ mole H_2 consumed, i.e. 1 mole of surface hydrides

2½ C_2H_4 + ½ H_2 → -C_5H_{11}

1 mole pentyl produced = ½ mole H_2 consumed, i.e. 1 mole of surface hydrides

Total surface hydrides counted = ***38 µmol***

Ethylene Mass balance

6.54×10^{-5} mol (introduced) - 6.02×10^{-5} mol (detected by GC) = 5.2 µmol ~ 8 % error

2.5.7 H-D exchange

A 2mL sample of the RuNP solution in the IL was introduced under argon into a Schlenk, which was then treated under dynamic vacuum (10^{-5} mbar) during a period of 1h or 4h. This was then charged with deuterium (1 bar) and stirred at 25°C during a period of 1 or 4 days. The gas phase was subsequently expanded into an airtight Young tube for NMR analysis.

2.5.8 TON calculations

Butenyl IL → butyl IL

Ru(COT)(COD) – 2.2×10^{-4} moles

RuNPs, 1.1 ± 0.2 nm, dispersion ~75%

Ru_s – 1.7×10^{-4} moles

Butenyl IL 7.5g/ 417g mol^{-1} = 1.8×10^{-2} moles

15 % converted → 2.7×10^{-3} moles

TON → 2.7×10^{-3} moles/ 1.7×10^{-4} moles = ***16***

Benzyl IL → methylenecyclohexyl IL

Ru(COT)(COD) – 2.2×10^{-4} moles

RuNPs, 3.2 ± 0.7 nm, dispersion ~35%

Ru_s – 7.7×10^{-5} moles

Benzyl IL 7.5g/ 453g mol^{-1} = 1.7×10^{-2} moles

30% converted → 4.9×10^{-3} moles

TON → 4.9×10^{-3} moles/7.7×10^{-5} moles = ***64***

2.6 References

1. J. Dupont and J. D. Scholten, *Chem. Soc. Rev.*, 2010, **39**, 1780-1804.
2. A. Corma, I. Dominguez, T. Rodenas and M. J. Sabater, *J. Catal.*, 2008, **259**, 26-35.
3. L. S. Ott and R. G. Finke, *Coord. Chem. Rev.*, 2007, **251**, 1075-1100.
4. A. P. Umpierre, G. Machado, G. H. Fecher, J. Morais and J. Dupont, *Adv. Synth. Catal.*, 2005, **347**, 1404-1412.
5. L. S. Ott and R. G. Finke, *Inorg. Chem.*, 2006, **45**, 8382-8393.
6. H. Bönnemann, K. S. Nagabhushana and R. M. Richards, in *Nanoparticles and Catalysis*, ed. D. Astruc, Wiley-VCH, Weinheim, 2008.
7. J. Dupont and D. De Oliveira Silva, in *Nanoparticle Catalysis*, ed. D. Astruc, Wiley-VCH, Weinheim, 2008.
8. S. Oezkar and R. G. Finke, *J. Am. Chem. Soc.*, 2002, **124**, 5796-5810.
9. G. S. Fonseca, G. Machado, S. R. Teixeira, G. H. Fecher, J. Morais, M. C. M. Alves and J. Dupont, *J. Colloid Interface Sci.*, 2006, **301**, 193-204.
10. D. Astruc, F. Lu and J. R. Aranzaes, *Angew. Chem. Int. Ed.*, 2005, **44**, 7852.
11. H. S. Schrekker, M. A. Gelesky, M. P. Stracke, C. M. L. Schrekker, G. Machado, S. R. Teixeira, J. C. Rubim and J. Dupont, *J. Colloid Interface Sci.*, 2007, **316**, 189-195.
12. L. S. Ott, S. Campbell, R. Seddon Kenneth and G. Finke Richard, *Inorg. Chem.*, 2007, **46**, 10335-10344.
13. L. S. Ott, M. L. Cline, M. Deetlefs, K. R. Seddon and R. G. Finke, *J. Am. Chem. Soc.*, 2005, **127**, 5758-5759.
14. J. N. A. Canongia Lopes and A. A. H. Padua, *J. Phys. Chem. B*, 2006, **110**, 3330-3335.
15. A. Triolo, O. Russina, H.-J. Bleif and E. Di Cola, *J. Phys. Chem. B*, 2007, **111**, 4641-4644.
16. A. A. H. Padua, M. F. Costa Gomes and J. N. A. Canongia Lopes, *Acc. Chem. Res.*, 2007, **40**, 1087-1096.
17. M. G. Del Popolo, C. L. Mullan, J. D. Holbrey, C. Hardacre and P. Ballone, *J. Am. Chem. Soc.*, 2008, **130**, 7032-7041.
18. M. Antonietti, D. Kuang, B. Smarsly and Y. Zhou, *Angew. Chem. Int. Ed.*, 2004, **43**, 4988-4992.

19. E. R. Cooper, C. D. Andrews, P. S. Wheatley, P. B. Webb, P. Wormald and R. E. Morris, *Nature*, 2004, **430**, 1012-1016.
20. J. N. Canongia Lopes, M. F. Costa Gomes and A. A. H. Padua, *J. Phys. Chem. B*, 2006, **110**, 16816-16818.
21. L. M. Rossi and G. Machado, *J. Mol. Catal. A,* 2009, **298**, 69-73.
22. C. Pan, K. Pelzer, K. Philippot, B. Chaudret, F. Dassenoy, P. Lecante and M.-J. Casanove, *J. Am. Chem. Soc.*, 2001, **123**, 7584-7593.
23. K. Pelzer, K. Philippot and B. Chaudret, *Z. Phys. Chem.*, 2003, **217**, 1539-1547.
24. E. T. Silveira, A. P. Umpierre, L. M. Rossi, G. Machado, J. Morais, G. V. Soares, I. J. R. Baumvol, S. R. Teixeira, P. F. P. Fichtner and J. Dupont, *Chem.--Eur. J.*, 2004, **10**, 3734-3740.
25. T. Gutel, J. Garcia-Anton, K. Pelzer, K. Philippot, C. C. Santini, Y. Chauvin, B. Chaudret and J.-M. Basset, *J. Mater. Chem.*, 2007, **17**, 3290-3292.
26. T. Gutel, C. C. Santini, K. Philippot, A. Padua, K. Pelzer, B. Chaudret, Y. Chauvin and J.-M. Basset, *J. Mater. Chem.*, 2009, **19**, 3624-3631.
27. K. Philippot and B. Chaudret, *C. R. Chimie*, 2003, **6**, 1019-1034.
28. T. Pery, K. Pelzer, G. Buntkowsky, K. Philippot, H.-H. Limbach and B. Chaudret, *ChemPhysChem*, 2005, **6**, 605-607.
29. J. Garcia-Anton, M. R. Axet, S. Jansat, K. Philippot, B. Chaudret, T. Pery, G. Buntkowsky and H.-H. Limbach, *Angew. Chem. Int. Ed.*, 2008, **47**, 2074-2078.
30. J. R. Anderson, *Structure of metallic Catalysts*, Acadamic Press, London, 1975.
31. R. Berthoud, P. Delichere, D. Gajan, W. Lukens, K. Pelzer, J.-M. Basset, J.-P. Candy and C. Coperet, *J. Catal.*, 2008, **260**, 387-391.
32. J. Okal, *Catal. Commun.*, 2010, **11**, 508-512.
33. M.-C. Daniel and D. Astruc, *Chem. Rev.*, 2004, **104** 293-346.
34. J. L. Anthony, J. L. Anderson, E. J. Maginn and J. F. Brennecke, *J. Phys. Chem. B*, 2005, **109**, 6366-6374.
35. R. Van Hardeveld and F. Hartog, *Surf. Sci.*, 1969, **15**, 189-230.
36. J.-M. Basset *et al.*, in *Modern Surface Organometallic Chemistry*, ed. J. M. Basset, Psaro Rinaldo, Roberto Dominique, Ugo Renato, Wiley VCH, Weinheim, 2009, pp. 23-68.
37. M. Leconte, A. Theolier and J. M. Basset, *J. Mol. Catal. A*, 1985, **28**, 217-231.

38. M. Leconte, A. Theolier, D. Rojas and J. M. Basset, *J. Am. Chem. Soc.*, 1984, **106**, 1141-1142.
39. I. M. Ciobica, A. W. Kleyn and R. A. Van Santen, *J. Phys. Chem. B* 2003, **107**, 164-172.
40. T. H. Rod, A. Logadottir and J. K. Norskov, *J. Chem. Phys.*, 2000, **112**, 5343–5347.
41. J. Wang, C. Y. Fan, Q. Sun, K. Reuter, K. Jacobi, M. Scheffler and G. Ertl, *Angew. Chem. Int. Ed.*, 2003, **42**, 2151-2154.
42. M. P. Stracke, M. V. Migliorini, E. Lissner, H. S. Schrekker, D. Back, E. S. Lang, J. Dupont and R. S. Goncalves, *New J. Chem.*, 2009, **33**, 82-87.
43. A. Roucoux, A. Nowicki and K. Philippot, in *Nanoparticles*, ed. D. Astruc, Wiley-VCH, Weinheim, 2007, p. 351.
44. L. Cammarata, S. G. Kazarian, P. A. Salter and T. Welton, *Phys. Chem. Chem. Phys.*, 2001, **3**, 5192-5200.
45. Y.-Y. Jiang, Z. Zhou, Z. Jiao, L. Li, Y.-T. Wu and Z.-B. Zhang, *J. Phys. Chem. B*, 2007, **111**, 5058-5061.
46. A. Mele, C. D. Tran and S. H. De Paoli Lacerda, *Angew. Chem. Int. Ed.*, 2003, **42**, 4364-4366.
47. A.-L. Rollet, P. Porion, M. Vaultier, I. Billard, M. Deschamps, C. Bessada and L. Jouvensal, *J. Phys. Chem. B,* , 2007, **111** 11888 -11891.
48. B. L. Bhargava and M. L. Klein, *J. Phys. Chem. B*, 2009, **113**, 9499-9505.
49. B. L. Bhargava and M. L. Klein, *Soft Matter*, 2009, **5**, 3475-3480.
50. S. Pickering, *J. Chem. Soc.*, 1907, **91**, 307.
51. L. Lu, M. L. Sui and K. Lu, *Science*, 2000, **287**, 1436.
52. H. Wang, X. Jiao and D. Chen, *J. Phys. Chem. C*, 2008, **112**, 18793-18797.
53. N. Cordente, C. Amiens, B. Chaudret, M. Respaud, F. Senocq and M.-J. Casanove, *J. Appl. Phys.* , 2003, **94**, 6358-6365.
54. N. Cordente, M. Respaud, F. Senocq, M.-J. Casanove, C. Amiens and B. Chaudret, *Nano Lett.*, 2001, **1**, 565-568.
55. T. Ould Ely, C. Amiens and B. Chaudret, *Chem. Mater.*, 1999, **11**, 526-529.
56. P. Migowski, G. Machado, S. R. Texeira, M. C. M. Alves, J. Morais, A. Traverse and J. Dupont, *Phys. Chem. Chem. Phys.*, 2007, **9**, 4814-4821.

57. P. Migowski, S. R. Teixeira, G. Machado, M. C. M. Alves, J. Geshev and J. Dupont, *J. Electron Spectrosc.*, 2007, **156-158**, 195-199.
58. T. N. Rostovshchikova, *Catal. Today*, 2005, **105**, 344-349.
59. P. Migowski and J. Dupont, *Chem.--Eur. J.*, 2007, **13**, 32-39.
60. I. Aiken, J. D., and R. G. Finke, *J. Am. Chem. Soc.*, 1998, **120**, 9545-9554.
61. K. Pelzer, O. Vidoni, K. Philippot, B. Chaudret and V. Collière, *Adv. Funct. Mater.*, 2003, **13**, 118-126.
62. R. G. Finke, *Coord. Chem. Rev.*, 2007, **251**, 1075–1100.
63. P. Pertici, G. Simonelli, G. Vitulli, G. Deganello, P. Sandrini and A. Mantovani, *Chem. Commun.*, 1977, 132-133.
64. E. Shevchenko, V.,, D. V. Talapin, H. Schnablegger, A. Kornowski, O. Festin, P. Svedlindh, M. Haase and H. Weller, *J. Am. Chem. Soc.*, 2005, **125**, 9092-9101.
65. E. A. Crespo, M. Ruda and S. Ramos de Debiaggi, *Int. J. Hydrogen Energy*, 2008, **33**, 3561-3565.
66. A. Geissler, M. He, J.-M. Benoit and P. Petit, *J. Phys. Chem. C*, 2010, **114**, 89-92.
67. P. S. Campbell, C. C. Santini, D. Bouchu, B. Fenet, K. Philippot, B. Chaudret, A. A. H. Padua and Y. Chauvin, *Phys. Chem. Chem. Phys.*, 2010, **12**, 4217-4223.
68. V. Lecocq and H. Olivier-Bourbigou, *Oil & Gas Sci. Tech*, 2007, **62**, 761-773.
69. L. Magna, Y. Chauvin, G. P. Niccolai and J.-M. Basset, *Organometallics*, 2003, **22**, 4418-4425.
70. C. M. Crudden and D. P. Allen, *Coord. Chem. Rev.*, 2004, **248**, 2247-2273.
71. U. Hintermair, T. Gutel, A. M. Z. Slawin, D. J. Cole-Hamilton, C. C. Santini and Y. Chauvin, *J. Organometal. Chem.*, 2008, **693**, 2407-2414.
72. D. S. McGuinness, W. Mueller, P. Wasserscheid, K. J. Cavell, B. W. Skelton, A. H. White and U. Englert, *Organometallics*, 2002, **21**, 175-181.
73. N. D. Clement, K. J. Cavell, C. Jones and C. J. Elsevier, *Angew. Chem. Int. Ed.*, 2004, **43**, 1277-1279.
74. D. C. Graham, K. J. Cavell and B. F. Yates, *Dalton Trans.*, 2007, **41**, 4650-4658.
75. S. Gruendemann, A. Kovacevic, M. Albrecht, J. W. Faller Robert and H. Crabtree, *Chem. Commun.*, 2001, 2274-2275.
76. P. Ireland, *Thin Solid Films* 1997, **304**, 1-12.

77. S. Murarka and S. Hymes, *Crit. Rev. Solid State Mater. Sci.* 1995, **20**, 87-124.
78. J. Dufourcq, S. Bodnar, G. Gay, D. Lafond, P. Mur, G. Molas, J. Nieto, L. Vandroux, L. Jodin, F. Gustavo and T. Baron, *App. Phys. Lett.*, 2008, **92**.
79. C. C. Santini, J.-M. Basset, T. Gutel, P. Campbell, S. Deleonibus and P.-H. Haumesser, CEA-LETI /Univ Lyon 1 -CNRS, Fr0901463, 2009.
80. C. C. Santini, J.-M. Basset, T. Gutel, P. Campbell, S. Deleonibus and P.-H. Haumesser, CEA-LETI /Univ Lyon 1 -CNRS, Fr0901464, 2009.
81. G. Schmid, *Nanoparticles: From Theory to Application*, Wiley-VCH, Weinheim, 2004.
82. E. Redel, R. Thomann and C. Janiak, *Chem. Commun.*, 2008, 1789-1791.
83. Y. Wang, Z. Cui and Z. Zhang, *Mater. Lett.*, 2004, **58**, 3017-3020.
84. A. F. Wells, *Structural Inorganic Chemistry*, Clarendon Press, Oxford, 1986.
85. H. Z. D. R. Sadoway, *J. Mater. Chem.*, 2001, **16**, 2544.
86. J. Y. Li, *Rare Met. Mater. Eng.*, 1994, 61.
87. S. Nemana, N. L. Okamoto, N. D. Browning and B. C. Gates, *Langmuir*, 2007, **23**, 8845-8854.
88. S. Z. El Abedin, *Trans. Inst. Met. Finish.*, 2008, **86**, 220-226.
89. S. Z. El Abedin and F. Endres, *ChemPhysChem*, 2006, **7**, 58-61.
90. S. Z. El Abedin and F. Endres, *Acc. Chem. Res.*, 2007, **40**, 1106-1113.
91. J. Dupont, in *Nanoparticles and catalysis*, Wiley-VCH, Weinheim, 2008.
92. D. Astruc, *Nanoparticles and Catalysis*, Wiley-VCH, Weinheim, 2008.
93. R. R. Schrock and J. D. Fellmann, *J. Am. Chem. Soc.*, 1978, **100**, 3359-3370.
94. F. Favre, H. Olivier-Bourbigou, D. Commereuc and L. Saussine, *Chem. Commun.*, 2001, 1360-1361.
95. P. Pertici, G. Vitulli, M. Paci and L. Porri, *Dalton Trans.*, 1980, 1961-1964.

III

Chapter 3

Imidazolium Ionic Liquids as Media for Homogeneous Catalysis

Chapter 3

Imidazolium Ionic Liquids as Media for Homogeneous Catalysis

3.1 Introduction

Ionic liquids are up-and-coming solvents for catalysis, with the number of publications in this field growing at an exponential rate.[1-10,11,12] Indeed, the *"green"* nature of ILs is often cited, and recyclability is a recurring theme to justify such great interest. This recyclability can be two-fold, as ILs may act to immobilise certain ionic,[13, 14]or colloidal catalysts,[15] preventing catalyst leaching; and due to their negligible vapour pressure, they themselves may be recycled more easily than traditional solvents, the products being recovered by simple distillation or liquid-liquid extraction.[16, 17] For the latter, the extraction solvent is often present during the reaction, thus many papers describe *"biphasic catalysis"*.[18-22]

ILs of course are unlike traditional solvents. As reaction media, they have specific properties that may have consequences on the catalytic process. In some catalytic reactions, the difference between the use of ILs and traditional solvents can be related to the chemical role of ILs, which may interfere with the reaction. For instance, imidazolium moieties of the IL may be deprotonated *in situ* and coordinate to metal centres such as Pd, Ir and Rh as imidazolylidene *N*-heterocyclic carbene ligands, as shown in Scheme 1.[23, 24] Due to the acidic C_2-H, this reaction can occur under mild conditions and in the absence of a base.[25] This has a significant effect on catalytic reactions. In the case of palladium-catalysed telomerisation of butadiene with methanol, catalyst deactivation occurs due to the formation of highly stable palladium imidazolylidene complexes.[26] During biphasic Ni-catalysed ethylene oligomerisation in ILs, the formation of NHCs *in situ* has also been evidenced by the formation of an imidazolium cation substituted with an ethyl group on C_2, Scheme 2.[27]

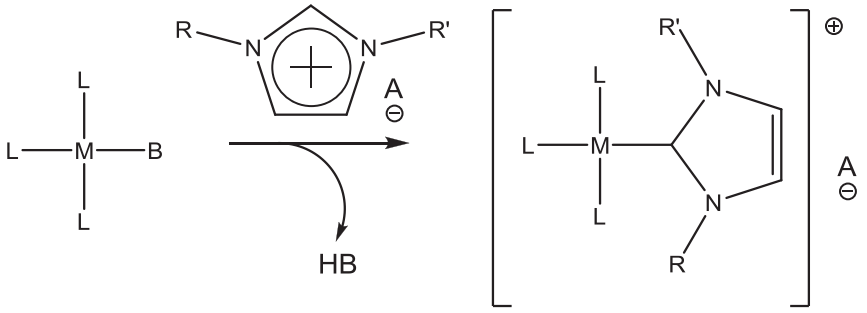

Scheme 1. Typical pathway for in situ NHC formation in imidazolium ILs

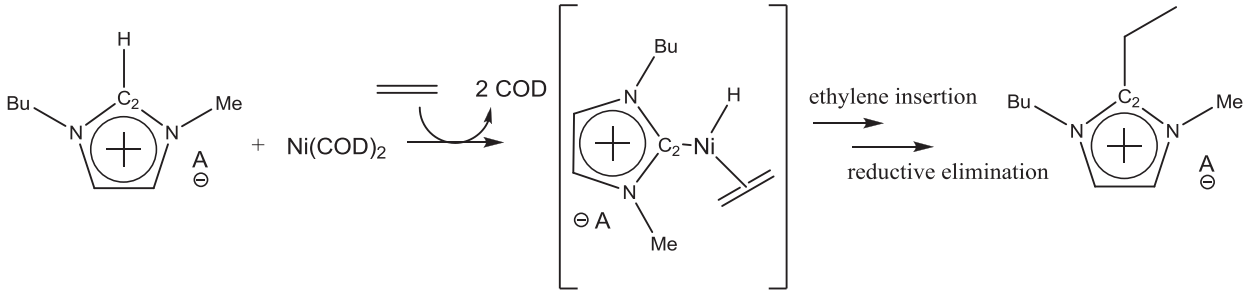

Scheme 2. Ethyl substituted ionic liquid resulting from the *in situ* formation of NHC

However, it has also been reported by Hintermair *et al.* that the nature of such ligands can have positive effect in on both the thermal stability and selectivity of the resulting catalyst compared to phosphine ligands.[28] Thus the potential for chemical interference may be considered either an advantage or disadvantage, depending on the desired outcome of the catalytic process.

It is well worth mentioning that certain ILs themselves exhibit catalytic activity. For instance Lewis acidic ILs, particularly dialkylimidazolium chloroaluminates, which are amongst the first described ionic liquids, can be used successfully as both solvent and catalyst simultaneously. The acidity of such ionic liquids is easily tuned by simply altering the stoichiometry of the dialkylimidazolium chloride versus the aluminium trichloride; an excess of the latter leads to the presence of $Al_2Cl_7^-$. Due both to this and to the fact that aromatics are highly soluble in IL media, Friedel-Crafts alkylations and acylations occur readily in these dual-purpose solvents, Scheme 3.[6, 29]

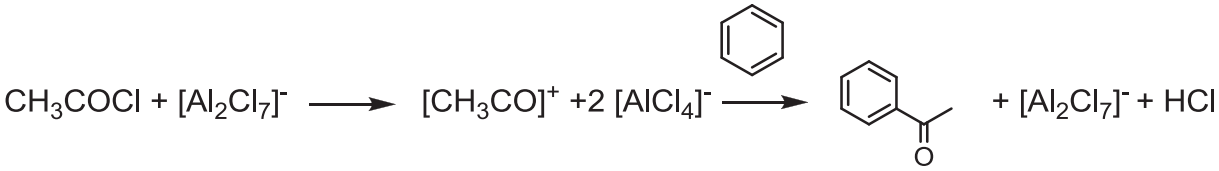

Scheme 3. Friedel-Crafts acylation catalysed by the choroaluminate anion in ILs

In other cases, differences in reactivity have a purely physical-chemical origin. Numerous experimental studies have been carried out providing strong evidence for local structuring of pure ILs, be it through sophisticated NMR spectroscopy focusing on through-space NOE interactions,[30] X-ray diffraction,[31, 32,33] or neutron scattering.[34] Neutron scattering experiments have uncovered evidence for significant charge ordering in the IL $[C_1C_2Im][NTf_2]$, even in the liquid state, while X-ray diffraction patterns of supercooled and liquid imidazolium ionic liquids

with varying chain lengths, have found structural heterogeneities that varied in size with the alkyl chain length, Figure 1.

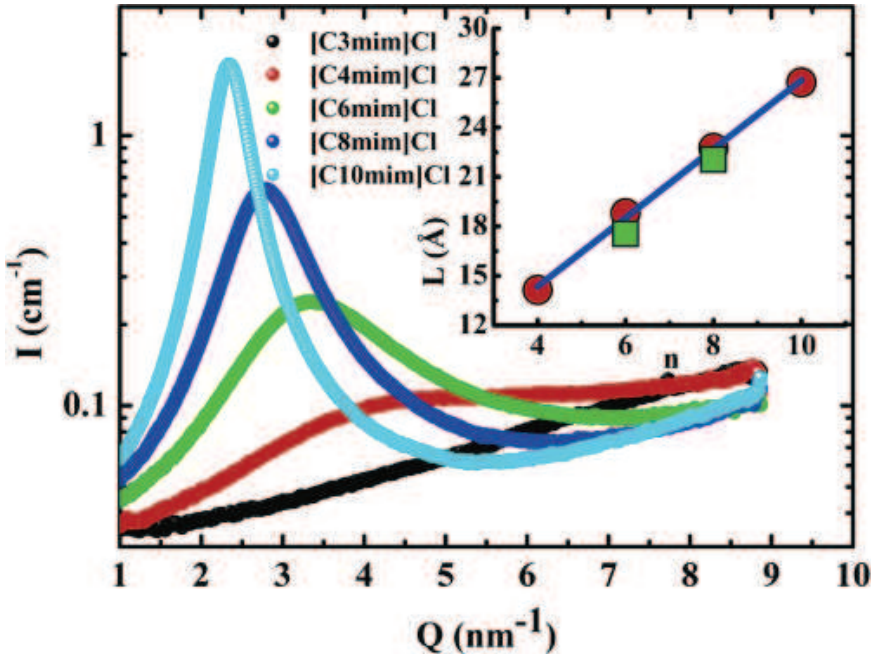

Figure 1. X-ray diffraction patterns from the series of supercooled liquid RTILs: $[C_1C_nIm]Cl$, n) 3, 4, 6, 8, 10, at 25 °C. In the inset the spatial correlation L) $2\pi/Q_{MAX}$, Q_{MAX} being the interference peak position, is plotted (circles) as a function of n, the alkyl chain length,for $4 \leq n$. The corresponding data are also reported for the cases n = 6 and 8 for $[C_1C_nIm][BF_4]$ (squares). [31]

Indeed ionic liquids, especially those based on imidazolium, are widely claimed to exhibit a non-homogenous structure, with close anion-cation association existing throughout the solution, as demonstrated through molecular simulation,[35] and coarse grain modelling.[36] The order and structure therefore depends greatly on both the coordination strength of the anion and on the alkyl chains which group together in lipophilic domains. Short alkyl chains ($n < 4$) are too short to associate with one another, whereas intermediate length chains ($4 \leq n < 10$) will form "pockets", as seen in Figure 2,[35, 37] explaining the heterogeneities observed by X-ray diffraction. Longer chains lead to mesophases and ionic liquid crystals as demonstrated through SAXS experiments.[38] This therefore leads to the question: how do these self-organised media interact with different substrates and what is the upshot in catalysis?

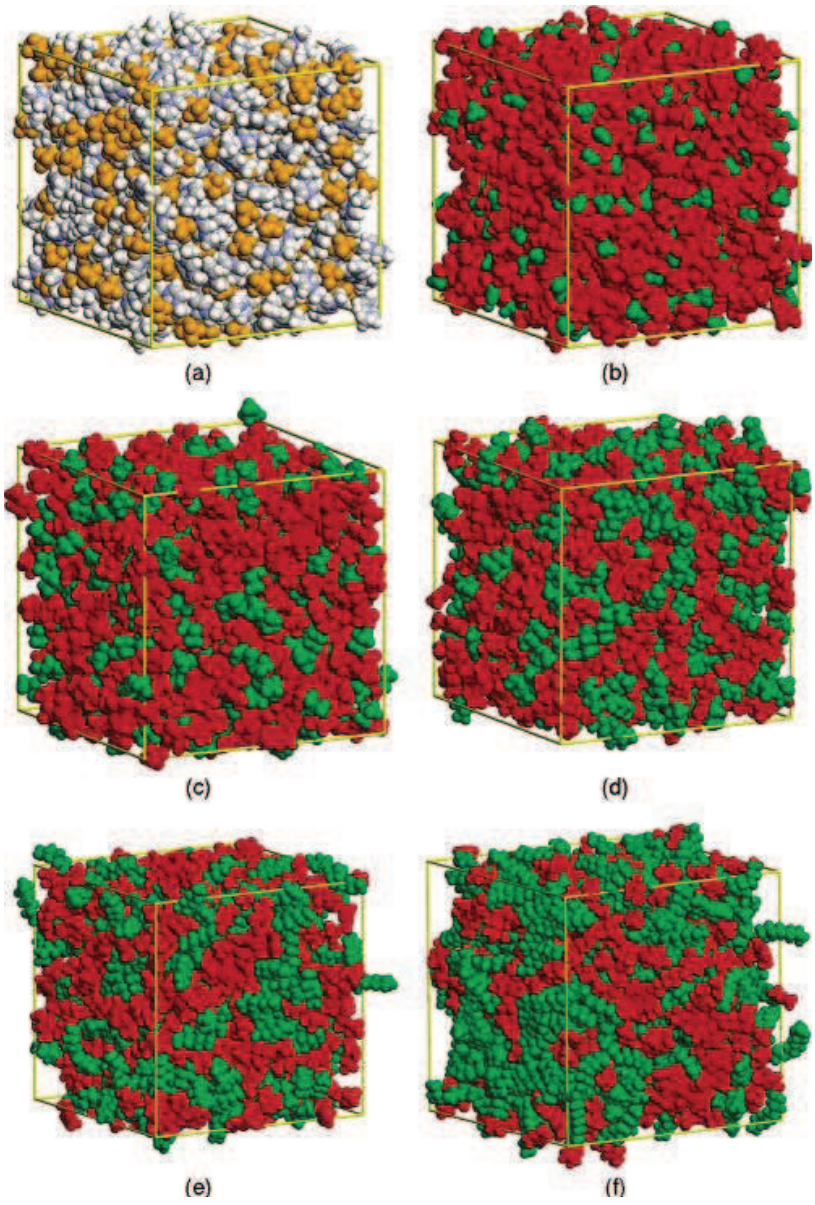

Figure 2. Molecular simulations of $[C_1C_nIm][PF_6]$ ionic liquid structures. In a) $[C_1C_2Im][PF_6]$, colouring is used to distinguish anions from cations, anions being yellow. In b)-f) colouring distinguishes charged species from non-polar species, red being charged and green being non-polar: b) $[C_1C_2Im][PF_6]$, c) $[C_1C_4Im][PF_6]$, d) $[C_1C_6Im][PF_6]$, e) $[C_1C_8Im][PF_6$ and f) $[C_1C_{10}Im][PF_6]$

Ionic liquids have been shown to exhibit specific interactions with themselves, so specific interactions between the ionic liquid and the substrate may also exist and play an important role. Indeed, molecular simulation and determination of radial distribution functions predict that non-polar solutes dissolve in non-polar domains, polar solvents dissolve in polar regions, and amphiphilic solvents, e.g. methanol and acetonitrile display more complicated behaviour.[39] Polarity is not the only consideration however, as X-ray structural determination of benzene-

$[C_1C_2Im][NTf_2]$ mixtures with various compositions have shown evidence for strong π-cation interactions, as shown in Figure 3.[40] Similarly, through combined ROESY NMR and molecular simulation studies, such interactions have been shown to exist in toluene-IL mixtures for the trialkyl IL $[C_1C_1C_4Im][NTf_2]$. By contrast, for the dialkyl IL $[C_1C_4Im][NTf_2$, π-cation interactions with toluene are inhibited by the strong H-bond network between anion and cation, induced by the relatively acidic C_2-H. In this case, toluene penetrates the non-polar alkyl regions of the IL.[41] Another NMR study has provided supporting evidence that the nature of the IL, and thus the interactions within, is crucial in determining the placement of thiiophene in thiophene-IL mixtures. Figure 4 shows the different hypothesised arrangements for thiophene in the ILs $[C_1C_1Im][MeOPHO_2]$ and $[C_1C_4Im][SCN]$ based on this NMR evidence.[42]. Furthermore, the arrangement of CS_2 dissolved in the IL $[C_1C_5Im][NTf_2]$ has been studied as a function of concentration at 295 K by the use of optical heterodyne-detected Raman-induced Kerr effect spectroscopy. The optical Kerr effect (OKE) spectrum suggest that, at low concentration, CS_2 molecules are isolated from each other and mainly localised in the non-polar domains of the IL, Figure 5.[43]

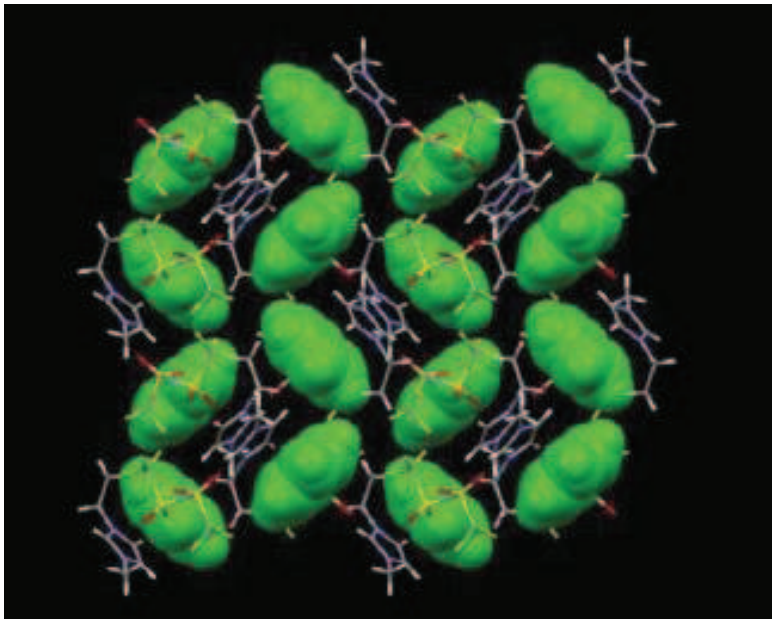

Figure 3. Crystal structure of benzene-$[C_1C_2Im][NTf_2]$ inclusion crystal for a 1:1 molar ratio

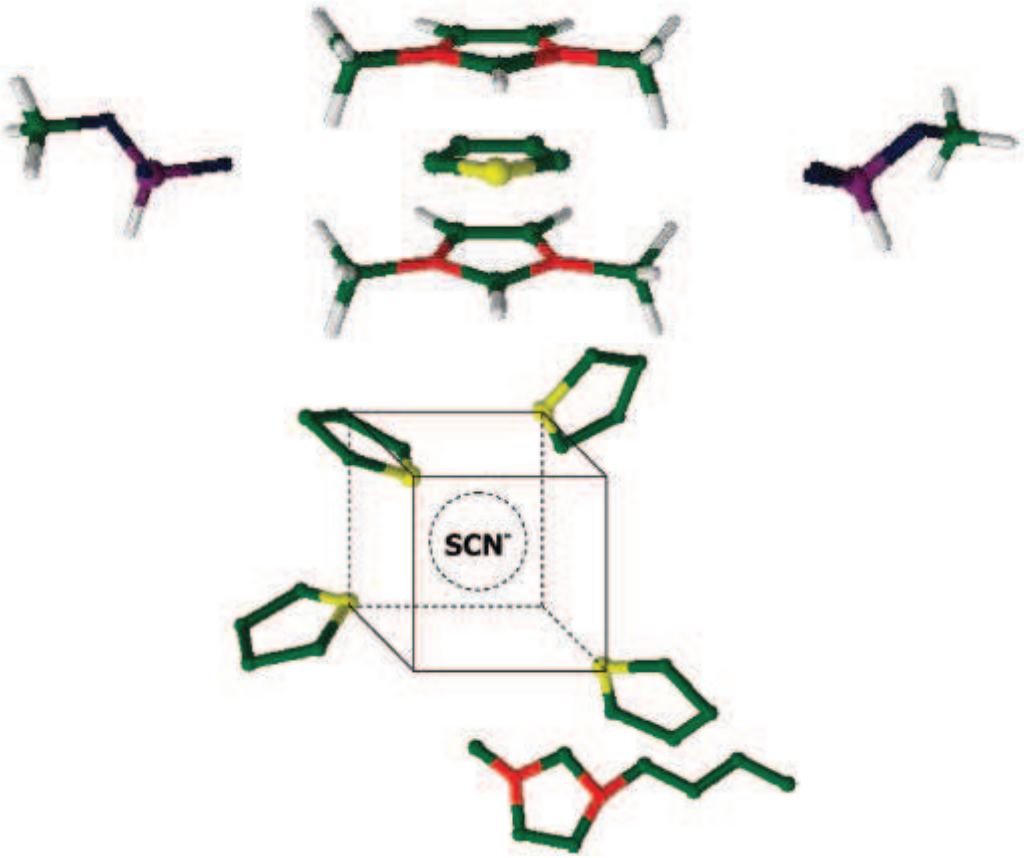

Figure 4. Proposed structure of thiophene in the ionic liquids $[C_1C_1Im][MeOPHO_2]$ (upper) and $[C_1C_4Im][SCN]$ (lower), [42]

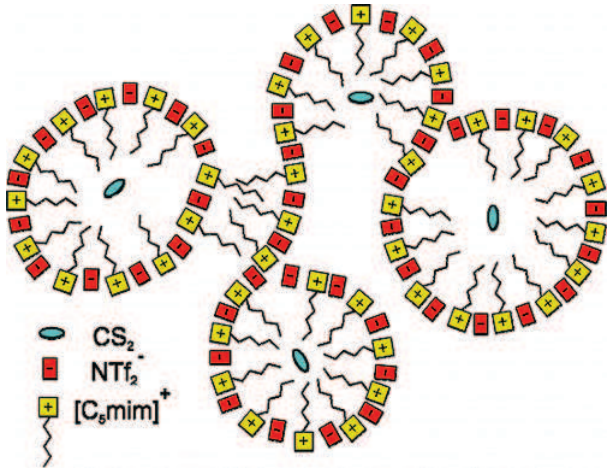

Figure 5. CS_2 molecules are isolated from each other and mainly localised in the nonpolar domains of the IL.[43]

Finally, issues such as density and viscosity in ionic liquids, which are more significant than in most traditional solvents, will play an important role in catalysis through dictating the

diffusion of molecules in the medium.[44, 45, 46] The viscosity varies greatly with the nature of the IL and, although related to the strength of the cation-anion association, is often difficult to predict.[47-48]

In this chapter, we study how in ILs, the activity and selectivity of a model catalytic reaction (hydrogenation of 1,3-cyclohexadiene, CYD, Scheme 4) are dependent on the solvation of substrate and of the physical-chemical properties of the resultant catalytic medium.

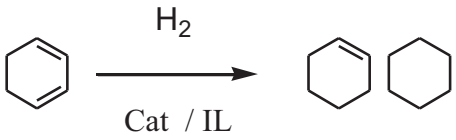

Scheme 4. Catalytic hydrogenation of CYD

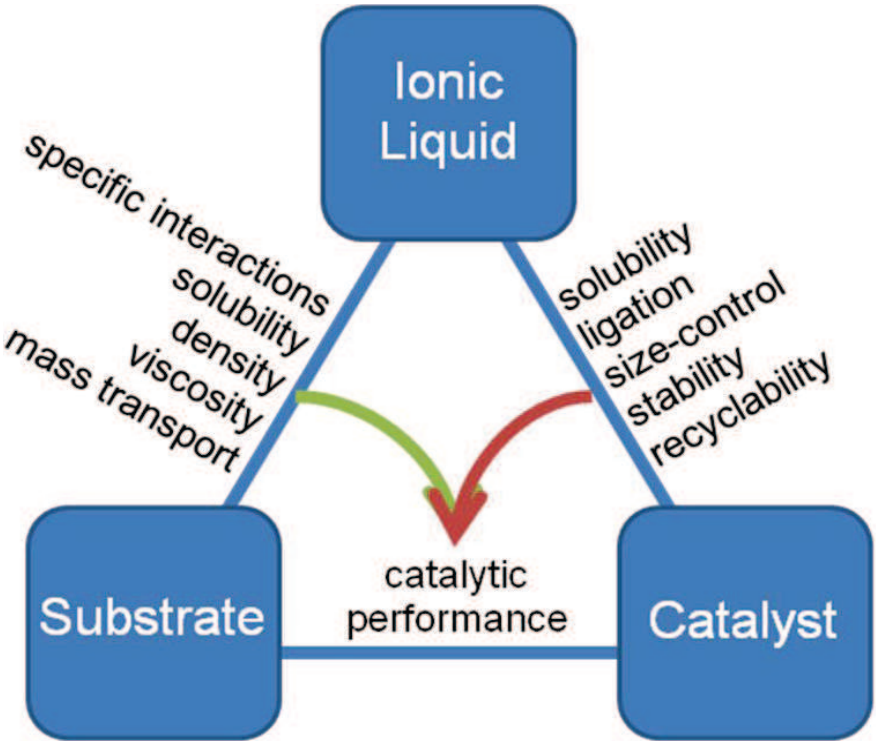

3.2 The influence of the ionic liquid medium on the catalytic hydrogenation of 1,3-cyclohexadiene by an Osborn-type catalyst

Selective hydrogenation of 1,3-cyclohexadiene (CYD) into cyclohexene (CYE) can be carried out, with good conversion rates, using Osborn's complex $[Rh(NBD)(PPh_3)_2]PF_6$ (NBD = norbornadiene) in IL media such as $[C_1C_4Im][SbF_6]$ or $[C_1C_4Im][PF_6]$.[14] The aim of this chapter is to study the influence of the nature of the ionic liquid on this catalytic hydrogenation.

As previously mentioned, work carried out in our laboratory has already described the difference in intermolecular interactions existing in mixtures of toluene in the ILs 1-butyl-3-methylimidazolium bis(trifluoromethylsulfonyl)imide, $[C_1C_4Im][NTf_2]$, and 1-butyl-2,3-dimethylimidazolium bis(trifluoromethylsulfonyl)imide, $[C_1C_1C_4Im][NTf_2]$, stronger π-cation stacking existing for the latter due to disruption of the anion-cation H-bonding caused by the methyl group. For a non-aromatic π-system, such as 1,3-cyclohexadiene, solvation is probably a combination of more subtle interactions with the ionic liquid.

The ILs $[C_1C_4Im][NTf_2]$ and $[C_1C_1C_4Im][NTf_2]$ are chosen in order to avoid impurities such as chloride and water, since they are hydrophobic, liquid at room temperature, and their purification is well controlled.[26] Firstly, the molecular interactions between the ILs and CYD must be assessed through:

- NMR characterisation
- study of the microscopic structure of the IL-substrate mixtures
- measurement of the thermodynamic properties of mixing (such as the solubility and the heat of mixing)
- determination of the viscosity of the reaction media
- measurement of diffusivity of CYD in ILs

Following this, the difference in catalytic performance in the two different media must be quantified, and explained using the findings from the previously conducted analyses. (Anion exchange between the IL and the catalyst can be circumvented by replacing Osborn's complex with $[Rh(COD)(PPh_3)_2]NTf_2$, COD = 1,5-cyclooctadiene).

3.2.1 Solvation of 1,3-cyclohexadiene and molecular structure of the mixtures

3.2.1.1 Solubility

Figure 6 shows cloud-point temperatures as a function of composition for CYD-[C_1C_4Im][NTf_2] and CYD-[$C_1C_1C_4Im$][NTf_2].[49,50] The observation of the cloud point with decreasing the temperature was difficult, especially for the CYD-[C1C1C4Im][NTf2] system, because in this case the mixtures often remained in a metastable state and cloudiness persisted despite overheating. Observation of the cloud point with decreasing temperature was not reproducible during this experiment. Such difficulty with ionic liquid systems has already been discussed and may be mainly due to the effect of pre-cooling and slow kinetics of demixing. Consequently, the solubility was determined at only two temperatures.

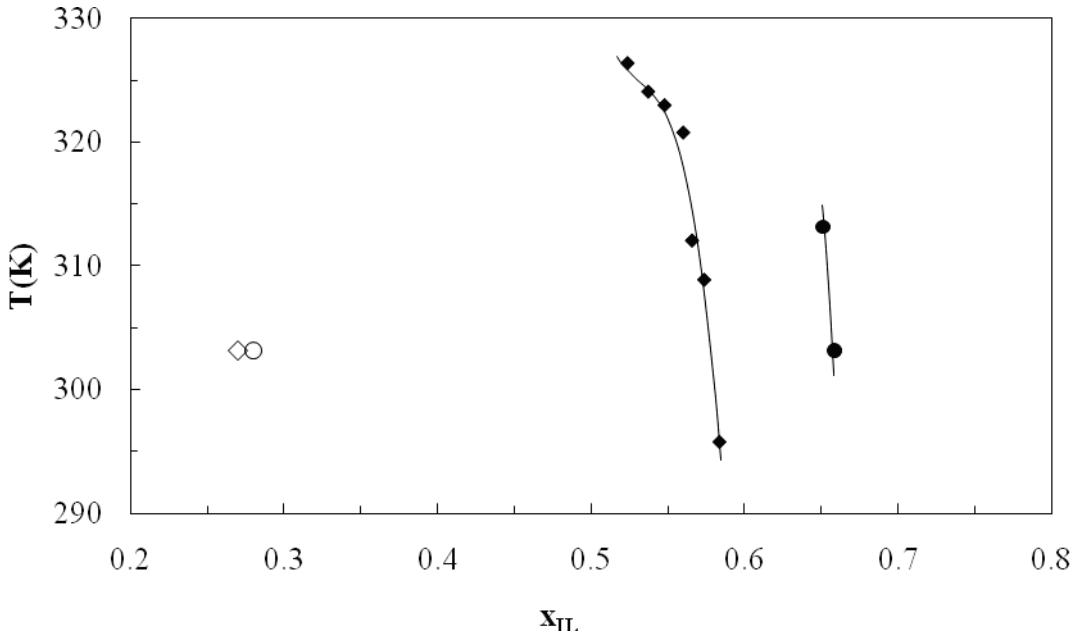

Figure 6. Liquid-liquid equilibrium diagrams for the mixture of toluene and [C_1C_4Im][NTf_2] (o) or [$C_1C_1C_4Im$][NTf_2] (□) and solubility of CYD in [C_1C_4Im][NTf_2] (♦) or [$C_1C_1C_4Im$][NTf_2] (●) x_{IL} = IL molar fraction: [IL]/([IL]+{CYD]).

The solubility of CYD at 303.15 K, expressed in mole fraction is 0.42 in [C_1C_4Im][NTf_2] and 0.34 in [$C_1C_1C_4Im$][NTf_2] (see Figure 6) which could indicate less favourable interactions between CYD and the [$C_1C_1C_4Im$] ion in comparison with the [C_1C_4Im] ion. In the temperature range studied, both systems CYD-[C_1C_4Im][NTf_2] and CYD-[$C_1C_1C_4Im$][NTf_2] show behaviour compatible with the existence of upper critical solution temperatures and very steep liquid-liquid

equilibrium lines. In comparison with aromatic molecules in these ILs, CYD is much less soluble. For instance, the solubility of toluene at 303.15 K expressed in mole fraction is 0.73 in $[C_1C_4Im][NTf_2]$ and 0.72 in $[C_1C_1C_4Im][NTf_2]$,[41] the solubility of benzene in $[C_1C_4Im][NTf_2]$ being even higher (mole fraction of 0.78 at 303.15 K). [40] The small difference in solubility of toluene with respect to benzene can be attributed to the presence of an additional methyl group, whereas the much lower solubility of CYD is explained by less favourable interactions between the solute and the ILs. Disruption of the aromatic system changes the interactions between solute and ionic liquid and thus decreases the solubility.

3.2.1.2 Enthalpy of mixing

The energy involved in the interactions of different solutes dissolved in ILs can be assessed by measuring the excess molar enthalpy. This was carried out for both systems; CYD-$[C_1C_4Im][NTf_2]$ and CYD-$[C_1C_1C_4Im][NTf_2]$. The excess molar enthalpy of mixing ΔH_{mix}^{E} was determined by isothermal titration calorimetry, from the heat effect involved in injections of small quantities of CYD into the ionic liquid, Q_{CYD}. The partial molar excess enthalpy of solute, H_{CYD}^{E}, was calculated according to equation (1).

$$H_{CYD}^{E} = \left(\frac{\partial \Delta H_{mix}^{E}}{\partial n_{CYD}} \right)_{nIL,\, p,T} \approx \frac{Q_{CYD}}{\Delta n_{CYD}} \qquad (1)$$

where n_{CYD} and n_{IL} denote the quantity of CYD and IL, respectively, ΔH_{mix}^{E} is the excess molar enthalpy of the entire system (enthalpy of mixing) and Δn_{CYD} is the quantity of solute *per* injection. Δn_{CYD} was calculated from the injected volumes and the density of CYD was obtained from the literature. In these calculations, heat due to evaporation of the solute from IL solution is assumed to be negligible. Hence, no correction for the vapour pressure of the solute was made.

Figure 7 represents partial molar excess enthalpies of CYD in both ILs at 303.15 K as a function of composition. A larger dispersion of the values (up to 3%), especially at higher concentration, was observed. At times, before each injection of CYD into the IL, an exothermic effect was detected, mainly originating from insufficient mixing of both components at the beginning of the injection period. As already observed in the case of aromatic hydrocarbons, [51] the rate of dissolution of non-polar, low density and low viscosity CYD in the IL is slow and sometimes leads to formation of a solute-rich layer on the surface of the solution. This is often

accompanied by partial evaporation or even polymerisation[#] of CYD before the mixing process is complete, hence disturbing the measurements. A large number of injections were made to ensure reliability.

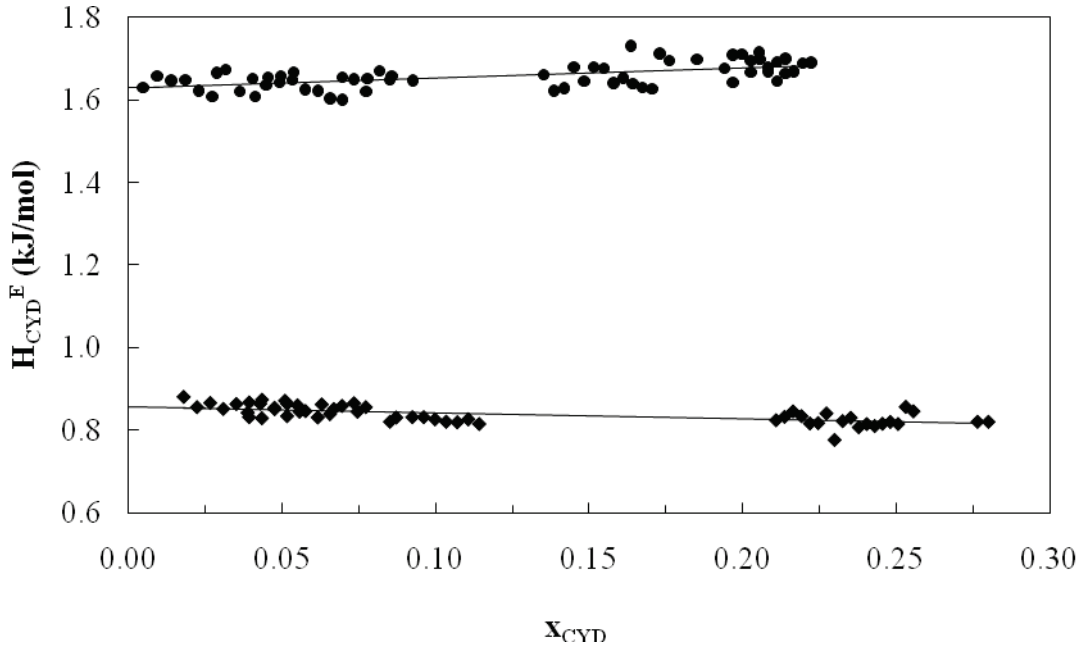

Figure 7. Partial molar excess enthalpies vs. mole fraction of CYD in the binary mixture with $[C_1C_4Im][NTf_2]$(●) or $[C_1C_1C_4Im][NTf_2]$(♦) at 303.15 K. The lines represent functions: $H_{CYD}^{E}=1.6285+0.2481x_{CYD}$ (●) and $H_{CYD}^{E}=0.8574-0.1518x_{CYD}$ (♦).x_{CYD} = CYD molar fraction: [CYD]/([IL]+{CYD])

Comparison of $[C_1C_4Im][NTf_2]$ and $[C_1C_1C_4Im][NTf_2]$ shows that introduction of an additional methyl group on C_2 carbon of the imidazolium ring strongly affects the interaction with molecules of CYD, which becomes less favourable. In order to rationalise the differences in the solvation of CYD in both ILs, and to complement the enthalpic data with structural information, the microscopic structure of the mixtures was investigated using NMR experiments and molecular simulation.

[#] The formation of a polymer was observed and confirmed by NMR analysis.[52] This side-reaction is attributed to the fact that CYD has been distilled to eliminate the stabiliser BHT before the physical chemical measurements.

1-butyl-3-methylimidazolium cation [C_4C_1Im] 1-butyl-2,3-dimethylimidazolium cation [$C_4C_1C_1Im$]

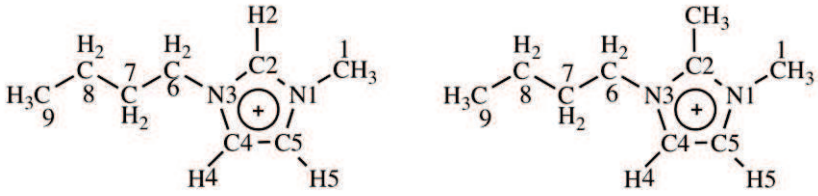

1,3-cyclohexadiene (CYD)

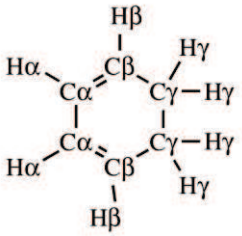

Scheme 5. Atom labelling of CYD, 1-butyl-3-methylimidazolium and 1-butyl-2,3-dimethylimidazolium cations.

3.2.1.3 ROESY NMR spectroscopy

NOESY (nuclear Overhauser effect spectroscopy) experiments exhibited very weak or null cross peak intensities. Rotating frame NOE experiments (ROESY) allowed us to obtain positive NOEs irrespective of the long rotational correlation time due to the high viscosity of the system. In ^{1}H-^{1}H ROESY techniques based on cross-space relaxations, the selective irradiation of a proton group affects the signal intensities of all proton groups which are spatially close but not necessarily connected by chemical bonds. The method is based on the assumption of short-range intermolecular distances (4 – 5 Å).{Frezzato, 2006 #2063} The strength of the ROE signal is proportional to the inverse sixth power of the distance between the atoms, $I \propto 1/r^6$. In the liquid state, this relationship is possible if the intermolecular association is tight enough to turn the intermolecular relaxation into "intramolecular" within the ion pair or ion-molecule association.[53] Highly structured, bulk ionic liquids seem to fulfill these requirements, thus allowing the use of the intermolecular ROESY to derive lower limits for interionic distances. Consequently, the intensity of the integrals ($I_{CYD\text{-}IL}$) could be considered as roughly inversely proportional to the intermolecular distances. The resultant ROESY correlation spectra for CYD-[C_1C_4Im][NTf_2] and CYD-[$C_1C_1C_4Im$][NTf_2], R = 0.5, (R = CYD/IL) are depicted in Figures 8 and 9, respectively.

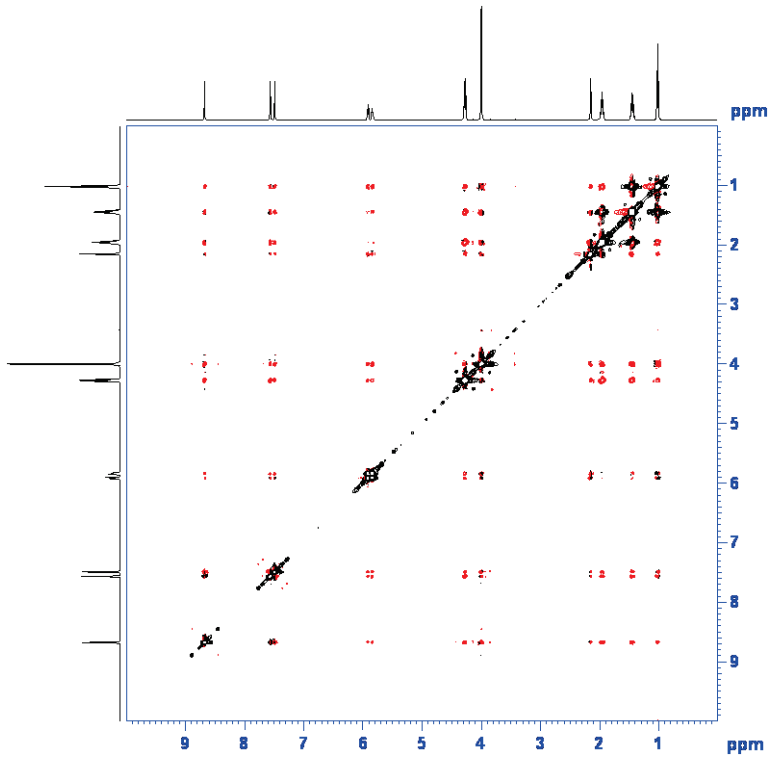

Figure 8. ROESY NMR spectrum for the mixture of 1,3-cyclohexadiene and $[C_1C_4Im][NTf_2]$ at R = 0.5.

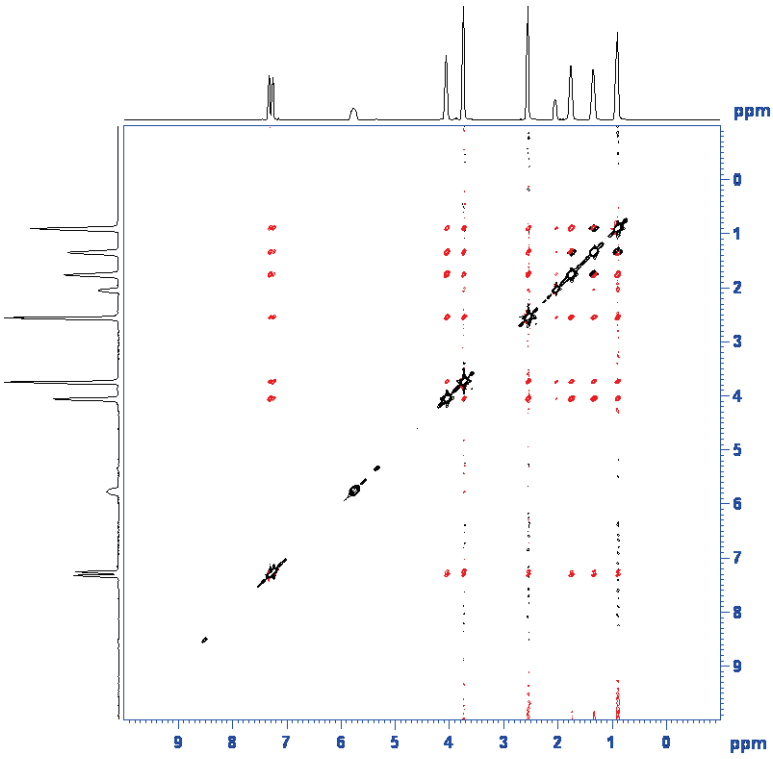

Figure 9. ROESY NMR spectrum for the mixture of 1,3-cyclohexadiene and $[C_1C_1C_4Im][NTf_2]$ at R = 0.5.

Molecular mechanics calculations have been performed, using the SYBYL software with the TRIPOS force field,[54] on isolated pairs of CYD and imidazolium cations. Intermolecular distances were fixed using results from NMR ROESY experiments and the energy of both systems, CYD-[C_1C_4Im] and CYD-[$C_1C_1C_4Im$], were minimised. The average distances between molecules of CYD and the imidazolium cations were determined from their geometry and orientation at the potential energy minimum. This model, pictured in Figure 10, suggests that CYD is probably located nearer to the butyl chain of [C_1C_4Im][NTf_2], the π-bonds being oriented towards the imidazolium cation, a configuration similar to that previously observed for toluene.[41]

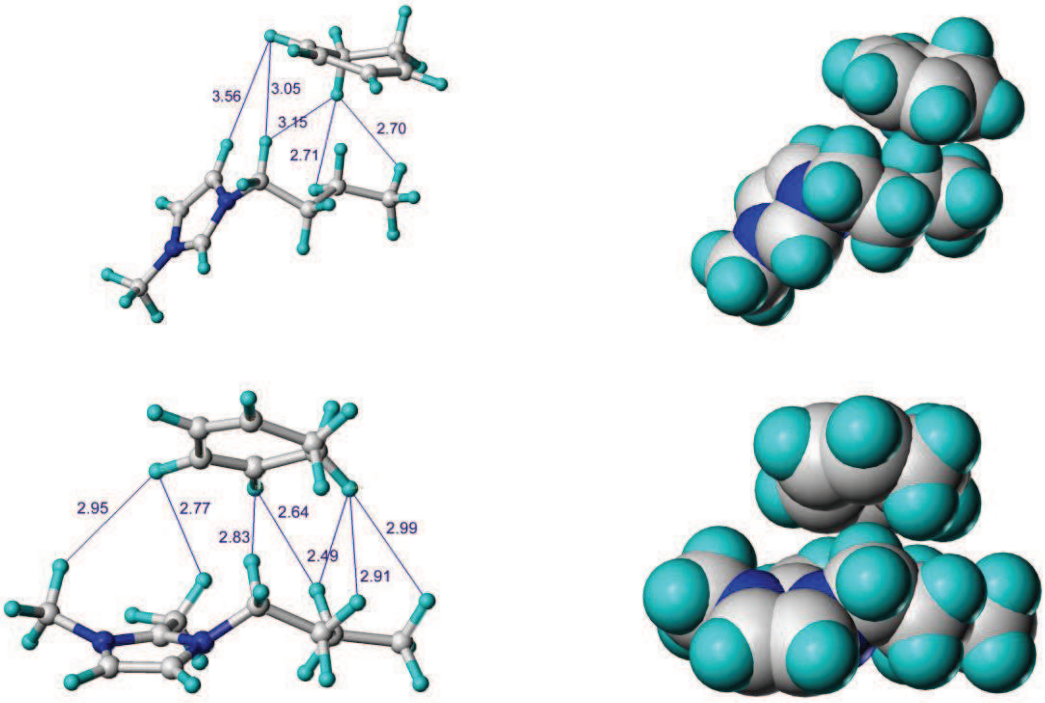

Figure 10. Representation of molecular positions in saturated solutions of CYD-[C_1C_4Im][NTf_2] (upper) and CYD-[$C_1C_1C_4Im$][NTf_2] (lower) from ROESY NMR extrapolation.

3.2.1.4 Molecular dynamics simulations

Access to the microscopic structure of the mixtures in the condensed liquid phase is possible using molecular dynamics simulation with all atoms explicitly present and periodic boundary conditions employed to represent a virtually infinite system. Condensed-phase simulations take into account all the two-body interactions from the environment of each

molecule or ion. The molecular simulation details are given in the experimental section 3.5.10. In Figure 11 are plotted the site-site radial distribution functions — the probability of finding pairs of atoms at a given distance, compared to the average — between the hydrogens on Cβ of CYD, Hβ, and selected atoms of the [C_1C_4Im] and [$C_1C_1C_4Im$] cations at R = 0.5 (atoms are labelled as indicated in Scheme 5). In both cases, there is a higher probability (a stronger association) of finding all hydrogen atoms of CYD near the side chain than in the vicinity of the aromatic nucleus region of imidazolium cation. This means that CYD is preferentially solvated in the non-polar domain of the ILs, as already observed for saturated hydrocarbons and for the methyl group of toluene. This orientation effect relative to the cation is less distinct for CYD than for toluene,[41] as expected given the weaker π-cation interactions.

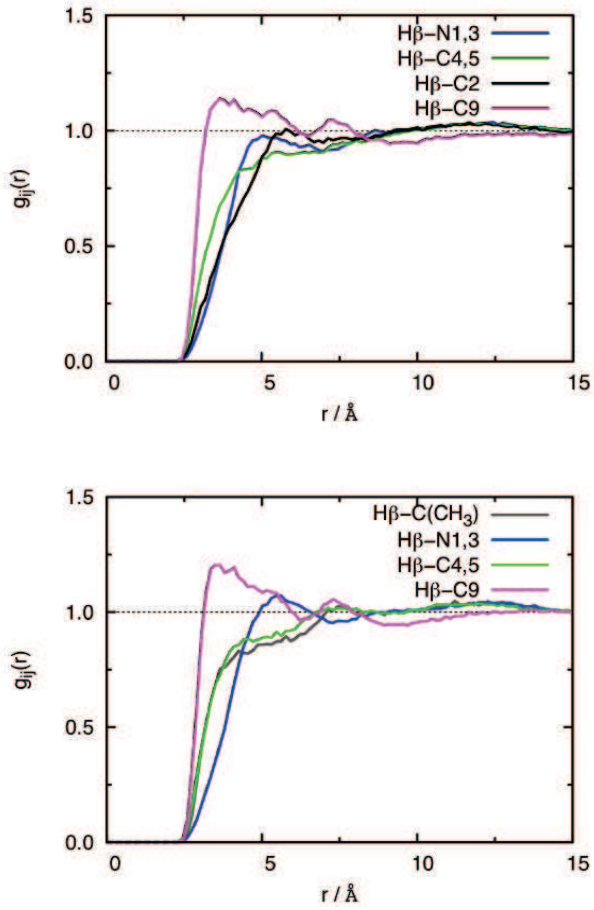

Figure 11. Radial distribution functions between hydrogen on Cβ of CYD, Hβ, and selected sites in the [C_1C_4Im] cation (top) and [$C_1C_1C_4Im$] cation (bottom), for R = 0.5. Atoms are labeled as indicated in Scheme 5.

Figure 12 represents the comparison of the radial distribution functions of the mixtures CYD-[C_1C_4Im][NTf_2] and CYD-[$C_1C_1C_4Im$][NTf_2], again at R = 0.5, between hydrogen on Cβ

and Cα of CYD and C_2 of the imidazolium rings. It can be seen that both these hydrogen atoms are found with a higher probability closer to C_2 in $[C_1C_1C_4Im][NTf_2]$ than in $[C_1C_4Im][NTf_2]$. The strong hydrogen bond between C_2-H and the anion in $[C_1C_4Im][NTf_2]$ prevents such an interaction with CYD. This observation is consistent with the distances between the IL cations and CYD obtained from ROESY experiments and molecular mechanics calculations on isolated pairs, as seen in Figure 10.

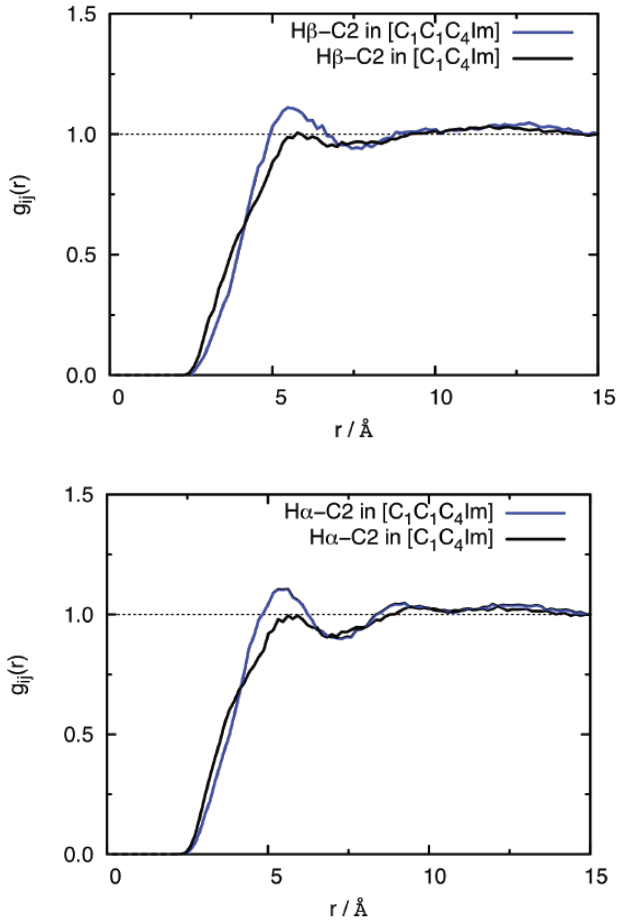

Figure 12. Comparison of site-site radial distribution functions between chosen atoms in CYD and the cations, in CYD-$[C_1C_4Im][NTf_2]$ (top) and CYD-$[C_1C_1C_4Im][NTf_2]$ (bottom) for R = 0.5. Atoms are labeled as indicated in Scheme 5.

Detailed structural features are much better perceived in 3-dimensional spatial distribution functions. In Figure 13 is represented the distribution of ions around a CYD molecule. In blue is plotted the iso-surface corresponding to a local density of twice the average density of C_2 carbon atoms of the imidazolium cations. Cation headgroups (the blue regions) are located above and below the CYD ring, interacting preferentially with the π-system of CYD. It can be seen that the terminal carbons of the alkyl side chain, C_9, (the grey regions) surround

CYD molecule. Oxygen atoms of the NTf_2^- anion (plotted in red) are found in the plane of CYD interacting with the hydrogen atoms of the double bonds. Similar results have been previously obtained for toluene in the same ILs. [41] This shows that although in CYD the π-system is smaller than that of a fully aromatic system, it still determines the structure of the solvation shell in ILs with cations positioned above and below the plane of CYD and anion in the plane.

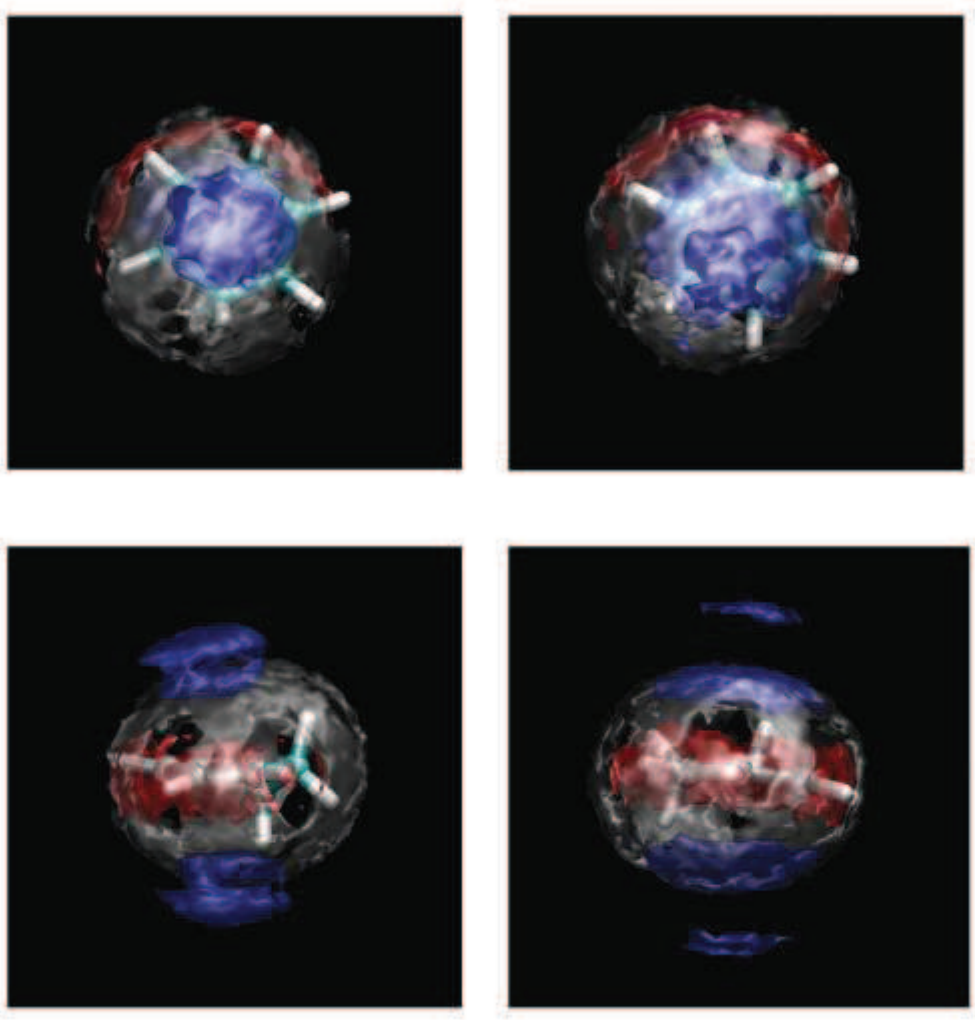

Figure 13. Spatial distribution functions around the C2 carbon of CYD in CYD-[C_1C_4Im][NTf_2] (left) and CYD-[$C_1C_1C_4Im$][NTf_2] (right) at R = 0.5. In blue is plotted the iso-surface corresponding to a local density of twice the average density of C_2 carbon of the imidazolium cations. In grey is plotted the iso-surface corresponding to a local density of twice the average density of terminal methyl carbons from the butyl side chain, C_9. In red is plotted the iso-surface corresponding to a local density of twice the average density of oxygen atoms from the NTf_2^- anion. Oxygen atoms are located in the CYD plane interacting with hydrogen atoms of double bonds, Hα and Hβ.

Figure 14 shows spatial distribution functions around the [C_1C_4Im] and the [$C_1C_1C_4Im$] cations. With both cations, CYD (the white regions) is preferentially located above and below the plane of the imidazolium ring at distances greater than those of the closest cation-anion pairs.

In red is plotted the iso-surface corresponding to a local density of 4 times the average density of the oxygen atoms from [NTf_2] anions. As can be seen, for [C_1C_4Im][NTf_2] the probability of finding the oxygen of [NTf_2] near the C_2-H of the imidazolium cation is higher than the carbon of CYD, indicating a strong H-bond. The situation is completely different for [$C_1C_1C_4Im$][NTf_2], where the probability of finding the carbon of CYD near the C_2 of the cation is higher than that of the oxygen atoms of [NTf_2]. As already found in case of solvation of toluene,[41] interactions of the [$C_1C_1C_4Im$] cation with the anion are mainly through H_4, H_5 and also through the nitrogen atoms, N_1 and N_3, whereas in [C_1C_4Im] cation-anion interactions are mainly through C_2-H bonds.

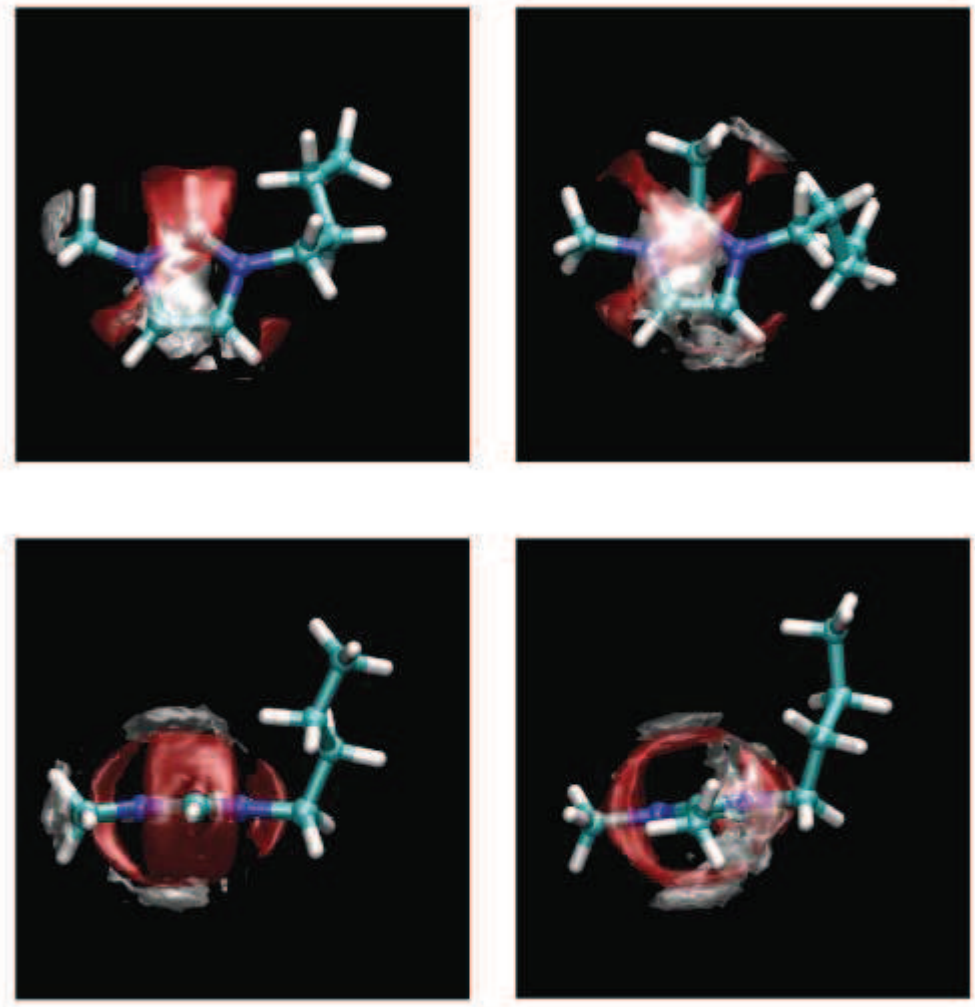

Figure 14. Spatial distribution functions around the C_2 carbon of the cations in CYD-[C_1C_4Im][NTf_2] (left) and CYD-[$C_1C_1C_4Im$][NTf_2] (right) at $R = 0.5$. Above and below are different views of the same iso-surfaces. In white is plotted the iso-surface corresponding to a local density of twice the average density of Cα of CYD. In red is plotted the iso-surface corresponding to a local density of 4 times the average density of oxygen atoms from the NTf_2^- anion.

3.2.1.5 ^{1}H NMR shift variation with R

We have also examined the effect of introducing CYD into each IL on the chemical shifts of all hydrogen atoms of the IL, Tables 1 and 2. Curves of mean chemical shift change, Δδ, are plotted with respect to *R* in Figure 15. Atom labelling is depicted in Scheme 5.

Table 1. The ^{1}H NMR chemical shifts of neat $[C_1C_4Im][NTf_2]$, and those of the IL, in the presence of CYD. *R* = [CYD]/[IL]. Protons numbered as indicated in Scheme 5.

Proton.	R_0=0	R_1=0.11	Δ(R_1- R_0)	R_2=0.21	Δ(R_2- R_0)	R_3=0.34	Δ(R_3- R_0)	R_4=0.54	Δ(R_4- R_0)	R_5=0.81	Δ(R_5- R_0)
2	8.60	8.62	0.02	8.64	0.04	8.67	0.07	8.71	0.11	8.76	0.16
4	7.45	7.52	0.07	7.54	0.09	7.56	0.11	7.59	0.14	7.63	0.18
5	7.38	7.44	0.06	7.46	0.08	7.49	0.11	7.52	0.14	7.55	0.17
6	4.14	4.22	0.08	4.24	0.10	4.27	0.13	4.30	0.16	4.34	0.20
1	3.91	3.95	0.04	3.97	0.06	3.99	0.08	4.02	0.11	4.07	0.16
7	1.86	1.91	0.05	1.93	0.07	1.95	0.09	1.98	0.12	2.03	0.17
8	1.36	1.39	0.03	1.42	0.06	1.44	0.08	1.48	0.12	1.53	0.17
9	0.95	0.95	0.00	0.98	0.03	1.01	0.06	1.05	0.10	1.10	0.15
mean Δ			0.04		0.07		0.09		0.13		0.17

Table 2. The ^{1}H NMR chemical shifts of neat $[C_1C_1C_4Im][NTf_2]$, and those of the IL, in the presence of CYD. *R* = [CYD]/[IL]. Protons numbered as indicated in Scheme 5.

Proton.	R_0=0	R_1=0.08	Δ(R_1- R_0)	R_2=0.18	Δ(R_2- R_0)	R_3=0.30	Δ(R_3- R_0)	R_4=0.40	Δ(R_4- R_0)	R_5=0.69	Δ(R_5- R_0)
4	7.35	7.36	0.01	7.39	0.04	7.41	0.06	7.42	0.07	7.46	0.11
5	7.28	7.29	0.01	7.32	0.04	7.34	0.06	7.36	0.08	7.40	0.12
6	4.08	4.09	0.01	4.12	0.04	4.14	0.06	4.16	0.08	4.20	0.12
1	3.76	3.78	0.02	3.81	0.05	3.83	0.07	3.85	0.09	3.89	0.13
2	2.57	2.59	0.02	2.62	0.05	2.64	0.07	2.66	0.09	2.71	0.14
7	1.77	1.79	0.02	1.82	0.05	1.85	0.08	1.87	0.10	1.91	0.14
8	1.36	1.37	0.01	1.41	0.05	1.44	0.08	1.46	0.10	1.51	0.15
9	0.91	0.93	0.02	0.97	0.06	1.00	0.09	1.02	0.11	1.08	0.17
mean Δ			0.02		0.05		0.07		0.09		0.14

Unlike in the case of toluene-IL mixtures,[41] it is found that all peaks are generally shifted downfield with increasing molar ratio of CYD, *R = [CYD]/[IL]*, demonstrating the deshielding effect CYD has on all hydrogen nuclei. The upfield shift of IL proton NMR shifts in toluene-IL mixtures was attributed to π-cation interactions, which according to our molecular models do not exist in the case of CYD.

Excluding the first point of each series, Δδ versus *R* follows a straight line, Figure 15. The slopes (0.17 ppm for $[C_1C_4Im][NTf_2]$; 0.18 ppm for $[C_1C_1C_4Im][NTf_2]$) are almost identical for both ILs. The similar linear variation of the deshielding effect for both ILs shows that no

structural reorganisation occurs with increasing CYD concentration. Indeed, a lipophilic substrate that displays little specific interactions with the IL moieties, such as CYD, will be mostly solvated in the non-polar pockets, causing them to swell. When these pockets become saturated, demixing will occur. Furthermore, the absolute mean chemical shift change, $|\Delta\delta|$, is greater in the IL $[C_1C_4Im][NTf_2]$ i.e. CYD has a stronger impact on the electronic structure of this IL.

The first point of each series lies beneath the linear regression. This signifies that with the incorporation of very small quantities of CYD, i.e. $R < 0.2$, a reorganisation of the medium with respect to the pure IL occurs. This is more significant in the case of $[C_1C_4Im][NTf_2]$, yet again suggesting stronger specific interactions in this case.

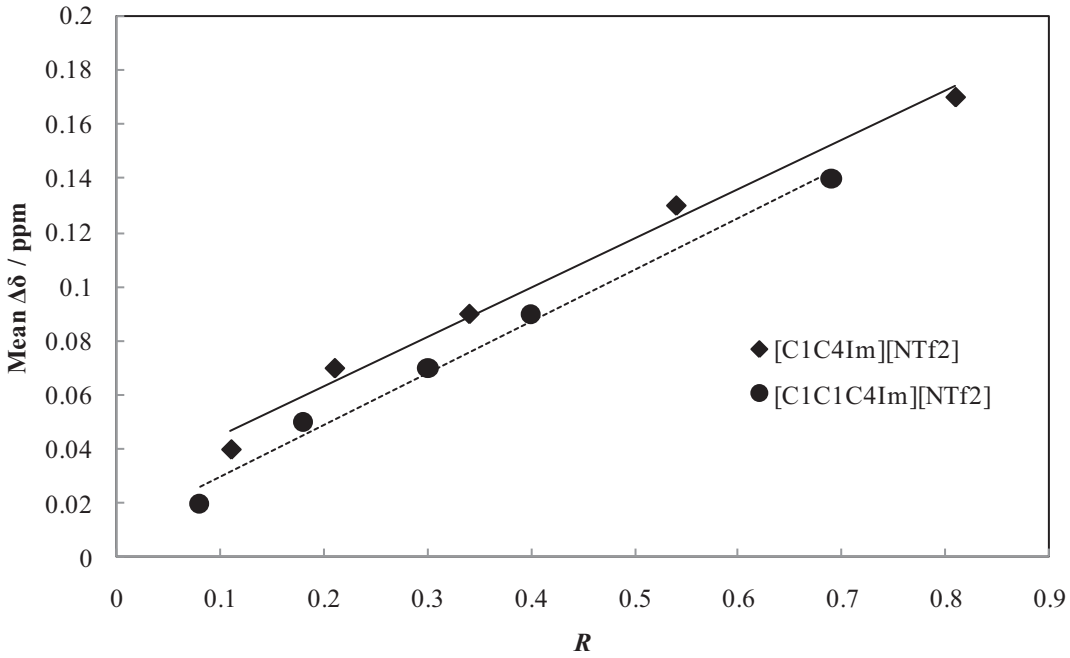

Figure 15. Mean deviation of proton chemical shifts in IL-CYD mixtures with respect to *R*

The variation of the CYD chemical shifts when changing *R* were also studied and are tabulated in Table 3. As for the shifts of the IL moieties, CYD shifts are shifted downfield demonstrating once again the deshielding effect of CYD, even on itself. At low concentration the CYD molecules interact mostly with the alkyl chains of the ILs, but as the concentration increases, CYD molecules will also interact with one another.

Table 3. ^{1}H NMR chemical shifts of CYD in the ILs. *R* = [CYD]/[IL]. Protons labelled as indicated in Scheme 5.

R	[C_1C_4Im][NTf_2]/CYD			*R*	[$C_1C_1C_4$Im][NTf_2]/CYD		
	α	β	γ		α	β	γ
0.11	5.84	5.79	2.08	**0.08**	5.81	5.75	2.06
0.21	5.88	5.81	2.11	**0.18**	5.85	5.78	2.10
0.34	5.92	5.85	2.15	**0.30**	5.87	5.82	2.13
0.54	5.94	5.88	2.19	**0.40**	5.91	5.83	2.16
0.81	6.00	5.93	2.41	**0.69**	5.97	5.90	2.22

3.2.2 Mass transport in the reaction media

Differences in the rate of catalytic hydrogenation of CYD could also be related to differences in thermophysical properties of the reaction media, which affect the mobility of molecules.

Density and Viscosity

The density and viscosity of the mixtures of CYD-[C_1C_4Im][NTf_2] and CYD-[$C_1C_1C_4$Im][NTf_2] were measured at 298.15 K and atmospheric pressure, at various molar ratios *R* (Table 4). The additional methyl group on the imidazolium carbon C_2 in [$C_1C_1C_4$Im][NTf_2] naturally lowers both the mass and molar density of the liquid in comparison with [C_1C_4Im][NTf_2]. Furthermore, the viscosity of pure [$C_1C_1C_4$Im][NTf_2] and also of its mixture with CYD is roughly twice that of [C_1C_4Im][NTf_2], as reported in Table 4. For both ionic liquids the viscosity of the mixtures is seen to drop sharply with increasing CYD concentration.

Table 4. Density and viscosity, at 298.15 K and atmospheric pressure, of mixtures of CYD-[C_1C_4Im][NTf_2] and CYD-[$C_1C_1C_4$Im][NTf_2] at *R* = CYD/IL.

R	x_{CYD}	ρ (g/mL)	*η* (mPas)	*R*	x_{CYD}	ρ (g/mL)	*η* (mPas)
[C_1C_4Im][NTf_2]				*[$C_1C_1C_4$Im][NTf_2]*			
0.000	0.000	1.4376	48.5	0.000	0.000	1.4177	105
0.100	0.091	1.4202	44.0	0.101	0.091	1.4013	83.0
0.156	0.135	1.4081	40.0	0.201	0.167	1.3858	67.2
0.200	0.167	1.3999	37.0	0.250	0.200	1.3784	60.9
0.248	0.199	1.3937	35.4	0.304	0.233	1.3705	54.5
0.300	0.231	1.3874	33.3	0.407	0.289	1.3538	49.8
0.397	0.284	1.3718	31.0	0.510	0.338	1.3442	47.1
0.498	0.333	1.3597	24.8				

Diffusivity

Another possible way to obtain information on how the media influences the mobility of molecules is to determine their diffusion coefficients, *D*, by NMR spectroscopy. Diffusion Order SpectroscopY, DOSY*, is an NMR diffusion experiment, which provides a way to separate the different compounds in a mixture, based on the differing translational diffusion coefficients (and therefore differences in the size and shape of the molecule, as well as physical properties of the surrounding environment such as viscosity, temperature, etc.) of each chemical species in solution.

Generally, according to the Stokes-Einstein equation (2), the diffusion coefficient is inversely proportional to the viscosity of the medium.

$$D = \frac{k_B T}{6\pi\eta r_H} \qquad (2)$$

k_B = *Boltzman constant,* r_H = *hydrodynamic radius*

For instance, when *R* is around 0.5, the diffusion coefficients found for CYD are 187.5 $\mu m^2/s$ in $[C_1C_4Im][NTf_2]$ against 97 $\mu m^2/s$ in $[C_1C_1C_4Im][NTf_2]$, i.e. diffusion of CYD in $[C_1C_4Im][NTf_2]$ is 1.9 times faster than in $[C_1C_1C_4Im][NTf_2]$ in agreement with their viscosity ratio.

The diffusion coefficients (*D*) of CYD in both ILs while increasing *R* were thus determined from extrapolation of DOSY NMR data, and are plotted in Figure 16. The diffusion coefficients were found to increase with *R* in both ILs.

* see experimental section 3.5.9 for further details

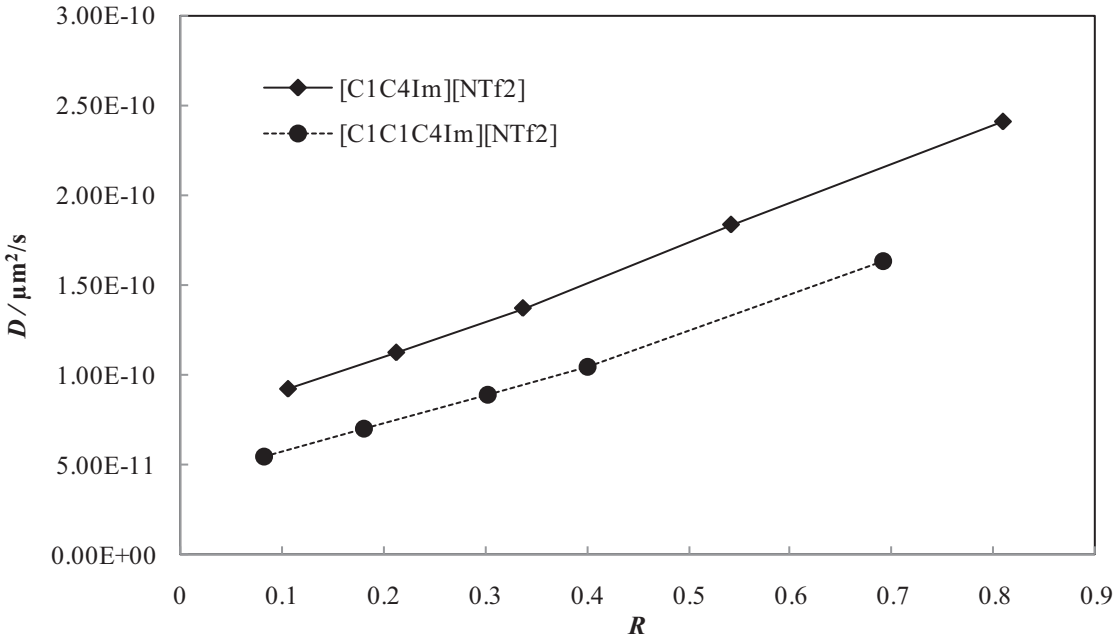

Figure 16. *D* for CYD in CYD-IL mixtures plotted as a function of R

When η^{-1} is plotted as a function of *D* an interesting phenomenon is observed as seen in Figure 17. Here, the relationship is not perfectly linear as predicted by the Stokes-Einstein equation (2), yet seems to incorporate two components with different gradients.

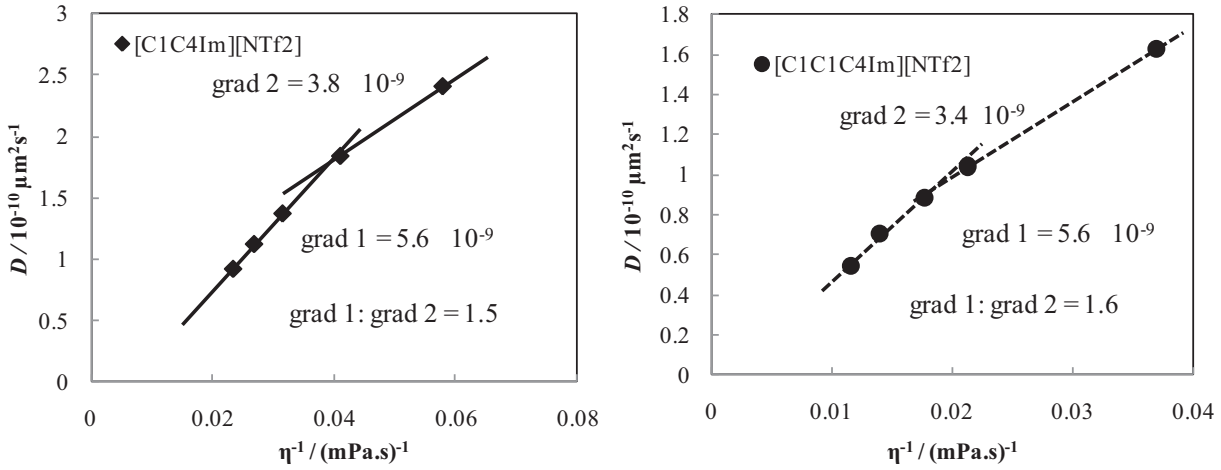

Figure 17. Calculated inverse viscosity η^{-1} plotted as a function of *D* for CYD in CYD-IL mixtures.

This may indicate different mobility mechanism for low and high concentration mixtures i.e. for different viscosity. Indeed, in certain cases the Stokes-Einstein model may not be

applicable. The predecessor of the Stokes-Einstein equation, described by Sutherland,[55] takes into account a sliding friction coefficient of molecules, β (3), based on the intermolecular interactions. For the perfectly "sticking surface" (strong intermolecular interactions), $\beta \rightarrow \infty$, and the Sutherland coefficient, θ, tends to 6, i.e. equation (3) is reduced to the Stokes-Einstein equation (2). On the other hand, for a perfectly "sliding surface", i.e. one that exhibits no interactions with the surrounding medium, $\beta \rightarrow 0$, therefore $\theta \rightarrow 4$, as in equation (4).

$$D = \frac{k_B T}{\theta \pi \eta r_H} \qquad \theta = 6\left(\frac{1 + 2\eta / \beta r_H}{1 + 3\eta / \beta r_H}\right) \tag{3}$$

$$D = \frac{k_B T}{4\pi \eta r_H} \tag{4}$$

Indeed, a recent study of the diffusion of ferrocene in imidazolium ionic liquids found that due to the lack of specific interactions between ferrocene and the surrounding medium, the Sutherland coefficient of 4 was more applicable.[46] We have already demonstrated in section 3.2.1 that CYD does not display strong specific interactions with the IL. This brings into question the suitability of the Stokes-Einstein equation in the case under study.

When we calculate the ratio of the gradients of the curves of η^{-1} plotted as a function of *D,* Figure 17, at low vs. high concentration of CYD, we find a ratio of 1.5 for $[C_1C_4Im][NTf_2]$ and 1.6 for $[C_1C_1C_4Im][NTf_2]$. This could be explained by Stokes-Einstein behaviour at high concentration (i.e. low viscosity) θ = 6, and "sliding surface" behaviour at low concentration, θ = 4. This corroborates the lack of intermolecular interactions found between the CYD and the ILs. More measurements are underway to confirm this.

Nevertheless, it is clear that the viscosity is a complex issue that must be taken into account when ILs are used as media for catalysis.

3.2.3 Hydrogenation of 1,3-cyclohexadiene

In organic solvents, during the hydrogenation of 1,3-cyclohexadiene, the catalyst first undergoes a ligand exchange yielding $[Rh(CYD)(PPh_3)_2]^+$. This occurs more rapidly than the rate at which it then reacts with H_2.[56, 57] The two reaction steps, depicted in Scheme 6, were investigated in both ILs.

3.2.3.1 Monitoring by UV-vis spectroscopy in both ILs

Firstly, $[Rh(CYD)(PPh_3)_2]NTf_2$ was synthesised from $[Rh(COD)(PPh_3)_2]NTf_2$ and fully characterised. As $[Rh(COD)(PPh_3)_2]NTf_2$ is yellow (λ_{max} = 450 nm) and $[Rh(CYD)(PPh_3)_2]NTf_2$

is red (λ_{max} = 500 nm), the ligand exchange COD-CYD could be monitored by UV-Vis spectroscopy (λ = 500 nm) in both ILs, as shown in Figure 18. This reaction is much slower in $[C_1C_1C_4Im][NTf_2]$ than in $[C_1C_4Im][NTf_2]$.

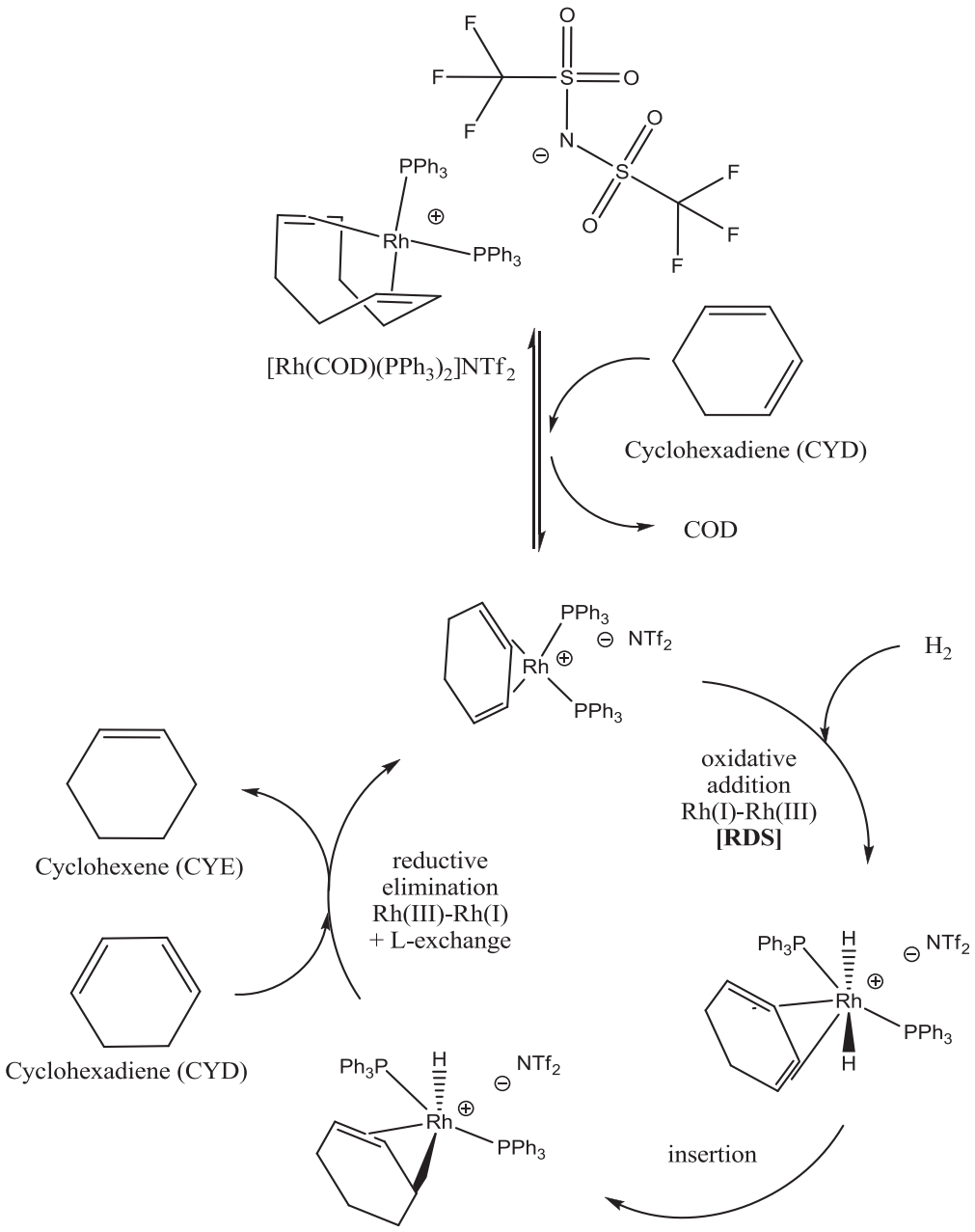

Scheme 6. Ligand exchange and catalytic cycle for the hydrogenation of CYD using an Osborn-type catalyst in ILs

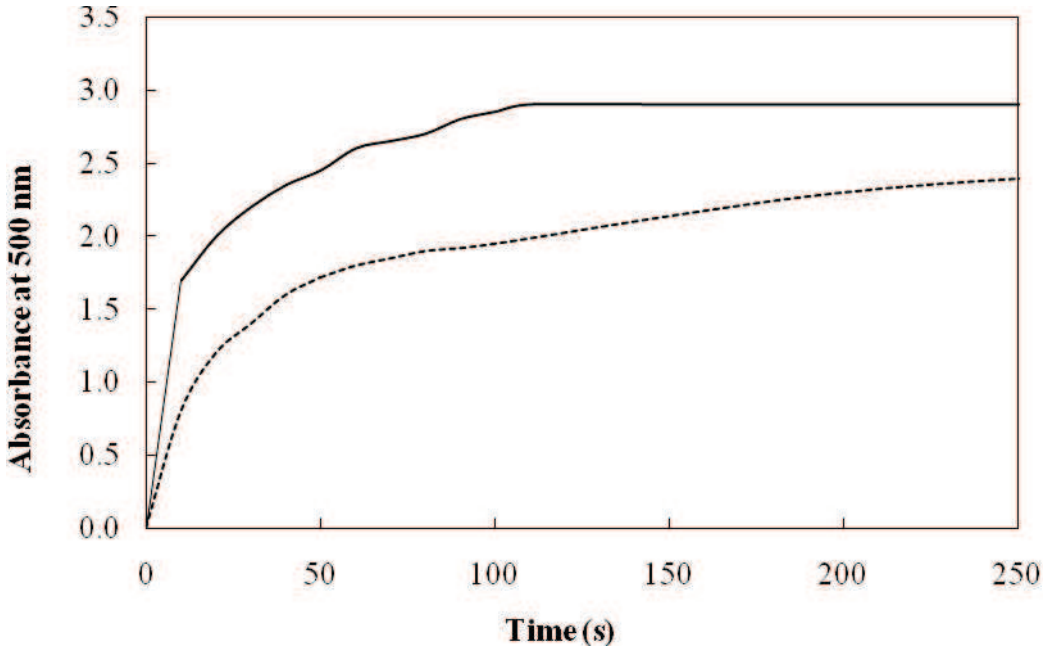

Figure 18. Evolution as a function of time of the ligand exchange reaction COD-CYD for $[Rh(COD)(PPh_3)_2]NTf_2$ in $[C_1C_4Im][NTf_2]$ (full line) and $[C_1C_1C_4Im][NTf_2]$ (dashed line) monitored at λ = 500 nm by UV-Vis spectroscopy. UV-visible spectra of $[Rh(COD)(PPh_3)_2]NTf_2$ and $[Rh(CYD)(PPh_3)_2]NTf_2$ are provided in section 3.5.3

Following this, the red solutions of $[Rh(CYD)(PPh_3)_2]NTf_2$ in $[C_1C_4Im][NTf_2]$ or $[C_1C_1C_4Im][NTf_2]$ were exposed to hydrogen, leading to discolouration with the concomitant formation of CYE. This hydrogenation reaction of CYD in $[Rh(CYD)(PPh_3)_2]NTf_2$ was also monitored by UV-Vis spectroscopy in both ILs, the absorbances represented in Figure 19. The results indicate that the hydrogenation step is also faster in $[C_1C_4Im][NTf_2]$ than in $[C_1C_1C_4Im][NTf_2]$. The two processes, however, do not occur on the same time scale (hours *versus* seconds) and, as in organic solvents, ligand exchange is faster than hydrogenation. We can conclude therefore, in accordance with the literature,[56, 57] that in the hydrogenation of CYD, this attack by H_2 is the rate-determining step (Scheme 7).

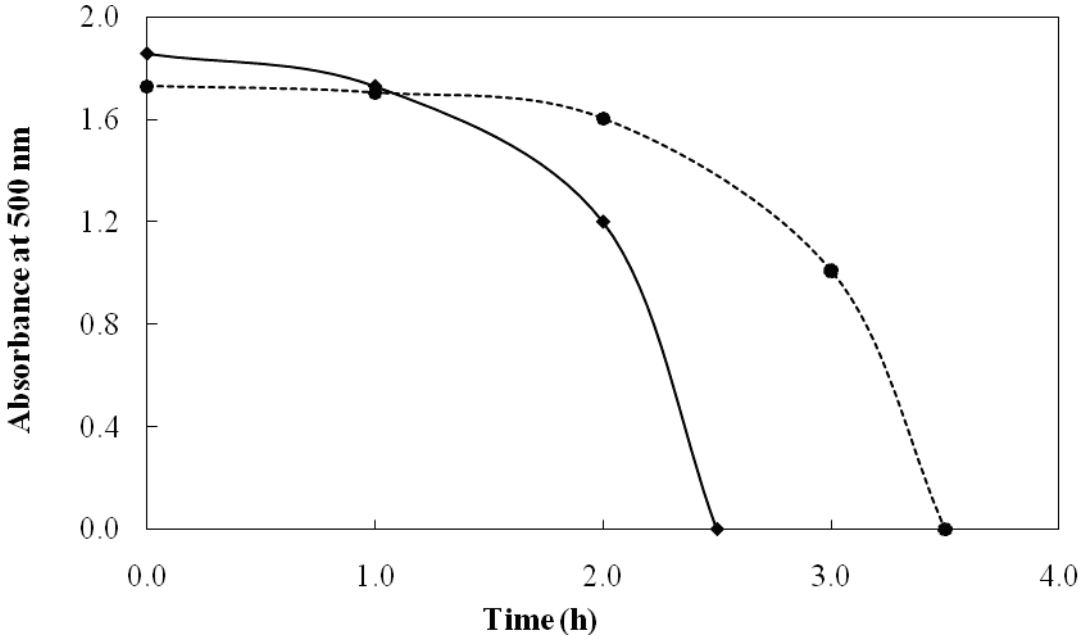

Figure 19. Evolution of the absorbance at λ = 500 nm as a function of time during the hydrogenation reaction of CYD in the presence of $[Rh(CYD)(PPh_3)_2]NTf_2$ in $[C_1C_4Im][NTf_2]$(●) and $[C_1C_1C_4Im][NTf_2]$(♦).

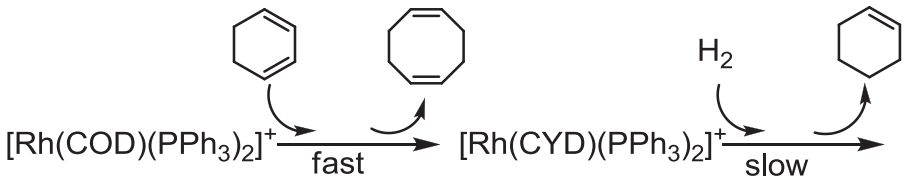

Scheme 7. The two steps involved in the catalytic hydrogenation of CYD, the attack by H_2 being rate-determining.

3.2.3.2 CYD catalytic hydrogenation in both ILs

In the hydrogenation experiment the appropriate quantity of CYD was added to the yellow solution of $[Rh(COD)(PPh_3)_2]NTf_2$ in $[C_1C_4Im][NTf_2]$ or $[C_1C_1C_4Im][NTf_2]$ to reach a molar ratio between CYD and IL $R = 0.5$, corresponding to a molar ratio substrate/Rh atom $r = 500$. The resulting red solution was stirred under 1.2 bar of hydrogen at 303 K. The formation of cyclohexene (CYE) was followed by GC analysis. Note that CYE is less soluble than CYD in both IL media so the system will tend to become biphasic during the course of the reaction. In order to avoid errors in the determination of the composition of the reaction mixture, resulting from the heterogeneity of the system, the conversion was measured using GC analysis of the

entire reaction system after dissolution in a mixture of acetonitrile and toluene 99:1. Each point, repeated at least twice, presented in Figure 20, corresponds to a different experiment

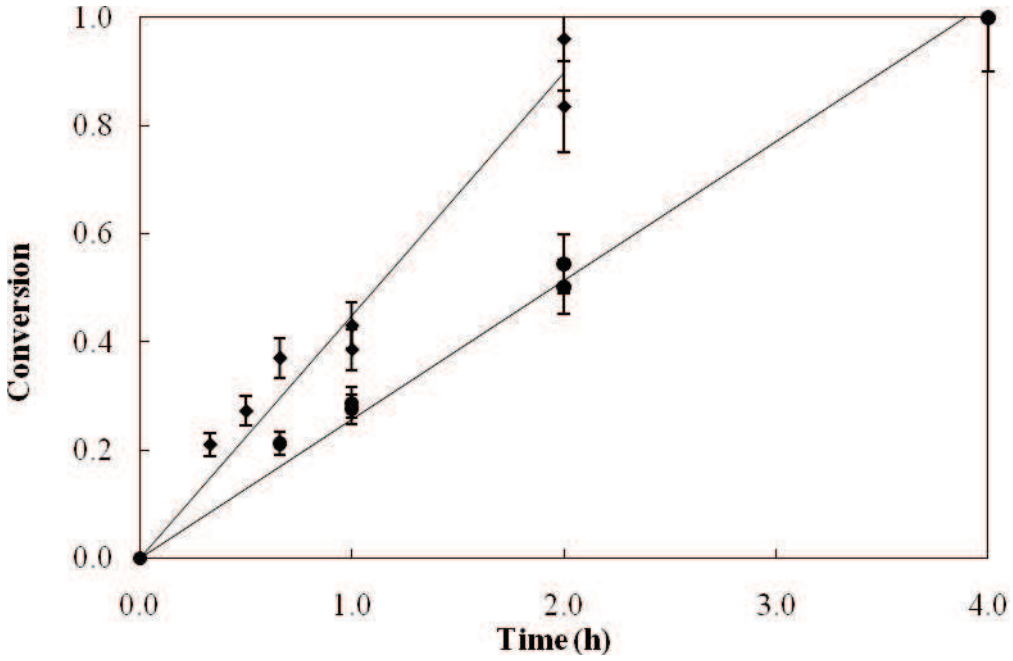

Figure 20. Hydrogenation of CYD at 303 K under 1.2 bar H_2 (R = 0.5 and $r = n$(CYD)/n(Rh) = 500) in $[C_1C_4Im][NTf_2]$(♦) and $[C_1C_1C_4Im][NTf_2]$(●).

As can be seen in Figure 18, hydrogenation of CYD in both ILs by $[Rh(COD)(PPh_3)_2]NTf_2$ leads quantitatively and selectively to CYE. In both cases, no significant amount (less than 2 % at high or complete conversion) of cyclohexane (CYA) was detected by GC. As described in the literature, the rate of CYD reduction remains constant until near 100% conversion (1 mol of H_2 absorbed per CYD) and CYE is produced quantitatively before it is hydrogenated to CYA.[56, 57] In $[C_1C_4Im][NTf_2]$ the conversion is complete in 2 h. This result is similar to that observed in organic solvents, [56, 57] and in other ionic liquids, such as $[C_1C_4Im][PF_6]$ or $[C_1C_4Im][SbF_6]$.[14] In $[C_1C_1C_4Im][NTf_2]$, only 50 % conversion is reached after 2 h with an initial rate of hydrogenation *ca.* half of that in $[C_1C_4Im][NTf_2]$.

When all possible experimental factors are identical ([CYD], [Rh], pressure, temperature, stirring), the fact that both reaction steps proceed twice as fast in a medium that is half as viscous ($[C_1C_4Im][NTf_2]$) would indicate that the difference in reactivity can be mainly assigned to the difference in viscosity, and therefore in mass transport, of CYD in the exchange reaction and both H_2 and CYD in the hydrogenation reaction.

3.2.3.3 Varying the viscosity in [C_1C_4Im][NTf_2]

To confirm the dependence of the rate of reaction on the mass transport, the viscosity of the medium may be varied, by changing the CYD concentration in [C_1C_4Im][NTf_2] as previously demonstrated in section 3.2.2. Therefore for [C_1C_4Im][NTf_2], solutions of CYD were prepared as described in Table 3.

Table 3. Chosen compositions for catalytic media

R	**0.5**	**0.4**	**0.3**	**0.2**	**0.1**
CYD (g)	0.2268	0.1865	0.1438	0.0987	0.0508
LI (g)	2.4531	2.5211	2.5930	2.6690	2.7497
Rh complex (g)	0.0029	0.0024	0.0018	0.0013	0.0006
CYD (mmol)	2.8301	2.3269	1.7949	1.2317	0.6345
LI (mmol)	5.6603	5.8171	5.9830	6.1585	6.3446
Rh complex (mmol)	0.0028	0.0023	0.0018	0.0012	0.0006

In these conditions, at 303 K, and under 1.2 bar H_2, conversion curves for different values of *R* are plotted in Figure 21. It can clearly be seen that the rate of this reaction increases with increasing molar ratio *R*. When *R* = 0.1, the conversion rate is found to be very low, values obtained falling within the experimental error, thus this result is not depicted in Figure 21.

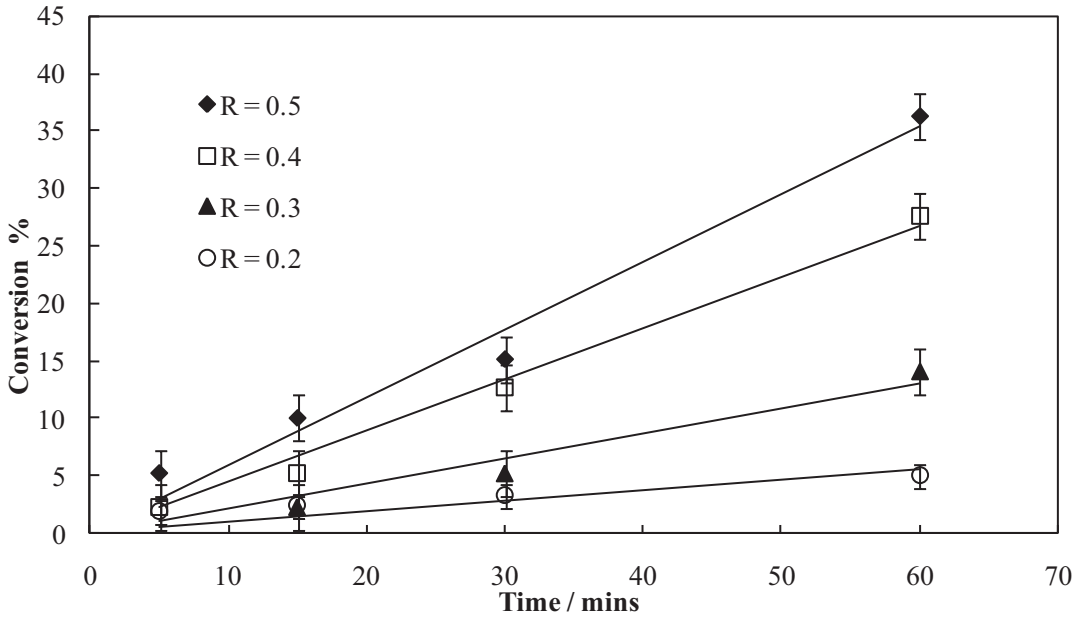

Figure 21. Conversion curves for the hydrogenation of CYD with varying molar ratio *R* = CYD/IL, in [C_1C_4Im][NTf_2]

From literature data and previous results obtained by UV, we hypothesised that the rate determining step in this reaction is the attack by H_2 on the catalyst and not the coordination of the substrate. In such situations the rate law should be expressed as (5). [58]

$$MS + H_2 \xrightarrow{k} M + P$$

M = metal
S = substrate
P = product

$$rate = k\,[MS][H_2] \qquad (5)$$

As the coordination of the substrate to the catalyst is rapid, we can consider the concentration of substrate-coordinated catalyst, [MS] in (5), equal to the concentration of catalyst.

The concentration and diffusivity of H_2 in these media (IL:CYD mixture) has been neither measured nor calculated. Even in neat ILs, no experimental data were found on the diffusivity of hydrogen. Nevertheless, the diffusivity is expected to be inversely proportional to the viscosity of the liquid medium since H_2 interacts weakly with ILs[59-62]

In an attempt to establish a rough approximation to the rate law of this reaction, a graph is plotted of the initial reaction rate versus a combination of these known and controlled variables, potentially affecting the rate of reaction, i.e. concentration of CYD and catalyst, also including a term for the viscosity, η^{-1}. As seen in Figure 22, this gives us a near linear relationship, passing close to origin, indicating that the rate varies inversely with viscosity as expected from previous results. The rate also varies linearly with the concentration of both catalyst and substrate. (Note that plots accounting for only one or two of these variables do not give straight lines.) Our curve therefore seems to indicate that the rate is proportional to $[Rh][CYD]\eta^{-1}$.

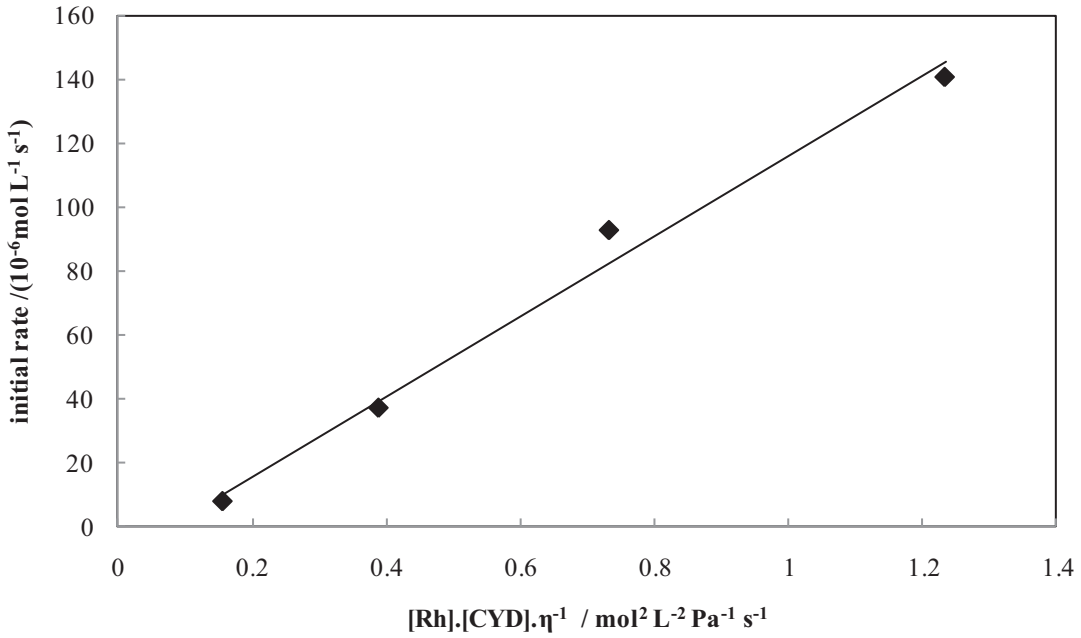

Figure 22. linear relationship of initial rate against the inverse viscosity measured experimentally

It is clear that the system under investigation is complex. To establish the correct rate law for this reaction, the solubility of H_2 in ILs, CYD and IL-CYD binary mixtures must be accurately measured. We must also determine the effect of changing pressure on both the solubility of H_2 in the media and the viscosity. Furthermore, conductivity must be taken into account as this may affect the mobility of the ionic catalyst.[63]

3.3 Conclusion

In this chapter, we have attempted to determine the physical-chemical parameters influencing the catalytic activity of an Osborn-type catalyst $[Rh(COD)(PPh_3)_2]NTf_2$ in the hydrogenation of 1,3-cyclohexadiene CYD performed in the ionic liquids 1-butyl-3-methylimidazolium bis(trifluoromethylsulfonyl)imide, $[C_1C_4Im][NTf_2]$ and 1-butyl-2,3-dimethylimidazolium bis(trifluoromethylsulfonyl)imide, $[C_1C_1C_4Im][NTf_2]$.

Firstly, the solvation of CYD in the two ILs was investigated by molecular dynamics simulations, ROESY NMR experiments and compared to previous results involving toluene. In both ILs, CYD is found to be located in the lipophilic domains. In $[C_1C_1C_4][NTf_2]$, CYD is found closer to the C_2-Me, whereas in $[C_1C_4Im][NTf_2]$, strong interactions between C_2-H and the anion $[NTf_2]$ do not allow for such proximity.

Unlike for toluene, it was found that that no strong interactions (e.g. π-cation) exist between CYD and either of the cations, while calorimetric measurements showed that the existing weak interactions are more favourable in the case of $[C_1C_4Im][NTf_2]$. These results show that solvation phenomena of the substrate should have little impact on the catalytic activity.

Secondly the role of mass transport factors has been studied in both ILs. For this, the viscosity, η, of CYD-IL mixtures of various molar ratios, R = CYD/IL, was measured, and shown to vary radically with changing R. The viscosity values measured in $[C_1C_1C_4Im][NTf_2]$ were consistently found to be roughly double those measured in $[C_1C_4Im][NTf_2]$.

The diffusion D of CYD in both ILs while varying R was also experimentally determined by DOSY NMR. We observed that in these media, D does not vary perfectly linearly with η^{-1}, as predicted by the Stokes-Einstein equation, suggesting different diffusion behaviour at low and high R. At high R, i.e. low viscosity, the Stokes-Einstein relationship holds, whereas at low R, i.e. high viscosity, fluid "sliding surface" behaviour seems more suitable indicating little sliding friction between the molecules. For the latter case, the Sutherland factor of 6 in the Stokes-Einstein equation is replaced by 4.

$$D = \frac{k_B T}{6\pi\eta r_H} \rightarrow D = \frac{k_B T}{4\pi\eta r_H}$$

The chosen model catalytic reaction was the hydrogenation of 1,3-cyclohexadiene (CYD) with which occurs in two steps: the ligand exchange $[Rh(COD)(PPh_3)_2]NTf_2$ to

$[Rh(CYD)(PPh_3)_2]NTf_2$, and the catalytic hydrogenation of CYD itself (COD=1,5-cyclooctadiene). It was found that both steps, monitored here by UV-vis spectroscopy, are twice as fast in $[C_1C_4Im][NTf_2]$, implying that the reaction rate is strongly dependent on the viscosity and diffusion of the substrate.

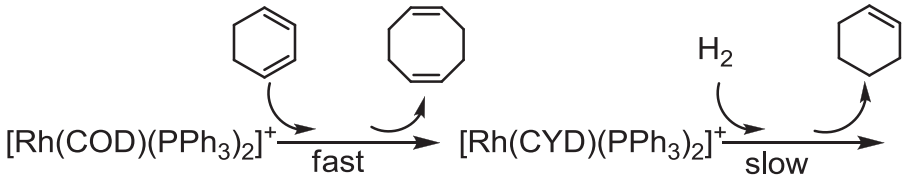

Furthermore, when the reaction is performed in $[C_1C_4Im][NTf_2]$ whilst varying *R*, the initial rate is found to be inversely proportional to η confirming that for this hydrogenation reaction the viscosity and thus mass transport is indeed the deciding factor when performed in ILs.

The exact kinetic rate law cannot be determined without precise knowledge of H_2 solubility and diffusivity in the media and also studies of conductivity and its potential effect on the mobility of the ionic catalyst. This work is currently underway.

We have successfully demonstrated in this chapter that to fully understand the kinetics of catalytic processes carried out in IL media, a comprehensive study of all physical-chemical variables is necessary. Consequently, when comparing literature data on catalytic activity in ILs the differences in physical-chemical properties must be taken into account, and may shed light on differences noted. In the case under study it has been found that mass transport factors play a decisive role.

3.4 Outlooks

For the hydrogenation of CYD in these ILs, we have demonstrated that the rate determining step involves the insertion of H_2. Future work is planned to determine the rate law of this reaction through a full kinetic study varying conditions such as H_2 pressure. For this, due to the complicated viscosity-dependent behaviour and the interesting solvation properties of ILs, a study of the viscosity and H_2 solubility dependence on H_2 pressure must first be undertaken. Also, a study of conductivity in CYD-IL mixtures, with varying *R* may give useful information on the mobility of the ionic catalyst in the different media.

Finally, as aromatic substrates such as toluene have already been shown to display more complicated behaviour when dissolved in ILs, i.e. π-cation interactions, it may be interesting to observe the effect of such interactions in catalysis.

3.5 Experimental Section

3.5.1 Materials and methods

1-methylimidazole (>99%, Aldrich) and 1,2-dimethylimidazole (>98%, Aldrich) were distilled prior to use. Anhydrous 1,3-cyclohexadiene (99.8%, Aldrich) and 1,3-cyclohexadiene stabilised (96%, Acros Organics, stabilised with 50 ppm of 2,6-di-tert-butyl-4-methylphenol, BHT) distilled over NaK alloy and stored on zeolites were used for the reaction and the physical chemical measurements, respectively. Bis(trifluoromethanesulphonyl)imide lithium salt (>99%, Solvionic) and $[Rh(COD)Cl]_2$ (>99%, Strem) were used without further purification. All other reagents and solvents were commercially available and were used as received. Ionic liquids, synthesised as previously reported,[26] were dried overnight under high vacuum and stored in a glovebox (Jacomex) in order to guarantee rigorously anhydrous products.

3.5.2 Synthesis of the catalysts

$[Rh(COD)(PPh_3)_2]NTf_2$: The procedure followed was adapted from the literature. [56]A mixture of $[Rh(COD)Cl]_2$ (100 mg, 0.2 mmol) dissolved in 2 mL of dichloromethane and of $LiNTf_2$ (107 mg, 0.37 mmol) dissolved in 2 mL of water was stirred vigorously while triphenylphosphine (405 mg, 1.5 mmol) was added. After 2 h, the dichloromethane layer was removed, washed three times with 2 mL of water and dried over anhydrous Na_2SO_4. Ethanol (1 mL) and diethyl ether (2 mL) were slowly added to complete crystallisation. The orange crystals were filtered off and dried under reduced pressure. Yield: 200 mg (99%). ^{1}H NMR (300 MHz, CD_2Cl_2): δ = 2.2 (m, 8H), 4.6 (s, 4H), 7.5 (m, 30H). ^{31}P NMR (121 MHz, CD_2Cl_2): δ = 23.6 with $J_{Rh\text{-}P}$ = 147 Hz. ^{103}Rh NMR (500 MHz, CD_2Cl_2): δ = -80 ppm with $J_{Rh—P}$ = 147 Hz. Mass spectrometry (ESI): positive mode: m/z= 473 ⇒ $Rh(COD)(PPh_3)^+$; 627 ⇒ $Rh(PPh_3)_2^+$. UV-Vis spectroscopy (6.6 mg of $[Rh(COD)(PPh_3)_2]NTf_2$ dissolved in 2 mL of one of ionic liquids, $[C_1C_4Im][NTf_2]$ or $[C_1C_1C_4Im][NTf_2]$); spectrum recorded at λ_{max} = 450 nm.

$[Rh(CYD)(PPh_3)_2]NTf_2$: $[Rh(COD)(PPh_3)_2]NTf_2$ (100 mg, 9.84×10^{-5} mol) was dissolved in 1 mL of CYD. After 10 min, the excess of solvent was removed under reduced pressure.

Yield: 100 mg (99%). ^{1}H NMR (300 MHz, CD_2Cl_2): δ = 2.1 (s, 2H), 5.3 (s, 2H), 7.5 (m, 30H). ^{31}P NMR (121 MHz, CD_2Cl_2): δ = 25.2ppm with $J_{Rh\text{-}P}$ = 17 Hz. Mass spectrometry (ESI): positive mode: m/z=707 $\Rightarrow$ Rh(cyclohexadiène)$(PPh_3)_2^+$; m/z=627 $\Rightarrow$ $Rh(PPh_3)_2^+$. UV-Vis spectroscopy (6.6 mg of $[Rh(CYD)(PPh_3)_2]NTf_2$ dissolved in 2 mL of one of ionic liquids, $[C_1C_4Im][NTf_2]$ or $[C_1C_1C_4Im][NTf_2]$); spectrum recorded at λ_{max} = 500 nm.

3.5.3 Ligand exchange

Ligand exchange in $[Rh(CYD)(PPh_3)_2]NTf_2$ was followed by UV-Vis spectroscopy. CYD (0.15 mL, 1.6 mmol) was added to a system of $[Rh(COD)(PPh_3)_2]NTf_2$ (1.6 mg, 1.6 µmol) in one of the ionic liquids, $[C_1C_4Im][NTf_2]$ or $[C_1C_1C_4Im][NTf_2]$ (1 mL). The UV-visible spectra of 1 mL of the solution were recorded on the Perkin-Elmer LAMBDA 950 Spectrophotometer in stirred and closed UV cells at λ_{max} = 500 nm every second. The spectra for both complexes are depicted in Figure 23.

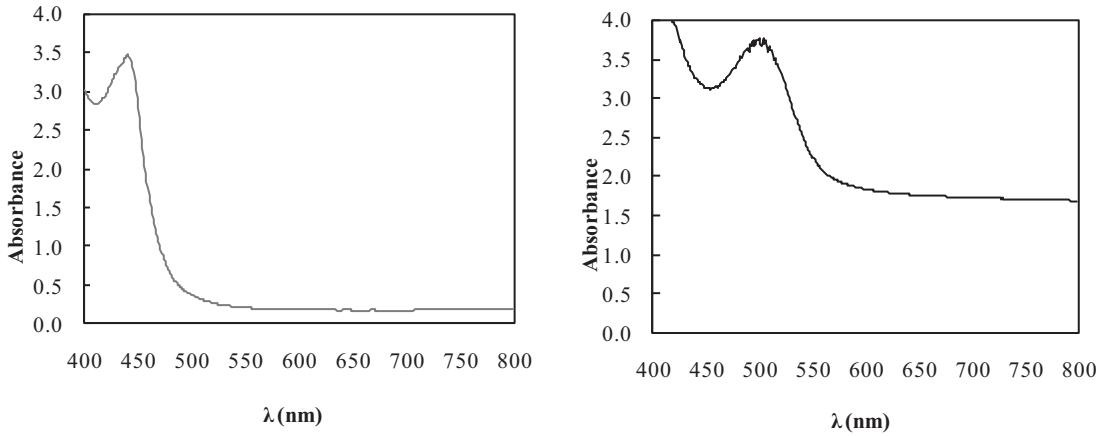

Figure 23. UV-vis absorption spectra for $[Rh(COD)PPh_3]$ (left), and $[Rh(CYD)PPh_3]$ (right)

3.5.4 Reaction with H_2

$[Rh(CYD)(PPh_3)_2]NTf_2$ (8 mg, 8.1×10^{-6} mmol) was dissolved in one of the ionic liquids, $[C_1C_4Im][NTf_2]$ or $[C_1C_1C_4Im][NTf_2]$ (5 mL) and pressurised under 1.2 bar of hydrogen. The UV-visible spectra of 1 mL of the solution were recorded at a given time at λ_{max} = 500 nm.

3.5.5 Hydrogenation of 1,3-cyclohexadiene

The hydrogenation of CYD was carried out at 1.2 atm of H_2 and 30 °C. CYD (0.15 mL, 1.6 mmol) (0.06 mL, 0.63 mmol) was dissolved in a system of $[Rh(COD)(PPh_3)_2]NTf_2$ (3.2 mg, 3.2 µmol) in one of ionic liquids, $[C_1C_4Im][NTf_2]$ or $[C_1C_1C_4Im][NTf_2]$ (1mL), under argon resulting in red homogeneous solutions. The reaction mixture was kept under hydrogen

atmosphere (1.2 atm, constant pressure) until 4 mL of acetonitrile were added to the catalytic solution. The product distribution in the reaction mixture and the conversion were determined by GC analyses in presence of toluene as an internal standard. A HP6890 chromatograph equipped with FID detector and an Al_2O_3/KCl column (L = 50 m, ϕ_{int} = 0.32 mm, film thickness = 5 μm) was used. Injector and detector temperature were set to 230 °C. Samples were injected in volume of 1 μL. The temperature of the column was fixed at 190 °C. From those relative response factors, the mass of each product can be determined by thegeneral formula:

$$M(x) = K(x)\left(\frac{A(x)}{A(s)}\right)M(s) \quad (7)$$

M(x); mass of product x
K(x); relative response factor of product x
A(x); peak area of product x
A(s); peak area of standard (butylbenzene)
M(s); mass of standard in the sample

Conversion, yields and mass balance are defined by the following equations, where conversion of substrates was calculated from unreacted substrates remaining after reaction:

$$\text{Conv. of substrate} = \frac{\text{moles of substrate introduced - moles of substrate final}}{\text{moles of substrate introduced}}$$

$$\text{Yield of A} = \frac{\text{moles of product A after reaction - moles of product A introduced}}{\text{moles of substrate introduced}}$$

$$\text{Mass balance} = \frac{\text{moles of product after reaction}}{\text{moles of substrate introduced}}$$

3.5.6 Solubility and phase diagrams

Liquid-liquid phase equilibria of the mixture of $[C_1C_4ImNTf_2]$ or $[C_1C_1C_4Im][NTf_2]$ and CYD at atmospheric pressure were determined using a dynamic method with visual detection of solution turbidity, as already described.[49] The mixtures of ionic liquid and CYD at different compositions were prepared gravimetrically in a glass vial equipped with a stirring bar. First, the ionic liquid was introduced into a glass vial, then the appropriate amount of CYD was added and the vial was sealed. In order to minimize the volume of the vapour phase in equilibrium with the ionic liquid solution and to reduce the error in composition due to differential evaporation, the glass vial was almost completely filled with the mixture. The uncertainty of the mole fraction is estimated as ± 0.0001. The cells were then immersed in a thermostatic water bath whose

temperature was monitored using a platinum resistance thermometer with a precision of ± 0.1 K. The temperature of the bath was first increased slowly until one phase was observed. The clear homogenous system was then cooled down very slowly (5 K/h) under continuous stirring. The temperature at which the first sign of turbidity (first cloudiness) appeared was considered as the temperature of the liquid-liquid phase transition. The overall accuracy in the measurement of cloud-point temperatures is estimated to be ± 2 K.

3.5.7 Isothermal titration calorimetry

The heat effects resulting from mixing of aliquots of CYD with the ionic liquid were measured at 303.15 K using an isothermal titration nanocalorimeter equipped with 4 mL glass cells in a Thermal Activity Monitor TAM III from TA Instruments. An electrical calibration was done before each experiment and the instrument was chemically calibrated 5 times by titration of 0.01 M aqueous solution of 18-crown-6 ethers with 0.2 M aqueous solution of $BaCl_2$.

Approximately 2.75 mL of degassed ionic liquid was introduced into 4 mL glass measuring and reference cells. The liquid in the measuring cell was stirred by a turbine stirrer at 160 rpm and volumes of 4 μL of CYD were injected during 180 seconds using a motor driven pump (Thermometric 3810 Syringe Pump) equipped with a 100 μL gas-tight Hamilton syringe. In all experiments, the intervals between consecutive injections were of 35 to 40 minutes, which provided a good thermal stabilisation of the ionic liquid solution and the return to a stable baseline. To minimise the undesirable effects of diffusion of the ionic liquid into the canula linking the CYD syringe to the cell, the canula was immersed in the sample 10 minutes prior the first injection.

A peak with an area proportional to the resulting heat effect Q_i translates to the thermal effect due to each injection of CYD. The integration of peaks from the recorded calorimetric plots was performed using the TAM III Assistant software. Each experiment was repeated four times to obtain reproducible values of Q_i at different concentrations within the error bar of ± 2 %.

3.5.8 Density and viscosity

The mixtures of ionic liquid and CYD at different compositions were prepared gravimetrically following the procedure already described, including the precautions to minimize vapour head-space.[41]The viscosity of the mixture was measured at 298.15 K (controlled to within ± 0.005 K and measured with the accuracy better than ± 0.05 K) using a rolling ball viscometer from Anton Paar, model AMVn, equipped with capillary tubes of 3.0 and 1.8 mm in diameter.

Before starting the measurements, the 3.0 mm diameter capillary tube was calibrated as a function of temperature and angle of measurement with standard viscosity oil from Cannon (N35). The 1.8 mm diameter tube was calibrated with water by the manufacturer. The overall uncertainty of the viscosity is estimated as ± 2.0 %.

The densities of the mixtures, necessary to calculate the viscosities were measured in an Anton Paar vibrating tube densimeter model 512 P, at 298.15 K (measured by a calibrated PRT with an accuracy of ± 0.02 K). The densimeter was calibrated using *n*-heptane, bromobenzene and 2,4-dichlorotoluene. The overall uncertainty of the density is estimated as ± 0.01 %.

3.5.9 NMR spectroscopy

^{1}H, ^{13}C and ^{31}P solution NMR data were collected at room temperature on a Bruker AC 300 MHz spectrometer with the resonance frequency at 300.130 MHz for ^{1}H nucleus. ^{103}Rh solution NMR was carried out on a Bruker DRX 500 instrument at 298 K (nominal) with a resonance frequency at 500.130 MHz. The solvent used (CD_2Cl_2) was distilled and kept in a rotaflo with molecular sieves. Chemical shifts are reported in ppm (singlet = s, doublet = d, doublet of doublet = dd, and multiplet = m) and were measured relative to the residual proton of the solvent to $CHDCl_2$ for ^{1}H, to CD_2Cl_2 for ^{13}C and to H_3PO_4 for ^{31}P spectra.

For ^{1}H 1D NMR spectroscopy**,** the samples with molar ratio $R = 0.5$ (R is the molar ratio between the amount of substance of the hydrocarbon and the amount of substance of IL) were prepared. The mixtures of ionic liquids and hydrocarbon were prepared in closed vials in a glove box by adding the appropriate amount of CYD to each ionic liquid, $[C_1C_4Im][NTf_2]$ or $[C_1C_1C_4Im][NTf_2]$. The resulting systems were stirred for 24 h at 303 K resulting in homogeneous monophasic solutions. Approximately 0.3 mL of the sample was then introduced into a 5 mm NMR tube. A stem coaxial capillary tube loaded with CD_2Cl_2 was inserted into the 5 mm NMR tube to avoid any contact between the deuterated solvent and the analysed mixture. The deuterium in CD_2Cl_2 was used for the external lock of the NMR magnetic field and the residual $CHDCl_2$ in CD_2Cl_2 was used as the ^{1}H NMR external reference at 5.32 ppm. When ^{1}H NMR data are obtained in this way, the reference signal of $CHDCl_2$ remains constant and is not affected by changes in sample concentration.

For ROESY (Nuclear Overhauser Effect SpectroscopY) experiments in the rotating frame, the 2D sequence was built with the scheme proposed by Bodenhausen (the pulse sequence shown in Figure 24).[64] The mixing time (200 ms) is split into two parts separated by a p-pulse.

At each side of the spin lock the B1 field is ramped linearly (4.5 ms) to ensure adiabatic conditions for spinlock. During the first spinlock pulse, the frequency is shifted to O1 + Df whereas the second pulse frequency is set to O1 – Df; O1 is the offset frequency and Df set to give a B1 field at the magic angle. By this way, the ROESY response is roughly constant across the spectra of interest. 1D sequence, PFGSE (Pulse Field Gradient Spin Echo for Selective Excitation) have been used and spinlock followed the same scheme as previously.

Figure 24. ROESY pulse sequence.

Molecules in liquid or solution state move. This translational motion is, in contrast to rotational motion, known as Brownian molecular motion and is often simply called diffusion or self-diffusion. It depends on a lot of physical parameters like size and shape of the molecule, temperature, and viscosity. Assuming a spherical size of the molecule the diffusion coefficient *D* is described by the Stokes-Einstein equation (2):

Pulsed field gradient NMR spectroscopy can be used to measure translational diffusion of molecules and is sometimes referred to as q-space imaging. By use of a gradient, molecules can be spatially labelled, i.e. marked depending on their position in the sample tube. If they move after this encoding during the following diffusion time *D*, their new position can be decoded by a second gradient. The measured signal is the integral over the whole sample volume and the NMR signal intensity is attenuated depending on the diffusion time *D* and the gradient parameters (*g*, *δ*). This intensity change is described by equation (4):

$$I = I_0 e^{-D\gamma^2 g^2 \delta^2} \qquad (4)$$

I; the observed intensitu

I_0; reference intensity (unattenuated signal intensity)

D; diffusion coefficient

g; gradiant strength

γ; gyromagnetic ratio

δ; length of the gradient

Δ; diffusion time

To simplify this equation some parameters are often combined to emphasize the exponential decay behaviour.

$$I = I_0 e^{-Dq^2(\Delta - \frac{\delta}{3})} \text{ or } I = I_0 e^{-DQ} \quad (8)$$

If bipolar gradients are used for dephasing and rephasing a correction for the time t between those bipolar gradients has to be applied (6).

$$I = I_0 e^{-D\gamma^2 g^2 \delta^2 (\Delta - \delta/3 - r/2)} \quad (9)$$

2D DOSY experiments used a slightly modified Bruker experiment ledbpgp2s to improve lineshape and trapezoidal gradients where implemented for shorter pulses gradients (the pulse sequences shown in Figure 25). The diffusion evolution time was set to 100 ms, the constant amplitude part of the gradient was set to 3 ms, and the cosine raising and falling part of gradient where set to 150 μs. The diffusion space where sampled by 32 linearly spaced gradients. Values obtained for *D* using this technique are tabulated in Tables 4 and 5, as well as viscosity values and the hydrodynamic radii calculated from these experimental data according to the Stokes-Einstein relationship (2).

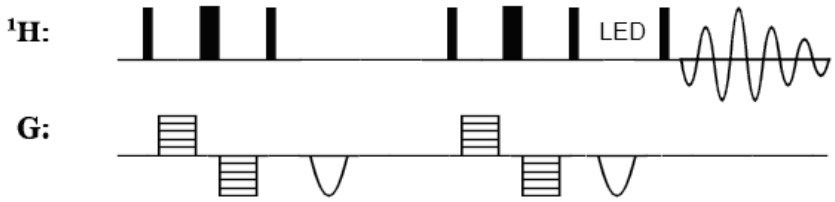

Figure 25. DOSY pulse sequences.

Table 5. The viscosity values **η**, diffusion coefficients, *D*, and hydrodynamic radii, $\mathbf{r_H}$, calculated from experimental results, for CYD-[C_1C_4Im][NTf_2] mixtures with varying molar ratio R.

R	η [mPa·s]	1/η [mPa$^-$]	D(CYD) [μm^2/s]	r_H [10^{-11} m]
0	51.02	0.020		
0.11	42.39	0.024	91.7	5.52
0.21	36.39	0.027	112.1	5.26
0.34	31.39	0.032	136.9	4.99
0.54	25.93	0.039	183.7	4.50
0.81	21.57	0.046	241.4	4.12

Table 6. The viscosity values **η**, diffusion coefficients, *D*, and hydrodynamic radii, $\mathbf{r_H}$, calculated from experimental results, for CYD-[$C_1C_1C_4$Im][NTf_2] mixtures with varying molar ratio R.

R	η [mPa·s]	1/η [mPa$^-$]	D(CYD) [μm^2/s]	r_H [10^{-11} m]
0.00	107.25	0.009		
0.08	86.04	0.012	54.5	4.58
0.18	68.94	0.015	70.4	4.42
0.30	54.90	0.018	88.6	4.41
0.40	47.05	0.021	104.4	4.37
0.69	33.11	0.030	163.4	3.97

3.5.10 Molecular simulation

The microscopic structures of the IL-CYD mixtures studied experimentally were also investigated by molecular simulation, using an atomistic force field that describes interactions and conformations. [65, 66, 67] CYD was represented by the Optimized Potential for Liquid Simulations force field in its all-atom explicit version (OPLS-AA).[68] ILs were represented by a specifically parameterized force field of the OPLS-AA family in which particular attention was paid to the description of electrostatic charge distributions and torsion energy profiles. The OPLS-AA force field is known to reproduce H-bonds well; the electron density of aromatic systems is represented by the values of electrostatic charges on the relevant atoms that account for the molecular mutipoles, combined with the Lennard-Jones sites that account for dispersion interactions. Explicit polarisation of electron clouds is not included in the present model. Although this may be important to correctly reproduce dynamic properties of ILs, structural features and thermodynamic quantities have been described to equivalent levels of accuracy using fixed-charge models.[69]

Molecular dynamics simulations of condensed-phase CYD-[C_1C_4Im][NTf_2] and CYD-[$C_1C_1C_4$Im][NTf_2] mixtures were performed using the DL_POLY program.[70] System sizes were chosen so as to contain about 10000 atoms, and so the numbers of cations, anions and CYD molecules varied according to composition (*e.g.* 128 ion pairs and 64 molecules of CYD for $R = 0.5$). Initial low-density configurations, with ions and molecules placed at random in periodic cubic boxes, were equilibrated to attain liquid-like densities and structures at 400 K and 1 bar. Temperature and pressure were maintained using Nosé-Hoover thermostat and barostat, respectively. Production runs then took 500 ps with an explicit cut-off distance of 16 Å for non-bonded interactions, and long-range corrections applied for repulsive-dispersive interactions. Electrostatic energies were calculated using the Ewald summation method with a relative accuracy of 10^{-4}. Structural quantities such as radial and spatial distribution functions were calculated from configurations generated during the production runs

3.6 References

1. H. Olivier-Bourbigou, L. Magna and D. Morvan, *Appl. Catal., A*, 2010, **373**, 1-56.
2. V. I. Parvulescu and C. Hardacre, *Chem. Rev.*, 2007, **107**, 2615-2665.
3. T. Welton, in *Multiphase Homogeneous Catalysis*, eds. B. Cornils, W. A. Herrmann, I. T. Horvath, W. Leitner, S. Mecking, H. Olivier-Bourbigou and D. Vogt, Wiley, Weinheim, 2005, pp. 431-454.
4. P. J. Dyson and T. J. Geldbach, *Metal Catalysed Reactions in ionic liquid*, Springer, Dordrecht, 2005.
5. J. S. Wilkes, *J. Mol. Catal. A*, 2004, **214**, 11-17.
6. T. Welton, *Coord. Chem. Rev.*, 2004, **248**, 2459-2477.
7. P. J. Dyson, in *Comprehensive Coordination Chemistry II*, ed. a. M. T. J. Mc Cleverty, Elsevier, Amsterdam, 2004, pp. 557-566.
8. P. Wasserscheid, in *Ionic Liquids in Synthesis*, Wiley-VCH, Weinheim, 2003, pp. 213-257.
9. J. Dupont, G. S. Fonseca, A. P. Umpierre, P. F. P. Fichtner and S. R. Teixeira, *J. Am. Chem. Soc.*, 2002, **124**, 4228-4229.
10. T. Welton, *Chem. Rev.*, 1999, **99**, 2071-2083.
11. Chauvin Y., B. Gilbert and I. Guibard, *Chem. Commun.*, 1990, 1715.
12. G. W. Parshall, *J. Am. Chem. Soc.*, 1972, **94**, 8716-8719.
13. C. Vallee, C. Valerio, Y. Chauvin, G. P. Niccolai, J.-M. Basset, C. C. Santini, J.-C. Galland and B. Didillon, *J. Mol. Catal. A*, 2004, **214**, 71-81.
14. Chauvin Y., Mussmann L. and B. H. Olivier, *Angew. Chem. Int. Ed.*, 1995, **34**, 2698-2700.
15. D. Zhao, Z. Fei, T. J. Geldbach, R. Scopelliti and P. J. Dyson, *J. Am. Chem. Soc.*, 2004, **126**, 15876-15882.
16. P. Wasserscheid and T. Welton, *Ionic liquids in synthesis*, Wiley-VCH, Weinheim, 2008.
17. D. J. Cole-Hamilton and R. P. Tooze, *Catalyst separation, recovery and recycling: Chemistry and Process Design*, Springer, Dordrecht, 2006.
18. M. Lombardo and C. Trombini, *ChemCatChem*, 2010, **2**, 135-145.

19. H. Olivier-Bourbigou, F. Favre, A. Forestiere and F. Hugues, in *Handbook of Green Chemistry: Green Catalysis,* ed. P. T. C. Anastas, Robert H., Wiley-VCH, Weinheim, 2009, pp. 101-126. .
20. M. Haumann and A. Riisager, *Chem. Rev.*, 2008, **108**, 1474-1497.
21. P. G. Jessop and D. J. Heldebrant, *Environ. Catal.*, 2005, 627-648.
22. H. Olivier-Bourbigou and C. Vallee, in *Multiphase Homogeneous Catalysis*, Wiley-VCH, Weinheim, 2005, pp. 413-431.
23. C. J. Mathews, P. J. Smith and T. Welton, *J. Mol. Catal. A,* 2004, **214**, 27-32.
24. H. Lebel, M. K. Janes, A. B. Charette and S. P. Nolan, *J. Am. Chem. Soc.*, 2004, **126**, 5046-5047.
25. S. P. Nolan and *N-Heterocyclic Carbenes in Synthesis*, Wiley-VCH, Weinheim., 2006.
26. L. Magna, Y. Chauvin, G. P. Niccolai and J.-M. Basset, *Organometallics*, 2003, **22**, 4418-4425.
27. V. Lecocq and H. Olivier-Bourbigou, *Oil & Gas Sci. Tech*, 2007, **62**, 761-773.
28. U. Hintermair, T. Gutel, A. M. Z. Slawin, D. J. Cole-Hamilton, C. C. Santini and Y. Chauvin, *J. Organometal. Chem.*, 2008, **693**, 2407-2414.
29. J. A. Boon, J. A. Levisky, J. L. Pflug and J. S. Wilkes, *J. Org. Chem.*, 1986, **51**, 480-483.
30. A. Mele, G. Romano, M. Giannone, E. Ragg, G. Fronza, G. Raos and V. Marcon, *Angew. Chem. Int. Ed.*, 2006, **45**, 1123-1126.
31. A. Triolo, O. Russina, H.-J. Bleif and E. Di Cola, *J. Phys. Chem. B*, 2007, **111**, 4641-4644.
32. A. Triolo, O. Russina, B. Fazio, G. B. Appetecchi, M. Carewska and S. Passerini, *J. Chem. Phys.*, 2009, **130**, 164521/164521-164521/164526.
33. J. Fuller, R. T. Carlin, H. C. De Long and D. Haworth, *J. Chem. Soc., Chem. Commun.*, 1994, 299-300.
34. C. Hardacre, J. D. Holbrey, S. E. J. McMath, D. T. Bowron and A. K. Soper, *J. Chem. Phys.*, 2003, **118**, 273-278.
35. J. N. A. Canongia Lopes and A. A. H. Padua, *J. Phys. Chem. B*, 2006, **110**, 3330-3335.
36. Y. Wang, S. Izvekov, T. Yan and G. A. Voth, *J. Phys. Chem. B*, 2006, **110**, 3564-3575.
37. A. A. H. Padua, M. F. Costa Gomes and J. N. A. Canongia Lopes, *Acc. Chem. Res.*, 2007, **40**, 1087-1096.

38. A. E. Bradley, C. Hardacre, J. D. Holbrey, S. Johnston, S. E. J. McMath and M. Nieuwenhuyzen, *Chem. Mater.*, 2002, **14**, 629-635.
39. J. N. Canongia Lopes, M. F. Costa Gomes and A. A. H. Padua, *J. Phys. Chem. B*, 2006, **110**, 16816-16818.
40. J. Lachwa, I. Bento, M. T. Duarte, J. N. C. Lopes and L. P. N. Rebelo, *Chem. Commun.*, 2006, 2445-2447.
41. T. Gutel, C. C. Santini, A. A. H. Padua, B. Fenet, Y. Chauvin, J. N. Canongia Lopes, F. Bayard, M. F. Costa Gomes and A. S. Pensado, *J. Phys. Chem. B*, 2009, **113**, 170-177.
42. A.-L. Revelli, F. Mutelet and J.-N. Jaubert, *J. Phys. Chem. B*, 2010, **114**, 4600-4608.
43. D. Xiao, L. G. Hines, Jr., R. A. Bartsch and E. L. Quitevis, *J. Phys. Chem. B*, 2009, **113**, 4544-4548.
44. T. Umecky, Y. Saito and H. Matsumoto, *J. Phys. Chem. B*, 2009, **113**, 8466-8468.
45. T. Umecky, Y. Saito and H. Matsumoto, *ECS Transactions*, 2010, **25**, 23-29.
46. M. A. Vorotyntsev, V. A. Zinovyeva and M. Picquet, *Electrochim. Acta* 2010, **55**, 5063-5070.
47. V. Kempter and B. Kirchner, *J. Mol. Struct.*, 2010, **972**, 22-34.
48. P. A. Hunt, *J. Phys. Chem. B*, 2007, **111**, 4844-4853.
49. M. Blesic, J. N. Canongia Lopes, A. A. H. Padua, K. Shimizu, M. F. Costa Gomes and L. P. N. Rebelo, *J. Phys. Chem. B*, 2009 **113**, 7631.
50. U. Domańska, Z. Żołek-Tryznowska and M. Królikowski, *J. Chem. Eng. Data*, 2007, **52**, 1872.
51. W. Marczak, S. P. Verevkin and A. Heintz, *J. Solution Chem.*, 2003, **32**, 519-526.
52. I. Natori, K. Imaizumi, H. Yamagishi and M. Kazunori, *J. Polym. Sci. B* 1998, **36**, 1657.
53. D. Frezzato, F. Rastrelli and A. Bagno, *J. Phys. Chem. B*, 2006, **110**, 5676-5689.
54. M. Clark, R. D. Cramer, III and N. Van Opdenbosch, *J. Comp. Chem.*, 1989, **10**, 982-1012.
55. W. Sutherland, *Philos. Mag.*, 1905, 781.
56. R. R. Schrock and J. A. Osborn, *J. Am. Chem. Soc.*, 1976, **98**, 4450-4455.
57. R. R. Schrock and J. A. Osborn, *J. Am. Chem. Soc.*, 1976, **98**, 2134-2143.
58. P. W. N. M. Van Leeuwen, *Homogeneous Catalysis Understanding the art*, Kluwer, Dordrecht, 2004.

59. J. Jacquemin, M. F. Costa Gomes, P. Husson and V. Majer, *J. Chem. Thermodyn.*, 2006, **38**, 490-502.
60. J. Jacquemin, P. Husson, V. Majer and M. F. Costa Gomes, *Fluid Phase Equilib.*, 2006, **240**, 87.
61. M. F. Costa Gomes, *J. Chem. Eng. Data*, 2007, **52**, 472-475.
62. W. Shi, D. C. Sorescu, D. R. Luebke, M. J. Keller and S. Wickramanayake, *J. Phys. Chem. B*, 2010, **114**, 6531-6541.
63. K. Ueno, H. Tokuda and M. Watanabe, *Phys. Chem. Chem. Phys.* , 2010, **12**, 1649-1658.
64. B. Cutting, R. Ghose and G. Bodenhausen, *J. Magn. Reson.*, 1999, **138**, 326-329.
65. J. N. Canongia Lopes, J. Deschamps and A. A. H. Pádua, *J. Phys. Chem. B*, 2004, **108**, 2038-2047.
66. J. N. Canongia Lopes and A. A. H. Pádua, *J. Phys. Chem. B*, 2004, **108**, 16893-16898.
67. J. N. Canongia Lopes, A. A. H. Padua and K. Shimizu, *J. Phys. Chem. B* 2008, **112**, 5039-5046.
68. W. L. Jorgensen, D. S. Maxwell and J. Tirado-Rives, *J. Am. Chem. Soc.*, 1996, **118**, 11225-11236.
69. E. J. Maginn, *Acc. Chem. Res.*, 2007, **40**, 1200-1207.
70. W. Smith, T. R. Forester and I. T. Todorov, ed. T. D. P. m. s. package, STFC Daresbury Laboratories, , Warrington , UK, 2007, p. The DL_POLY molecular simulation package.

IV

Chapter 4

Nanoparticle Catalysis in Imidazolium Ionic Liquids

The influence of size on catalytic performance

Chapter 4

Nanoparticle Catalysis in Imidazolium Ionic Liquids
The influence of size on catalytic performance

4.1 Introduction

Transition metal nanoparticles (NPs) of 1–10 nm in size exhibit physical-chemical properties intermediate to those of the smallest element from which they can be composed and those of the bulk material.[1-3] In catalysis, the performance (activity and selectivity) of NPs is often said to be related to their size, as this controls the number of corner, edge and face atoms available for adsorption and activation of substrates.[4-9]

For example, depicted in Figure 1 are crystalline NPs of a face centred cubic crystal structure adopting a truncated octahedral shape. A given substrate will coordinate differently to each of the different sites labelled. The relative numbers of each site varies with the size of the NPs, hence the reactivity varies.

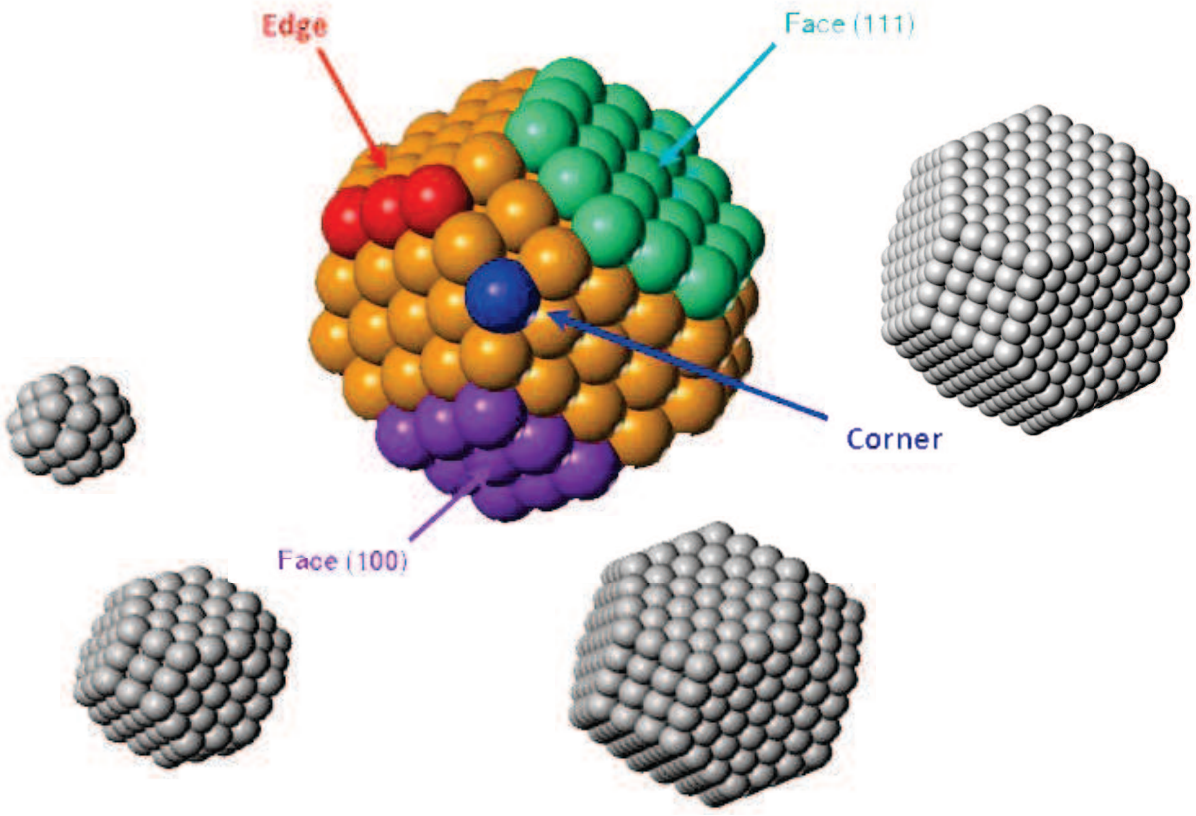

Figure 1. Simplified model of NPs of metals adopting an fcc crystal lattice.

4.1.1 The influence of size on activity

First of all, the catalytic activity may be related to the size. For example, a study of ammonia synthesis over Fe single crystals found an increase in turnover frequency, TOF, with

increasing size, which was attributed to the greater availability of the (111) face, the most active site for this reaction.[10] The activity in CO hydrogenation of supported RhNPs with hcp structure has been found to increase drastically with NP size, due to the larger number of steps on the surface. [11] In contrast, in ethane hydrogenolysis to methane over Pt nanoparticles, the turnover rate has been shown to decrease with particle size while activation energy increases, indicating that the more unsaturated vertex and/or edge positions are responsible for activity.[12]

4.1.2 The influence of size on selectivity

When several different products are possible, selectivity becomes an important issue. This has been shown to vary with particle size. For instance, the hydrogenation/dehydrogenation of cyclohexene over PtNPs has been shown to exhibit size-dependent selectivity, smaller NPs favouring benzene production, Figure 2.[13]

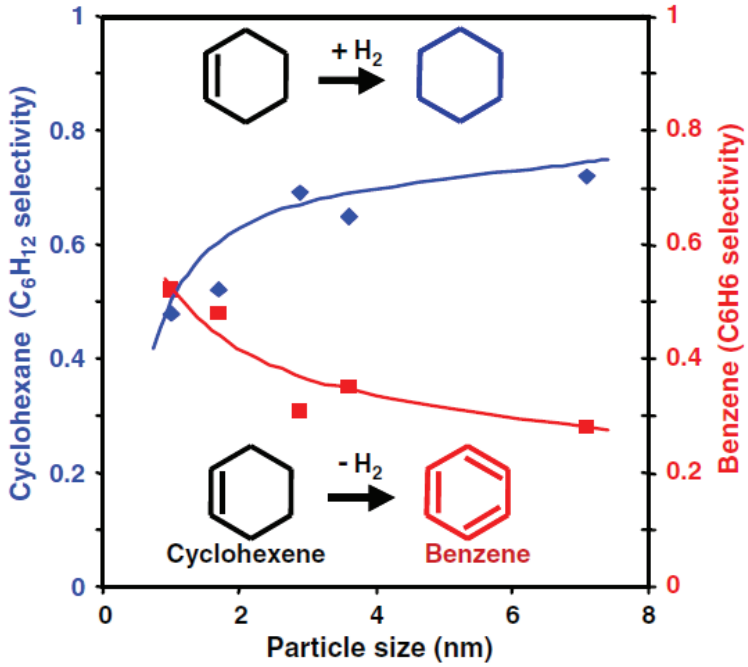

Figure 2. The size dependence of Pt nanoparticles on the selectivity of cyclohexene hydrogenation/dehydrogenation.

Furthermore, it has also been reported in a study of the hydrogenation of benzene over Pt, that on the (111) face cyclohexane and cyclohexene are produced, whereas on the (100) face only cyclohexene is produced. This result implies that cubic NPs, exhibiting uniquely (100) faces, would produce selectively cyclohexene in the hydrogenation of benzene.[6, 13]

From the results mentioned above and many more examples in the literature,[6] it is clear that the size of NPs can be a deciding factor in catalytic processes. Nonetheless, the synthesis of nanoparticles (NPs) with a controlled size in the range of 1–10 nm in order to corroborate this theory is a challenging issue.[14] The aim of this chapter is to use the ionic liquid route to synthesise catalytically active RuNPs of distinct and controlled sizes, and thus investigate thoroughly the consequences of changing NP size on the catalytic process, in particular hydrogenation.

4.2 Catalyst synthesis and characterisation

It has been previously demonstrated that the size of RuNPs generated from the decomposition of (η^4-1,5-cyclooctadiene)(η^6-1,3,5-cyclooctatriene)ruthenium(0), [Ru(COD)(COT)] under H_2, may be governed by the degree of self-organisation of the imidazolium based ionic liquid in which they are formed: the more structured the ionic liquid, the smaller the size.[15] In the same IL, the organisation and structure may be altered by simply altering the experimental conditions, i.e. temperature and stirring. Therefore, following these principles and previously described methods, RuNPs were synthesised at 0 °C, 25 °C, 50 °C and 75 °C in an attempt to obtain a selection of mono-disperse sizes of RuNP in the same IL. The IL chosen is 1-butyl-3-methylimidazolium bis(trifluorosulphonyl)imide, $[C_1C_4Im][NTf_2]$.

4.2.1 TEM

Analysis of the suspensions obtained by transition electron microscopy, TEM, allowed determination of the sizes obtained; 1.1 ± 0.2 nm, 2.3 ± 0.3 nm, 2.9 ± 0.4 nm and 3.1 ± 0.7 nm, for RuNPs generated at 0 °C (Ru_0), 25 °C (Ru_{25}), 50 °C (Ru_{50}) and 75 °C (Ru_{75}), respectively, Figure 3. As can be seen from the TEM image of Ru_{75} and the consequent size distribution histogram, Figure 4, the size of these NPs does not vary significantly compared to those of Ru_{50} although a poorer size control (wider distribution) is apparent. For this reason, these NPs are not used in catalytic tests. High resolution electron microscopy, HREM, revealed the crystalline nature of the RuNPs formed through elucidation of the crystal planes. For Ru_0, only a larger NP of ≈ 2 nm was observed by HREM, probably due to the difficulty in observing the smallest NPs with limited contrast, although this may be indicative of a lower degree of crystallinity in very small RuNPs, as already observed by reverse Monte Carlo simulations.[16]

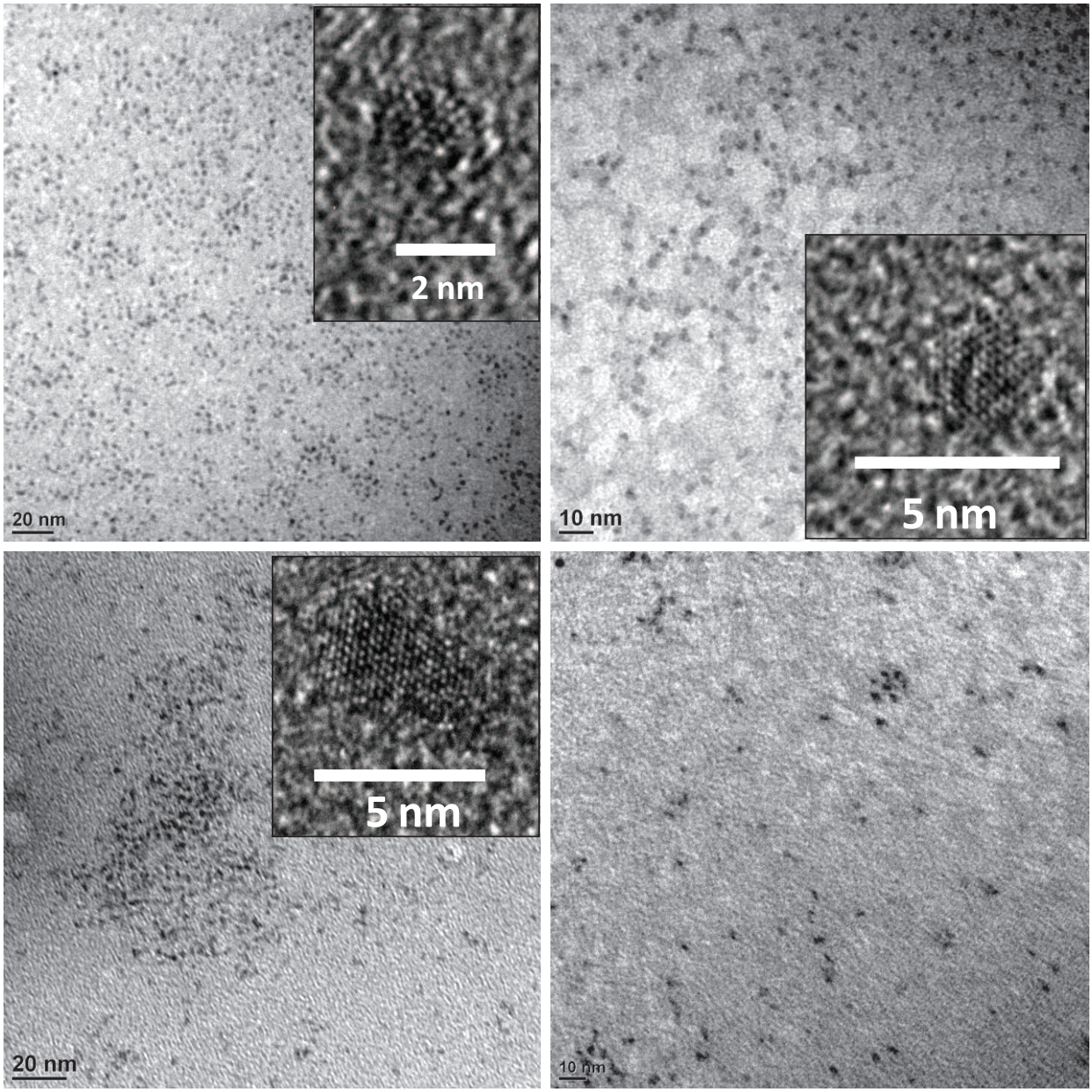

Figure 3. Transition electron micrograph of RuNPs and high resolution electron micrograph examples showing crystallinity for Ru_0 (top left), Ru_{25} (top right), Ru_{50} (bottom left) and Ru_{75} (bottom right).

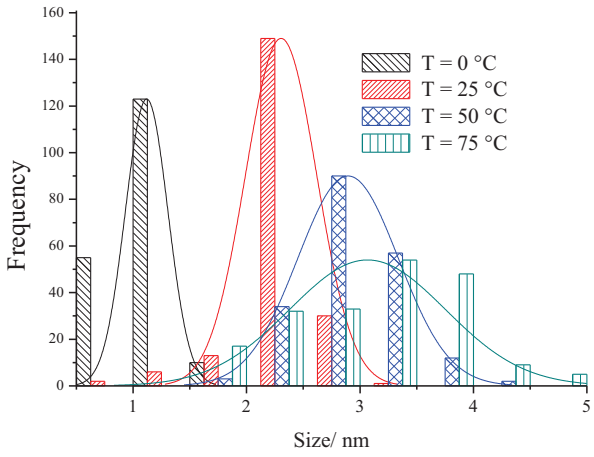

Figure 4. Size distribution histograms for RuNPs prepared in $[C_1C_4Im][NTf_2]$ at different temperatures.

4.2.2 X-ray photoelectron spectroscopy

In order to establish the oxidation state of the RuNPs, X-ray photoelectron spectroscopy, XPS, was performed. Due to the weak concentration of the solution and the fact that the only photoelectrons from a maximum depth of 10 nm may be detected, no peaks corresponding to Ru binding energies were observed when the analyses were carried out directly on the RuNP/IL solutions. Samples were therefore prepared by filtering the RuNPs onto silica under inert atmosphere and eliminating as much IL as possible. The resulting spectra of the Ru 3p region are depicted in Figure 5. It is clear that in each case, fine peaks are observed, indicating the presence of only one Ru species. The low $3p_{3/2}$ binding energy observed in each case, 460.3 eV, and doublet separation of 22.2 eV correspond closely to metallic zero-valent ruthenium, often reported with a $3p_{3/2}$ binding energy of around 461 eV.[17] The small difference may be attributed to the presence of small crystallites, which tend to exhibit lower binding energies than bulk metal. Indeed, as recently shown for AuNPs,[18] the d-band narrows with decreasing particle size and shifts towards the Fermi level.

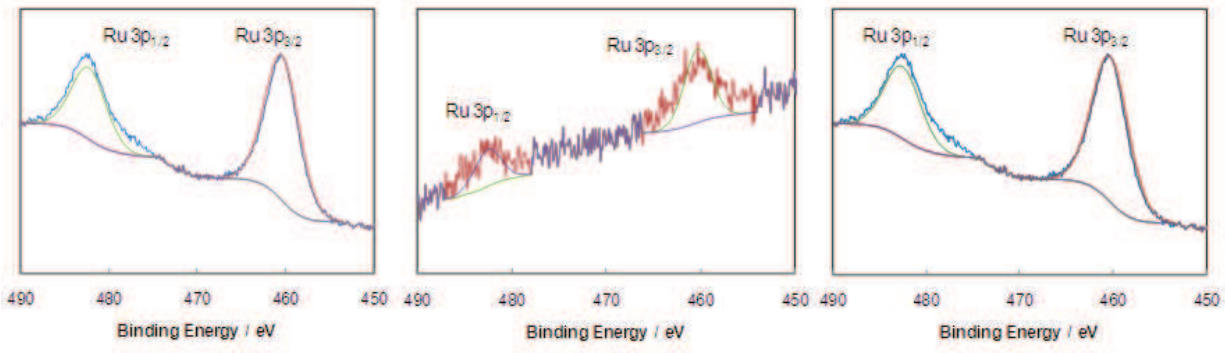

Figure 5. XPS spectra of the Ru 3p region after NP filtration onto SiO_2, experimental data and fitted peaks. Left Ru_0, middle Ru_{25} and right Ru_{50}.

4.2.3 Ru_s concentration

In order to investigate uniquely the effect of changing NP size on catalysis all other variables must remain unchanged. Therefore maintaining constant the initial ratio of substrate to catalyst is imperative. In NP catalysis, as in heterogeneous catalysis, only the atoms at the surface (Ru_s) take part in reaction. The dispersion (D) presents the ratio between surface atoms, Ru_s and the total number of atoms, Ru_T ($D = Ru_s/Ru_T$) and varies with the size of the NPs, smaller particles of course having a larger percentage of surface atoms. The different dispersion values must therefore be taken into account for each size of nanoparticle formed.

Ruthenium is known to exhibit a hexagonal close-packed crystal structure, with the following lattice parameters: a: 270.59 pm b: 270.59 pm c: 428.15 pm α: 90° β: 90° γ: 120°.[19] Using these parameters, SYBYL software can be applied to extrapolate the lattice until the measured diameters, in order to model the structure of the different size NPs, assuming crystallinity. It is seen that crystalline hexagonal close-packed RuNPs would adopt a truncated hexagonal bipyramid form, with two symmetric hexagonal faces (0001) and twelve irregular and uneven trapezoid faces ($10\ \bar{1}1$).[20] From these findings a curve of D with respect to diameter can be plotted and then used to estimate D for each size of nanoparticle, Figure 6.

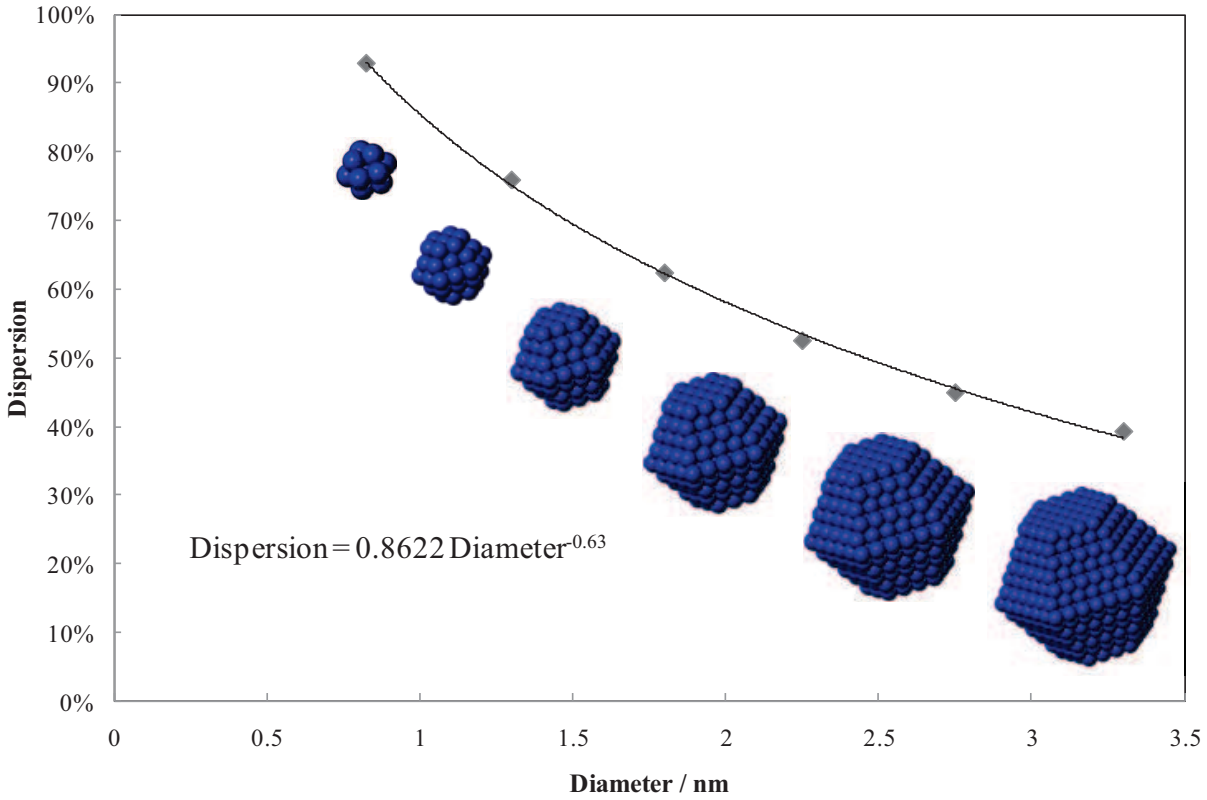

Figure 6. Curve of dispersion against mean diameter of crystalline hcp RuNPs.

4.3 Substrate

The substrate principally investigated is the conjugated diene, 1,3-cyclohexadiene (CYD). It has been shown that in ionic liquid media CYD may be partially hydrogenated with high selectivity by molecular catalysts due to the reduced miscibility of cyclohexene (CYE) in the medium.[21-23] Full hydrogenation would lead to cyclohexane (CYA), Scheme 1.

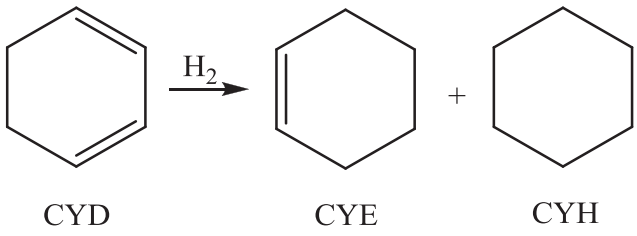

Scheme 1. 1,3-cyclohexadiene and its hydrogenation products.

4.3.1 Solubility

The solubilities of the substrate and potential products may play an important role in the activity and/or selectivity of the system. For example, selective hydrogenation of butadiene to butenes has been performed by Dupont's group in ionic liquids due to the difference in solubility

of the partially hydrogenated product.[24] The same group has also described the possibility of extracting cyclohexene during benzene hydrogenation using this solubility difference.[25] For this reason, solubilities of CYD, CYE and CYA were measured. It was found that the solubility of the hydrogenated products (6 ± 1 % wt - CYE, 4 ± 1 % wt- CYA) is much lower than that of CYD (12 ± 2 % wt), therefore the medium may tend to a biphasic system during the course of the reaction. As a result, the collection of aliquots from a single batch would render inaccurate results. Consequently, each measure of conversion recorded in this work, hence each point plotted, corresponds to a separate experiment, quenched after time *t* by opening the reaction vessel to air, thus releasing the hydrogen, and dissolving the catalytic system entirely in a 1 molar solution of toluene in acetonitrile for gas phase chromatography.

4.3.2 Viscosity

Thermophysical properties of the reaction medium such as density and viscosity may also influence the catalytic performance. As demonstrated in Chapter 3, and by others, reaction kinetics in IL media are highly dependent on the mobility of molecules.[21,26-28] Furthermore, knowledge of the viscosity is very important from engineering point of view as it plays a major role in stirring, mixing and pumping processes. Consequently, identical concentrations of substrate must be used in each case in order to maintain constant viscosity and eliminate effects due to mass transport. The densities and viscosities of the pure $[C_1C_4Im][NTf_2]$ and that of the mixtures with CYD were measured at different molar ratio CYD/IL (*R*) at 25 °C and atmospheric pressure. The results are presented in Table 1.

Table 1. Density, ρ, and viscosity, η, of CYD-IL mixtures of different compositions at 298 K and atmospheric pressure. x_{IL}= molar fraction of IL, R = molar ratio CYD/IL

R	x_{IL}	ρ/g cm^{-3}	η/mPa s
0.000	1.000	1.4376±0.0001	48.5±0.4
0.100	0.909	1.4202±0.0001	44±1
0.200	0.833	1.3999±0.0001	37.0±0.4
0.300	0.769	1.3874±0.0003	33.3±0.3
0.397	0.716	1.3718±0.0001	31.0±0.3
0.498	0.667	1.3597±0.0001	24.8±0.3

As can be seen, the viscosity of the mixtures of CYD in IL varies greatly with the concentration of CYD. From the Stokes-Einstein equation, the diffusion coefficient, *D*, which reflects the mobility of molecules, varies inversely with η, equation (1), see Chapter 3.

$$D = \frac{kT}{\theta \pi \eta r_H} \qquad (1)$$

For the purpose of our investigations the concentration of CYD is fixed at 10 % wt. (corresponding to a molar ratio $R = 0.59$), which is lower than the limit of solubility, limiting phenomena due to formation of a biphasic system. According to results reported in Chapter 3, a molar ratio of $R = 0.59$ gives a perfectly "sticking" medium for which the Stokes-Einstein equation (1) is followed with the Sutherland coefficient, $\theta = 6$.

4.4 Catalysis mixture preparation

Table 2. Calculations for the composition of the catalytic systems. Column 1- Name of catalyst, Column 2- Average RuNP diameter measured by TEM, Column 3- Calculated dispersion, Column 4- Initial Ru(COD)(COT) concentration, Column 5- Consequent Ru_s concentration, Column 6- Volume of IL/RuNP solution ,Column 7- Volume of pure IL added, Column 8- Consequent number of moles of Ru_s in the 5 mL mixture, Column 9- mass of IL, Column 10- mass of substrate, Column 11- Substrate-Catalyst ratio, Column 12- Substrate-IL ratio.

1	2	3	4	5	6	7	8	9	10	11	12
	d/nm	D	[Ru]/ mmol L	[Ru_s]/ mmol L	Vol. IL-RuNP solution/ mL	Vol. IL pure/ mL	Ru_s / 10^{-5} moles	m IL/ g	m CYD/ g	CYD/Ru_s	CYD/IL
Ru_0	1.1	82%	43.0	35.2	2.42	2.58	9.52	7.0	0.78	105	0.59
Ru_{25}	2.3	53%	43.0	22.9	3.74	1.26	9.52	7.0	0.78	105	0.59
Ru_{50}	2.9	43%	43.0	18.5	5.00	-	9.52	7.0	0.78	105	0.59

In Table 2, are collected all data concerning the hydrogenation of CYD. In columns 1-3, size and dispersion values of (Ru_0), (Ru_{25}), (Ru_{50}) are reported. Given the concentration of NP precursor (column 4) and the size of NPs generated (column 2), it is possible to calculate the concentration of Ru_s for Ru_0, Ru_{25} and Ru_{50} (column 5). The more concentrated solutions of Ru_s (Ru_o and Ru_{25}) can be easily diluted to match the least concentrated (Ru_{50}) by simple addition of the appropriate amount of pure IL (columns 6 and 7), resulting in identical quantities of Ru_s

(column 8). Identical concentrations of substrate may then be used, below the limit of solubility to avoid demixing (10 % wt) (columns 9 and 10), permitting as a result both a constant substrate-catalyst ratio (column 11) and a constant substrate-IL ratio (column 12) hence constant viscosity.

Using solutions prepared as described, the reaction was carried out in parallel in several 0.5 mL batches under 1.2 bars of pure molecular hydrogen, which were stirred and heated with the aid of a thermostatic carousel, ensuring identical reaction conditions.

4.5 Influence of NP size on catalytic activity

4.5.1 1,3-cyclohexadiene

It can be seen in Table 3 that the largest NPs (2.9 nm) are the most active in the hydrogenation of CYD, activity decreasing with decreasing size.

Table 3. Conversion and selectivity for the hydrogenation of CYD

	Pressure H_2 / bar	Conversion at 90min	Selectivity CYE	TON	TOF / h^{-1}
Ru_0 (1.1 nm)	1.2	66±5 %	97 %	70±5	46± 3
Ru_{25} (2.3 nm)	1.2	75±5 %	86 %	79±5	53± 3
Ru_{50} (2.9 nm)	1.2	83±5 %	80 %	87±5	58± 3

In a similar fashion, the three sizes of RuNP were tested in the catalytic hydrogenation of other substrates to determine whether this size-related activity could be generalised.

4.5.2 Cyclohexene

To establish whether or not a difference in activity is also apparent in the case of a monoene, the hydrogenation of cyclohexene (CYE) to cyclohexane (CYA) was studied. The results tabulated in Table 4 show that the larger NPs are indeed more active, however the difference in activity is less substantial than in the case of the conjugated diene CYD, and falls within experimental error.

Table 4. Conversion for the hydrogenation of CYE

	Conversion at 90min	TON	TOF / h^{-1}
Ru_0 (1.1 nm)	61± 5 %	64± 5	43± 3
Ru_{25} (2.3 nm)	64± 5%	67± 5	45± 3
Ru_{50} (2.9 nm)	67± 5 %	70± 5	47± 3

4.5.3 Limonene

The naturally occurring terpene, (*R*)-(+)-limonene, or 1-methyl-4-isopropenyl-1-cyclohexene, Lim, was also chosen as a substrate. This molecule is also a non-conjugated diene as can be seen in Scheme 2.

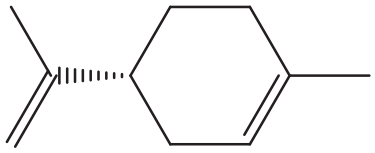

Lim

Scheme 2. (*R*)-(+)-limonene.

Kinetic tests for the hydrogenation of Lim were carried out in the same way as those for CYD, using this time only 5 % wt. of substrate with respect to the IL, due to its lower solubility in the medium. Mixture compositions are given in Table 5.

Table 5. Compositions of the catalytic systems for the hydrogenation of limonene and conversion after 120 minutes

	d/nm	D	[Ru]/ mmol L^{-1}	[Ru_s]/ mmol L^{-1}	Vol. IL-RuNP solution/ mL	Vol. IL pure/ mL	Ru_s / 10^{-5} moles	mass IL/ g	mass Lim/ g	Lim/Ru_s	Lim/IL	Conversion at 120 mins %
Ru_0	1.1	82%	43.0	35.2	2.42	2.58	9.52	7.0	0.37	28	0.16	90%
Ru_{25}	2.3	53%	43.0	22.9	3.74	1.26	9.52	7.0	0.37	28	0.16	88%
Ru_{50}	2.9	43%	43.0	18.5	5.00	-	9.52	7.0	0.37	28	0.16	92%

At 30 °C, after 2 hours of reaction ~ 90 % of Lim was converted in each case, Table 5. Here, no remarkable difference in activity is apparent.

4.5.4 Styrene

The hydrogenation of styrene, Sty, affords either a partially (ethylbenzene, EBn) or fully hydrogenated product (ethylcyclohexane, ECYA) (Scheme 3). Generally, the hydrogenation of the olefinic position is faster than the aromatic ring.

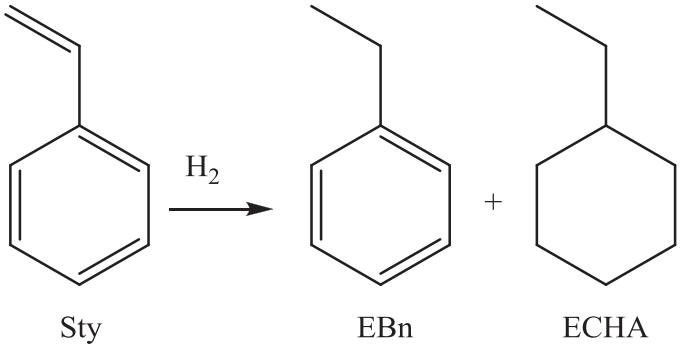

Scheme 3. The possible products from the hydrogenation of styrene.

As for CYD, CYE and Lim, kinetic tests for the hydrogenation of Sty were carried out using the three differently sized RuNPs produced in the ILs. Mixture compositions and conversions are given in Table 6.

Table 6. Compositions of the catalytic systems for the hydrogenation of styrene and conversion after 120 minutes.

	d/ nm	D	[Ru]/ mmol L^{-1}	[Ru_s]/ mmol L^{-1}	Vol. IL-RuNP solution/ mL	Vol. IL pure/ mL	Ru_s / 10^{-5} moles	mass IL/ g	mass Sty/ g	Sty /Ru_s	Sty/ IL	Conversion at 120 mins%
Ru_0	1.1	82%	43.0	35.2	2.42	2.58	9.52	7.0	0.78	81	0.45	60 %
Ru_{25}	2.3	53%	43.0	22.9	3.74	1.26	9.52	7.0	0.78	81	0.45	60 %
Ru_{50}	2.9	43%	43.0	18.5	5.00	-	9.52	7.0	0.78	81	0.45	63 %

At 30 °C, the hydrogenation of the external double bond in each case was rapid, leading to 70 % conversion after 2 h in all cases. Selectivity for EBn remained at 100% for all sizes of NP. As was the case for limonene and CYE, at 30 °C, no significant size effect was observed.

4.5.5 Comparison of the substrates

According to literature results, the catalytic activity of NPs depends on their size, and generally reaches a maximum for those of around 3 nm.[29,30] Here, only a size effect on activity

was observed for the case of CYD. The fact that the hydrogenation of CYD is faster with larger NPs can be related to two factors:

1) Larger NPs present the appropriate number of neighbouring surface sites to facilitate the π-bond activation of the conjugated system.[31]
2) Through this π-bonding activation, similarly to benzene, 1,3-cyclohexadiene would lose part of its resonance energy and react more readily.[20]

The coordination of monoenes such as CYE or the olefinic bond of styrene does not necessitate large surfaces, explaining the less pronounced size effect in these cases.

In the case of limonene, unlike in CYD, the double bonds are not conjugated and so a planar π-coordination to disrupt conjugation is not energetically advantageous, hence the result is similar to that of a monoene.

4.6 Influence of NP size on catalytic selectivity

4.6.1 1,3-cyclohexadiene

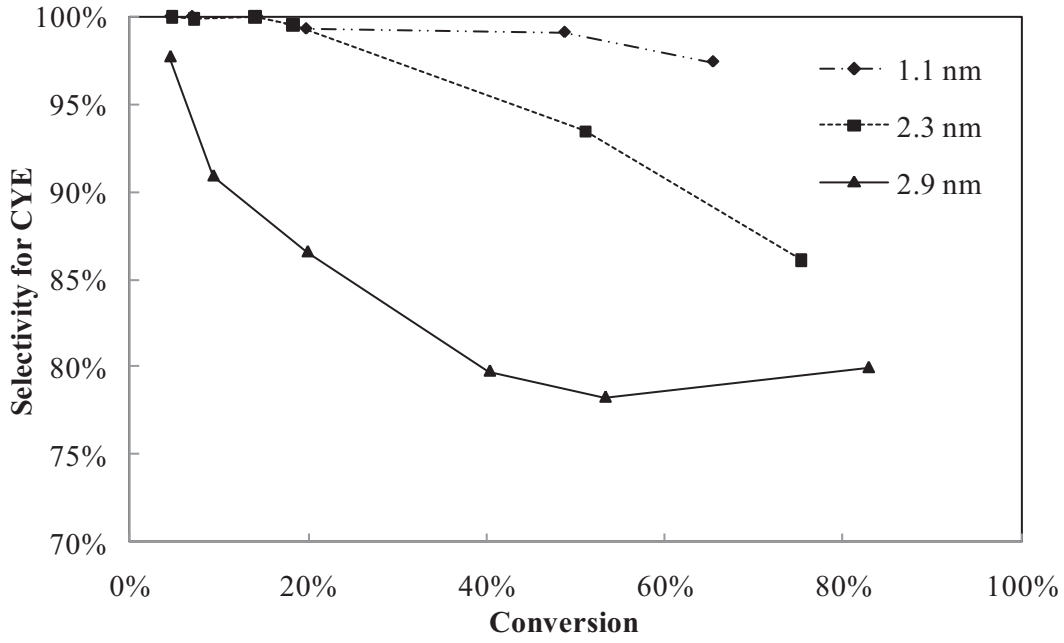

Figure 7. Selectivity for cyclohexene as a function of conversion for the three different sizes of RuNPs

In the hydrogenation of CYD, CYE is obtained as the major product. Interestingly, the selectivity for CYE diminishes with increasing NP size. Indeed, in the case of Ru_0, selectivity for CYE is 100% at low conversion and only slightly diminishes at high conversion (97%). In contrast, for Ru_{50} the hydrogenation is unselective even at low conversion (Figure 7).

Assuming highly crystalline particles with hcp structure, a particle of diameter 1.1 nm would have the vast majority of catalytic surface atoms occupying vertex or edge positions. Such vertex ruthenium atoms Ru_v, which under H_2 atmosphere are ligated by hydrides,[32] may coordinate one C=C double bond of CYD. The product of the subsequent hydrogenation is CYE, which must undergo a second coordination to give the fully hydrogenated CYA. Similarly, for a larger particle of average diameter 2.9 nm assuming high crystallinity and a hcp structure, it is evident that most of the catalytically active surface ruthenium atoms are found in facial positions, Ru_f. Indeed, here such crystallinity has already been observed by HREM, Figure 1. Ru_f may hydrogenate the olefin using the mechanism previously discussed, but due to the planar arrangement of Ru_f, another mechanism may be envisaged involving the double coordination of the diene, as generally found during the hydrogenation of 1,3-cyclohexadiene on metallic surfaces,[33,34] and thus rapid consecutive or simultaneous hydrogenation of both double bonds leading to the fully hydrogenated CYA may be possible. In Figure 8 are represented simplified SYBYL models of CYD molecules coordinating to the surface of perfectly crystalline RuNPs of calculated average diameter 1.3 nm and 2.8 nm. This illustrates nicely the greater facility of planar coordination to faces of the larger NPs. Through this π-bonding activation similarly to benzene, 1,3-cyclohexadiene would lose part of its resonance energy and react more readily. This could explain the lower selectivity of the larger RuNPs despite identical reaction conditions. Likewise, in the hydrogenation of 1,3-butadiene or 1-hexyne the selectivity of small NPs towards 1-butene or 1-hexene versus butane or hexane is still higher than that of larger NPs.[31, 33-35] In this work, in the hydrogenation CYD the selectivity in CYE versus CYA drops from 97% to 80% when the RuNP size increases from 1.1 to 2.9 nm.

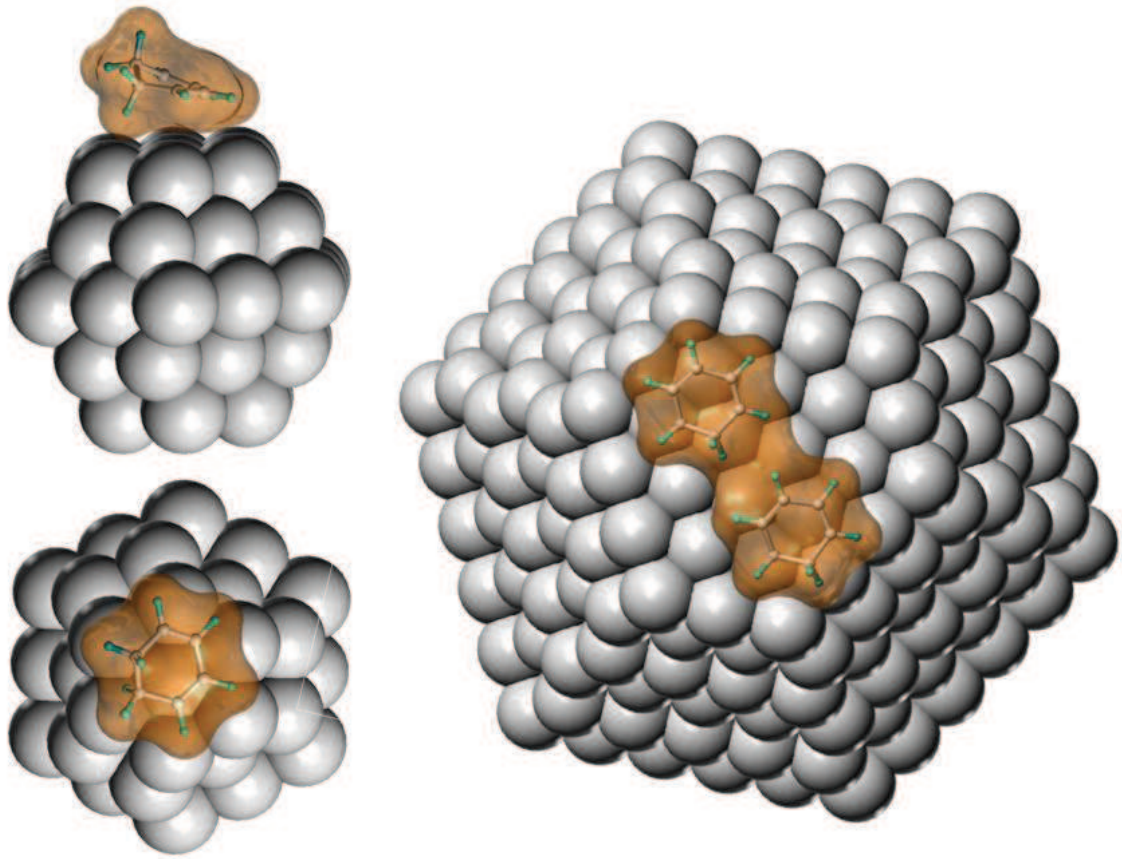

Figure 8. SYBYL representations of CYD coordinated to the face of highly crystalline RuNPs of mean diameter 1.3 nm (left) and 2.8 nm (right)

4.6.2 Limonene

Limonene, containing two double-bonds, both inside and outside of the cyclohexene ring, may also yield different products, as depicted in Scheme 4. Complete hydrogenation would yield mixture of *cis*- and *trans*-*p*-menthane, c and d, whereas partial hydrogenation may result in one of the intermediates *p*-1-menthene or 1-methyl-4-isopropenylcyclohexane, a and b. Several groups have reported however, that hydrogenation of the external double bond is preferential, so only *p*-1-menthene is detected as a partially hydrogenated product of this reaction.[36]

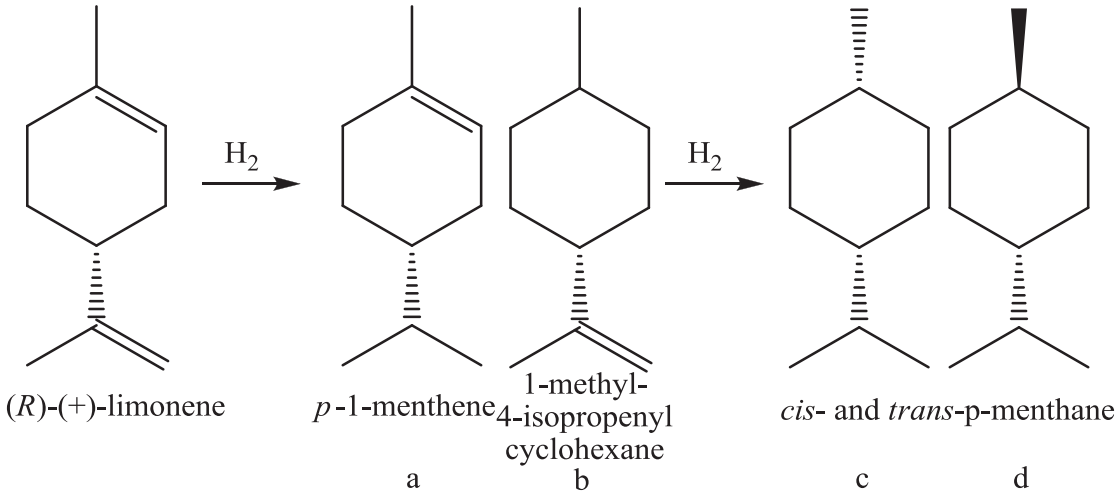

Scheme 4. The possible products resulting from the hydrogenation of limonene.

When the catalytic hydrogenation was performed at 30 °C, high selectivity for the partially hydrated product menthene was observed, although both menthanes are formed slowly over time. As for CYD hydrogenation the selectivity was the poorest in the case of Ru_{50}. Unlike for CYD, 100% selectivity is only observed at very low conversion (≤ 20 %) with Ru_0 (Figure 9).

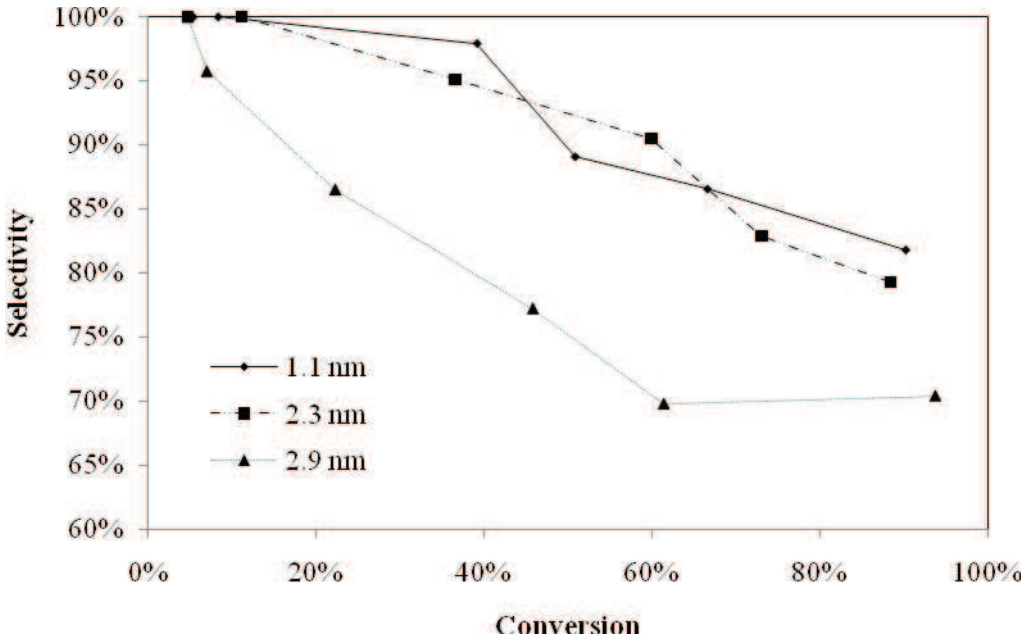

Figure 9. Selectivity for *p*-1-menthene at 30°C as a function of conversion for the three different sizes of RuNPs.

In an attempt to increase the selectivity, the same reaction was therefore performed at low temperature (-2 °C). For all sizes of nanoparticle, the selectivity for menthene is increased

compared to when carried out at ambient temperature. Interestingly the trend of selectivity although poor at the start of the reaction improved between 10 – 20 % conversion, Figure 10. This phenomenon must be due to the start of a biphasic system, thus leading to extraction of the product, inducing a better selectivity as already reported in the hydrogenation of butadiene to butenes,[24] and benzene to cyclohexene.[25]

For the hydrogenation of limonene which contains two non-conjugated double-bonds, the selectivity is NP size-dependent at 30 °C, 100 % selectivity for *p*-1-menthene being observed at low conversion for the smallest NPs. At -2 °C, decreasing the solubility of both substrate and products affords a higher selectivity in all cases, mainly due to the formation of biphasic media.

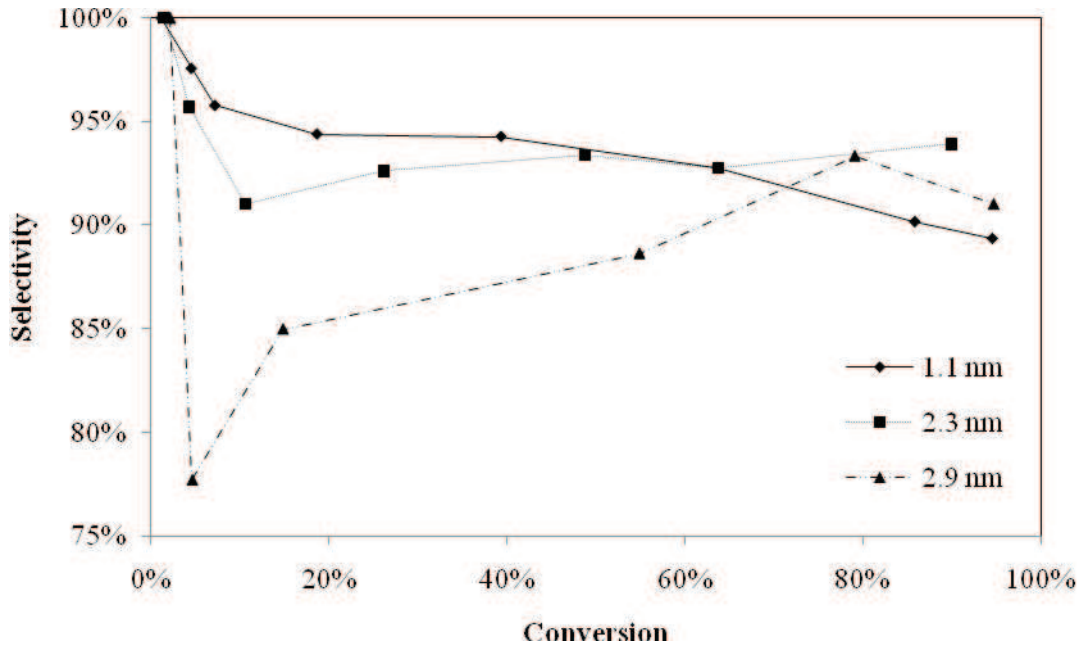

Figure 10. Selectivity for *p*-1-menthene at -2 °C as a function of conversion for the three different sizes of RuNPs.

4.6.3 Styrene

It is often reported that the activity and the selectivity in aromatic hydrogenation are size and face dependant.[4,6,13]

A common probe for chemo-selectivity in the hydrogenation of aromatics is styrene, Sty. Generally, the hydrogenation of the olefinic double bond is faster than the aromatic ring and occurred at 30 °C with 100 % selectivity for EBn, *vide supra*. This is because a greater energy barrier must be overcome when hydrogenating an aromatic compared to an olefin. Therefore to

force the hydrogenation of the aromatic ring, the same reaction must be carried out at higher temperature and for a longer duration, here 75 °C during a period of 6 h.

Once again, the hydrogenation of the external double bond was rapid and occurred quantitatively for each size of NP, Figure 11. Only at 100 % conversion was hydrogenation of the aromatic cycle observed, indicating a successive hydrogenation of the different functions.

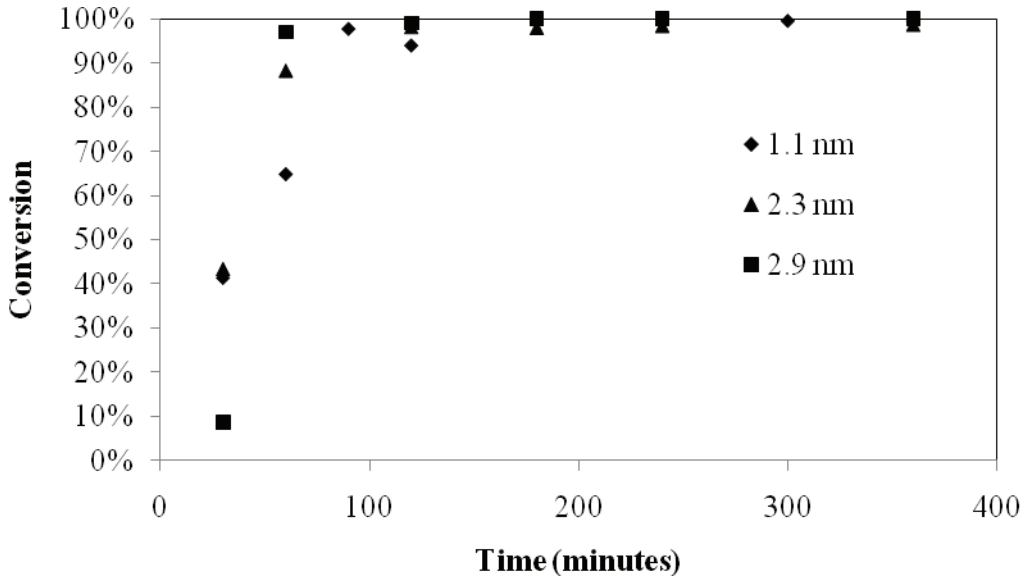

Figure 11. Hydrogenation of Sty at 75 °C under 1.2 bar H_2 in $[C_1C_4Im][NTf_2]$, for three different sized RuNPs.

In Figure 12 is depicted the yield in ECHA with respect to time. Here it can be clearly seen that the full hydrogenation of the aromatic occurs more readily on the large NPs, in agreement with results for the hydrogenation of CYD. Here, a planar coordination is even more crucial, as the inert aromatic ring must lose part of its resonance energy to be activated.[20]

Using styrene as a probe has emphasised the importance of planar π-coordination in aromatic hydrogenation as the larger NPs fully reduced styrene to ethylcyclohexane more readily than the smaller NPs

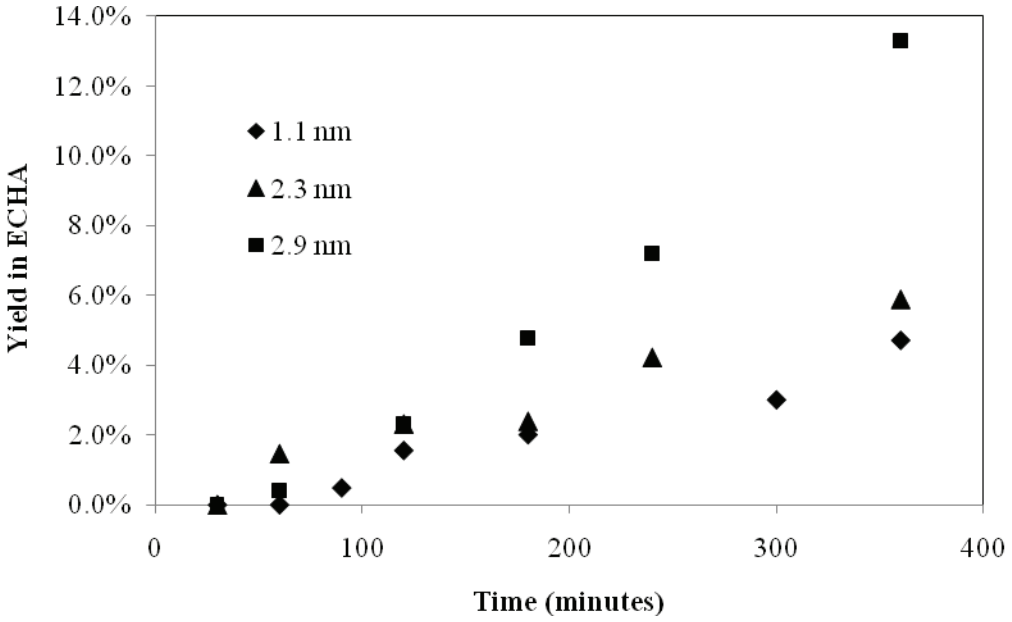

Figure 12. Hydrogenation of Sty at 75°C under 1.2 bar H_2 in $[C_1C_4Im][NTf_2]$, for three different sized RuNPs.

It is also interesting to note that during the course of the reaction small amounts of 1-ethylcyclohexene were produced, and identified by GC-MS: as much as 0.5 % for Ru_0, by the end of the reaction. Indeed the partial hydrogenation of aromatic cycles is an interesting and ongoing challenge and has already been reported in IL media for benzene.[25] It may be interesting in the future to optimise conditions to favour the production and extraction of this molecule from the medium.

4.7 Hydrogen effect

Increasing H_2 pressure to 4 bars in the case of Ru_0 and Ru_{50} is seen to affect neither the activity nor selectivity in a substantial manner, Table 7. It is generally reported that a higher H_2 concentration should not influence the activity of the small particles as the H_2 storage capacity is related to the particle volume and only large particles may experience an increase in availability of subsurface hydrogen.[30] In reality, a slight decrease in activity is observed, possibly indicating that it is the slight enhancement in viscosity with the increase in pressure that controls the mobility of the reactants.[37] This proves that the rate is not dictated by the availability and

adsorption of H_2, in agreement with observations of labile surface hydrides on the NP surface,[32] but the mobility and absorption of the substrate.[21]

Table 7. Results for the catalytic hydrogenation of CYD using Ru_0 and Ru_0 under 1.2 bars and 4 bars H_2

	Pressure H_2 / bar	Conversion at 90 min	Selectivity CYE	TON	TOF / h^{-1}
Ru_0 (1.1 nm)	1.2	66 %	97 %	70	46
Ru_{50} (2.9 nm)	1.2	83 %	80 %	87	58
Ru_0 (1.1nm)	4.0	57%	92%	59	40
Ru_{50} (2.9 nm)	4.0	73%	80%	77	51

4.8 Recycling

TEM images of the reaction media after hydrogenation of CYD show a reorganisation of the NPs, probably due to the presence of organic substrates, poorly soluble in the IL. For Ru_0 and Ru_{25}, circular patterns are present, possibly caused by the formation of aggregates, where the NPs would decorate the organic-IL interface Figure 13. In the case of Ru_{50} phase separation is apparent, which may be indicative of a larger amount of CYE and CYA present as a result of the higher activity and lower selectivity. In all cases, the mean RuNP size measured Table 8 does not differ greatly from the original size, in accordance with the stability of RuNPs in ILs under molecular hydrogen,[32] however the size distribution is larger, probably as an effect of stirring.[15]

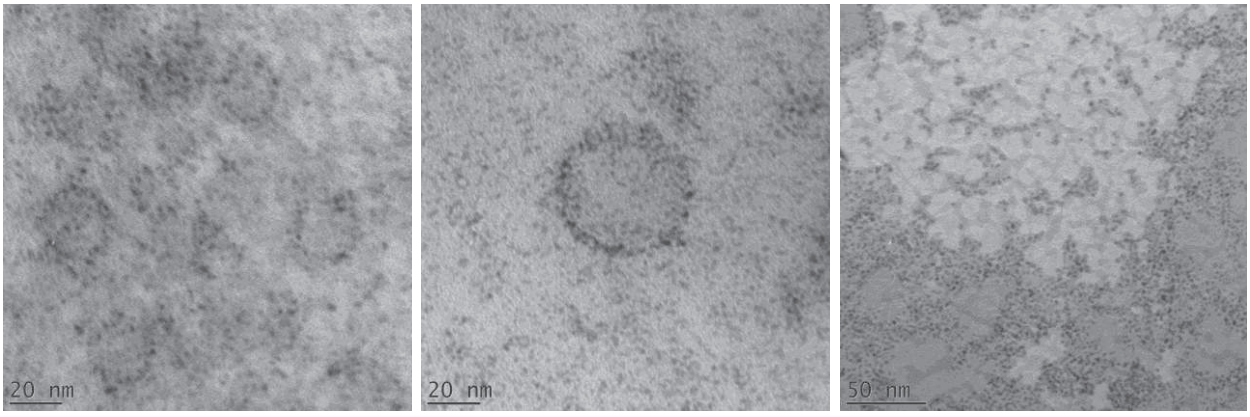

Figure 13. Transition electron micrographs of RuNPs after CYD hydrogenation for Ru_0 (left), Ru_{25} (middle) and Ru_{50} (right)

The apparent resistance to coalescence of the NPs means that they may be tested for their recyclability. Subsequently, using the most selective catalyst, Ru_0, recycling experiments were performed, by extracting *in vacuo* and quantifying the volatiles after each 90 minute run. More CYD was then added for hydrogenation. From the results (Table 8 and Figure 14) it can be seen that the activity and selectivity both remain high after 5 recycles, diminishing only slightly with each run. This small decrease of course is attributable to the gradual coalescence of the NPs, leading to a diminution in the number of active surface sites and larger, less selective NPs. Indeed, TEM images obtained of the NPs after all recycling experiments showed that the NPs had undergone coalescence to attain an average diameter of 1.8 ± 0.5 nm, approaching the size of Ru_{25}, and of course exhibiting a similar selectivity.

Table 8. Results from recycling experiments in the hydrogenation of CYD using Ru_0 and comparison with results obtained for Ru_{25} and Ru_{50}

	Pressure H_2 / bar	Conversion at 90 min	Selectivity CYE	TON	TOF / h^{-1}	Size after catalysis / nm
Ru_0 (1.1 nm)	1.2	66 %	97 %	70	46	1.3 ± 0.4
Ru_0 recycle 1	1.2	73 %	95 %	76	51	-
Ru_0 recycle 2	1.2	69 %	94 %	73	49	-
Ru_0 recycle 3	1.2	68 %	89 %	71	47	-
Ru_0 recycle 4	1.2	64 %	86 %	67	45	-
Ru_0 recycle 5	1.2	65 %	86 %	68	45	1.8 ± 0.5
Ru_{25} (2.3 nm)	1.2	75 %	86 %	79	53	2.1 ± 0.5
Ru_{50} (2.9 nm)	1.2	83 %	80 %	87	58	2.7 ± 0.5

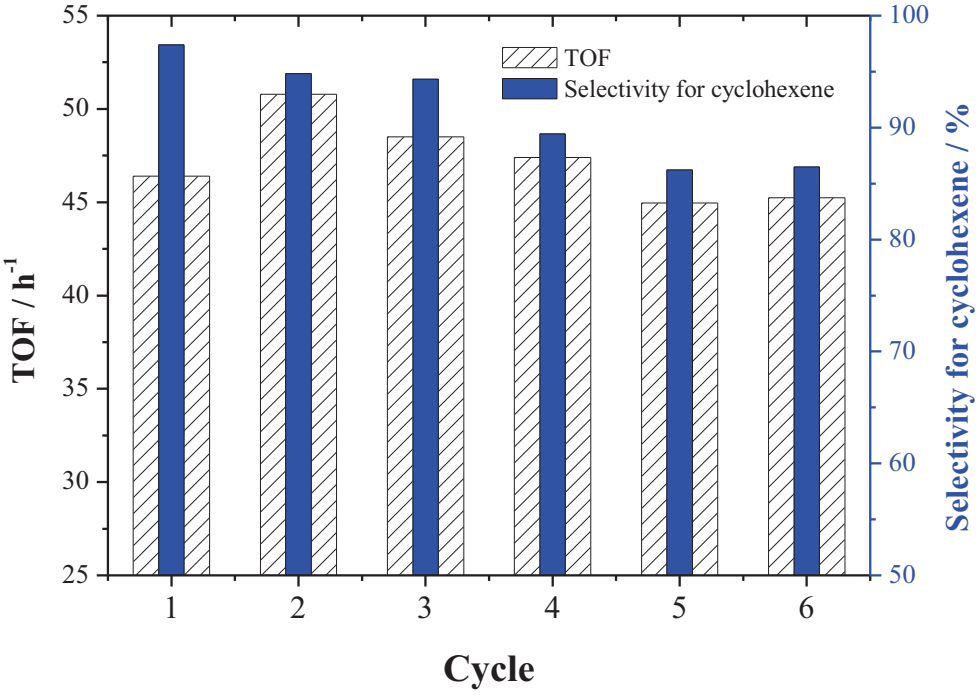

Figure 14. Evolution of TOF and selectivity with catalyst recycling

4.9 Conclusion

In this chapter, the catalytic hydrogenation in $[C_1C_4Im][NTf_2]$ of 1,3-cyclohexadiene (CYD), cyclohexene (CYE), limonene (Lim) and styrene (Sty) have been used as probes for the relationship between size and catalytic performance of RuNPs.

Firstly, tailor-made, size-controlled and zero-valent RuNPs (1 to 3 nm) were generated from the decomposition of [Ru(COD)(COT)] under H_2 in $[C_1C_4Im][NTf_2]$, by varying the experimental conditions. RuNPs were fully characterised *in situ* by TEM and HREM to determine their sizes and demonstrate their degree of crystallinity, and *ex situ* by XPS to verify their zero oxidation state.

Secondly, all catalytic reaction compositions were carefully calculated in order that all parameters except particle size were maintained constant, *i.e.* Ru_s concentration, substrate/Ru_s ratio and substrate/IL ratio, the latter governing solvation phenomena and mass transfer factors (viscosity and diffusivity).

For the hydrogenation of Lim, as for Sty, the effect of NP size on activity is not significant. However, the selectivity is NP size-dependent at 30 °C, 100 % selectivity for *p*-1-menthene being observed at low conversion (≤ 20 %) for the smallest NPs – Ru_0.

Conversely, it was found that for catalytic hydrogenation of CYD, the activity of catalyst increases with the NP size in agreement with the literature results on heterogeneous catalysts. Contrarily to activity, in the hydrogenation of CYD, the selectivity for CYE versus CYA drops from 97 % to 80 % when the RuNP size increases from 1.1 to 2.9 nm.

Both results, activity and selectivity, are in agreement with a mechanism involving a π-bond activation and a double coordination of diene substrates, necessitating several neighbouring surface atoms only found in facial positions on the larger NPs. Furthermore, these RuNPs show a high level of recyclability with neither loss of activity nor significant agglomeration.

4.10 Outlooks

A commonly reported advantage to generating NPs in ILs is that the resulting surfaces are ligand free, and therefore the potential in catalysis is maximised. However, certain ligands may have an important electronic effect on the catalyst. In our laboratory, we have recently reported a synthesis of RuNPs involving amine ligands in ionic liquids, giving very small NPs (1.2 nm) with a narrow size distribution, active in aromatic hydrogenation at 75 °C without coalescence.[38] It is planned therefore to compare the catalytic performance, i.e. activity, selectivity and recyclability of ligated and ligand-free NPs.

The partial hydrogenation of aromatics is a challenging issue. The complicated Asahi process, involving a tetraphasic mixture incorporating colloidal ruthenium as the catalyst, is the only industrial process, and can convert benzene to CYE with a yield of 60%.[39] In this work and in similar systems,[25] the partial hydrogenation of aromatics has been reported, using the solvation properties of ILs to extract partially hydrogenated species. Future work is planned to firstly determine whether these species are a result of partial hydrogenation or dehydrogenation of fully hydrogenated species, and then attempt to optimise conditions, for instance using wet ILs, to selectively extract the desired product in higher yields.

4.11 Experimental section

4.11.1 Materials and methods

1,3-cyclohexadiene, styrene and limonene (99% Aldrich) were distilled prior to use. To produce commercially unavailable menthane for characterisation, a 5 mL sample is stirred with 1 mL of Ru_{50}, and heated to 75°C under 4 bars of H_2 during 72h to force complete hydrogenation. Analysis of the products obtained by GC-MS show that no limonene remains. The majority products are the two diastereoisomers of *p*-menthane, and *p*-1-menthene, but also small amounts of previously unobserved menthene isomers, *cis- and trans-p*-2-menthene and *p*-3-menthene, e, f, and g in Scheme 5. This indicates the possibility of alkene isomerisation using RuNPs.

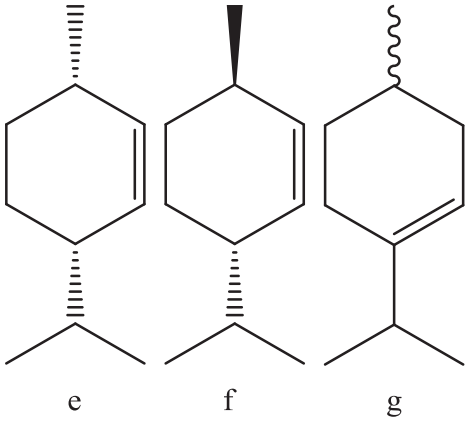

Scheme 5. Side products in the hydrogenation of limonene.

4.11.2 Catalysts synthesis

RuNPs were synthesised as already reported, here varying the temperature of decomposition of [Ru(COD)(COT)]; Ru_0 at 0 °C, Ru_{25} at 25 °C, Ru_{50} at 50 °C and Ru_{75} at 75 °C.[15]

4.11.3 Determination of particle size by TEM

Transmission electron microscopy (TEM) experiments were performed directly in the IL media. A thin film of RuNP solution in IL was deposited on a carbon film supported by a copper grid. Conventional TEM micrographs were obtained at the Centre Technologique des Microstructures, Université Claude Bernard Lyon 1, Villeurbanne, France, using a Philips 120 CX electron microscope with acceleration voltage of 120 kV. Size distribution histograms were constructed from the measurement of at least 200 different nanoparticles assuming a near spherical shape and random orientation. High resolution electron micrographs were obtained at

the "TEMSCAN" centre of the Université Paul Sabatier Toulouse 3, Toulouse, France, using a JEOL JEM 200CX electron microscope with acceleration voltage of 200 kV.

4.11.4 X-ray Photoelectron Spectroscopy (XPS)

X-ray photoelectron spectroscopy was performed in a Kratos Axis Ultra DLD spectrometer, using a monochromatic AlKα X-ray with a pass energy of 20 eV and a coaxial charge neutraliser. The base pressure in the analysis chamber was better than 5×10^{-8} Pa. XPS spectra of Ru3p, C1s, Si2p and O1s levels were measured at a normal angle with respect to the plane of the surface. High resolution spectra were corrected for charging effects by assigning a value of 284.6 eV to the C1s peak (adventitious carbon). Binding energies were determined with an accuracy of ± 0.2 eV. The data were analysed using Casa-XPS (v 2.3.13) employing a Shirley background subtraction prior to fitting and a peak shape with a combination of Gaussian and Lorentzian (30% Lorentzian). High resolution spectra were acquired in the region of Ru 3p as the Ru 3d region overlaps with the C 2p region of the residual ionic liquid.

4.11.5 Catalytic tests

Catalytic solutions were made in a glove box and left stirring for 12 h in a closed system to ensure homogenity. 0.5 mL aliquots were transferred to identical Schlenk tubes containing cross-shaped magnetic stirrer bars. The argon atmosphere was removed and the solution degassed in vacuo whilst cooling in liquid nitrogen (−196 °C). For reactions at 30 °C, 6 of these Schlenk tubes were placed in a thermostatic carousel to ensure identical temperature and stirring conditions. After 30 minutes, when the temperature had stabilised, the Schlenk tubes were opened to 1.2 bars of H_2. After t minutes, a Schlenk tube was isolated and opened to air, releasing the H_2 atmosphere thus stopping the reaction. The solution was entirely dissolved in 10 mL of acetonitrile containing a 1 molar concentration of toluene. The composition of the mixture was determined by gas phase chromatography using toluene as the internal standard. For reactions at 75 °C the same procedure was used as above. For reactions at -2 °C, the Schlenk tubes were cooled independently in a cryostatic bath and stirred. After 30 minutes, when the temperature had stabilised, the Schlenk tubes were opened to 1.2 bars of H_2. After t minutes, a Schlenk tube was isolated and opened to air, releasing the H_2 atmosphere thus stopping the reaction. The solution was entirely dissolved in 10 mL of acetonitrile containing a 1 molar concentration of toluene. The composition of the mixture was determined by gas phase chromatography using toluene as the internal standard.

4.11.6 Product quantification

The products were quantitatively analysed by gas chromatography on a HP-6890 chromatograph equipped with a flame ionisation detector (FID) and a HP-1 (crosslinked methylsiloxane) column (L: 30 m, int: 0.32 mm, film thickness: 0.25 μm). The injector and detector temperature was 270 °C, and the injection volume was 1 μL. The programme was as follows: initial temperature 70 °C for 13.5 minutes; ramp 40 °C/min to 250 °C, hold 2 minutes.

4.11.7 GC-MS

The gas chromatograph was a Focus DSQ from ThermoElectron. Xcalibur software was used for data acquisition and data treatment. The injector temperature was set at 220 °C, the transfer line at 280 °C and the ion source at 200 °C. The analysis was made on a fused-silica capillary column (J&W Scientific), 30 m x 0.25 mm i.d., with DB5-MS stationary phase and a 0.25 μm film thickness. The carrier flow (He) was maintained at 1.2 mL min^{-1}. The column temperature programme was as follows: initial temperature 70°C, maintained for 2 min, then ramped at 15 °C min^{-1} to 310 °C, which was maintained for 10 min.

4.11.8 Density and viscosity

The mixtures of and CYD at different compositions were prepared gravimetrically following the procedure already described.[27] The viscosity of the mixture was measured at 298.15 K (controlled to within ± 0.005 K and measured with the accuracy better than ± 0.05 K) using a rolling ball viscometer from Anton Paar, model AMVn.[27] The overall uncertainty of the viscosity is estimated as ± 2.0 %. The densities of the mixtures, necessary to calculate the viscosities were measured in an Anton Paar vibrating tube densimeter model 512 P, at 298.15 K (measured by a calibrated PRT with an accuracy of ± 0.02 K). The overall uncertainty of the density is estimated as ± 0.01 %.

4.11.9 Solubility

To measure the solubility, 1 mL of the substrate was stirred with the ionic liquid in a closed system at 298.15 K for 12 h then left to settle for a further 2 h. A 0.1 mL sample of the ionic liquid phase was weighed and its composition determined by GC using the procedure described in section 4.11.6. Tests were repeated 4 times for each substrate, to guarantee reproducibilty.

4.12 References

1. M. Valden, X. Lai and D. W. Goodman, *Science*, 1998, **281**, 1647.
2. A. T. Bell, *Science*, 2003, **299**, 1688 –1691.
3. G. Schmid, *Nanoparticles: From Theory to Application*, Wiley-VCH, Weinheim, 2004.
4. K. Lee, M. Kim and H. Kim, *J. Mater. Chem.*, 2010, **20**, 3791-3798.
5. A. Z. Moshfegh, *J. Phys. D: Apply. Phys.*, 2009, **42**, 233001(233032pp.).
6. G. A. Somorjai and J. Y. Park, *Top Catal.*, 2008, **49**, 126-135.
7. H. Boennemann, K. S. Nagabhushana and in *Metal Nanoclusters in Catalysis and Materials Science: The Issue of Size Control* eds. B. Corain, Schmid, G., Toshima, N., Elsevier B.V, Amsterdam, 2008, pp. 21-48.
8. H. Bönnemann, K. S. Nagabhushana and R. M. Richards, in *Nanoparticles and Catalysis*, ed. D. Astruc, Wiley-VCH, Weinheim, 2008.
9. H. Tada, T. Kiyonaga and S. Naya, *Chem. Soc. Rev.*, 2009, **38**, 1849.
10. N. D. Spencer, Schoonmaker R. C and G. A. Somorjai, *J. Catal.*, 1982, **74**, 129-135.
11. M. Ojeda, S. Rojas, M. Boutonnet, F. J. Perez-Alonso, F. J. Garcia-Garcia and J. L. G. Fierro, *Appl. Catal., A* 2004, **274**, 33-41.
12. H. Song, R. M. Rioux, J. D. Hoefelmeyer, R. Komor , K. Niesz, M. Grass, P. D. Yang and G. A. Somorjai, *J. Am. Chem. Soc.* 2006, **128**, 3027-3037.
13. K. Bratlie, H. Lee, K. Komvopoulos, P. Yang and G. A. Somorjai, *Nano Lett.*, 2007, **7**, 3097–3101.
14. D. Astruc, *Nanoparticles and Catalysis*, Wiley-VCH, Weinheim, 2008.
15. T. Gutel, J. Garcia-Anton, K. Pelzer, K. Philippot, C. C. Santini, Y. Chauvin, B. Chaudret and J.-M. Basset, *J. Mater. Chem.*, 2007, **17**, 3290-3292.
16. N. Bedford, C. Dablemont, G. Viau, P. Chupas and V. Petkov, *J. Phys. Chem. C*, 2007, **111**, 18214-18219.
17. R. Nyholm and N. Martensson, *J. Phys. Chem.*, 1980, **13**, L279.
18. J. A. Van Bokhoven and J. T. Miller, *J. Phys. Chem. C*, 2007, **111**, 9245.
19. V. A. Finkel, M. I. Palatnik and G. P. Kovtun, *Phys. Met. Metall.*, 1971, **32**, 231.
20. R. A. Van Santen, *Acc. Chem. Res.*, 2009, **42**, 57-66.

21. P. S. Campbell, A. Podgorsek, T. Gutel, C. C. Santini, A. A. H. Padua, M. F. Costa Gomes, F. Bayard, B. Fenet and Y. Chauvin, *J. Phys. Chem. B*, 2010, **114**, 8156-8165.
22. J. Huang, T. Jiang, B. Han, H. Gao, Y. Chang, G. Zhao and W. Wu, *Chem. Commun.*, 2003, 1654-1655.
23. Y. Chauvin, S. Einloft and B. H. Olivier, *Ind. Eng. Chem. Res.*, 1995, **34**, 1149-1155.
24. A. P. Umpierre, G. Machado, G. H. Fecher, J. Morais and J. Dupont, *Adv. Synth. Catal.*, 2005, **347**, 1404-1412.
25. E. T. Silveira, A. P. Umpierre, L. M. Rossi, G. Machado, J. Morais, G. V. Soares, I. J. R. Baumvol, S. R. Teixeira, P. F. P. Fichtner and J. Dupont, *Chem.--Eur. J.*, 2004, **10**, 3734-3740.
26. T. Umecky, Y. Saito and H. Matsumoto, *J. Phys. Chem. B*, 2009, **113**, 8466-8468.
27. T. Umecky, Y. Saito and H. Matsumoto, *Electrochem. Soc. Trans.*, 2010, **25**, 23-29.
28. M. A. Vorotyntsev, V. A. Zinovyeva and M. Picquet, *Electrochim. Acta* 2010, **55**, 5063-5070.
29. D. Y. Murzin, *Chem. Eng. Sci.*, 2009, **64**, 1046-1052.
30. A. Binder, M. Seipenbusch, M. Muhler and G. Kasper, *J. Catal.*, 2009, **268**, 150-155.
31. N. Semagina, A. Renken and L. Kiwi-Minsker, *J. Phys. Chem. C*, 2007, **111**, 13933-13937.
32. P. S. Campbell, C. C. Santini, D. Bouchu, B. Fenet, K. Philippot, B. Chaudret, A. A. H. Padua and Y. Chauvin, *Phys. Chem. Chem. Phys.*, 2010, **12**, 4217-4223.
33. M. Saeys, M.-F. Reyniers, M. Neurock and G. B. Marin, *Surf. Sci.*, 2006, **600**, 3121-3134.
34. W. L. Manner, G. S. Girolami and R. G. Nuzzo, *J. Phys. Chem. B*, 1998, **102**, 10295-10306.
35. J. Silvestre-Albero, G. Rupprechter and H.-J. Freund, *J. Catal.*, 2006, **240**, 58-65.
36. E. Bogel-Lukasik, I. Fonseca, R. Bogel-Lukasik, Y. A. Tarasenko, M. Nunes da Ponte, A. Paiva and G. Brunner, *Green Chem.*, 2007, **9**, 427-430.
37. A. Ahosseini and A. M. Scurto, *Int. J. Thermophys.* , 2008, **29**, 1222-1243.
38. G. Salas, Santini C. C., K. Philippot, V. Collière, B. Chaudret and B. Fenet, *Dalton Trans., submitted* 2010.
39. H. Nagara, *Appl. Surf. Sci.*, 1997, **121/122**, 448-451.

Conc

General Conclusion

General Conclusion

This thesis focuses on the peculiar physical-chemical properties of imidazolium based ionic liquids – more precisely, how we may exploit these properties in catalysis and how they may influence the outcome of the catalytic process. In this respect, the following two important factors were predominantly investigated:

1. The specific solvation properties of ionic liquids (ILs) – How may these be utilised to generate and stabilise *in situ* catalytically active metal nanoparticles (NPs) of controlled size?
2. The distinctive thermophysical properties of ILs (viscosity and diffusivity) – What is the influence on catalytic activity in both homogeneous and NP catalysis performed *in situ*?

First of all, a review of the most significant literature results in the synthesis and catalytic applications of ruthenium nanoparticles (RuNPs) highlighted the dependence of the catalytic properties on their size and surface properties. The ability to predict and control the size of the NPs produced, is therefore of the utmost importance. Furthermore, producing NPs free of ligands and other surface contaminants can only be advantageous in catalysis. Decomposition of organometallics under H_2 presents the advantage of producing only inert alkane by-products, easily removed under vacuum, while the use of ILs produces stable NPs of controlled size without the need for stabilising additives. Marrying these two techniques leads to a route to stable NPs of controlled size, with maximum surface availability. Consequently, throughout this work, NPs are produced by the decomposition of organometallic complexes under H_2 in ILs.

It has previously been explained that the phenomenon of crystal growth of RuNPs, generated *in situ* in imidazolium-based ILs from Ru(COD)(COT), is controlled by the size of non-polar domains created by the grouping of lipophilic alkyl chains and segregated by a rigid 3-D network of ionic channels. However, no information was available to explain the remarkable stability of the resulting systems. Is the RuNP surface really contaminant-free?

In this work, we have brought to light firstly the close proximity of the RuNPs to the non-polar R group of the cation, through *in situ* labelling experiments (deuteration and reduction), thus corroborating the hypothesis that the RuNPs are located within these non-polar pockets. Addition of water, destroying the ionic network, induces agglomeration of the RuNPs,

supporting the fact that the RuNPs are originally isolated within non-polar pockets by the 3-D network of ionic channels. Secondly, the presence of surface hydrides and their role in the stabilisation of the nanoparticles is demonstrated. The stabilisation mechanism is thus analogous to that described in colloidal organic solutions.

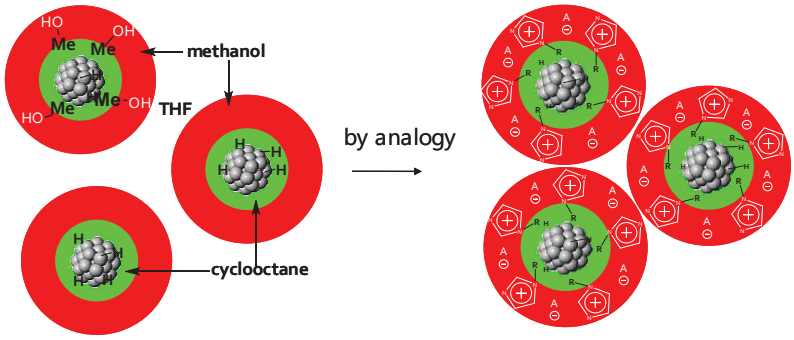

Literary results give conflicting views on the mechanism for the growth and stabilisation of transition metal nanoparticles in ionic liquids, leading to the conclusion that this depends on the nature of the metal, its precursor complex, the synthetic route and/or the ionic liquid used. This led to the question of whether the same would be true of NPs generated in the same way from an analogous organometallic compound of another metal. For this reason, we have also investigated the possibility of generalising these findings to the generation of nickel nanoparticles, NiNPs, as the organometallic complex bis(1,5-cyclooctadiene)nickel, $Ni(COD)_2$, analogous to Ru(COD)(COT), is commercially available.

The synthesis of NiNPs from $Ni(COD)_2$ under H_2 (4 bar) was carried out in various imidazolium based ionic liquids at 0 °C and 25 °C. Imidazolium cations substituted with longer chains $[C_1C_6Im][NTf_2]$, $[C_1C_8Im][NTf_2]$ and $[C_1C_{10}Im][NTf_2]$, were found to offer fairly good media for the preparation and stabilisation of nickel nanoparticles. NiNP size increased with increasing chain-length and in this way we were able to control NiNP size. Additionally, upon decreasing the reaction temperature to 0 °C, we were able to produce smaller NiNPs than those produced in the same IL media at 25 °C. The presence of surface hydrides on these NiNPs, as on RuNPs, has been evidenced by hydrogenation of ethylene in the absence of hydrogen. The resulting NiNPs in these ILs were found to be larger than RuNPs produced in the same media. This can be largely attributed to differences in the nucleation and growth processes for the two metals.

Unexpectedly, spontaneous decomposition of $Ni(COD)_2$ occurred without the addition of hydrogen upon dissolution into imidazolium ILs with short alkyl chains; $[C_1C_2Im][NTf_2]$,

$[C_1C_4Im][NTf_2]$ and $[C_1C_1C_4Im][NTf_2]$. In $[C_1C_2Im][NTf_2]$ and $[C_1C_4Im][NTf_2]$, TEM micrographs showed NiNPs of fairly large diameter were formed, as well as sponge-like super agglomerates. In $[C_1C_1C_4Im][NTf_2]$ well dispersed NiNPs are formed. In these cases, an explanation concerning the activation of the acidic protons on the imidazolium ring and the consequent nitrogen heterocyclic carbene formation leading to rapid decomposition of the complex, has been proposed. This is the first case of the use of pure, non-functionalised ILs for the direct decomposition of organometallics.

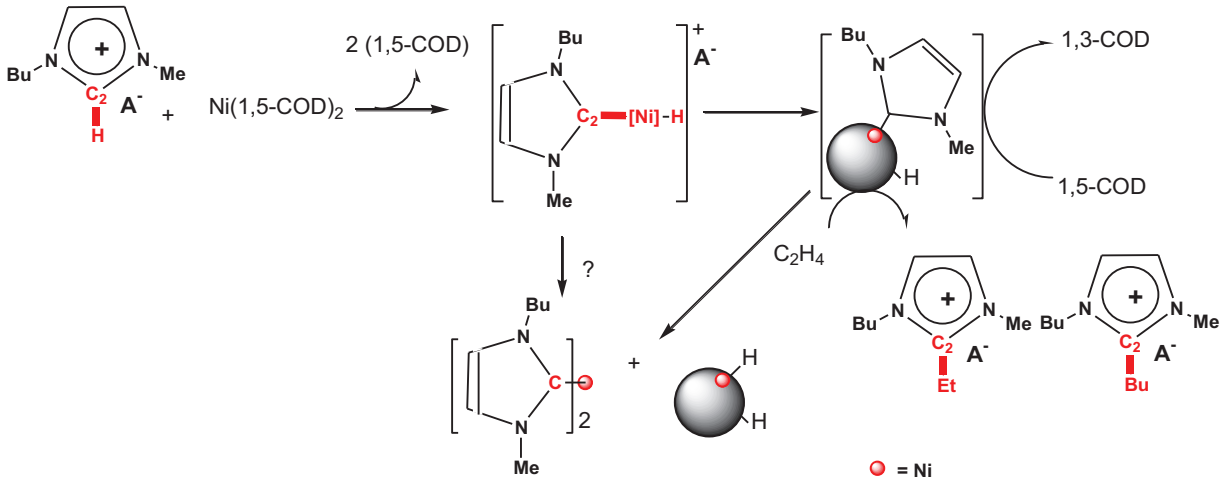

On changing the anion of the IL to the more strongly co-ordinating tetrafluoroborate $[C_1C_4Im][BF_4]$, the acidic protons of the imidazolium ring were protected, and more controlled NiNP formation took place, only in the presence of hydrogen. This medium was therefore successfully used to synthesise NiNPs smaller than 4 nm in diameter, (smaller than previously reported in the literature by chemical methods!)

We have also demonstrated that small monodisperse and zero-valent tantalum nanoparticles, Ta(0)NPs, may be generated under mild conditions, by the decomposition of the organometallic complex tris(neopentyl)neopentylidene-tantalum(V), under H_2 in imidazolium-derived ionic liquids. The control of the size and the factors of stabilisation of these NPs in ionic liquids are currently under investigation. This method has opened up the possibility of facile access to other oxophilic metal nanoparticles, which can **only** be achieved in ILs.

If we are to perform catalysis *in situ* we must understand the role that the ILs may play. Therefore, we have attempted to determine the physical-chemical parameters influencing a model homogeneous reaction, namely the hydrogenation of 1,3-cyclohexadiene (CYD) using an Osborn-type catalyst $[Rh(COD)(PPh_3)_2]NTf_2$ in different ionic liquids; 1-butyl-3-

methylimidazolium bis(trifluoromethylsulfonyl)imide, $[C_1C_4Im][NTf_2]$ and 1-butyl-2,3-dimethylimidazolium bis(trifluoromethylsulfonyl)imide, $[C_1C_1C_4Im][NTf_2]$.

Firstly, the solvation of CYD in the two ILs was investigated by molecular dynamics simulations and ROESY NMR experiments. In both ILs, CYD is found to be located in the lipophilic domains. In $[C_1C_1C_4][NTf_2]$, CYD is found closer to the C_2-Me, whereas in $[C_1C_4Im][NTf_2]$, strong interactions between C_2-H and the anion $[NTf_2]$ do not allow for such proximity.

Secondly, the role of mass transport factors has been studied in both ILs. For this, the viscosity, η, of CYD-IL mixtures of various molar ratios, R = CYD/IL, was measured, and shown to vary radically with R. The viscosity values measured in $[C_1C_1C_4Im][NTf_2]$ were consistently found to be roughly double those measured in $[C_1C_4Im][NTf_2]$.

The chosen model catalytic reaction was the hydrogenation of 1,3-cyclohexadiene (CYD), which occurs in two steps: (1) the ligand exchange $[Rh(COD)(PPh_3)_2]NTf_2$ to $[Rh(CYD)(PPh_3)_2]NTf_2$ (COD=1,5-cyclooctadiene), and (2) the catalytic hydrogenation of CYD itself. It was found that both steps, monitored here by UV-vis spectroscopy, are twice as fast in $[C_1C_4Im][NTf_2]$, implying that the reaction rate is strongly dependent on the viscosity and diffusion of the substrate. In conclusion, when comparing catalytic activity in ILs, the differences in physical-chemical properties must be taken into account, in particular the mass transport factors, which play a decisive role.

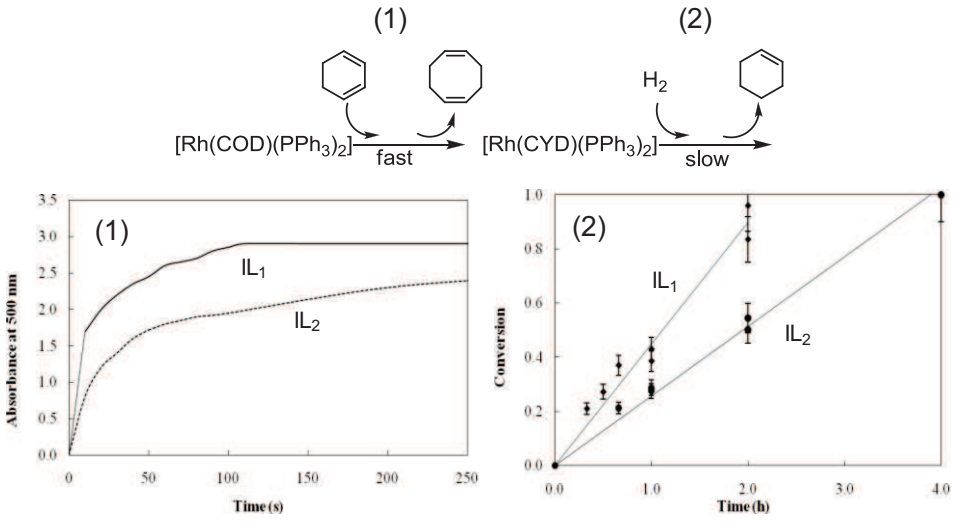

rate $\alpha\ \eta^{-1}$

Finally, the catalytic hydrogenation of 1,3-cyclohexadiene (CYD), cyclohexene (CYE), limonene (Lim), and styrene (Sty) has been used as a probe for the relationship between size and catalytic performance of RuNPs in $[C_1C_4Im][NTf_2]$.

Firstly, tailor-made, size-controlled and zero-valent RuNPs (1 to 3 nm) were generated from the decomposition of [Ru(COD)(COT)] under H_2 in $[C_1C_4Im][NTf_2]$, by varying the experimental conditions. RuNPs were fully characterised, both *in situ* by transition electron microscopy (TEM) and high resolution electron microscopy (HREM), to determine their sizes and demonstrate their degree of crystallinity, and *ex situ* by X-ray photoelectron spectroscopy (XPS), to verify their zero oxidation state. Secondly, all catalytic reaction compositions were carefully calculated in order that all parameters except particle size were maintained constant, *i.e.* Ru_s concentration, substrate/Ru_s and substrate/IL ratios, the latter governing solvation phenomena and mass transfer factors (viscosity and diffusivity).

For the hydrogenation of Lim, as for Sty the effect of NP size on activity is not significant. However, the selectivity is NP size-dependent at 30 °C – 100 % selectivity for *p*-1-menthene observed at low conversion (≤ 20 %) for the smallest NPs.

Nevertheless, it was found that for catalytic hydrogenation of CYD, the activity of the catalyst increases with the NP size in agreement with literature results on heterogeneous catalysts. Contrarily to activity, in the hydrogenation of CYD, the selectivity for CYE versus CYA drops from 97 % to 80 % when the RuNP size increases from 1.1 to 2.9 nm.

Both results, activity and selectivity, are in agreement with a preferred mechanism involving a π-bond activation and a double coordination of diene substrates, necessitating several neighbouring surface atoms only found in facial positions on the larger NPs.

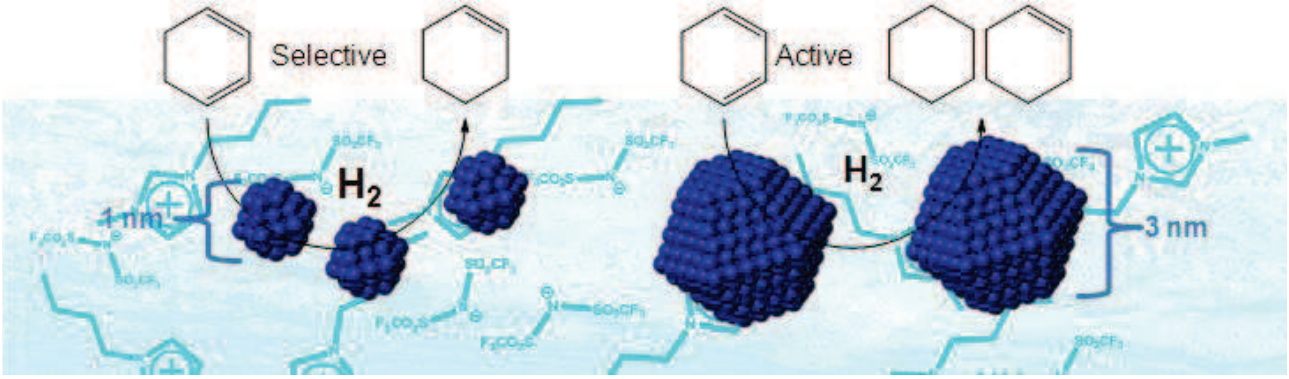

In summary, ILs have been shown to be excellent media for the controlled growth and stabilisation of metal NPs, and the importance of the size control in catalysis has been proven.

Outlooks

During this work, the synthesis and stabilisation of size-controlled RuNPs in imidazolium ionic liquids has been well established and understood. Their use in catalysis has been touched upon using some model reactions, during which, the partial hydrogenation of styrene giving ethylcyclohexene was observed. Although the yield was poor, this is nonetheless an interesting result, as the partial hydrogenation of aromatic cycles to cyclic olefins is an important and challenging industrial process. By investigating further this reaction, in order to understand the mechanism, it may be possible to optimise conditions in order to increase the yield of this interesting product. Is this product a result of partial hydrogenation, or full hydrogenation followed by dehydrogenation? Can we extract this product by using additive containing ILs (e.g. H_2O to alter the thermophysical properties and the solubility or organic moieties)?

It may also be interesting to use these well defined catalytic systems to attempt more interesting catalytic reactions, such as alkane oxidations or nitrogen activation.

Finally, some important and interesting preliminary results have been obtained regarding the possiblility of producing zero-valent NPs of oxophilic metals, such as tantalum. This opens up new innovative pathways to produce nano-objects with reduced process cost and could be of great potential interest in the drive for smaller and more efficient electronic devices. This is currently under development in collaboration with the "*Commissariat à l'Énergie Atomique* (CEA)", and is the subject of two Ph.D. theses.

Appendix 1

Characterisation of Nickel Nanoparticles by XPS

Characterisation of Nickel Nanoparticles by X-ray Photoelectron Spectroscopy

As spontaneous or H_2 induced decomposition of $Ni(COD)_2$ could take place in $[C_1C_6Im][NTf_2]$ depending on the temperature, comparisons of the resulting particles could be made without changing the solvent.

X-ray photoelectron spectroscopy can be used to determine elemental composition and oxidation states in a sample. Due to the weak concentration of the solution and the fact that only photoelectrons from a maximum depth of 10 nm may be observed, no peaks corresponding to Ni binding energies were observed when the analyses were carried out directly on the NiNP/IL solutions. Samples were therefore prepared by filtering the NiNPs onto silica under inert atmosphere and eliminating as much IL as possible. The XPS spectrum in the Ni 2p region for NPs prepared by decomposition under H_2 is shown in Figure 1. It is clear that two species exist, Ni^0 and Ni^{II}.

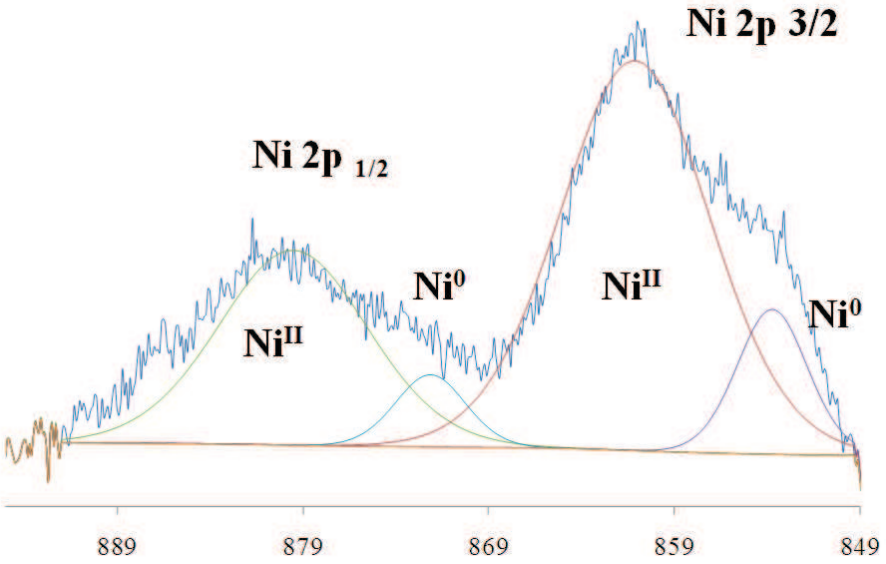

Figure 1. Ni 2p region of XPS spectrum obtained for NiNPs in $[C_1C_6Im][NTf_2]$

The data gathered during XPS analyses are tabulated in Table X. It can be seen that in both cases a large peak is present corresponding to Ni^{II}. It should be noted that when transferring the sample into the sample treatment chamber, it was subjected to air and ambient conditions for a short period of time (< 5 minutes). The high level of oxidation may be a result of air exposure. For this reason we rerun the analyses of the samples after a longer exposure period in air

(~ 5 hours). In the case of NiNPs produced through the H_2 decomposition of $Ni(COD)_2$, the intensity of the Ni 2p bands corresponding to Ni^{II} was greatly increased after prolonged air exposure, where as for the NiNPs produced from spontaneous decomposition, the amount of Ni^{II} remained constant. This could be explained by two factors; 1) the NiNPs produced by spontaneous decomposition exhibit less Ni surface susceptible to oxidation; 2) these NiNPs were already oxidised at the surface by oxidative addition of the imidazolium ring producing carbene ligands.

Table 1. XPS data gathered for NiNPs produced by autodecomposition and H_2 decomposition of $Ni(COD)_2$ in the IL $[C_1C_6Im][NTf_2]$

Sample	**Ni 2p peak**	**2p 3/2**	**2p 1/2**	**Doublet separation**	**Area**	**Ratio $Ni^{(0)}$:Ni^{II}**
(1) Decomposition under 4 bars H_2 at 25 °C in $[C_1C_6Im][NTf_2]$	$Ni^{(0)}$	853.7	873.4	19.7	1134	0.32
	Ni^{II}	861.1	880.8	19.7	3515	
(2) (1) After exposure to air (5 h)	$Ni^{(0)}$	853.7	873.1	19.4	717	0.15
	Ni^{II}	860.8	880.6	19.8	4754	
(3) Decomposition on stirring at 40 °C in$[C_1C_6Im][NTf_2]$	$Ni^{(0)}$	853.9	872.9	19	2265	0.29
	Ni^{II}	861.3	881.1	19.8	7703	
(4) (3) After exposure to air (5 h)	$Ni^{(0}$	853.2	872.8	19.6	3163	0.27
	Ni^{II}	861.3	881.4	20.1	11709	

The results obtained are inconclusive, as we cannot be sure whether the oxidised nickel was due to air exposure or if it already existed in the NiNP/IL mixture. Future tests are planned to run XPS using a system for transferring the sample into the chamber without exposure to air.

Magnetic measurements using a sensitive SQUID (*Superconducting Quantum Interference Device*) may also be useful in characterising the nickel nanoparticles. FC-ZFC (field cooled – zero field cooled) measurements of the magnetisation can be used to find the blocking temperature (T_b) of the superparamagnetic NPs, which may be related to their size. The percentage of non-oxidised Ni^0 may also be estimated from the magnetic hysteresis curve at obtained at low temperature (generally 2 K). This work is currently in progress.

ii

Appendix 2

Publications

Publications

The work reported in this thesis has contributed to the following papers and patents. Copies of the papers can be found in this appendix.

Papers

1) "A novel stabilisation model for ruthenium nanoparticles in imidazolium ionic liquids: in situ spectroscopic and labelling evidence."

P. S. Campbell, C. C. Santini, D. Bouchu, B. Fenet, K. Philippot, B. Chaudret, A. A. H. Padua and Y. Chauvin, *Phys. Chem. Chem. Phys.*, **2010**, *12*, 4217-4223.

2) "How do Physical-Chemical Parameters Influence the Catalytic Hydrogenation of 1,3-Cyclohexadiene in Ionic Liquids?"

P. S. Campbell, A. Podgoršek, T. Gutel, C. C. Santini, A. A. H. Pádua, M. F. Costa Gomes, F. Bayard, B. Fenet and Y. Chauvin, *J. Phys. Chem. B.*, **2010**, *114*, 8156-8165.

3) "Olefin hydrogenation by ruthenium nanoparticles in ionic liquid media: Does size matter?"

P. S. Campbell, C. C. Santini, F. Bayard, Y. Chauvin, V. Collière, A. Podgorsek, M.F. Costa Gomes and J. Sá., *J. Catal.*, **2010**, *275*, 99-107.

4) "Imidazolium ionic liquids as promoters and stabilising agents for the preparation of metal(0) nanoparticles by reduction and decomposition of organometallic complexes."

M. H. G. Prechtl, P. S. Campbell, J. D. Scholten, G. B. Fraser, G. Machado, C. C. Santini, J. Dupont and Y. Chauvin, *Nanoscale*, **2010**, doi: 10.1039/C0NR00574F

Patents

1) "Mémoires et Interconnections à base de Nanotubes de Carbone." Catherine Scampucci (ep. Santini), Jean-Marie Basset, Thibaut Gutel, Paul Campbell, Simon Deleonibus, Paul Haumesser, *Brevet CEA-LETI /Univ Lyon 1 CNRS/LCOMS : Fr 0901464 27/03/09*

2) "Procédé de réalisation d'un dispositif mémoire à grille flottante." Catherine Scampucci (ep. Santini) , Jean-Marie Basset, Thibaut Gutel, Paul Campbell, Simon Deleonibus, Paul Haumesser, *Brevet CEA-LETI /Univ Lyon 1 CNRS/LCOMS :* Fr *0901463 27/03/09*

A novel stabilisation model for ruthenium nanoparticles in imidazolium ionic liquids: *in situ* spectroscopic and labelling evidence†

Paul S. Campbell,[a] Catherine C. Santini,*[a] Denis Bouchu,[b] Bernard Fenet,[c] Karine Philippot,[d] Bruno Chaudret,[d] Agílio A. H. Pádua[e] and Yves Chauvin[a]

Received 1st December 2009, Accepted 8th February 2010
First published as an Advance Article on the web 10th March 2010
DOI: 10.1039/b925329g

In situ labelling and spectroscopic experiments are used to explain the key points in the stabilisation of ruthenium nanoparticles (RuNPs) generated in imidazolium-based ionic liquids (ILs) by decomposition of (η^4-1,5-cyclooctadiene)(η^6-1,3,5-cyclooctatriene)ruthenium(0), Ru(COD)(COT), under dihydrogen. These are found to be: (1) the presence of hydrides at the RuNP surface and, (2) the confinement of RuNPs in the non-polar domains of the structured IL, induced by the rigid 3-D organisation. These results lead to a novel stabilisation model for NPs in ionic liquids.

Introduction

Metal nanoparticles (MNPs) have lately become a new and exciting area of research interest. Defined as particles, whose dimensions are on the nanoscale, they coincide with a transition between bulk and molecular states, and exhibit unique characteristics related to the discontinuities and quantum effects of such a transition, *e.g.* enhanced magnetic and catalytic properties, *etc*. The controlled synthesis of nanoparticles in the range of 1–10 nm is still an ongoing challenge, as is the understanding of their stabilisation and agglomeration.[1–4] Indeed, transition-metal nanoparticles remain only kinetically stable, the thermodynamic minimum being bulk metal. Consequently, substantial effort has been centred on *stabilising* transition-metal nanoparticles. Furthermore, their *formation* and *stabilisation* (inhibition of coalescence) are closely related issues.[3]

In ionic liquids (ILs), particularly those based on the imidazolium cation, NPs can be generated by several physical and chemical routes.[5] Unlike traditional solvents, IL media are able to stabilise nanoparticles in the absence of further additives such as ligands, inhibiting metal agglomeration to the bulk.[6] However, the question of *precisely how* ILs stabilise transition metal NPs remains under debate.

Many papers have claimed possible electrostatic stabilisation by interactions between nanoparticles and weakly coordinating anions, such as $[BF_4]^-$, $[PF_6]^-$, or $[N(SO_2CF_3)_2]^-$,[7,8] all without compelling evidence.[3] Other possible explanations include ligand-type stabilisation by the IL moieties. Indeed, this has been illustrated for IrNPs in an imidazolium based IL, where H/D labelling experiments provided evidence for the formation of *N*-heterocyclic carbenes on the surface of the NPs.[8,9]

Very recently, a relationship between the size of IL non-polar domains calculated by molecular dynamics simulation and the mean diameter of ruthenium nanoparticles (RuNP), (generated *in situ* from the organometallic complex (η^4-1,5-cyclooctadiene)(η^6-1,3,5-cyclooctatriene) ruthenium(0), Ru(COD)(COT), has been found.[10] This suggests that the phenomenon of crystal growth occurs in these non-polar domains of the ILs and is controlled by the local concentration of the precursor complex. This can be supported by the fact that imidazolium-based ILs exhibit an extended hydrogen-bond network in the liquid state and a continuous three dimensional network of ionic channels, coexisting with non-polar domains created by the grouping of lipophilic alkyl chains.[11–13] We can thus hypothesise that the RuNPs are surrounded by these non-polar pockets.

Likewise, some of us have reported "solvent-only" stabilised nanoclusters prepared from the anion-free precursor Ru(COD)(COT) in THF–MeOH.[14] In this work, "nano-reactors" or "pockets" are hypothesised to be formed with cyclooctane (the by-product of the decomposition) in which ruthenium is confined and the particles stabilised, Scheme 1a.[15] Moreover, the same authors have proved the presence and the stability of hydrogen atoms on the surface of RuNPs.[16,17]

By analogy, novel stabilising factors for RuNPs in ILs are reported here, such as the presence of surface hydrides, and their encapsulation and segregation in the non-polar domains of the structured IL induced by the rigid 3-D organisation, Scheme 1b. It is worth noting that "stabilising factors" are often claimed based on *ex situ* methods such as TEM images and XPS experiments performed on **isolated** samples. In contrast, in this work, only *in situ* labelling methods and spectroscopic measurements made directly in the reaction mixture are used to identify these stabilising factors.

[a] *Université de Lyon, Institut de Chimie de Lyon, UMR 5265 CNRS-Université de Lyon-ESCPE Lyon, LC2P2, Equipe Chimie Organométallique de Surface, ESCPE 43 Boulevard du 11 Novembre 1918, F-69616 Villeurbanne, France. E-mail: santini@cpe.fr; Fax: 33(0)472431795; Tel: 33(0)472431794*
[b] *Centre Commun de Spectrométrie de Masse, UCB Lyon 1-ESCPE Lyon, 43 Boulevard du 11 Novembre 1918, F-69616 Villeurbanne, France*
[c] *Centre Commun de RMN, UCB Lyon 1-ESCPE Lyon, 43 Boulevard du 11 Novembre 1918, F-69616 Villeurbanne, France*
[d] *Laboratoire de Chimie de Coordination, UMR CNRS, 205, route de Narbonne, F-31077-Toulouse cedex 04, France*
[e] *Laboratoire de Thermodynamique des Solutions et des Polymères, Université Blaise Pascal, Clermont-Ferrand, 24 av. des Landais, 63177 Aubière, France*

† Electronic supplementary information (ESI) available: Mass spectra and calculations. See DOI: 10.1039/b925329g/

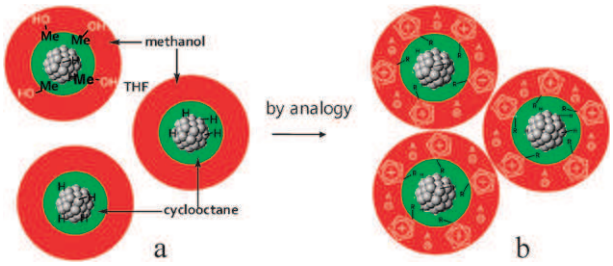

Scheme 1 Stabilisation model for RuNPs in (a) organic solvent and (b) IL.

Results and discussion

The decomposition of (η^4-1,5-cyclooctadiene)(η^6-1,3,5-cyclooctatriene)ruthenium(0), Ru(COD)(COT), by hydrogen is a well known route to obtaining RuNPs, in both organic[18,19] and ionic liquid media.[5,20] The main advantage of this halogen-free synthesis is that the only side product, cyclooctane, is easily removed under vacuum, Scheme 2.

When carried out at low temperatures (0 °C) in the absence of stirring in 1-butyl-3-methylimidazolium bis(trifluorosulfonyl)-imide, [C_1C_4Im][NTf_2], Scheme 3, this method yields very small NPs with a narrow size distribution (mean size: 1.1 ± 0.2 nm calculated from TEM images captured in the ILs).[21] These conditions are replicated throughout this work, obtaining fresh IL-stabilised colloidal solutions, on which NMR and mass spectroscopy experiments are performed, to determine the key points in their stabilisation. Note that no deposition of the RuNP suspension is observed after several months under argon atmosphere.

In situ evidence of surface hydrides

The presence of surface hydrides has already been reported on RuNPs in organic solvent.[16] In heterogeneous catalysis, it is well-known that under hydrogen atmosphere, the noble metal surface is covered by hydrides.[23] In ILs, is such coverage still possible? Given the current and general stabilisation theory concerning NPs in ILs, (strong interaction between the NPs and anion or cation, DLVO model),[1,3] the formation of surface hydrides could be inhibited. Surface hydrides on NPs in ILs have never been reported or envisaged.

1° H/D exchange by gas phase ^{1}H NMR spectroscopy

Due to the low solubility of H_2 in ILs,[22] the remaining H_2 dissolved is totally removed under high vacuum. A solution of freshly prepared RuNPs in C_1C_4Im NTf_2 (IL_1) is, thus, first treated under dynamic vacuum (10^{-5} mbar, 1 or 4 h) and then stirred under deuterium (1 bar at 25 °C, 1 or 4 d). The gas phase is then expanded into a Young NMR tube. The ^{1}H NMR

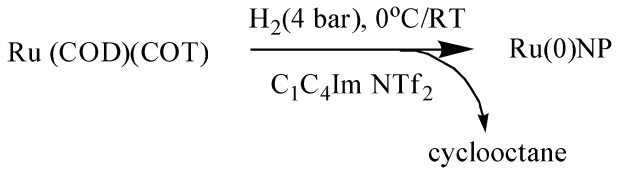

Scheme 2 Generation of RuNPs in IL_1.

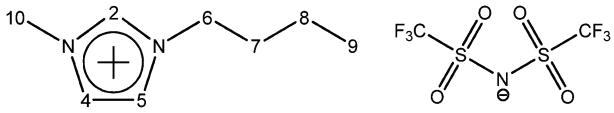

Scheme 3 IL_1: C_4C_1Im NTf_2, carbon numbering of the cation.

spectrum obtained exhibits a broad peak, ($w_{\frac{1}{2}}$ = 1200 Hz) corresponding to H_2, superimposed with a finer peak ($w_{\frac{1}{2}}$ 200 Hz) corresponding to HD, the intensity of which increases with reaction time, then remains constant, Fig. 1a. This is in agreement with previous findings[16] and allows us to assign the HD desorption as resulting from the deuterium activation on RuNPs and recombination with bound H atoms, as observed on metal surfaces.[16,23]

The fact that there is ~60% of H/D exchange on positions 2, 4 and 5 of the imidazolium ring, as proved by ^{1}H and ^{2}H NMR spectra of the IL, Fig. 1b, could suggest that the HD formed is due to this exchange and not from putative surface hydrides. Note that no H/D exchange is observed when IL is treated under D_2 in the absence of RuNPs, and hence, this H/D exchange must involve RuNPs' surface. To prove, therefore, the presence of these surface hydrides, further experiments are performed characteristic of metal surface reactivity, such as hydrogenation.

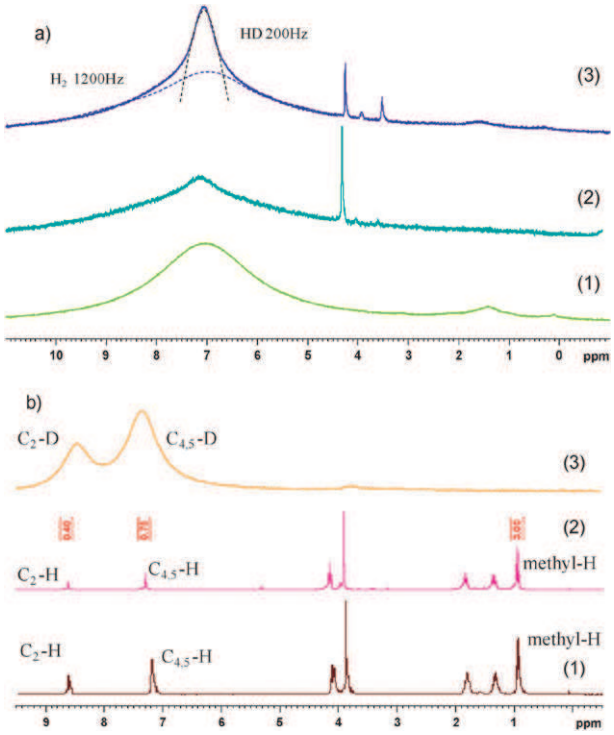

Fig. 1 (**a**) ^{1}H NMR of gas phase (1) pure H_2, (2) gas phase after 1 h dynamic vacuum and 1 d under deuterium, (3) gas phase after 4 h dynamic vacuum and 4 d stirring under deuterium. (**b**) (1) ^{1}H NMR spectrum of IL after NP formation under H_2 and evacuation of H_2 and cyclooctane, (2)^{1}H and (3) ^{2}H NMR spectra of the reaction medium after addition of D_2.‡

‡ H chemical shift of H_2/HD , here 7.1 ppm, is arbitrary as no internal reference was used.

2° Hydrogenation of ethylene

The reaction of alkenes with PVP (polyvinyl pyrrolidone)- and ligand-stabilised RuNPs has recently been used to quantify the surface hydrides.[17] A similar approach is transposed to a solution of RuNPs in IL_1. In the following discussion, the RuNPs are generated in 2 mL of IL_1 from 86 μmol of Ru(COD)(COT). Given that the dispersion of NPs, (*D*, *i.e.* the ratio surface atoms N_s per total number of atoms N_t, $D = N_s/N_t$), is correlated to their size,[24,25] we could estimate that for RuNPs of 1.1 nm the dispersion is 75%, corresponding, for 86 μmol of Ru(COD)(COT), to $N_s \approx 65$ μmol of Ru surface atoms. This IL_1-stabilised RuNP solution is flushed overnight with argon to remove dissolved hydrogen. Then, the solution is stirred under an ethylene atmosphere (105.5 mbar) at 25 °C. After 24 h of reaction, the system reaches equilibrium, *i.e.* the pressure remains constant. In the gas phase, analysed by GC, 11 ± 1 μmol of ethane and 0.1 μmol of *n*-butane are found, corresponding to at least 22 ± 1 μmol of surface hydride : ($C_2H_4 + H_2 \rightarrow C_2H_6$). Note that butenes (*trans*- and 1-) are also observed (0.2 μmol); however, no hydrogen would be consumed in their formation. In summary, IL_1-stabilised RuNPs react with ethylene at room temperature to give ethane (hydrogenation) and surface-bound alkyl species (homologation).[26,27]

To quantify the total amount of surface-bound alkyl species, the gas phase is evacuated and substituted with H_2 (120 mbar), and the medium is heated at 100 °C for 12 h. In the gas phase, methane (4.6 μmol), ethane (8.2 μmol), propane (2.7 μmol), *n*-butane (1.0 μmol) and *n*-pentane (0.1 μmol) are detected, corresponding to at least a further 16 μmol of hydrides. Knowing the total amount of surface Ru atoms available (65 μmol) and the number of surface hydrides consumed in all of the hydrogenation reactions (38 μmol), it is possible to calculate the ratio of hydrides per surface Ru atom: *ca.* 0.6 H per Ru_S, (see supplementary information for calculation†). The combination of these results provides substantial evidence for the existence of surface hydrides on the IL_1-stabilised RuNPs, although the level of error in the quantitative results means that it is difficult to establish accurately the quantity. The amount of H adsorbed on RuNPs is reported to be between 1.1–1.3 H/Ru_S for PVP- and ligand-stabilised in organic solvent,[16] and between 1 and 2 H/Ru_S when supported on oxides.[23] Note that if the IL_1-stabilised solutions of RuNP are treated under high vacuum (10^{-6} mbar) overnight at room temperature instead of being flushed with argon to remove the dissolved H_2, ethylene conversion is negligible.

Indeed, hydrides bound to metal surfaces are labile and the dissociation of H_2 adsorbed on a metal surface is reversible: $M + H_2 \leftrightarrow MH_2 \leftrightarrow 2M–H$. In the case of Ru, about 2/3 of the total amount of surface hydride is reversibly bound. These H species correspond to more weakly adsorbed hydrogen on the surface, which are easily removed by evacuating the sample under vacuum at 25 °C.[23] Consequently, this explains why the hydrogenation (in the absence of hydrogen) of ethylene does not occur with NPs previously treated under high dynamic vacuum (10^{-5} mbar) for an extended period (12 h), because very few surface hydrides remain.[23,28–30]

It is, nevertheless, very interesting that the presence of hydrides on ruthenium particles in ionic liquids is confirmed, since this is in agreement with the presence of these nanoparticles in uncharged lipophilic domains.

Stabilising effect of surface hydrides

In order to ascertain the stabilising effect of hydrogen, two aliquots of the $RuNP/IL_1$ solution are taken and stirred, at 100 °C, for a period of 24 h, either under H_2 or under Ar (1 bar). The resulting solutions are analysed by TEM. For the aliquot heated under H_2, the mean size of the RuNPs increases to 1.4 ± 0.7 nm, and for the aliquot heated under argon, the mean size increases to 2.2 ± 0.8 nm. This difference in size increase with the gas atmosphere proves the inferior stability of the particles when heated under argon compared to under H_2. In addition, when the $RuNP/IL_1$ solution is treated under high vacuum (10^{-6} mbar) overnight at room temperature, the TEM images show an increase in size from 1.1 ± 0.2 nm to 1.7 ± 0.4 nm, Fig. 2. From these results, it appears that there is less coalescence of the RuNPs when heated under H_2 at 100 °C than under argon at the same temperature. This may be explained by the elimination of the hydrogen atoms reversibly bound to the metal surface, which is favoured by heating under an inert atmosphere or treatment under high vacuum. In conclusion, the presence of surface Ru–H stabilises the RuNPs. These stability experiments are also consistent with the lability of the hydrides which can be desorbed from the nanoparticles *in vacuo* or at 100 °C.

Evidence for close proximity between the RuNP surface and the alkyl chains

The fact that in $C_1C_nImNTf_2$, the non-polar domains control the local concentration of Ru(COD)(COT) and consequently the size of RuNPs generated *in situ* could allow us to consider them as nanoreactors in which the phenomenon of crystal growth occurs.[10] If the RuNPs are contained within these non polar pockets, it would imply that the side alkyl groups of the ILs and the RuNP surface are in close proximity or even in interaction with one another.

To demonstrate this, RuNPs are synthesised under deuterium instead of hydrogen (following otherwise identical reaction conditions), since an H–D exchange on the side group of the IL would prove the existence of the NPs in these domains. In the case of IL_1, ^2H NMR spectra show us that, as expected, deuteration occurs at all positions on the imidazolium ring due to the relatively high acidity of these protons. One small peak is apparent at ~1.5 ppm, which may correspond to deuteration at position C_8, *i.e.* the penultimate carbon of the butyl chain; however, this is not irrefutable. The intensities of the peaks in the ^1H NMR spectrum are reduced by roughly 30% at positions C_2, C_4 and C_5, but no significant reduction in intensity is noted for any of the alkyl peaks. ESI mass spectra indicate the formation of mono-, di-, tri- and a trace amount of tetra-deuterated species. This is in agreement with the higher reactivity of the hydrogen bound to the imidazolium ring than to the alkyl side chain. Note that, in contrast to findings for IrNPs,[9] where deuteration was mainly at position

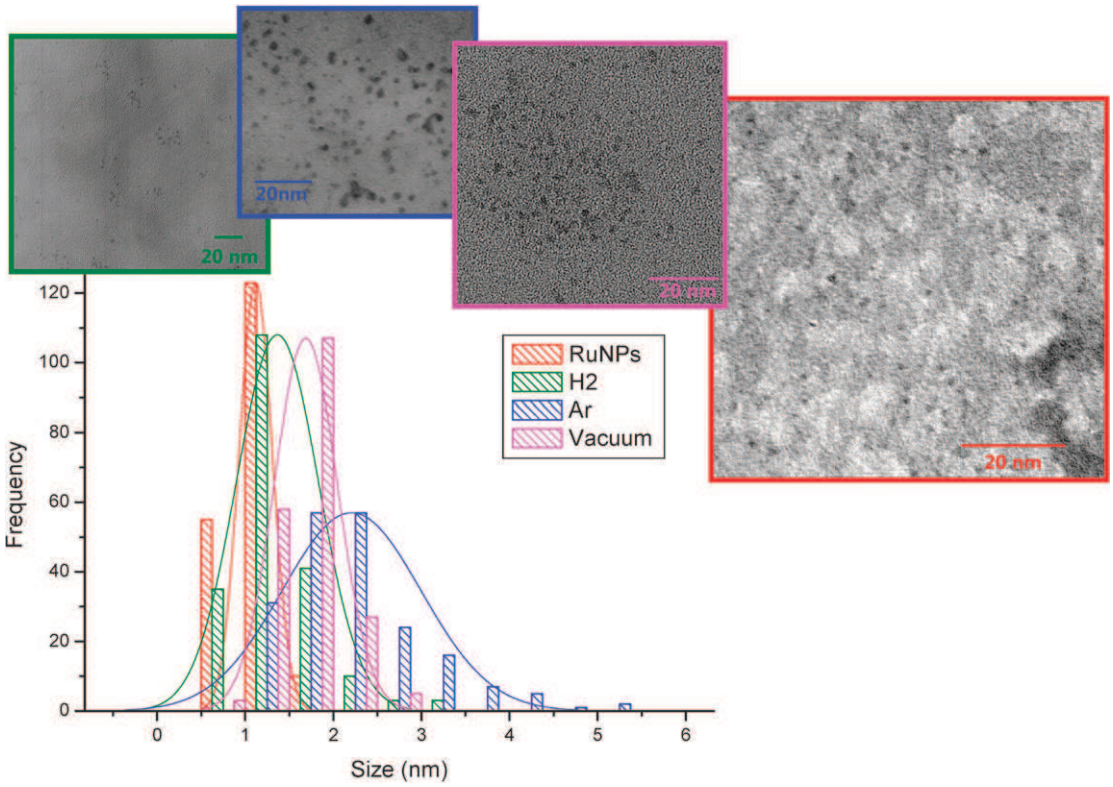

Fig. 2 TEM images captured *in situ* in ionic liquids and comparative size histograms of RuNPs/C_1C_4Im NTf_2 (1.1 ± 0.2 nm) heated to 100 °C for 24 h under H_2, under Ar and kept under dynamic vacuum (10^{-5} mbar) for 24 h at 25 °C.

C_2, for RuNPs deuterium incorporation occurs equally at positions C_2, C_4 and C_5 on the imidazolium ring.

This experiment is then carried out in ILs with unsaturated functional side groups: 1-(but-3-enyl)-3-methylimidazolium bis(trifluorosulfonyl)imide ($C_{4//}C_1Im$ NTf_2), IL_2 and 1-benzyl-3-methylimidazolium bis(trifluorosulfonyl)imide (BzC_1Im NTf_2), IL_3. These functionalised side groups are more susceptible to H–D exchange.

$C_{4//}C_1Im$ NTf_2, IL_2. TEM images of nanoparticles synthesised in IL_2 under deuterium at 0 °C show that the nanoparticle size distribution is similar to that of RuNPs synthesised in IL_1. This result provides supplementary evidence to suggest the size is dictated by the length of the IL's alkyl chain and that the RuNPs are formed in the non-polar domains of the ILs, Fig. 3.

For IL_2, ^2H NMR spectra show that deuteration takes place at positions C_8 and C_9, *i.e.* the olefinic positions, as well as at position C_2. Surprisingly, isotopic exchange is observed neither at positions C_4 and C_5 of the imidazolium ring, nor at positions C_6 and C_{10}. Instead, and more interestingly, a new set of peaks appears at high field, corresponding to a deuterated butyl group due to the deuteration (reduction) of the $C_8{=}C_9$ double bond, Fig. 4. Further heating of this solution under deuterium at 50 °C for 12 h leads to a pronounced growth of all peaks already deuterated, but no deuteration at other positions. The intensities of the peaks in the ^1H NMR spectrum of IL_2 after reaction are reduced significantly at positions C_2, C_8 and C_9, indicating that 24% of the ionic liquid undergoes at least one H–D exchange, and ESI spectra (see the supplementary information†) indicate that a further 15% is

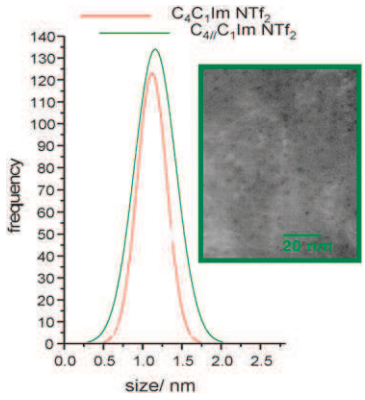

Fig. 3 Comparative size distribution curves for RuNPs synthesised in IL_1 and IL_2, and TEM image captured *in situ* IL for RuNPs synthesised in IL_2

reduced to a deuterated butyl species corresponding to a TON of ~16 with respect to Ru_s, at 0 °C, (see the supplementary information†). Also, besides the peaks due to IL_1 (labelled * in Fig. 5), new peaks appear (labelled ° in Fig. 5) in the C_{sp^2} and C_{sp^3} regions, corresponding to IL_{2isom}, in which there is an isomerisation of the butenyl chain, Scheme 4.

BzC_1ImNTf_2, IL_3. The TEM images of RuNPs synthesised in IL_3 under deuterium at 0 °C show a size distribution centred at 3.2 ± 0.7 nm. The larger size is expected due to the higher degree of supramolecular 3-D organisation of the ILs with the side chain substituted by an aryl group.[31]

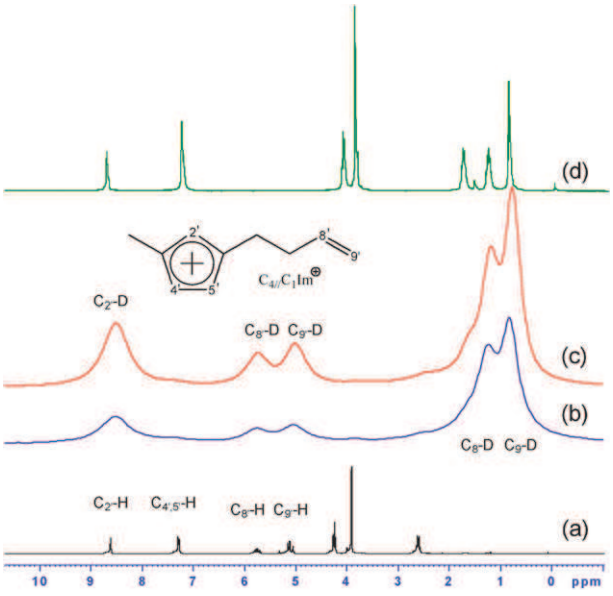

Fig. 4 (**a**) ^{1}H NMR spectra of $C_{4//}C_1Im$ NTf_2, neat IL_2; (**b**) ^{2}H NMR spectra of IL_2 after RuNP formation at 0 °C under deuterium; (**c**) ^{2}H NMR spectra of IL_2 after RuNP formation at 50 C under deuterium; (**d**) ^{1}H NMR spectra of C_4C_1Im NTf_2, neat.

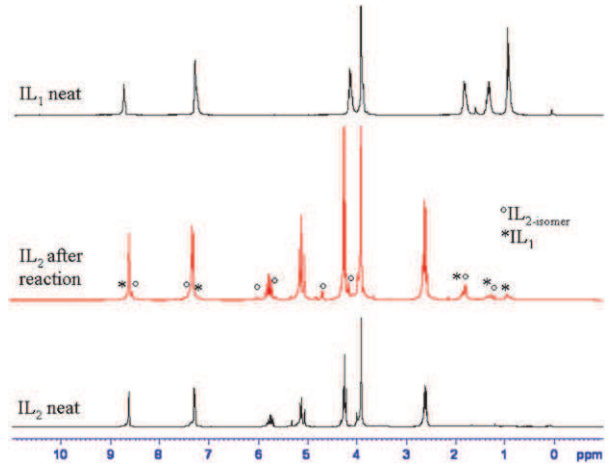

Fig. 5 ^{1}H NMR spectra of neat IL_2; IL_2 after RuNP formation at 0 °C under deuterium; neat IL_1.

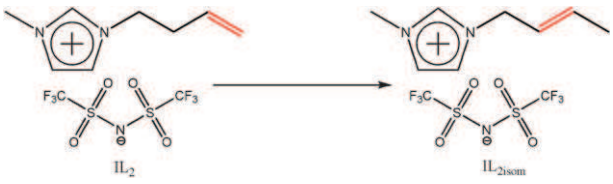

Scheme 4 Isomerisation of IL_2.

In the ^{2}H NMR spectra of IL_3 after reaction, deuterium incorporation at position C_2, and at positions C_4 and C_5 of the imidazolium ring and/or at the aromatic positions is observed. Also, a new set of aliphatic peaks appears at high field centred at 1.4 ppm, corresponding to a reduced methylenecyclohexyl group, Fig. 6. The intensities of the peaks in the ^{1}H NMR spectrum of IL_3 after reaction are reduced at positions C_2, C_4 and C_5, but even more significantly at the aromatic positions, where peak intensity is reduced by 35%. ESI spectra (see supplementary information†) indicate that 60% of the ionic liquid undergoes at least one H–D exchange, 50% of which is transformed into the deuterated methylenecyclohexyl $CH_2C_6D_xH_{11-x}$ form, with a corresponding TON of ~64 with respect to Ru_s. Further heating of this solution under deuterium at 50 °C for 12 h leads to a pronounced growth of all peaks mentioned.

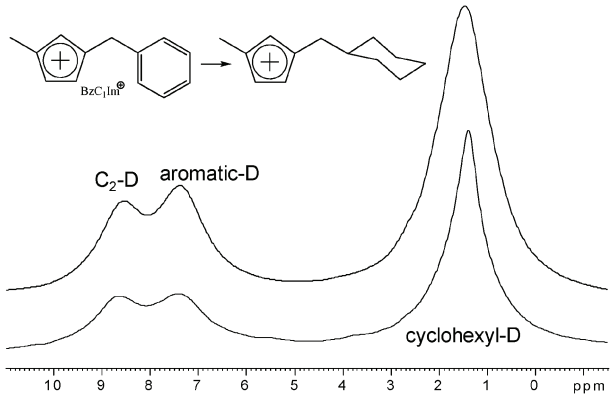

Fig. 6 ^{2}H NMR spectra of BzC_1Im NTf_2, IL_3, after RuNP formation at 0 °C under deuterium (lower) and after a further 12 h of heating to 50 °C under deuterium (upper).

The hydrogenation of an aryl substituent, which does not occur with any molecular ruthenium complexes derived from Ru(COD)(COT), must occur on the nanoparticle surface.[32] This observed reduction, therefore, clearly demonstrates the proximity between the benzyl groups of the IL_3 and the RuNP surface.

During the formation of RuNPs under deuterium in both IL_2 and IL_3, the side groups of the imidazolium rings are saturated with deuterium. In neither case is the C_2 position the primary site for H–D exchange, in contrast to literature results.[9] Furthermore, in the case of IL_2, no exchange is observed at positions C_4 and C_5. Note that no exchange occurs at positions C_6 and C_{10} in either IL. These results indicate that the side chains of the imidazolium are situated in close proximity of the RuNP surface, where activation of the deuterium occurs.

Role of the continuous 3-D network of ionic channels in the isolation of RuNPs

Addition of coordinating substrates, such as water, solvate the rigid ionic channels of the IL through the formation of strong hydrogen bonds with the anions and also weaker hydrogen bonds between the H bound to the C_2 of the cation.[33–35] Solvation of this ionic network alters the structure of the ionic liquid causing aggregation of the non-polar domains.[36–38] The following question arises: what happens to the RuNPs if the structure of the IL is disrupted?

When, under argon atmosphere, an amount of water is added to a stable RuNP suspension in IL, TEM images show agglomeration of the NPs after treatment, Fig. 7, supporting the fact that the RuNPs are originally isolated within non-polar pockets by this network. It is clear that before coalescing,

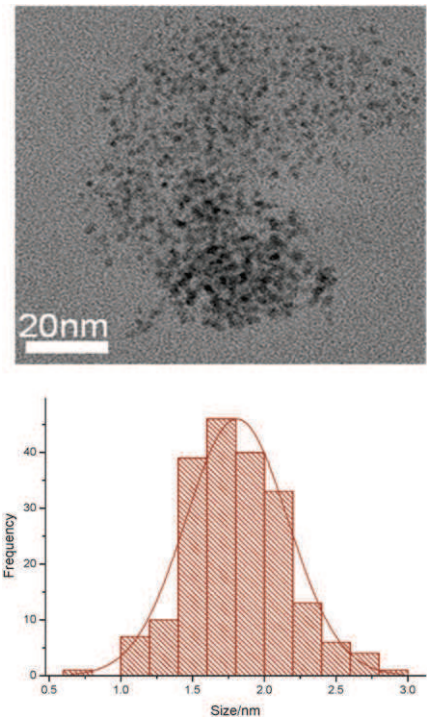

Fig. 7 TEM image of RuNPs in IL_1 after treatment with water and resultant size distribution histogram.

NPs must agglomerate, so preventing agglomeration has an indirect influence on stability.

Conclusion

The phenomenon of crystal growth of RuNPs generated *in situ* from Ru(COD)(COT), in imidazolium-based ILs is found to be controlled by the size of non-polar domains created by the grouping of lipophilic alkyl chains. Close proximity of the RuNPs to the non polar R group of the cation is evidenced by *in situ* labelling experiments (deuteration and reduction), thus corroborating the hypothesis that RuNPs are surrounded by these non-polar pockets. Addition of water, destroying the ionic network, induces agglomeration of the RuNPs, supporting the fact that the RuNPs are originally isolated within non-polar pockets by the 3-D network of ionic channels. Furthermore, the presence of surface hydrides and their role in the stabilisation of the nanoparticles is demonstrated. Finally, the RuNPs are shown to be hydrophobic.

Experimental section

All operations were performed in the strict absence of oxygen and water under a purified argon atmosphere using glovebox (Jacomex or MBraun) or vacuum-line techniques. Imidazolium ionic liquids C_4C_1Im NTf_2, IL_1 $C_{4//}C_1Im$ NTf_2, IL_2 BzC_1Im NTf_2, IL_3,[39] Ru(COD)(COT),[40] and RuNPs were synthesised as already reported.[21,41] The halide content is under 200 ppm (E.A), and water under 5 ppm, (limit of Karl Fischer titration).

1-Methylimidazole (>99%) was purchased from Aldrich and distilled prior to use. Chlorobutane, benzyl chloride and 4-chlorobut-1-ene (>99%, Aldrich) were used without further purification. Bis(trifluoromethanesulfonyl)imide lithium salt (Solvionic) was used without further purification.

Elemental analyses were performed at the CNRS Central Analysis Department of Solaize.

Solution NMR spectra were recorded on Bruker Avance 300 spectrometer for ^1H and ^{13}C DRX 500 for ^2H. Gas phase ^1H NMR spectra were obtained on a Bruker DRX 500 instrument at 298 K (nominal) with a resonance frequency at 500.130 MHz.

Mass spectra were acquired on a ThermoFinnigan LCQ Advantage ion trap instrument, detecting positive (+) an negative (−) ions in the ESI mode. Samples (1–10 μg mL^{-1} in acetonitrile) were infused directly into the source (5 μL min^{-1}) using a syringe pump. The following source parameters were applied: spray voltage 3.0–3.5 kV, nitrogen sheath gas flow 5–20 arbitrary units. The heated capillary was held at 200 °C. MS spectra were obtained by applying a relative collision energy of 25–40% of the instrumental maximum. (Spectra in supplementary information.†)

Transmission electron microscopy (TEM) experiments were performed directly in the IL media.[21] A thin film of RuNP solution in IL was deposited on a carbon film supported by a copper grid. Conventional TEM micrographs were obtained at the "Centre Technologique des Microstructures", UCBL1, Villeurbanne, France, using a Philips 120 CX electron microscope with acceleration voltage of 120 kV. Size distribution histograms were constructed from the measurement of at least 200 different nanoparticles assuming a near spherical shape and random orientation.

GC analyses

The products were quantitatively analysed by gas chromatography on a P6890 chromatograph equipped with a flame ionisation detector (FID) and an Al_2O_3/KCl column (*L*: 50 m, *φ*int: 0.32 mm, film thickness: 5 μm). The injector and detector temperature was 230 °C, and the injection volume was 1 μL. The temperature was fixed at 190 °C.

Hydrogenation of ethylene by RuNPs in the IL

A 2 mL sample of RuNP solution in IL was introduced under argon into a Schlenk tube of known volume. The sample was treated under flow of argon for 18 h. The argon atmosphere was replaced with a known pressure of ethylene using a vacuum line and the system was stirred. A decrease of the internal pressure was observed, and the composition of the gas phase was monitored by gas chromatography. After 12 h, the atmosphere was replaced by a H_2 atmosphere and the system was heated and stirred for 12 h. The composition of the gas phase was again monitored by gas chromatography.

H–D exchange

A 2 mL sample of RuNP solution in IL was introduced under argon into a Schlenk tube, which was then treated under dynamic vacuum (10^{-5} mbar) during a period of 1 or 4 h. This was then charged with deuterium (1 bar) and stirred at 25 °C for a period of 1 or 4 d. The gas phase was subsequently expanded into an airtight Young tube for NMR analysis.

Acknowledgements

We would like to thank ANR CALIST and *Ministère de l'Enseignement Supérieur* (P.S.C.) for financial support. Anne Baudouin for ^{2}H NMR experiments.

Notes and references

1 (*a*) H. Bönnemann, K. S. Nagabhushana and R. M. Richards, in *Nanoparticles and Catalysis*, ed. D. Astruc, Wiley-VCH, Weinheim, 2008; (*b*) M.-C. Daniel and D. Astruc, *Chem. Rev.*, 2004, **104**, 293–346.
2 G. A. Somorjai and J. Y. Park, *Top. Catal.*, 2008, **49**, 126–135.
3 L. S. Ott and R. G. Finke, *Coord. Chem. Rev.*, 2007, **251**, 1075–1100.
4 G. Schmid, *Nanoparticles: From Theory to Application*, Wiley-VCH, Weinheim, 2004.
5 (*a*) J. Dupont and D. d. O. Silva, in *Nanoparticles and Catalysis*, ed. D. Astruc, Wiley-VCH Verlag GmbH & Co. KGaA, Weinheim, 2008, pp. 195–218; (*b*) A. Taubert and Z. Li, *Dalton Trans.*, 2007, 723–727; (*c*) R. E. Morris, *Angew. Chem., Int. Ed.*, 2008, **47**, 442–444; (*d*) J. Kraemer, E. Redel, R. Thomann and C. Janiak, *Organometallics*, 2008, **27**, 1976–1978.
6 A. Corma, I. Dominguez, T. Rodenas and M. J. Sabater, *J. Catal.*, 2008, **259**, 26–35.
7 A. P. Umpierre, G. Machado, G. H. Fecher, J. Morais and J. Dupont, *Adv. Synth. Catal.*, 2005, **347**, 1404–1412.
8 L. S. Ott and R. G. Finke, *Inorg. Chem.*, 2006, **45**, 8382–8393.
9 L. S. Ott, M. L. Cline, M. Deetlefs, K. R. Seddon and R. G. Finke, *J. Am. Chem. Soc.*, 2005, **127**, 5758–5759.
10 T. Gutel, C. C. Santini, K. Philippot, K. Pelzer, Agilio Padua, B. Chaudret, Y. Chauvin and J.-M. Basset, *J. Mater. Chem.*, 2009, **19**, 3624–3631.
11 A. A. H. Padua, M. F. Costa Gomes and J. N. A. Canongia Lopes, *Acc. Chem. Res.*, 2007, **40**, 1087–1096.
12 M. G. Del Popolo, C. L. Mullan, J. D. Holbrey, C. Hardacre and P. Ballone, *J. Am. Chem. Soc.*, 2008, **130**, 7032–7041.
13 T. Gutel, C. C. Santini, A. A. H. Padua, B. Fenet, Y. Chauvin, J. N. Canongia Lopes, F. Bayard, M. F. Costa Gomes and A. S. Pensado, *J. Phys. Chem. B*, 2009, **113**, 170–177.
14 K. Pelzer, O. Vidoni, K. Philippot, B. Chaudret and V. Collière, *Adv. Funct. Mater.*, 2003, **13**, 118–126.
15 K. Philippot and B. Chaudret, *C. R. Chimie*, 2003, **6**, 1019–1034.
16 T. Pery, K. Pelzer, G. Buntkowsky, K. Philippot, H.-H. Limbach and B. Chaudret, *ChemPhysChem*, 2005, **6**, 605–607.
17 J. Garcia-Anton, M. R. Axet, S. Jansat, K. Philippot, B. Chaudret, T. Pery, G. Buntkowsky and H.-H. Limbach, *Angew. Chem., Int. Ed.*, 2008, **47**, 2074–2078.
18 C. Pan, K. Pelzer, K. Philippot, B. Chaudret, F. Dassenoy, P. Lecante and M.-J. Casanove, *J. Am. Chem. Soc.*, 2001, **123**, 7584–7593.
19 K. Pelzer, K. Philippot and B. Chaudret, *Z. Phys. Chem.*, 2003, **217**, 1539–1547.
20 J. Dupont, G. S. Fonseca, A. P. Umpierre, P. F. P. Fichtner and S. R. Teixeira, *J. Am. Chem. Soc.*, 2002, **124**, 4228–4229.
21 T. Gutel, J. Garcia-Anton, K. Pelzer, K. Philippot, C. C. Santini, Y. Chauvin, B. Chaudret and J.-M. Basset, *J. Mater. Chem.*, 2007, **17**, 3290–3292.
22 J. L. Anthony, J. L. Anderson, E. J. Maginn and J. F. Brennecke, *J. Phys. Chem. B*, 2005, **109**, 6366–6374.
23 R. Berthoud, P. Delichere, D. Gajan, W. Lukens, K. Pelzer, J.-M. Basset, J.-P. Candy and C. Coperet, *J. Catal.*, 2008, **260**, 387–391; J. P. Candy, A. Elmansour, O. A. Ferretti, G. Mabillon, J. P. Bournonville, J. M. Basset and G. Martino, *J. Catal.*, 1988, **112**, 201–209.
24 R. Van Hardeveld and F. Hartog, *Surf. Sci.*, 1969, **15**, 189–230.
25 J.-M. Bassett, A. Baudouin, F. Bayard, J.-P. Candy, C. Copéret, A. de Mallmann, G. Godard, E. Kuntz, F. Lefebvre, C. Lucas, S. Norsic, K. Pelzer, A. Quadrelli, C. Santini, D. Soulivong, F. Stoffelbach, M. Taoufik, C. Thieuleux, J. Thivolle-Cazat and L. Veyre, in *Modern Surface Organometallic Chemistry*, ed. J. M. Basset, A. Psaro Rinaldo, A. Roberto Dominique and A. Ugo Renato, Wiley VCH, Weinheim, 2009, pp. 23–68.
26 M. Leconte, A. Theolier and J. M. Basset, *J. Mol. Catal.*, 1985, **28**, 217–231.
27 M. Leconte, A. Theolier, D. Rojas and J. M. Basset, *J. Am. Chem. Soc.*, 1984, **106**, 1141–1142.
28 I. M. Ciobica, A. W. Kleyn and R. A. Van Santen, *J. Phys. Chem. B*, 2003, **107**, 164–172.
29 T. H. Rod, A. Logadottir and J. K. Norskov, *J. Chem. Phys.*, 2000, **112**, 5343–5347.
30 J. Wang, C. Y. Fan, Q. Sun, K. Reuter, K. Jacobi, M. Scheffler and G. Ertl, *Angew. Chem., Int. Ed.*, 2003, **42**, 2151–2154.
31 M. P. Stracke, M. V. Migliorini, E. Lissner, H. S. Schrekker, D. Back, E. S. Lang, J. Dupont and R. S. Gonçalves, *New J. Chem.*, 2009, **33**, 82–87.
32 A. Roucoux, A. Nowiki and K. Philippot, in *Nanoparticles*, ed. D. Astruc, Wiley-VCH, Weinheim, 2007.
33 L. Cammarata, S. G. Kazarian, P. A. Salter and T. Welton, *Phys. Chem. Chem. Phys.*, 2001, **3**, 5192–5200.
34 J. N. Canongia Lopes, M. F. Costa Gomes and A. A. H. Padua, *J. Phys. Chem. B*, 2006, **110**, 16816–16818.
35 Y.-Y. Jiang, Z. Zhou, Z. Jiao, L. Li, Y.-T. Wu and Z.-B. Zhang, *J. Phys. Chem. B*, 2007, **111**, 5058–5061.
36 A. Mele, C. D. Tran and S. H. De Paoli Lacerda, *Angew. Chem., Int. Ed.*, 2003, **42**, 4364–4366.
37 A.-L. Rollet, P. Porion, M. Vaultier, I. Billard, M. Deschamps, C. Bessada and L. Jouvensal, *J. Phys. Chem. B*, 2007, **111**, 11888–11891.
38 B. L. Bhargava and M. L. Klein, *J. Phys. Chem. B*, 2009, **113**, 9499–9505.
39 L. Magna, Y. Chauvin, G. P. Niccolai and J.-M. Basset, *Organometallics*, 2003, **22**, 4418–4425.
40 P. Pertici, G. Vitulli, M. Paci and L. Porri, *J. Chem. Soc., Dalton Trans.*, 1980, 1961–1964.
41 T. Gutel, C. C. Santini, K. Philippot, A. A. H. Padua, K. Pelzer, B. Chaudret, Y. Chauvin and J.-M. Basset, *J. Mater. Chem.*, 2009, **19**, 3624–3631.

How do Physical−Chemical Parameters Influence the Catalytic Hydrogenation of 1,3-Cyclohexadiene in Ionic Liquids?

Paul S. Campbell,[†] Ajda Podgoršek,[‡] Thibaut Gutel,[†] Catherine C. Santini,*[,†] Agílio A. H. Pádua,[‡,§] Margarida F. Costa Gomes,*[,‡,§] François Bayard,[†] Bernard Fenet,[||] and Yves Chauvin[†]

Université de Lyon Institut de Chimie de Lyon, UMR 5265 CNRS-Université de Lyon 1-ESCPE Lyon, C2P2, Equipe Chimie Organométallique de Surface, ESCPE 43 Boulevard du 11 Novembre 1918, F-69616 Villeurbanne, France, Laboratoire de Thermodynamique et Interactions Moléculaires, CNRS, UMR 6272 24 Avenue des Landais, 63177 Aubière, France, Clermont Université and Université Blaise Pascal, Clermont-Ferrand, France, and Centre Commun de RMN, UCB Lyon 1 - ESCPE Lyon, 43 Boulevard du 11 Novembre 1918, F-69626 Villeurbanne Cedex, France

Received: April 1, 2010; Revised Manuscript Received: May 11, 2010

The catalytic hydrogenation of 1,3-cyclohexadiene using $[Rh(COD)(PPh_3)_2]NTf_2$ (COD = 1,5-cyclooctadiene) was performed in two ionic liquids: 1-butyl-3-methylimidazolium bis(trifluoromethylsulfonyl)imide, $[C_1C_4Im][NTf_2]$, and 1-butyl-2,3-dimethylimidazolium bis(trifluoromethylsulfonyl)imide, $[C_1C_1C_4Im][NTf_2]$. It is observed that the reaction is twice as fast in $[C_1C_4Im][NTf_2]$ than in $[C_1C_1C_4Im][NTf_2]$. To explain the difference in reactivity, molecular interactions and the microscopic structure of ionic liquid +1,3-cyclohexadiene mixtures were studied by NMR and titration calorimetry experiments, and by molecular simulation in the liquid phase. Diffusivity and viscosity measurements allowed the characterization of mass transport in the reaction media. We could conclude that the diffusivity of 1,3-cyclohexadiene is 1.9 times higher in $[C_1C_4Im][NTf_2]$ than in $[C_1C_1C_4Im][NTf_2]$ and that this difference could explain the lower reactivity observed in $[C_1C_1C_4Im][NTf_2]$.

1. Introduction

The application of ionic liquids (ILs) in catalyzed reactions is of increasing importance,[1,2] in particular, they provide excellent media for conducting catalytic hydrogenations.[1−3] Several research groups report differences in the rates and selectivities in ILs when compared to corresponding reactions in molecular solvents.[2]

As reaction media, ILs have specific properties that may have consequences on the catalytic process. In some catalytic reactions, the difference between the use of ILs and traditional solvents has been related to the chemical role of ILs, which can serve as new ligands for the catalytic metal center, as catalyst activators, as cocatalysts, or even as catalysts themselves.[1,4,5] In other cases, differences in reactivity have a physical-chemical origin,[1,6] resulting from peculiar solvation phenomena including specific interactions between the IL and the substrate (H-bonds, cation−π),[7−9] mass transfer factors (viscosity, diffusivity),[1] and effects attributed to the highly structured nature of ILs.[10−12]

ILs have a high degree of self-organization due to the coexistence of charged moieties and hydrophobic alkyl chains, to the importance of both Coulombic and van der Waals interactions, and frequently to the presence of hydrogen bonds between the cation and the anion. In butylimidazolium ionic liquids, the alkyl side chain is sufficiently long to allow the formation of nonpolar domains that coexist with an ionic network.[13] This heterogeneous structure influences the way solutes are solvated in the ionic liquid:[14] nonpolar species will be solvated within the hydrophobic domains whereas polar substrates tend to interact with the polar network. The strength of cation−anion association[15] can also influence the possibility of establishing ion−solute specific interactions (e.g., π−cation interactions), as has been shown in the case of toluene.[9] For a nonaromatic π-system, such as 1,3-cyclohexadiene, solvation is probably a combination of more subtle interactions with the ionic liquid. This information can be assessed through the study of the thermodynamic properties of solution (solubility, enthalpy of solution) and from the characterization of the mass transfer through viscosity and diffusivity data.

The aim of this work is to study the influence of the nature of the ionic liquid on the catalytic hydrogenation of 1,3-cyclohexadiene (CYD) with $[Rh(COD)(PPh_3)_2]NTf_2$ (COD = 1,5-cyclooctadiene). First, we have quantified the difference in reactivity when the reaction is performed in two ionic liquids: 1-butyl-3-methylimidazolium bis(trifluoromethylsulfonyl)imide, $[C_1C_4Im][NTf_2]$, and 1-butyl-2,3-dimethylimidazolium bis(trifluoromethylsulfonyl)imide, $[C_1C_1C_4Im][NTf_2]$. Following this, we have attempted to rationalize the differences encountered through NMR characterization of the molecular interactions between the ionic liquids and the substrate, the study of the microscopic structure of the IL-substrate mixtures, the measurement of the thermodynamic properties of mixing (such as the solubility and the heat of mixing), the determination of the viscosity of the reaction media, and the measurement of diffusivity of CYD in the ionic liquids.

2. Experimental Section

Materials. 1-Methylimidazole (>99%, Aldrich) and 1,2-dimethylimidazole (>98%, Aldrich) were distilled prior to use.

* To whom correspondence should be addressed. E-mail: C.C.S., santini@cpe.fr; M.F.C.G., margarida.costa-gomes@univ-bpclermont.fr.
[†] Université de Lyon.
[‡] CNRS.
[§] Clermont Université and Université Blaise Pascal.
[||] Centre Commun de RMN.

10.1021/jp102941n
Published on Web 05/26/2010

Anhydrous 1,3-cyclohexadiene (99.8%, Aldrich) and 1,3-cyclohexadiene stabilized (96%, Acros Organics, stabilized with 50 ppm of 2,6-di-*tert*-butyl-4-methylphenol, BHT) distilled over NaK alloy and stored on zeolites were used for the reaction and the physical chemical measurements, respectively. Bis(trifluoromethanesulfonyl)imide lithium salt (>99%, Solvionic) and $[Rh(COD)Cl]_2$ (>99%, Strem) were used without further purification. All other reagents and solvents were commercially available and were used as received. Ionic liquids, synthesized as previously reported,[16] were dried overnight under high vacuum and stored in a glovebox (Jacomex) to guarantee rigorously anhydrous products.

Synthesis of the Catalysts. ***[Rh(COD)(PPh$_3$)$_2$]NTf$_2$.*** The procedure followed was adapted from the literature.[17] A mixture of $[Rh(COD)Cl]_2$ (100 mg, 0.2 mmol) dissolved in 2 mL of dichloromethane and of $LiNTf_2$ (107 mg, 0.37 mmol) dissolved in 2 mL of water was stirred vigorously while triphenylphosphine (405 mg, 1.5 mmol) was added. After 2 h, the dichloromethane layer was removed, washed three times with 2 mL of water and dried over anhydrous Na_2SO_4. Ethanol (1 mL) and diethyl ether (2 mL) were slowly added to complete crystallization. The orange crystals were filtered off and dried under reduced pressure. Yield: 200 mg (99%). ^{1}H NMR (300 MHz, CD_2Cl_2): $\delta = 2.2$ (m, 8H), 4.6 (s, 4H), 7.5 (m, 30H). ^{31}P NMR (121 MHz, CD_2Cl_2): $\delta = 23.6$ with $J_{Rh-P} = 147$ Hz. ^{103}Rh NMR (500 MHz, CD_2Cl_2): $\delta = -80$ ppm with $J_{Rh-P} = 147$ Hz. Mass spectrometry: positive mode: $m/z = 473 \Rightarrow Rh(COD)(PPh_3)^+$; $627 \Rightarrow Rh(PPh_3)_2^+$. UV−vis spectroscopy (6.6 mg of $[Rh(COD)(PPh_3)_2]NTf_2$ dissolved in 2 mL of one of ionic liquids, $[C_1C_4Im][NTf_2]$ or $[C_1C_1C_4Im][NTf_2]$); spectrum recorded at $\lambda_{max} = 450$ nm.

[Rh(CYD)(PPh$_3$)$_2$]NTf$_2$. $[Rh(COD)(PPh_3)_2]NTf_2$ (100 mg, 9.84×10^{-5} mol) was dissolved in 1 mL of CYD. After 10 min, the excess of solvent was removed under reduced pressure. Yield: 100 mg (99%). ^{1}H NMR (300 MHz, CD_2Cl_2): $\delta = 2.1$ (s, 2H), 5.3 (s, 2H), 7.5 (m, 30H). ^{31}P NMR (121 MHz, CD_2Cl_2): $\delta = 25.2$ ppm with $J_{Rh-P} = 17$ Hz. Mass spectrometry: positive mode: $m/z = 707 \Rightarrow$ Rh(cyclohexadiene)$(PPh_3)_2^+$; $m/z = 627 \Rightarrow Rh(PPh_3)_2^+$. UV−vis spectroscopy (6.6 mg of $[Rh(CYD)(PPh_3)_2]NTf_2$ dissolved in 2 mL of one of ionic liquids, $[C_1C_4Im][NTf_2]$ or $[C_1C_1C_4Im][NTf_2]$); spectrum recorded at $\lambda_{max} = 500$ nm.

Ligand Exchange. In $[Rh(CYD)(PPh_3)_2]NTf_2$ was followed by UV−vis spectroscopy. CYD (0.15 mL, 1.6 mmol) was added to a system of $[Rh(COD)(PPh_3)_2]NTf_2$ (1.6 mg, 1.6 μmol) in one of the ionic liquids, $[C_1C_4Im][NTf_2]$ or $[C_1C_1C_4Im][NTf_2]$ (1 mL). The UV−visible spectra of 1 mL of the solution were recorded on the Perkin-Elmer LAMBDA 950 Spectrophotometer in stirred and closed UV cells at $\lambda_{max} = 500$ nm every second.

Reaction with H$_2$. $[Rh(CYD)(PPh_3)_2]NTf_2$ (8 mg, 8.1×10^{-6} mmol) was dissolved in one of the ionic liquids, $[C_1C_4Im][NTf_2]$ or $[C_1C_1C_4Im][NTf_2]$ (5 mL) and pressurized under 1.2 bar of hydrogen. The UV−visible spectra of 1 mL of the solution were recorded at a given time at $\lambda_{max} = 500$ nm.

Hydrogenation of 1,3-Cyclohexadiene. The hydrogenation of CYD was carried out at 1.2 atm of H_2 and 30 °C. CYD (0.15 mL, 1.6 mmol) was dissolved in a system of $[Rh(COD)(PPh_3)_2]NTf_2$ (3.2 mg, 3.2 μmol) in one of ionic liquids, $[C_1C_4Im][NTf_2]$ or $[C_1C_1C_4Im][NTf_2]$ (1 mL), under argon resulting in red homogeneous solutions. The reaction mixture was kept under a hydrogen atmosphere (1.2 atm, constant pressure) until 4 mL of acetonitrile was added to the catalytic solution. The product distribution in the reaction mixture and the conversion were determined by GC analyses in presence of toluene as an internal standard. A HP6890 chromatograph equipped with FID detector and an Al_2O_3/KCl column ($L = 50$ m, $\phi_{int} = 0.32$ mm, film thickness $= 5$ μm) was used. The injector and detector temperatures were set to 230 °C. Samples were injected in a volume of 1 μL. The temperature of the column was fixed at 190 °C (see Supporting Information for calculations).

Solubility and Phase Diagrams. Liquid−liquid phase equilibria of the mixture of $[C_1C_4ImNTf_2]$ or $[C_1C_1C_4Im][NTf_2]$ and CYD at atmospheric pressure were determined using a dynamic method with visual detection of solution turbidity, as already described.[18]

The mixtures of ionic liquid and CYD at different compositions were prepared gravimetrically in a glass vial equipped with a stirring bar. First, the ionic liquid was introduced into a glass vial, then the appropriate amount of CYD was added and the vial was sealed. To minimize the volume of the vapor phase in equilibrium with the ionic liquid solution and to reduce the error in composition due to differential evaporation, the glass vial was almost completely filled with the mixture. The uncertainty of the mole fraction is estimated as ±0.0001. The cells were then immersed in a thermostatic water bath whose temperature was monitored using a platinum resistance thermometer with a precision of ±0.1 K. The temperature of the bath was first increased slowly until one phase was observed. The clear homogeneous system was then cooled very slowly (5 K/h) under continuous stirring. The temperature at which the first sign of turbidity (first cloudiness) appeared was considered as the temperature of the liquid−liquid phase transition. The overall accuracy in the measurement of cloud-point temperatures is estimated to be ±2 K.

Isothermal Titration Calorimetry. The heat effects resulting from mixing aliquots of CYD with the ionic liquid were measured at 303.15 K using an isothermal titration nanocalorimeter equipped with 4 mL glass cells in a Thermal Activity Monitor TAM III from TA Instruments. An electrical calibration was done before each experiment, and the instrument was chemically calibrated 5 times by titration of a 0.01 M aqueous solution of 18-crown-6 ethers with an 0.2 M aqueous solution of $BaCl_2$. The enthalpies of binding of Ba^{2+} ions to 18-crown-6 were found to be slightly higher than those reported in the literature, 2.5%[19] and 1.6%,[20,21] respectively. No correction attributable to these differences was introduced in the raw data.

Approximately 2.75 mL of degassed ionic liquid were introduced into 4 mL glass measuring and reference cells. The liquid in the measuring cell was stirred by a turbine stirrer at 160 rpm and volumes of 4 μL of CYD were injected during 180 s using a motor driven pump (Thermometric 3810 Syringe Pump) equipped with a 100 μL gastight Hamilton syringe. In all experiments, the intervals between consecutive injections were 35−40 min, which provided a good thermal stabilization of the ionic liquid solution and the return to a stable baseline. To minimize the undesirable effects of diffusion of the ionic liquid into the canula linking the CYD syringe to the cell, the canula was immersed in the sample 10 min prior the first injection.

A peak with an area proportional to the resulting heat effect Q_i translates to the thermal effect due to each injection of CYD. The integration of peaks from the recorded calorimetric plots was performed using the TAM III Assistant software. Each experiment was repeated four times to obtain reproducible values of Q_i at different concentrations within the error bar of ±2%.

Density and Viscosity. The mixtures of ionic liquid and CYD at different compositions were prepared gravimetrically follow-

ing the procedure already described, including the precautions to minimize vapor headspace.[9] The viscosity of the mixture was measured at 298.15 K (controlled to within ±0.005 K and measured with the accuracy better than ±0.05 K) using a rolling ball viscometer from Anton Paar, model AMVn, equipped with capillary tubes of 3.0 and 1.8 mm in diameter. Before starting the measurements, the 3.0 mm diameter capillary tube was calibrated as a function of temperature and angle of measurement with a standard viscosity oil from Cannon (N35). The 1.8 mm diameter tube was calibrated with water by the manufacturer. The overall uncertainty of the viscosity is estimated as ±2.0%.

The densities of the mixtures, necessary to calculate the viscosities were measured in an Anton Paar vibrating tube densimeter model 512 P, at 298.15 K (measured by a calibrated PRT with an accuracy of ±0.02 K). The densimeter was calibrated using *n*-heptane, bromobenzene, and 2,4-dichlorotoluene. The overall uncertainty of the density is estimated as ±0.01%.

NMR Spectroscopy. ^{1}H, ^{13}C, and ^{31}P solution NMR data were collected at room temperature on a Bruker AC 300 MHz spectrometer with the resonance frequency at 300.130 MHz for the ^{1}H nucleus. ^{103}Rh solution NMR was carried out on a Bruker DRX 500 instrument at 298 K (nominal) with a resonance frequency at 500.130 MHz. The solvent used (CD_2Cl_2) was distilled and kept in a rotaflo with molecular sieves. Chemical shifts are reported in ppm (singlet = s, doublet = d, doublet of doublet = dd, and multiplet = m) and were measured relative to the residual proton of the solvent to $CHDCl_2$ for ^{1}H, to CD_2Cl_2 for ^{13}C, and to H_3PO_4 for ^{31}P spectra.

For ^{1}H 1D NMR spectroscopy, the samples with molar ratio $R = 0.5$ (R is the molar ratio between the amount of substance of the hydrocarbon and the amount of substance of IL) were prepared. The mixtures of ionic liquids and hydrocarbon were prepared in closed vials in a glovebox by adding the appropriate amount of CYD to each ionic liquid, $[C_1C_4Im][NTf_2]$ or $[C_1C_1C_4Im][NTf_2]$. The resulting systems were stirred for 24 h at 303 K, resulting in homogeneous monophasic solutions. Approximately 0.3 mL of the sample was then introduced into a 5 mm NMR tube. A stem coaxial capillary tube loaded with CD_2Cl_2 was inserted into the 5 mm NMR tube to avoid any contact between the deuterated solvent and the analyzed mixture. The deuterium in CD_2Cl_2 was used for the external lock of the NMR magnetic field and the residual $CHDCl_2$ in CD_2Cl_2 was used as the ^{1}H NMR external reference at 5.32 ppm. When ^{1}H NMR data are obtained in this way, the reference signal of $CHDCl_2$ remains constant and is not affected by changes in sample concentration.

For ROESY (nuclear overhauser effect spectroscopy) experiments in the rotating frame, the 2D sequence was built with the scheme proposed by Bodenhausen (the pulse sequence shown in Figure S-3 in Supporting Information).[22] The mixing time (200 ms) is split into two parts separated by a p-pulse. At each side of the spin lock the B1 field is ramped linearly (4.5 ms) to ensure adiabatic conditions for spin lock. During the first spin lock pulse, the frequency is shifted to O1 + Df whereas the second pulse frequency is set to O1 − Df; O1 is the offset frequency and Df set to give a B1 field at the magic angle. In this way, the ROESY response is roughly constant across the spectra of interest. 1D sequence PFGSE (pulse field gradient spin echo for selective excitation) has been used, and spin lock followed the same scheme as previously.

For the 2D DOSY (diffusion order spectroscopy) experiments a Bruker sequence ledbpgp2s was implemented for shorter pulse gradients to improve line shape and trapezoidal gradients (the pulse sequences shown in Figure S-6 in Supporting Information). The diffusion evolution time was 100 ms, the constant amplitude part of the gradient was 3 ms, and the cosine raising and falling part of gradient were 150 μs. The diffusion space was sampled by 32 linearly spaced gradients.

Molecular Simulation. The microscopic structures of the IL-CYD mixtures studied experimentally were also investigated by molecular simulation, using an atomistic force field that describes interactions and conformations.[23−25] CYD was represented by the optimized potential for the liquid simulations force field in its all-atom explicit version (OPLS-AA).[26] ILs were represented by a specifically parametrized force field of the OPLS-AA family in which particular attention was paid to the description of electrostatic charge distributions and torsion energy profiles. The OPLS-AA force field is known to reproduce H-bonds well; the electron density of aromatic systems is represented by the values of electrostatic charges on the relevant atoms that account for the molecular mutipoles, combined with the Lennard-Jones sites that account for dispersion interactions. Explicit polarization of electron clouds is not included in the present model. Although this may be important to correctly reproduce dynamic properties of ILs, structural features and thermodynamic quantities have been described to equivalent levels of accuracy using fixed-charge models.[27]

Molecular dynamics simulations of condensed-phase CYD−$[C_1C_4Im][NTf_2]$ and CYD−$[C_1C_1C_4Im][NTf_2]$ mixtures were performed using the DL_POLY program.[28] System sizes were chosen so as to contain about 10 000 atoms, and so the numbers of cations, anions, and CYD molecules varied according to composition (e.g., 128 ion pairs and 64 molecules of CYD for $R = 0.5$). Initial low-density configurations, with ions and molecules placed at random in periodic cubic boxes, were equilibrated to attain liquid-like densities and structures at 400 K and 1 bar. Temperature and pressure were maintained using a Nosé−Hoover thermostat and barostat, respectively. Production runs then took 500 ps with an explicit cutoff distance of 16 Å for nonbonded interactions, and long-range corrections applied for repulsive−dispersive interactions. Electrostatic energies were calculated using the Ewald summation method with a relative accuracy of 10^{-4}. Structural quantities such as radial and spatial distribution functions were calculated from configurations generated during the production runs.

3. Results and Discussion

Hydrogenation of 1,3-Cyclohexadiene. Selective hydrogenation of CYD into cyclohexene can be carried out, with good conversion rates, using Osborn's complex $[Rh(NBD)(PPh_3)_2]PF_6$ (NBD = norbornadiene) in IL media such as $[C_1C_4Im][SbF_6]$ or $[C_1C_4Im][PF_6]$.[29] To avoid impurities such as chloride and water, ILs based on the bis(trifluoromethylsulfonyl)imide anion, $[C_1C_4Im][NTf_2]$ and $[C_1C_1C_4Im][NTf_2]$, were chosen here since they are hydrophobic and liquid at room temperature and their purification is well controlled.[16] Anion exchange between the IL and the catalyst can be circumvented by replacing Osborn's complex with $[Rh(COD)(PPh_3)_2]NTf_2$ (COD = 1,5-cyclooctadiene).

In the hydrogenation experiment the appropriate quantity of CYD was added to the yellow solution of $[Rh(COD)(PPh_3)_2]$-NTf_2 in $[C_1C_4Im][NTf_2]$ or $[C_1C_1C_4Im][NTf_2]$ to reach a molar ratio between CYD and IL $R = 0.5$, corresponding to a molar ratio substrate/Rh atom $r = 500$. The resulting red solution was stirred under 1.2 bar of hydrogen at 303 K. The formation of cyclohexene (CYE) was followed by GC analysis. Note that

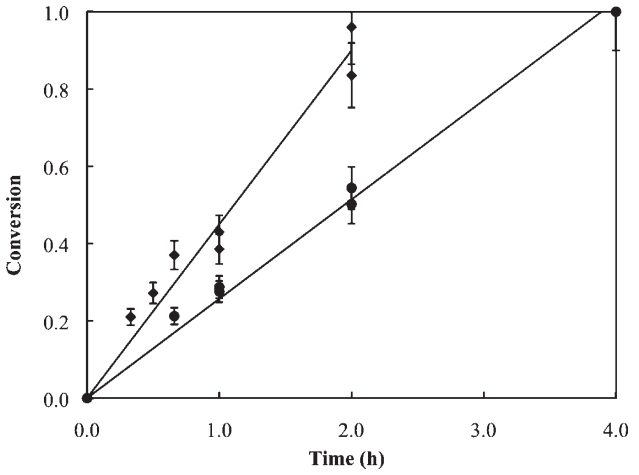

Figure 1. Hydrogenation of CYD at 303 K under 1.2 bar H_2 ($R = 0.5$ and $r = n(\text{CYD})/n(\text{Rh}) = 500$) in $[C_1C_4Im][NTf_2]$ (◆) and $[C_1C_1C_4Im][NTf_2]$ (●).

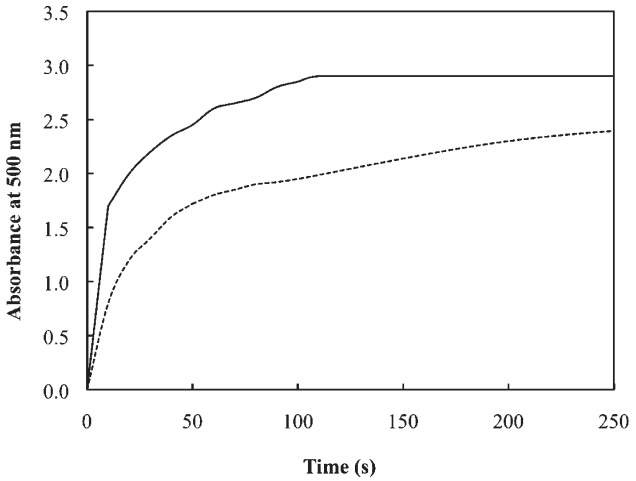

Figure 2. Evolution as a function of time of the ligand exchange reaction COD−CYD for $[Rh(COD)(PPh_3)_2]NTf_2$ in $[C_1C_4Im][NTf_2]$ (full line) and $[C_1C_1C_4Im][NTf_2]$ (dashed line) monitored at $\lambda = 500$ nm by UV−vis spectroscopy. UV−visible spectra of $[Rh(COD)(PPh_3)_2]NTf_2$ and $[Rh(CYD)(PPh_3)_2]NTf_2$ are provided in the Supporting Information (Figures S-1 and S-2).

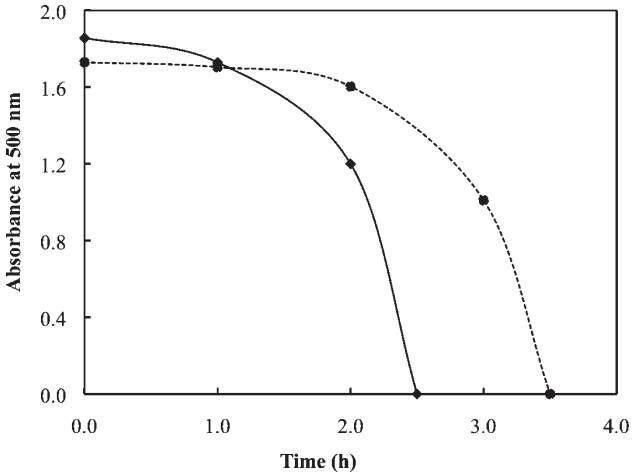

Figure 3. Evolution of the absorbance at $\lambda = 500$ nm as a function of time during the hydrogenation reaction of CYD in the presence of $[Rh(CYD)(PPh_3)_2]NTf_2$ in $[C_1C_4Im][NTf_2]$ (◆) and $[C_1C_1C_4Im][NTf_2]$ (●).

CYE is less soluble than CYD in both IL media so the system will tend to become biphasic during the course of the reaction. To avoid errors in the determination of the composition of the reaction mixture, resulting from heterogeneity of the system, the conversion was measured using GC analysis of the entire reaction system after dissolution in a mixture of acetonitrile and toluene 99:1. Each point, presented in Figure 1, corresponds to a different experiment.

As can be seen in Figure 1, hydrogenation of CYD in both ILs by $[Rh(COD)(PPh_3)_2]NTf_2$ leads quantitatively and selectively to CYE. In both cases, no significant amount (less than 2% at high or complete conversion) of cyclohexane (CYH) was detected by GC. As described in the literature, the rate of CYD reduction remains constant until near 100% conversion (1 mol of H_2 absorbed per CYD) and CYE is produced quantitatively before it is hydrogenated to CYH.[17] In $[C_1C_4Im][NTf_2]$ the conversion is complete in 2 h. This result is similar to that observed in organic solvents[17] and in other ionic liquids, such as $[C_1C_4Im][PF_6]$ or $[C_1C_4Im][SbF_6]$.[29] In $[C_1C_1C_4Im][NTf_2]$, only 50% conversion is reached after 2 h with an initial rate of hydrogenation ca. half of that in $[C_1C_4Im][NTf_2]$.

In organic solvents, during the hydrogenation of 1,3-cyclohexadiene, the catalyst first undergoes a ligand exchange, yielding $[Rh(CYD)(PPh_3)_2]^+$. This occurs more rapidly than the rate at which it then reacts with H_2.[30] The two reaction steps were investigated in both ILs. First, $[Rh(CYD)(PPh_3)_2]NTf_2$ was synthesized from $[Rh(COD)(PPh_3)_2]NTf_2$ and fully characterized. As $[Rh(COD)(PPh_3)_2]NTf_2$ is yellow ($\lambda_{max} = 450$ nm) and $[Rh(CYD)(PPh_3)_2]NTf_2$ is red ($\lambda_{max} = 500$ nm), the ligand exchange COD-CYD could be monitored by UV−vis spectroscopy ($\lambda = 500$ nm) in both ILs, as shown in Figure 2. This reaction is also much slower in $[C_1C_1C_4Im][NTf_2]$ than in $[C_1C_4Im][NTf_2]$.

Secondly, the red solutions of $[Rh(CYD)(PPh_3)_2]NTf_2$ in $[C_1C_4Im][NTf_2]$ or $[C_1C_1C_4Im][NTf_2]$ were exposed to hydrogen and the color disappeared with the concomitant formation of CYE. This hydrogenation reaction of CYD in $[Rh(CYD)(PPh_3)_2]NTf_2$ was also monitored by UV−vis spectroscopy in both ILs, the absorbances being represented in Figure 3. The discoloration of the medium, indicating the hydrogenation step, is also faster in $[C_1C_4Im][NTf_2]$ than in $[C_1C_1C_4Im][NTf_2]$. These results indicate that both ligand exchange and hydrogenation reactions are faster in $[C_1C_4Im][NTf_2]$. These processes, however, do not occur on the same time scale (hours versus seconds) and, as in organic solvents, ligand exchange is faster than hydrogenation. More importantly, the rate at which the CYE is produced (Figure 1) is similar to the rate of discoloration due to attack of $[Rh(CYD)(PPh_3)_2]$ by H_2 (Figure 3). Consequently, in accordance with the literature,[30] in the hydrogenation of CYD, this attack is the rate-determining step.

As solubilities of H_2 are similar in both ionic liquids,[31] the same overall rate of reaction would be expected. However, this is not the case and could be attributed to differences in the availability of H_2 in the different media. Indeed, even though no literature data are available for H_2 in ILs, it is generally found that the diffusion of gases is inversely dependent on the viscosity of the medium.[32] Because the same difference in the rate of reaction is noted in the ligand exchange, where H_2 is not involved, the differences in the inherent properties of each IL must be considered. For instance, studies by molecular simulations and NMR of solvation and molecular structure of similar mixtures showed that according to the nature of the IL, specific interactions with the solute differ.[7−9] In addition, mass transport factors (viscosity, diffusivity) have also been related to the

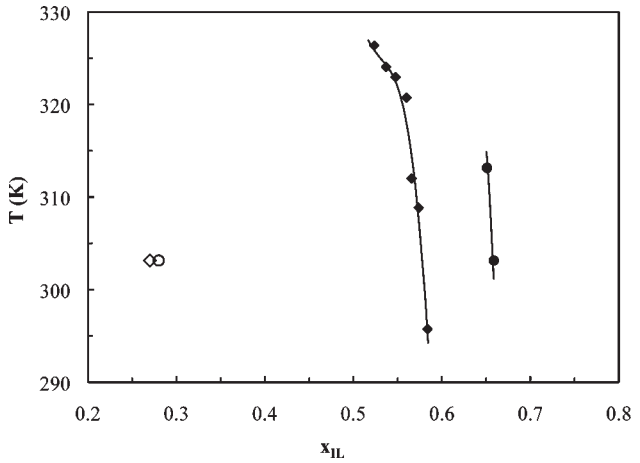

Figure 4. Liquid−liquid equilibrium diagrams for the mixture of CYD and $[C_1C_4Im][NTf_2]$ (●) or $[C_1C_1C_4Im][NTf_2]$ (◆) and solubility of toluene in $[C_1C_4Im][NTf_2]$ (◇) or $[C_1C_1C_4Im][NTf_2]$ (○).

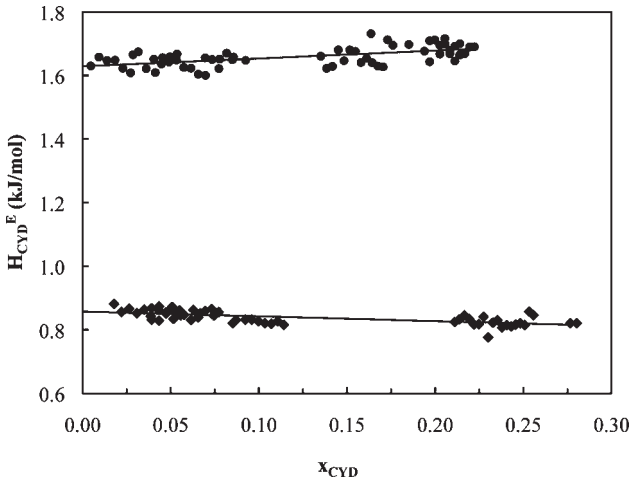

Figure 5. Partial molar excess enthalpies vs mole fraction of CYD in the binary mixture with $[C_1C_4Im][NTf_2]$ (◆) or $[C_1C_1C_4Im][NTf_2]$ (●) at 303.15 K. The lines represent functions: $H^E_{CYD} = 1.6285 + 0.2481x_{CYD}$ (●) and $H^E_{CYD} = 0.8574 - 0.1518x_{CYD}$ (◆).

reactivity[1,33] and therefore are also important parameters that we will determine and discuss here.

Solvation of 1,3-Cyclohexadiene. Figure 4 shows cloud-point temperatures as a function of composition for $[C_1C_4Im][NTf_2]$-CYD and $[C_1C_1C_4Im][NTf_2]$-CYD.[18,34] The observation of the cloud point with decreasing temperature was difficult, especially for the $[C_1C_1C_4Im][NTf_2]$-CYD system, because in this case the mixtures often remained in a metastable state and cloudiness persisted despite overheating. The observation of the cloud point while decreasing the temperature was not reproducible during this experiment, mainly because of the effect of precooling and kinetics of demixing, as already discussed,[33] and consequently the solubility was determined at only two temperatures. Determination of the solubility of CYD in ionic liquids by liquid−vapor equilibria measurements using a static apparatus[35,36] was not possible due to the chemical properties of CYD, such as its tendency to polymerize[37] and its compatibility with o'ring materials.

The solubility of CYD at 303.15 K, expressed in mole fraction is 0.42 in $[C_1C_4Im][NTf_2]$ and 0.34 in $[C_1C_1C_4Im][NTf_2]$ (see Figure 4), which could indicate less favorable interactions between CYD and the $[C_1C_1C_4Im]$ ion in comparison with the $[C_1C_4Im]$ ion. In the temperature range studied, both systems CYD−$[C_1C_4Im][NTf_2]$ and CYD−$[C_1C_1C_4Im][NTf_2]$ show a behavior compatible with the existence of upper critical solution temperatures and very steep liquid−liquid equilibrium lines. With this method the solubility of the ionic liquid in CYD could not be detected, as it lies below the limit of detection. From measurements and from calculations using COSMO-RS,[38] it is known that the concentration of hydrocarbons in the ionic liquid rich phase is very low, with mole fractions on the order of 10^{-4}. In comparison with aromatic molecules in these ILs, CYD is much less soluble. For instance, the solubility of toluene at 303.15 K expressed in mole fraction is 0.73 in $[C_1C_4Im][NTf_2]$ and 0.72 in $[C_1C_1C_4Im][NTf_2]$,[9] the solubility of benzene in $[C_1C_4Im][NTf_2]$ being even higher (mole fraction of 0.78 at 303.15 K).[39] The small difference in solubility of toluene with respect to benzene can be attributed to the presence of an additional methyl group, whereas the much lower solubility of CYD is explained by less favorable interactions between the solute and the ILs. Disruption of the aromatic system changes the interactions between solute and ionic liquid and thus decreases the solubility.

The energy involved in the interactions of different solutes dissolved in ILs can be assessed by measuring the excess molar enthalpy. We have done so for both systems, CYD−$[C_1C_4Im][NTf_2]$ and CYD−$[C_1C_1C_4Im][NTf_2]$. The excess molar enthalpy of mixing ΔH^E_{mix} was determined by isothermal titration calorimetry, from the heat effect involved in injections of small quantities of CYD into the ionic liquid, Q_{CYD}. The partial molar excess enthalpy of solute, H^E_{CYD}, was calculated according to eq 1.

$$H^E_{CYD} = \left(\frac{\partial \Delta H^E_{mix}}{\partial n_{CYD}}\right)_{n_{IL},p,T} \approx \frac{Q_{CYD}}{\Delta n_{CYD}} \quad (1)$$

where n_{CYD} and n_{IL} denote the quantity of CYD and IL, respectively, ΔH^E_{mix} is the excess molar enthalpy of the entire system (enthalpy of mixing) and Δn_{CYD} is the quantity of solute per injection. Δn_{CYD} was calculated from the injected volumes and the density of CYD was obtained from the literature.[40] In these calculations, heat due to evaporation of the solute from IL solution is assumed to be negligible. Hence, no correction for the vapor pressure of the solute was made.

Figure 5 represents partial molar excess enthalpies of CYD in both ILs at 303.15 K as a function of composition. A larger dispersion of the values (up to 3%), especially at higher concentration, was observed. At times, before each injection of CYD into the IL, an exothermic effect was detected, mainly originating from insufficient mixing of both components at the beginning of the injection period. As already discussed in the literature[41] in the case of aromatic hydrocarbons, the rate of dissolution of nonpolar, low density and low viscosity CYD in the IL is slow and sometimes leads to formation of a solute-rich layer on the surface of the solution. This is often accompanied by partial evaporation or even polymerization of CYD before the mixing process is complete, hence disturbing the measurements. A large number of injections were made to ensure reliability. [The formation of a polymer was observed and confirmed by NMR analysis.[37] This side reaction is attributed to the fact that CYD has been distilled to eliminate the stabilizer BHT before the physical chemical measurements.]

The dependence of partial molar excess enthalpy of CYD in $[C_1C_4Im][NTf_2]$ and $[C_1C_1C_4Im][NTf_2]$ on the mole fraction was approximated by a linear regression, eq 2 and Figure 5. The partial excess molar enthalpies of CYD in both ILs at infinite dilution, $H^{E,\infty}_{CYD}$, were obtained from eq 2 by setting $x_{CYD} = 0$

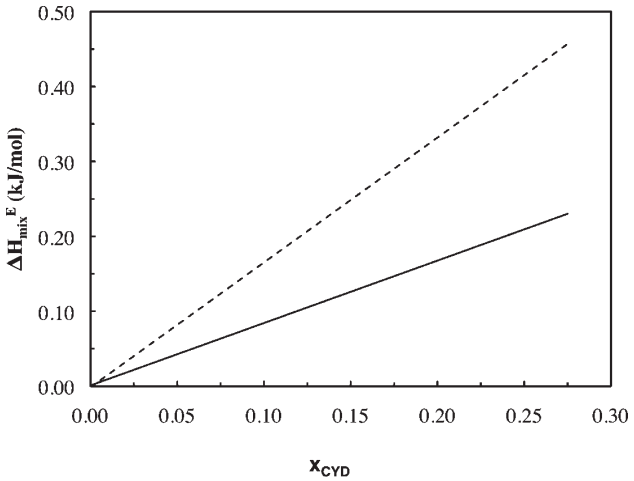

Figure 6. Excess molar enthalpies of the systems: CYD−[C_1C_4Im]-[NTf_2] (—) and CYD−[$C_1C_1C_4$Im][NTf_2] (---) vs the mole fraction of CYD at 303.15 K.

TABLE 1: Excess Molar Enthalpies of Mixing of Organic Solutes and Ionic Liquids at Mole Fraction of Solute 0.1

ionic liquid	solute	ΔH^E_{mix} (J/mol)	T (K)
[C_1C_4Im][NTf_2]	1,3-cyclohexadiene	+85 ± 9	303.15
[$C_1C_1C_4$Im][NTf_2]	1,3-cyclohexadiene	+164 ± 10	303.15
[C_1C_4Im][NTf_2]	benzene	−189.8[42]	363.15
[C_1C_4Im][NTf_2]	toluene	−150.4[40]	363.15
[C_1C_4Im][NTf_2]	methylcyclohexane	+435.6[40]	363.15
[C_1C_2Im][NTf_2]	benzene	−112.7[34]	323.15
[C_1C_2Im][NTf_2]	toluene	−115.6[39]	298.15
[C_1C_2Im][NTf_2]	cyclohexene	+356.5[34]	323.15
[C_1C_2Im][NTf_2]	cyclohexane	+394.0[34]	323.15

and were found to be 0.857 kJ mol^{-1} for CYD−[C_1C_4Im][NTf_2] and 1.629 kJ mol^{-1} for CYD−[$C_1C_1C_4$Im][NTf_2].

$$H^E_{CYD}\,(\text{kJ/mol}) = a + bx_{CYD} \tag{2}$$

By integrating eq 1 and taking into account eq 2, we calculated the excess molar enthalpy of mixing ΔH^E_{mix} by

$$\begin{aligned}\Delta H^E_{mix}\,(\text{kJ/mol}) &= \Delta H_{mix} = \int_0^{n_{CYD}} H^E_{CYD}\,dn_{CYD}/(n_{CYD} + n_{IL}) \\ &= (a+b)x_{CYD} + b(1 - x_{CYD})\ln(1 - x_{CYD})\end{aligned} \tag{3}$$

From Figure 6, it can be seen that the excess molar enthalpies of mixing for the binary mixtures of CYD and [C_1C_4Im][NTf_2] and [$C_1C_1C_4$Im][NTf_2] are positive over the studied range of compositions. The values of excess molar enthalpy of mixing of several aromatic and nonaromatic solutes in ILs together with our results are presented in Table 1. To the best of our knowledge the energetics of solvation of organic solutes in [$C_1C_1C_4$Im][NTf_2] had never been studied; therefore, we could establish comparisons only for 3-alkyl-1-methylimidazolium bis(trifluoromethylsulfonyl)imide, [C_1C_nIm][NTf_2]. Negative values of ΔH^E_{mix} for benzene and toluene in [C_1C_4Im][NTf_2] indicate more favorable interactions between aromatic systems and imidazolium ILs than for methylcyclohexane, for which the enthalpy of mixing is positive. A similar effect was observed in [C_1C_2Im][NTf_2], where the aromatic solutes have more favorable interactions leading to negative enthalpies of mixing and higher solubilities. Cyclohexene, due to the presence of a double bond, also has lower enthalpy of mixing than cyclohexane in [C_1C_2Im][NTf_2]. As expected, the values of ΔH^E_{mix} for CYD obtained here are intermediate between the values for cyclohexene and benzene. Comparison of [C_1C_4Im][NTf_2] and [$C_1C_1C_4$Im][NTf_2] shows that introduction of an additional methyl group on the C2 carbon of the imidazolium ring strongly affects the interaction with molecules of CYD, which becomes less favorable. To rationalize the differences in the solvation of CYD in both ILs, and to complement the enthalpic data with structural information, the microscopic structure of the mixtures was investigated using NMR and molecular simulation.

Molecular Structure of the Reaction Media. The molecular structure of the mixture of CYD and ILs, [C_1C_4Im][NTf_2] and [$C_1C_1C_4$Im][NTf_2], and therefore the sites of specific interactions were studied by ^{1}H NMR and ROESY experiments. The ^{1}H NMR chemical shifts of the CYD−IL mixtures at $R = 0.5$ were not significantly different from those of the neat CYD and ILs, in both cases (Table S-1 in Supporting Information).

NOESY experiments exhibited very weak or null cross peak intensities. This was probably due to the fact that the quantity $\omega\tau c$ was such that the NOE intensity was close to the null point. Rotating frame NOE experiments (ROESY) allowed us to obtain positive NOEs irrespective of the long rotational correlation time due to the high viscosity of the system. In ^{1}H−^{1}H ROESY techniques based on space cross relaxations, the selective irradiation of a proton group affects the intensities of integrals of all proton groups that are spatially close but not necessarily connected by chemical bonds. The method is based on the assumption of short-range intermolecular distances (4−5 Å).[43] The strength of the ROE signal is proportional to the inverse sixth power of the distance between the atoms, $I \propto 1/r$.[6] In the liquid state, this relation is possible if the intermolecular association is tight enough to turn the intermolecular relaxation into "intramolecular" within the ion pair or ion−molecule association.[41] Highly structured, bulk ionic liquids seem to fulfill these requirements, thus allowing the use of the intermolecular ROESY to derive lower limits for interionic distances. Consequently, the intensity of the integrals (I_{CYD-IL}) could be considered as roughly inversely proportional to the intermolecular distances (Figure S-4 and S-5, Supporting Information).

Molecular mechanics calculations have been performed using the SYBYL software with the TRIPOS force field developed by Clark et al.[44] on isolated pairs of CYD and imidazolium cations. Intermolecular distances were fixed using results from NMR ROESY experiments and the energy of both systems, CYD−[C_1C_4Im] and CYD−[$C_1C_1C_4$Im], were minimized. The average distances between molecules of CYD and the imidazolium cations were determined from the geometry at the potential energy minimum. CYD is mainly located near the butyl chain of [C_1C_4Im][NTf_2], the π bonds being located closer to the imidazolium cation, a configuration similar to that previously observed for toluene (Figure 7).[9]

Access to the microscopic structure of the mixtures in the condensed liquid phase is possible using molecular dynamics simulation with all atoms explicitly present and periodic boundary conditions to represent a vitually infinite system. Condensed-phase simulations take into account all the two-body interactions from the environment of each molecule or ion. The molecular simulation details are given in the Experimental Section. In Figure 8 are plotted the site−site radial distribution functions—the probability of finding pairs of atoms at a given distance, compared to the average—between the hydrogens on Cβ of CYD, Hβ, and selected atoms of the [C_1C_4Im] and [$C_1C_1C_4$Im] cations at $R = 0.5$ (atoms are labeled as indicated in Scheme 1). In both cases, there is a higher probability (a

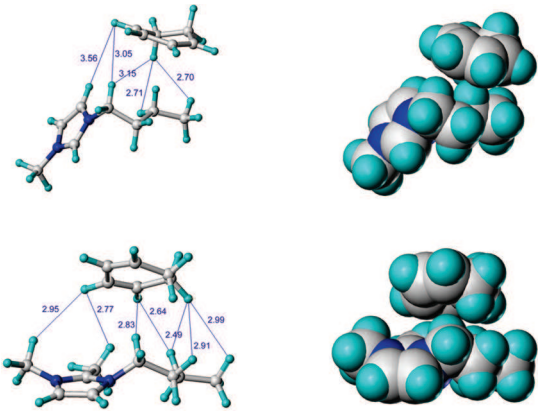

Figure 7. Representation of molecular positions in saturated solutions of CYD−[C_1C_4Im][NTf_2] and CYD−[$C_1C_1C_4Im$][NTf_2] from ROESY NMR extrapolation.

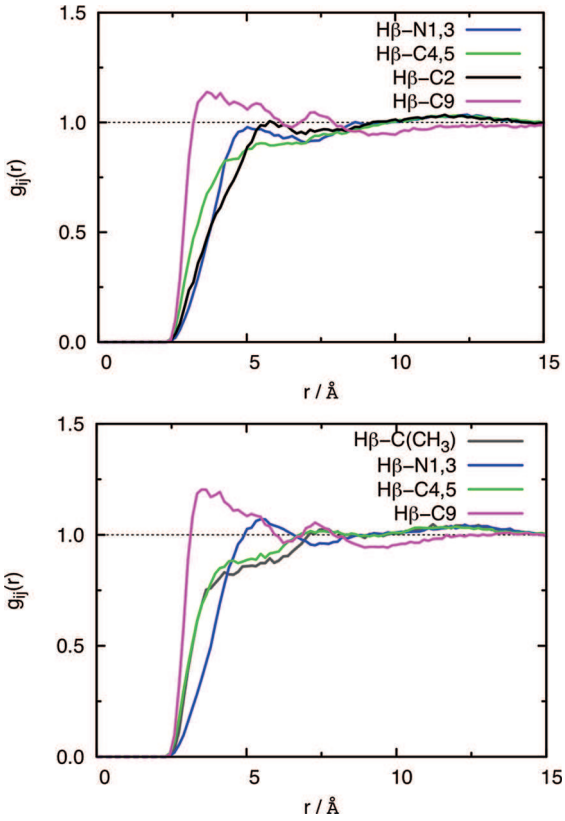

Figure 8. Radial distribution functions between hydrogen on Cβ of CYD, Hβ, and selected sites in the [C_1C_4Im] cation (top) and [$C_1C_1C_4Im$] cation (bottom), for $R = 0.5$. Atoms are labeled as indicated in Scheme 1.

stronger association) of finding all hydrogen atoms of CYD near the side chain rather than in the vicinity of the aromatic nucleus region of the imidazolium cation. This means that CYD is preferentially solvated in the nonpolar domain of the ILs, as already observed for saturated hydrocarbons and for the methyl group of toluene. This orientation effect relative to the cation is less distinct for CYD than for toluene,[9] as expected given the weaker cation−π interactions of the former.

Figure 9 represents the comparison of the radial distribution functions of the mixtures CYD−[C_1C_4Im][NTf_2] and CYD−[$C_1C_1C_4Im$][NTf_2], again at $R = 0.5$, between hydrogen on Cβ and Cα of CYD and C_2 of the imidazolium rings. It can be seen that both these hydrogen atoms are found with a higher probability closer to C_2 in [$C_1C_1C_4Im$][NTf_2] than in [C_1C_4Im][NTf_2]. The strong hydrogen bond between C2−H and the anion in [C_1C_4Im][NTf_2] prevents such an interaction with CYD. This observation is consistent with the distances between the IL cations and CYD obtained from ROESY experiments and molecular mechanics calculations on isolated pairs, as seen in Figure 7.

Detailed structural features are much better perceived in 3-dimensional spatial distribution functions. In Figure 10 is represented the distribution of ions around a CYD molecule. In blue is plotted the iso-surface corresponding to a local density of twice the average density of C_2 carbon atoms of the imidazolium cations. Cation headgroups (the blue regions) are located above and below the CYD ring, interacting preferentially with the π-system of CYD. It can be seen that the terminal carbons of the alkyl side chain, C_9 (the gray regions), surround the CYD molecule. Oxygen atoms of the NTf_2^- anion (plotted in red) are found in the plane of CYD interacting with the hydrogen atoms of the double bonds. Similar results have been previously obtained for toluene in the same ILs.[9] This shows that although in CYD the π-system is smaller than that of a fully aromatic system, it still determines the structure of the solvation shell in ILs with cations positioned above and below the plane of CYD and anion in the plane.

Figure 11 shows spatial distribution functions around the [C_1C_4Im] and the [$C_1C_1C_4Im$] cations. With both cations, CYD (the white regions) is preferentially located above and below the plane of the imidazolium ring at distances greater than those of the closest cation−anion pairs. In red is plotted the iso-surface corresponding to the local density of 4 times the average density of the oxygen atoms from NTf_2^- anions. As can be seen, for [C_1C_4Im][NTf_2] the probability of finding the oxygen of NTf_2^- near the C_2−H of the imidazolium cation is higher than the carbon of CYD, indicating a strong H-bond. The situation is completely different for [$C_1C_1C_4Im$][NTf_2], where the probability of finding the carbon of CYD near the C_2 of the cation is higher than that of the oxygen atoms of NTf_2^-. As already found in the case of solvation of toluene,[9] interactions of the [$C_1C_1C_4Im$] cation with the anion are mainly through H_4, H_5 and also the nitrogen atoms, N_1 and N_3, whereas in [C_1C_4Im] cation−anion interactions are mainly through C_2−H bonds.

Mass Transport in Reaction Media. To establish whether the difference in rate of catalytic hydrogenation of CYD can be attributed to the specific interactions or only to differences in thermophysical propreties of the reaction media, which affect the mobility of molecules, the density and viscosity of the mixtures of [C_1C_4Im][NTf_2]-CYD and [$C_1C_1C_4Im$][NTf_2]-CYD at $R = 0.5$ were measured at 298.15 K and atmospheric pressure (Table 2 and Figure S-7 in Supporting Information). The additional methyl group on the imidazolium carbon C_2 in [$C_1C_1C_4Im$][NTf_2] naturally lowers both the mass and molar density of the liquid in comparison with [C_1C_4Im][NTf_2]. On the other hand, the viscosity of pure [$C_1C_1C_4Im$][NTf_2] and also of its mixture with CYD is roughly twice that of [C_1C_4Im][NTf_2], as reported in Table 2. Diffusion coefficients (D) of CYD in both ILs at $R = 0.5$ were determined from extrapolation of DOSY data (Figure S-6 in Supporting Information): 187.5 $\mu m^2/s$ in [C_1C_4Im][NTf_2] against 97 $\mu m^2/s$ in [$C_1C_1C_4Im$][NTf_2], meaning that diffusion of CYD in [C_1C_4Im][NTf_2] is 1.9 times faster than in [$C_1C_1C_4Im$][NTf_2]. Since, according to the Stokes−Einstein relation, the diffusion coefficient is inversely proportional to the viscosity of the medium, the ratio of values of D obtained is in agreement with the ratio of measured viscosities of both mixtures at $R = 0.5$, which is η(CYD−[$C_1C_1C_4Im$][NTf_2])/η(CYD−[C_1C_4Im][NTf_2])

SCHEME 1: Atom Labeling of CYD, 1-Butyl-3-methylimidazolium, and 1-Butyl-2,3-dimethylimidazolium Cations

1-butyl-3-methylimidazolium cation [C_4C_1Im] 1-butyl-2,3-dimethylimidazolium cation [$C_4C_1C_1Im$]

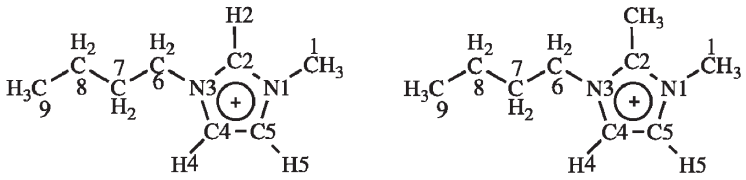

1,3-cyclohexadiene (CYD)

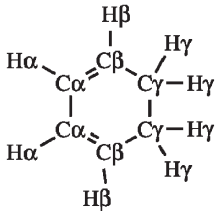

= 1.9. The availability of H_2 for the hydrogenation reaction is also dependent on the diffusivity of the gas in both ILs. No experimental data were found on the diffusivity of hydrogen in ILs, but it is expected that it will also be inversely proportional to the viscosity of the liquid medium since H_2 interacts weakly with ILs (its solubility is very low[45,46]). Molecular simulation results for the diffusivity of H_2 in [C_6C_1Im][NTf_2] at different temperatures have recently been published.[47] We have calculated that the increase of diffusivity of hydrogen and the decrease in viscosity of [C_6C_1Im][NTf_2] at the different temperatures[48] are comparable within the same order of magnitude. This is commensurate with the expected precision of the molecular simulation results.[27] All these results indicate that the difference in reactivity of both systems at $R = 0.5$ can be mainly assigned to the difference in viscosity and therefore in mobility of the molecules, namely, CYD in the exchange reaction and both H_2 and CYD in the hydrogenation reaction.

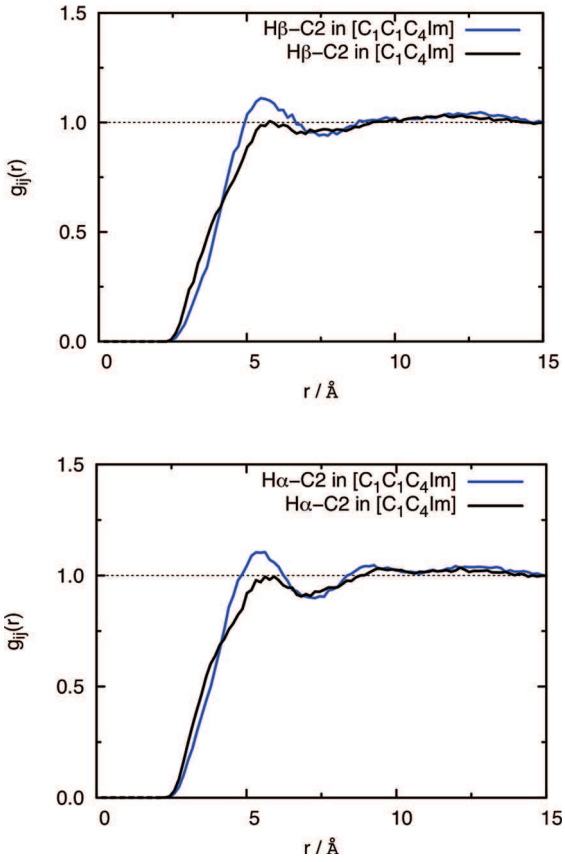

Figure 9. Comparison of site−site radial distribution functions between chosen atoms in CYD and the cations, in CYD−[C_1C_4Im][NTf_2] (top) and CYD−[$C_1C_1C_4Im$][NTf_2] (bottom) for $R = 0.5$. Atoms are labeled as indicated in Scheme 1.

4. Conclusion

In this work, we studied the impact of two ionic liquid solvents on the rates of two reaction steps of the catalytic hydrogenation of 1,3-cyclohexadiene (CYD) with [Rh(COD)-(PPh_3)$_2$]NTf_2: the ligand exchange [Rh(COD)(PPh_3)$_2$]NTf_2 to [Rh(CYD)(PPh_3)$_2$]NTf_2, and the catalytic hydrogenation of CYD itself (COD = 1,5-cyclooctadiene). It was found that

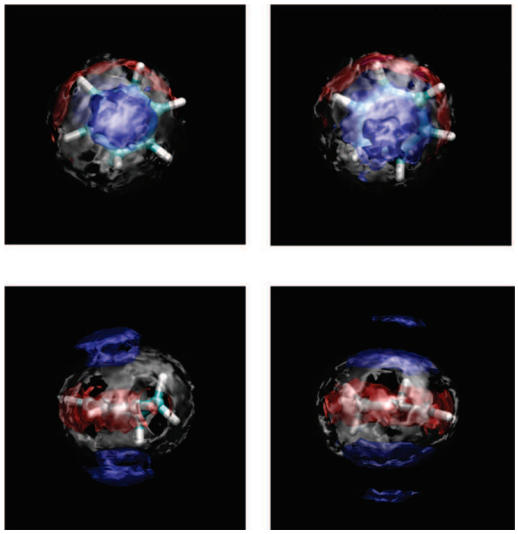

Figure 10. Spatial distribution functions around the C_2 carbon of CYD in CYD−[C_1C_4Im][NTf_2] (left) and CYD−[$C_1C_1C_4Im$][NTf_2] (right) at $R = 0.5$. In blue is plotted the iso-surface corresponding to a local density of twice the average density of the C_2 carbon of the imidazolium cations. In gray is plotted the iso-surface corresponding to a local density of twice the average density of terminal methyl carbons from the butyl side chain, C_9. In red is plotted the iso-surface corresponding to a local density of twice the average density of oxygen atoms from the NTf_2^- anion. Oxygen atoms are located in the CYD plane interacting with hydrogen atoms of double bonds, Hα and Hβ.

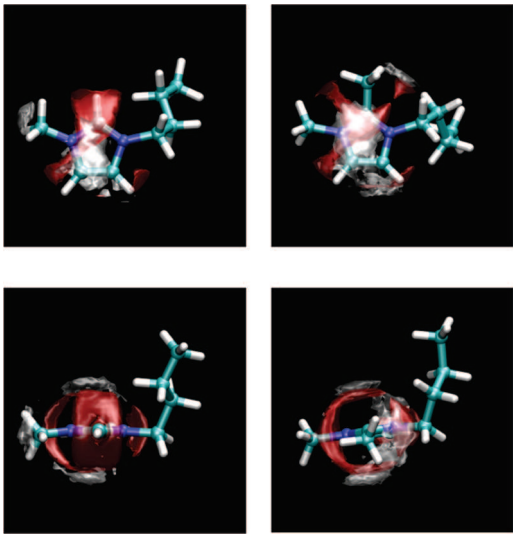

Figure 11. Spatial distribution functions around the C_2 carbon of the cations in CYD−$[C_1C_4Im][NTf_2]$ (left) and CYD−$[C_1C_1C_4Im][NTf_2]$ (right) at $R = 0.5$. Above and below are different views of the same iso-surfaces. In white is plotted the iso-surface corresponding to a local density of twice the average density of Cα of CYD. In red is plotted the iso-surface corresponding to a local density of 4 times the average density of oxygen atoms from the NTf_2^- anion.

TABLE 2: Density and Viscosity, at 298.15 K and Atmospheric Pressure, of Mixtures of CYD−$[C_1C_4Im][NTf_2]$ and CYD−$[C_1C_1C_4Im][NTf_2]$ at $R = 0.5$

x_{IL}	R	ρ (g cm^{-3})	η (mPa s)
		CYD−$[C_1C_4Im][NTf_2]$	
1.000	0.000	1.4375	48.45
0.667	0.498	1.3597	24.87
		CYD−$[C_1C_1C_4Im][NTf_2]$	
1.000	0.000	1.4177	105.00
0.662	0.510	1.3442	47.13

both steps are twice as fast in 1-butyl-3-methylimidazolium bis(trifluoromethylsulfonyl)imide, $[C_1C_4Im][NTf_2]$, than in 1-butyl-2,3-dimethylimidazolium bis(trifluoromethylsulfonyl)imide, $[C_1C_1C_4Im][NTf_2]$. The rate-determining step in both ionic liquids is the hydrogenation of CYD step.

Molecular dynamics simulations and NMR experiments indicate that in both ILs, for a molar ratio CYD/IL equal to 0.5, CYD is solvated preferentially in lipophilic regions (in close proximity to the alkyl side chains of the cations) as already observed for saturated hydrocarbons and the methyl group of toluene. In addition, in $[C_1C_1C_4Im][NTf_2]$ the probability of finding CYD near the C2 of the cation is higher than in $[C_1C_4Im][NTf_2]$, in agreement with the shorter CYD−$[C_1C_1C_4Im]$ distances determined by ROESY NMR. On the other hand, a higher solubility of CYD in $[C_1C_4Im][NTf_2]$ and smaller positive enthalpies of mixing for the CYD−$[C_1C_4Im]$-$[NTf_2]$ system in comparison with CYD−$[C_1C_1C_4Im][NTf_2]$ indicate more favorable interactions between CYD and the $[C_1C_4Im]$ cation than with the $[C_1C_1C_4Im]$ cation. These thermodynamic factors concur with the differences in catalytic activity, although they cannot fully explain the differences observed. Association between macroscopic thermodynamic information, thermophysical data, and microscopic structural information is necessary to fully explain the differences in reactivity found in both IL media.

Pure $[C_1C_1C_4Im][NTf_2]$ has a higher viscosity than pure $[C_1C_4Im][NTf_2]$, and the same relative values are observed in the mixtures with CYD. These differences in viscosity induce higher diffusion coefficients in $[C_1C_4Im][NTf_2]$ (187.5 μm^2/s) when compared to those in $[C_1C_1C_4Im][NTf_2]$ (97 μm^2/s), meaning that diffusion of CYD in $[C_1C_4Im][NTf_2]$ is 1.9 times faster than in $[C_1C_1C_4Im][NTf_2]$. Since the diffusion coefficient is inversely proportional to the viscosity of the medium, the values obtained are in agreement with the Stokes−Einstein relation, since the ratio of measured viscosities of both ionic liquids at $R = 0.5$ η(CYD−$[C_1C_1C_4Im][NTf_2]$)/η(CYD−$[C_1C_4Im][NTf_2]$) is also 1.9. The diffusion coefficient of gases is also expected to vary inversely with the viscosity of the medium. These results indicate that the difference in the rate of both ligand exchange and hydrogenation of CYD with $[Rh(COD)(PPh_3)_2]NTf_2$ in $[C_1C_4Im][NTf_2]$ and $[C_1C_1C_4Im][NTf_2]$ can be attributed to the difference in viscosity of both ionic liquids, hence the mobility of the molecules in solution.

Acknowledgment. A.P. acknowledges the postdoctoral grant by the project ANR CALIST and P.C. acknowledges the Ph.D. grant attributed by the *Ministère de l'Enseignement Supérieur et de la Recherche*, France.

Supporting Information Available: Determination of the conversion and the composition of the reaction mixture by GC. UV−vis spectra of $[Rh(COD)(PPh_3)_2]NTf_2$ and $[Rh(CYD)(PPh_3)_2]NTf_2$, ROESY and DOSY NMR pulse sequences, ^{1}H NMR shifts and ROESY NMR spectra of the mixture of CYD in $[C_1C_4Im][NTf_2]$ and $[C_1C_1C_4Im][NTf_2]$. This material is available free of charge via the Internet at http://pubs.acs.org.

References and Notes

(1) Wasserscheid, P.; Welton, T. *Ionic Liquids in Synthesis*; Wiley VCH: Weinheim, Germany, 2008.
(2) Parvulescu, V. I.; Hardacre, C. *Chem. Rev.* **2007**, *107*, 2615.
(3) Dyson, P. J.; Zhao, D. Hydrogenation. *Multiphase Homogeneous Catalysis*; Wiley-VCH: Weinheim, 2005; Vol. 2, pp 494.
(4) Olivier-Bourbigou, H.; Vallee, C. *Multiphase Homogeneous Catalysis*; Wiley-VCH: Weinheim, 2005; Vol. 2, pp 413−431.
(5) Hintermair, U.; Gutel, T.; Slawin, A. M. Z.; Cole-Hamilton, D. J.; Santini, C. C.; Chauvin, Y. *J. Organomet. Chem.* **2008**, *693*, 2407.
(6) Dupont, J.; Suarez, P. A. Z. *Phys. Chem. Chem. Phys.* **2006**, *8*, 2441.
(7) Dupont, J.; Suarez, P. A. Z.; De Souza, R. F.; Burrow, R. A.; Kintzinger, J.-P. *Chem.−Eur. J.* **2000**, *6*, 2377.
(8) Lachwa, J.; Bento, I.; Duarte, M. T.; Canongia Lopes, J. N.; Rebelo, L. P. N. *Chem. Commun.* **2006**, 2445.
(9) Gutel, T.; Santini, C. C.; Padua, A. A. H.; Fenet, B.; Chauvin, Y.; Canongia Lopes, J. N.; Bayard, F.; Costa Gomes, M. F.; Pensado, A. S. *J. Phys. Chem. B* **2009**, *113*, 170.
(10) Mele, A.; Romano, G.; Giannone, M.; Ragg, E.; Fronza, G.; Raos, G.; Marcon, V. *Angew. Chem., Int. Ed.* **2006**, *45*, 1123.
(11) Padua, A. A. H.; Costa Gomes, M. F.; Canongia Lopes, J. N. A. *Acc. Chem. Res.* **2007**, *40*, 1087.
(12) Triolo, A.; Russina, O.; Bleif, H.-J.; Di Cola, E. *J. Phys. Chem. B* **2007**, *111*, 4641.
(13) Canongia Lopes, J. N.; Padua, A. A. H. *J. Phys. Chem. B* **2006**, *110*, 3330.
(14) Canongia Lopes, J. N.; Costa Gomes, M. F.; Padua, A. A. H. *J. Phys. Chem. B* **2006**, *110*, 16816.
(15) Hunt, P. A. *J. Phys. Chem. B* **2007**, *111*, 4844.
(16) Magna, L.; Chauvin, Y.; Niccolai, G. P.; Basset, J.-M. *Organometallics* **2003**, *22*, 4418.
(17) Schrock, R. R.; Osborn, J. A. *J. Am. Chem. Soc.* **1976**, *98*, 4450.
(18) Blesic, M.; Canongia Lopes, J. N.; Padua, A. A. H.; Shimizu, K.; Costa Gomes, M. F.; Rebelo, L. P. N. *J. Phys. Chem. B* **2009**, *113*, 7631.
(19) Izatt, R. M.; Terry, R. E.; Haymore, B. L.; Hansen, L. D.; Dalley, N. K.; Avondet, A. G.; Christensen, J. J. *J. Am. Chem. Soc.* **1976**, *98*, 7620.
(20) Liu, Y. F.; Sturtevant, J. M. *Protein Sci.* **1995**, *4*, 2559.
(21) Briggner, L. E.; Wadso, I. *J. Biochem. Biophys. Methods* **1991**, *22*, 101–118.
(22) Cutting, B.; Ghose, R.; Bodenhausen, G. *J. Magn. Reson.* **1999**, *138*, 326.
(23) Canongia Lopes, J. N.; Deschamps, J.; Padua, A. A. H. *J. Phys. Chem. B* **2004**, *108*, 2038.

(24) Canongia Lopes, J. N.; Padua, A. A. H. *J. Phys. Chem. B* **2004**, *108*, 16893.
(25) Canongia Lopes, J. N.; Shimizu, K.; Padua, A. A. H.; Umebayashi, Y.; Fukuda, S.; Fujii, K.; Ishiguro, S. I. *J. Phys. Chem. B* **2008**, *112*, 9449.
(26) Jorgensen, W. L.; Maxwell, D. S.; Tirado-Rives, J. *J. Am. Chem. Soc.* **1996**, *118*, 11225.
(27) Maginn, E. J. *Acc. Chem. Res.* **2007**, *40*, 1200.
(28) Smith, W.; Forester, T. R.; Todorov, I. T.; *The DL_POLY molecular simulation package*, 2.20 ed.; T. D. P. m. s., Ed.; STFC Daresbury Laboratorys, Warrington, U.K., 2007.
(29) Chauvin, Y.; Mussmann, L.; Olivier, H. *Angew. Chem., Int. Ed.* **1996**, *34*, 2698.
(30) Schrock, R. R.; Osborn, J. A. *J. Am. Chem. Soc.* **1976**, *98*, 2134.
(31) Costa Gomes, M. F. Unpublished results.
(32) Camper, D.; Becker, C.; Koval, C.; Noble, R. *Ind. Eng. Chem. Res.* **2006**, *45*, 445.
(33) Cui, Y.; Biondi, I.; Chaubey, M.; Yang, X.; Fei, Z.; Scopelliti, R.; Hartinger, C. G.; Li, Y.; Chiappe, C.; Dyson, P. J. *Phys. Chem. Chem. Phys.* **2010**, *12*, 1834.
(34) Domañska, U.; Żołek-Tryznowska, Z.; Królikowski, M. *J. Chem. Eng. Data* **2007**, *52*, 1872.
(35) Kato, R.; Krummen, M.; Gmehling, J. *Fluid Phase Equilib.* **2004**, *224*, 47.
(36) Husson, P.; Pison, L.; Jacquemin, J.; Costa Gomes, M. F. *Fluid Phase Equilib.* **2010**, DOI: 10.1016/j.fluid.2010.02.021.
(37) Natori, I.; Imaizumi, K.; Yamagishi, H.; Kazunori, M. *J. Polym. Sci., Part B* **1998**, *36*, 1657.
(38) Domanska, U.; Pobudkowska, A.; Eckert, F. *Green Chem.* **2006**, *8*, 268.
(39) Lachwa, J.; Bento, I.; Duarte, M. T.; Canongia Lopes, J. N.; Rebelo, L. P. N. *Chem. Commun.* **2006**, 2445.
(40) Letcher, T. M.; Marsicano, F. *J. Chem. Thermodyn.* **1974**, *6*, 509.
(41) Marczak, W.; Verevkin, S. P.; Heintz, A. *J. Solution Chem.* **2003**, *32*, 519.
(42) Nebig, S.; Bolts, R.; Gmehling, J. *Fluid Phase Equilib.* **2007**, *258*, 168.
(43) Frezzato, D.; Rastrelli, F.; Bagno, A. *J. Phys. Chem.B* **2006**, *110*, 5676.
(44) Clark, M.; Cramer, R. D., III; Van Opdenbosch, N. *J. Comput. Chem.* **1989**, *10*, 982–1012. Sybil program version 7.0, Tripos Inc., 1699 South Hanley Rd., St. Louis, MO 63144, U.S.A.
(45) Jacquemin, J.; Costa Gomes, M. F.; Husson, P.; Majer, V. *J. Chem. Thermodyn.* **2006**, *38*, 490. Jacquemin, J.; Husson, P.; Majer, V.; Costa Gomes, M. F. *Fluid Phase Equilib.* **2006**, *240*, 87.
(46) Costa Gomes, M. F. *J. Chem. Eng. Data* **2007**, *52*, 472.
(47) Shi, W.; Sorescu, D. C.; Luebke, D. R.; Keller, M. J.; Wickramanyake, S. *J. Phys. Chem. B* **2010**, *114*, 6431.
(48) Marsh, K. N.; Brennecke, J. F.; Chirico, R. D.; Frenkel, M.; Heintz, A.; Magee, J. W.; Peters, C. J.; Rebelo, L. P. N.; Seddon, K. R. *Pure Appl. Chem.* **2009**, *81*, 781.

JP102941N

Journal of Catalysis 275 (2010) 99–107

Contents lists available at ScienceDirect

Journal of Catalysis

journal homepage: www.elsevier.com/locate/jcat

Olefin hydrogenation by ruthenium nanoparticles in ionic liquid media: Does size matter?

Paul S. Campbell [a], Catherine C. Santini [a,*], François Bayard [a], Yves Chauvin [a], Vincent Collière [b], Ajda Podgoršek [c], Margarida F. Costa Gomes [c], Jacinto Sá [d]

[a] Université de Lyon, Institut de Chimie de Lyon, UMR 5265 CNRS-Université de Lyon-ESCPE Lyon, C2P2, Equipe Chimie Organométallique de Surface, ESCPE 43 Boulevard du 11 Novembre 1918, F-69616 Villeurbanne, France
[b] Laboratoire de Chimie de Coordination, UMR CNRS, 205, route de Narbonne, 31077-Toulouse cedex 04, France
[c] Laboratoire de Thermodynamique des Solutions et des Polymères, Université Blaise Pascal, Clermont-Ferrand, 24 Avenue des Landais, 63177 Aubière, France
[d] CenTACat, School of Chemistry and Chemical Engineering, Queen's University, Stranmillis Road, Belfast, Northern Ireland BT9 5AG, UK

ARTICLE INFO

Article history:
Received 1 June 2010
Revised 19 July 2010
Accepted 21 July 2010

Keywords:
Nanoparticles
Ruthenium
Ionic liquids
Size effect
Selective hydrogenation

ABSTRACT

Tailor-made and size-controlled ruthenium nanoparticles, RuNPs, of three distinct sizes between 1 and 3 nm are generated from the decomposition of (η^4-1,5-cyclooctadiene)(η^6-1,3,5-cyclooctatriene) ruthenium(0) [Ru(COD)(COT)], under H_2 in 1-butyl-3-methylimidazolium bis(trifluoromethanesulphonyl)imide, $C_1C_4ImNTf_2$, by simply varying experimental conditions. Catalytic hydrogenation of 1,3-cyclohexadiene, CYD, and cyclohexene, CYE, in $C_1C_4ImNTf_2$, has been used as a probe for the relationship between size and catalytic performance (activity and selectivity) of RuNPs. To allow comparison between different reactions, all catalytic reaction mixtures were diligently prepared in order that the parameters such as substrate/catalyst and substrate/ionic liquid ratio, and therefore, viscosity and mass transport factors remained constant. It was found that the catalytic activity increases with the NP size, while high selectivity is only observed with the smaller NPs. In addition, the studied RuNPs exhibit a high level of recyclability with neither loss of activity nor significant agglomeration.

1. Introduction

Transition-metal nanoparticles (NPs) of 1–10 nm in size exhibit physicochemical properties intermediate to those of the smallest element from which they can be composed and those of the bulk material [1–3]. In catalysis, the performance (activity and selectivity) of NPs is often said to be related to their size, as this controls the number of corner, edge and face atoms available for adsorption and activation of substrates [4–9]. However, the synthesis of nanoparticles (NPs) with a controlled size in the range of 1–10 nm in order to corroborate this theory is still a challenging issue [10].

The use of ionic liquids (ILs) in NP synthesis has recently become a popular route. The major advantage is that stabilising additives such as ligands, polymers and supports are not required. Also, we can tune the IL moieties and reaction conditions to obtain monodisperse and catalytically active NPs of controlled size [7,11–13]. This is because imidazolium-based ILs exhibit a 3-D organisation in the liquid state due to an extended hydrogen-bond network of ionic channels, coexisting with non-polar domains created by the grouping of lipophilic alkyl chains. Consequently, ILs present specific solvation properties [14]. Polar substrates are preferentially dissolved in polar domains and non-polar compounds in non-polar ones [15]. The non-polar organometallic complex, Ru(COD)(COT), is expected to be concentrated in the non-polar domains of ILs. Therefore, the phenomenon of crystal growth is controlled by the local concentration of Ru(COD)(COT) and consequently limited to the size of the non-polar domains. These play the role of nanoreactors in which the size of ruthenium nanoparticles generated *in situ* can be controlled [13,16,17].

Using NPs formed *in situ* in ILs directly in catalysis offers the opportunity to exploit the distinct physicochemical and solvation properties of these media, resulting in unique activities and selectivities [12,18–21].

When comparing the catalytic activity of differently sized nanoparticles, it is important to maintain constant all other possible variables. Indeed, differences in catalytic activity could have a physicochemical origin [22,23], resulting from peculiar solvation phenomena including specific interactions between the IL and the substrate (H bonds, cation-π) [24–26], mass transfer factors (viscosity, diffusivity) [22,27], and effects attributed to the highly structured nature of ILs [14,28,29].

It has been shown that it is possible to obtain ruthenium nanoparticles, RuNPs, of differing sizes from the decomposition of Ru(COD)(COT) in $C_1C_4ImNTf_2$, by simply varying the experimental conditions [16]. In this work, we use the catalytic hydrogenation

* Corresponding author. Fax: +33 472431795.
E-mail address: santini@cpe.fr (C.C. Santini).

0021-9517/$ - see front matter © 2010 Elsevier Inc. All rights reserved.
doi:10.1016/j.jcat.2010.07.018

of 1,3-cyclohexadiene, CYD, and cyclohexene, CYE, as probes for the relationship between size and catalytic performance of tailor-made and size-controlled RuNPs, generated in the ionic liquid, all other physicochemical variables being constant.

2. Experimental

2.1. Materials and methods

All operations were performed in the strict absence of oxygen and water under a purified argon atmosphere using glovebox (Jacomex or MBraun) or vacuum-line (Schlenk) techniques. The ionic liquid, $C_1C_4ImNTf_2$ [30], and the complex, [Ru(COD)(COT)] [31], were synthesised as reported. The halide content of the ionic liquid was under 200 ppm (E.A.) and water under 5 ppm (limit of Karl Fischer titration). Elemental analyses were performed at the CNRS Central Analysis Department of Solaize.

1-Methylimidazole (>99%) was purchased from Aldrich and distilled prior to use. Chlorobutane (>99%, Aldrich) and lithium bis(trifluoromethanesulfonyl)imide (Solvionic) were used without further purification.

2.2. Catalyst synthesis

A solution of (η^4-1,5-cyclooctadiene)(η^6-1,3,5-cyclooctatriene)ruthenium(0) Ru(COD)(COT) (43 mmol L^{-1}) in the ionic liquid 1-butyl-3-methylimidazolium bis(trifluoromethylsulphonyl)imide ($C_1C_4ImNTf_2$) was transferred under argon to a glass autoclave, the temperature of which was controlled with aid of a thermostatic bath (0, 25, 50 or 75 °C). Once stabilised, the argon atmosphere was evacuated and replaced with molecular hydrogen (4 bar) without stirring. The yellow solution turned black over time (up to 3 days) as RuNPs were generated releasing cyclooctane (COA) as the only by-product. The resulting solutions were treated under dynamic vacuum during a period of 6 h to remove all H_2 and cyclooctane. The black solutions could then be stored under argon atmosphere with long-term stability (at least 6 months – no precipitation, coalescence or agglomeration – verified by TEM).

2.3. Determination of particle size by TEM

Transmission electron microscopy (TEM) experiments were performed directly in the IL media. A thin film of RuNP solution in IL was deposited on a carbon film supported by a copper grid. Conventional TEM micrographs were obtained at the Centre Technologique des Microstructures, Université Claude Bernard Lyon 1, Villeurbanne, France, using a Philips 120 CX electron microscope with acceleration voltage of 120 kV. Size distribution histograms were constructed from the measurement of at least 200 different nanoparticles assuming a near spherical shape and random orientation. High-resolution electron micrographs were obtained at the "TEMSCAN" centre of the Université Paul Sabatier Toulouse 3, Toulouse, France, using a JEOL JEM 200CX electron microscope with acceleration voltage of 200 kV.

2.4. XPS

X-ray photoelectron spectroscopy was performed in a Kratos Axis Ultra DLD spectrometer, using a monochromated Al Kα X-ray with a pass energy of 20 eV and a coaxial charge neutraliser. The base pressure in the analysis chamber was better than 5×10^{-8} Pa. XPS spectra of Ru3p, C1s, Si2p and O1s levels were measured at a normal angle with respect to the plane of the surface. High-resolution spectra were corrected for charging effects by assigning a value of 284.6 eV to the C1s peak (adventitious carbon). Binding energies were determined with an accuracy of ±0.2 eV. The data were analysed using Casa-XPS (v 2.3.13) employing a Shirley background subtraction prior to fitting and a peak shape with a combination of Gaussian and Lorentzian (30% Lorentzian). High-resolution spectra were acquired in the region of Ru 3p as the Ru 3d region overlaps with the C 2p region of the residual ionic liquid.

2.5. Preparation of catalytic experiments

In Table 1 are collected all data concerning the studied hydrogenation reaction. In columns 1–3, size and dispersion values of (**Ru_0**), (**Ru_{25}**) and (**Ru_{50}**) are reported.

Each solution of NP was produced from the decomposition of 43.0 mmol L^{-1} solution of Ru(COD)(COT) as described in Section 2.2 and shown in column 4.

For each different temperature of decomposition, a different size of NP is obtained: at 0 °C, 1.1 nm (**Ru_0**); at 25 °C, 2.3 nm (**Ru_{25}**); and at 50 °C, 2.9 nm (**Ru_{50}**), shown in columns 1 and 2.

The value of dispersion, $\mathscr{D}$, describing the ratio of surface sites **Ru_s** to total number of ruthenium atoms, varies with the NP size and is given for each size of NP in column 3. Using this and the known concentration of ruthenium (43.0 mmol L^{-1}), it is possible to calculate for each size of catalyst the concentration of **Ru_s** (column 5). For example, for **Ru_0** (1.1 nm), we have a dispersion of 82% and therefore a **Ru_s** concentration of 35.2 mmol L^{-1}.

To prepare the catalytic mixtures, we must have the same number of catalyst sites. For this reason, we dilute the most concentrated solutions, i.e. **Ru_0** and **Ru_{25}**, to match the least concentrated, i.e. **Ru_{50}**, by the addition of the appropriate amount of pure IL.

Ru_{50} has a concentration of **Ru_s** of 18.5 mmol L^{-1}. A 5-mL sample of this solution therefore contains 9.52×10^{-5} mol of **Ru_s**.

Ru_{25} has a concentration of **Ru_s** of 22.9 mmol L^{-1}. A 3.74-mL sample of this solution is therefore taken, containing 9.52×10^{-5} mol of **Ru_s**, and then diluted with 1.26 mL of pure IL to make a 5-mL solution.

Ru_0 has a concentration of **Ru_s** of 35.2 mmol L^{-1}. A 2.58-mL sample of this solution therefore contains 9.52×10^{-5} mol of **Ru_s** diluted with 2.42 mL of pure IL to make a 5-mL solution (columns 6–8).

To each of these 5-mL catalyst/IL solutions, weighing 7.0 g (column 9), is added 0.78 g of CYD (column 10). This gives catalytic mixtures with constant substrate/catalyst ratios of 105 (column 11) and constant substrate/IL ratios of 0.59 (column 12) ensuring identical viscosities and a single phase.

Using solutions prepared as described, the reaction is carried out in parallel in several 0.5-mL batches under 1.2 bars of pure molecular hydrogen, which are stirred and heated with the aid of a thermostatic carousel, to ensure identical reaction conditions.

2.6. Catalytic tests

Catalytic solutions were made as described in Section 2.5 in a glove box and left stirring for 12 h in a closed system to ensure homogeneity. Aliquots of 0.5 mL were transferred to identical Schlenk tubes containing cross-shaped magnetic stirrer bars. The argon atmosphere was removed, and the solution was degassed *in vacuo* whilst cooling in liquid nitrogen (−196 °C). For reactions at 30 °C, six of these Schlenk tubes were placed in a thermostatic carousel to ensure identical temperature and stirring conditions. After 30 min, when the temperature had stabilised, the Schlenk tubes were opened to 1.2 bars of H_2. After ***t*** minutes, a Schlenk tube was isolated and opened to air, releasing the H_2 atmosphere thus quenching the reaction. The solution was entirely dissolved in 10 mL of acetonitrile containing a 1 M concentration of toluene.

Table 1
Calculations for the composition of the catalytic systems. Column 1 – name of catalyst, column 2 – average RuNP diameter measured by TEM, column 3 – calculated dispersion, column 4 – initial Ru(COD)(COT) concentration, column 5 – consequent $\mathbf{Ru_s}$ concentration, column 6 – volume of IL/RuNP solution, column 7 – volume of pure IL added, column 8 – consequent number of moles of $\mathbf{Ru_s}$ in the 5 mL mixture, column 9 – mass of IL, column 10 – mass of substrate, column 11 – substrate/catalyst ratio, column 12 – substrate/IL ratio.

1	2 d (nm)	3 D (%)	4 [Ru] (mmol L^{-1})	5 [Ru_s] (mmol L^{-1})	6 Vol. IL–RuNP solution (mL)	7 Vol. IL pure (mL)	8 $\mathbf{Ru_s}/10^{-5}$ (mol)	9 m (IL/g)	10 m (CYD/g)	11 CYD/$\mathbf{Ru_s}$	12 CYD/IL
$\mathbf{Ru_0}$	1.1	82	43.0	35.2	2.42	2.58	9.52	7.0	0.78	105	0.59
$\mathbf{Ru_{25}}$	2.3	53	43.0	22.9	3.74	1.26	9.52	7.0	0.78	105	0.59
$\mathbf{Ru_{50}}$	2.9	43	43.0	18.5	5.00	–	9.52	7.0	0.78	105	0.59

The composition of the mixture was determined by gas-phase chromatography using toluene as the internal standard.

2.7. Product quantification

The products were quantitatively analysed by gas chromatography on a HP-6890 chromatograph equipped with a flame ionisation detector (FID) and a HP-1 (crosslinked methylsiloxane) column (L: 30 m, int: 0.32 mm, film thickness: 0.25 μm). The injector and detector temperature was 270 °C, and the injection volume was 1 μL. The programme was as follows: initial temperature 70 °C for 13.5 min; ramp 40 °C/min to 250 °C, hold 2 min.

2.8. Density and viscosity

The mixtures of IL and CYD at different compositions were prepared gravimetrically following the procedure already described [27]. The viscosity of the mixture was measured at 298.15 K (controlled to within ±0.005 K and measured with the accuracy better than ±0.05 K) using a rolling-ball viscometer from Anton Paar, model AMVn [27]. The overall uncertainty of the viscosity is estimated as ±2.0%. The densities of the mixtures, necessary to calculate the viscosities, were measured in an Anton Paar vibrating tube densimeter model 512 P, at 298.15 K (measured by a calibrated PRT with an accuracy of ±0.02 K). The overall uncertainty of the density is estimated as ±0.01%.

2.9. Solubility

To measure the solubility, 1 mL of the substrate was stirred with the ionic liquid in a closed system at 298.15 K for 12 h and then left to settle for a further 2 h. A 0.1-mL sample of the ionic liquid phase was weighed, and its composition was determined by GC using the procedure described in Section 2.6. Tests were repeated four times for each substrate to guarantee reproducibility.

3. Results and discussion

3.1. Choice of substrate

The substrate investigated is the conjugated diene, 1,3-cyclohexadiene (**CYD**). It has been shown that in ionic liquid media, **CYD** may be partially hydrogenated with high selectivity by molecular catalysts due to the reduced miscibility of cyclohexene (**CYE**) in the medium [27,32,33]. Full hydrogenation would lead to cyclohexane (**CYA**), Scheme 1.

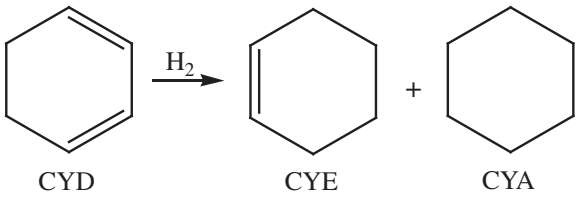

Scheme 1. 1,3-Cyclohexadiene and its hydrogenation products.

3.2. Solubility

The solubilities of the substrate and potential products may play an important role in the activity and/or selectivity of the system. For example, selective hydrogenation of butadiene to butenes has been performed by Dupont's group in ionic liquids due to the difference in solubility of the partially hydrogenated product [34]. The same group has also described the possibility of extracting cyclohexene during benzene hydrogenation using this solubility difference [35]. For this reason, solubilities of **CYD**, **CYE** and **CYA** are measured. It is found that the solubility of the hydrogenated products (6 ± 1% wt – **CYE**, 4 ± 1% wt – **CYA**) is much lower than that of **CYD** (12 ± 2% wt); therefore, the medium may tend to a biphasic system during the course of the reaction. As a result, the collection of aliquots from a single batch would render inaccurate results. Consequently, each point recorded in this work corresponds to a separate experiment, quenched after time ***t*** by opening the reaction vessel to air, thus releasing the hydrogen and dissolving the catalytic system entirely in a 1 M solution of toluene in acetonitrile for gas-phase chromatography.

3.3. Viscosity

Thermophysical properties of the reaction medium such as density and viscosity may also influence the catalytic performance. We have recently demonstrated that reaction kinetics in IL media are highly dependent on the mobility of molecules [27]. Consequently, identical concentrations of substrate must be used in each case in order to maintain constant viscosity and eliminate effects due to mass transport. Furthermore, knowledge of the viscosity is very important from engineering point of view as it plays a major role in stirring, mixing and pumping processes. The densities and viscosities of the pure $C_1C_4ImNTf_2$ and those of the mixtures with CYD were measured at different molar ratio CYD/IL (R) at 25 °C and atmospheric pressure. The results are presented in Table 2.

As can be seen, the viscosity of the mixtures of CYD in IL varies greatly with the concentration of CYD. From the Stokes–Einstein

Table 2
Density, ρ, and viscosity, η, of CYD–IL mixtures of different compositions. x_{IL} = molar fraction of IL, R = molar ratio CYD/IL.

R	x_{IL}	ρ (g cm^{-3})	η (m Pa s)
0.000	1.000	1.4376 ± 0.0001	48.5 ± 0.4
0.100	0.909	1.4202 ± 0.0001	44 ± 1
0.200	0.833	1.3999 ± 0.0001	37.0 ± 0.4
0.300	0.769	1.3874 ± 0.0003	33.3 ± 0.3
0.397	0.716	1.3718 ± 0.0001	31.0 ± 0.3
0.498	0.667	1.3597 ± 0.0001	24.8 ± 0.3

relation, the diffusion coefficient, $\mathscr{D}$, which reflects to the mobility of molecules, varies inversely with η,

$$\mathscr{D} = \frac{kT}{6\pi\eta r_s} \quad (1)$$

3.4. Catalyst characterisation

It has been previously demonstrated that the size of RuNPs generated from the decomposition of [Ru(COD)(COT)] under H_2 [36], may be governed by the degree of self-organisation of the imidazolium-based ionic liquid in which they are formed: the more structured the ionic liquid, the smaller the size [16]. Following previously described methods, RuNPs are synthesised at 0 °C, 25 °C, 50 °C and 75 °C in an attempt to obtain a selection of monodisperse sizes of RuNP in the same IL.

3.4.1. TEM

Analysis of the suspensions obtained by transition electron microscopy allows the determination of the sizes generated: 1.1 ± 0.2 nm, 2.3 ± 0.3 nm, 2.9 ± 0.4 nm and 3.1 ± 0.7 nm, for RuNPs generated at 0 °C (Ru_0), 25 °C (Ru_{25}), 50 °C (Ru_{50}) and 75 °C (Ru_{75}), respectively, Fig. 1. As can be seen from the TEM image of Ru_{75} and the consequent size distribution histogram Fig. 2, the size of these NPs does not vary significantly compared to those of Ru_{50} although a poorer size control (wider distribution) is apparent. For this reason, these NPs are not used in catalytic tests. High-resolution electron microscopy reveals the crystalline nature of the RuNPs formed through elucidation of the crystal planes. The Fourier transform images of the HREM have been exploited and indicate that the interplanar distances match with the hcp crystalline phase of Ru (see Supplementary information). For Ru_0, only a larger NP of ≈2 nm is observed by HREM, probably due to the difficulty in observing the smallest NPs with limited contrast although may be indicative of a lower degree of crystallinity in very small RuNPs, as already observed by reverse Monte Carlo simulations.[37].

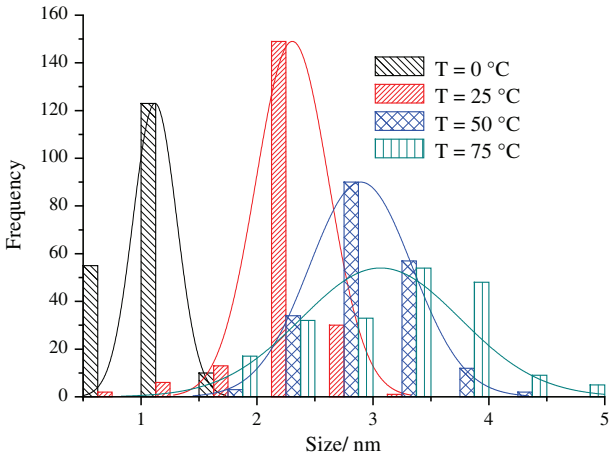

Fig. 2. Comparative size distribution histograms for RuNPs prepared in $C_1C_4Im\ NTf_2$ at different temperatures.

3.4.2. XPS

In order to establish the oxidation state of the RuNPs, X-ray photoelectron spectroscopy (XPS) is performed. Due to the weak

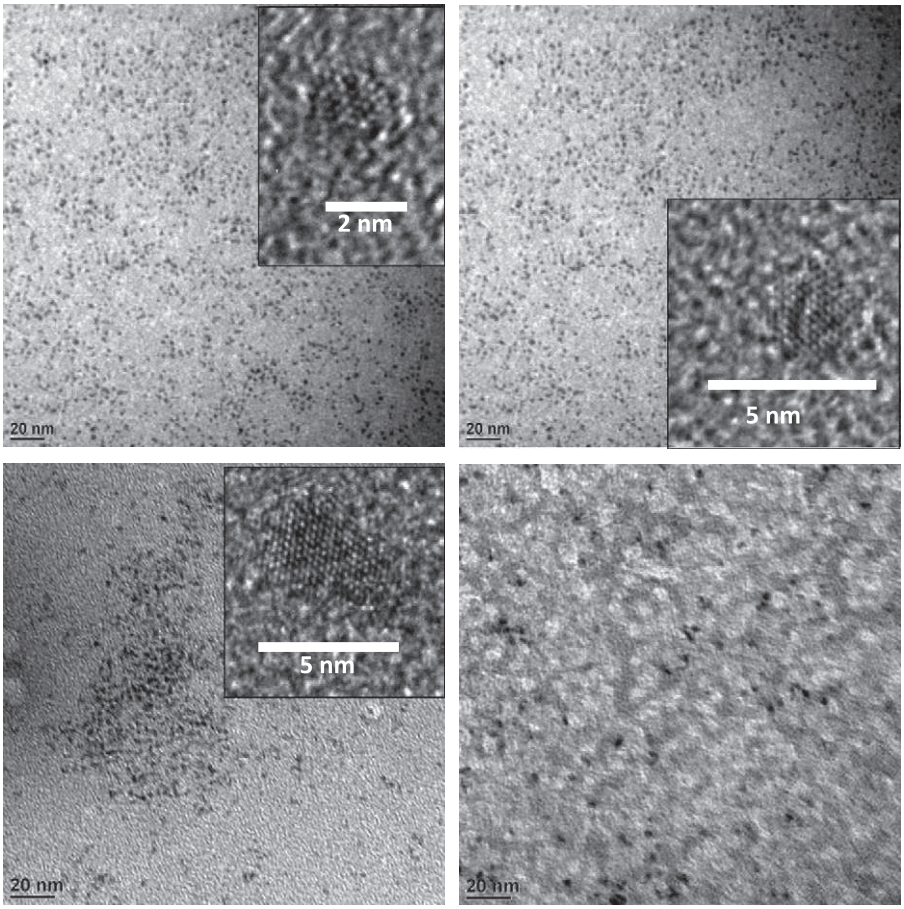

Fig. 1. Transition electron micrograph of RuNPs and high-resolution electron micrograph examples showing crystallinity for Ru_0 (top left), Ru_{25} (top right), Ru_{50} (bottom left) and Ru_{75} (bottom right).

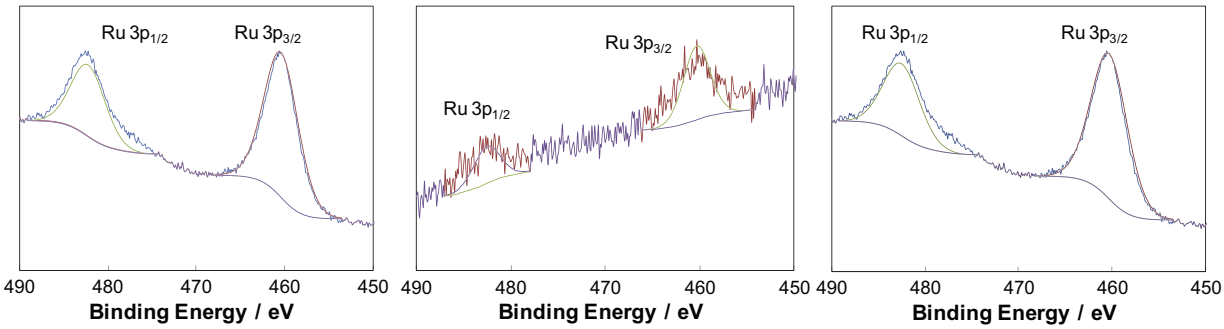

Fig. 3. XPS spectra of the Ru 3p region after NP filtration onto SiO_2, experimental data and fitted peaks. Left **Ru_0,** middle **Ru_{25}** and right **Ru_{50}**.

concentration of the solution and the penetration limit of the X-rays in the solution (maximum depth of 10 nm), no peaks corresponding to Ru binding energies are observed when the analyses are carried out directly on the RuNP/IL solutions. Samples are therefore prepared by filtering the RuNPs onto silica under inert atmosphere and eliminating as much IL as possible. The resulting spectra of the Ru 3p region are depicted in Fig. 3. It is clear that in each case, fine peaks are observed, indicating the presence of only one Ru species. The low $3p_{3/2}$ binding energy observed in each case, 460.3 eV, and doublet separation of 22.2 eV correspond closely to metallic zero-valent ruthenium, often reported with a $3p_{3/2}$ binding energy of around 461 eV [38]. The small difference may be attributed to the presence of small crystallites, which tend to exhibit lower binding energies than bulk metal. Indeed, as recently shown for AuNPs [39], the d band narrows with decreasing particle size and shifts towards the Fermi level.

3.5. Ru_s concentration

Maintaining constant the initial ratio of substrate to catalyst is imperative. In NP catalysis, as in heterogeneous catalysis, only the atoms at the surface (**Ru_s**) take part in reaction. The dispersion ($\mathscr{D}$) presents the ratio between surface atoms, **Ru_s**, and the total number of atoms, **Ru_T**, ($\mathscr{D}$ = **Ru_s/Ru_T**) and varies with the size of the NPs, smaller particles of course having a larger percentage of surface atoms. The different dispersion values must therefore be taken into account for each size of nanoparticle formed.

Ruthenium is known to exhibit a hexagonal close-packed crystal structure, with the following lattice parameters: *a*: 270.59 pm, *b*: 270.59 pm, *c*: 428.15 pm, α: 90°, β: 90°, γ: 120° [40]. Using these parameters, SYBYL software can be applied to extrapolate the lattice until the measured diameters in order to model the structure of the different size NPs, assuming crystallinity. It is seen that crystalline hexagonal close-packed RuNPs would adopt a truncated hexagonal bipyramid form, with two symmetric hexagonal faces (0 0 0 1) and 12 irregular and uneven trapezoid faces (1 0 (−1) 1) [41]. From these findings, a curve of $\mathscr{D}$ with respect to diameter can be plotted and then used to estimate $\mathscr{D}$ for each size of nanoparticle, Fig. 4.

3.6. Catalysis mixture preparation

In Table 2 (Section 2.6) are collected all data concerning the studied hydrogenation reaction. The experimental conditions are established to ensure identical concentrations of **Ru_s** (column 8) and substrate (columns 9 and 10), permitting as a result both a constant substrate/catalyst ratio (column 11) and a constant substrate/IL ratio (column 12) hence constant viscosity. Using solutions prepared as described, the reaction is carried out in parallel

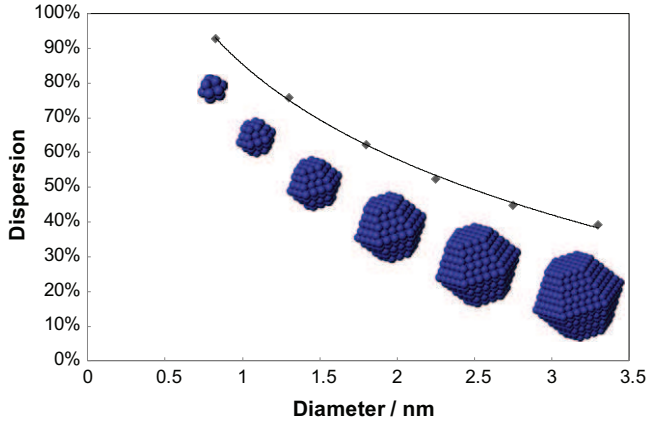

Fig. 4. Curve of dispersion $\mathscr{D}$ against mean diameter of crystalline hcp RuNPs.

in several 0.5-mL batches under 1.2 bars of pure molecular hydrogen, which are stirred and heated with the aid of a thermostatic carousel, to ensure identical reaction conditions.

3.7. Catalytic activity

It can be seen in Table 3 (Experiments 1–3) that the largest NPs (2.9 nm) are the most active in the hydrogenation of **CYD**. In a similar fashion, the three sizes of RuNP are tested in the catalytic hydrogenation of cyclohexene (**CYE**) to cyclohexane (**CYA**) to establish whether a difference in activity is also apparent in the case of a monoene. The results tabulated in Table 4 show that no substantial difference in activity is observed unlike the case of the conjugated diene **CYD**.

In the case of in the catalytic hydrogenation of cyclohexene (**CYE**) to cyclohexane (**CYA**), the TOF value for **Ru_0** is comparable to that reported by Roucoux's group with RuNPs (2.5 nm, TOF = 34) in water in the presence of cyclodextrins [42], although clearly here the experimental conditions are entirely different.

According to literature results, the catalytic activity of NPs depends on their size and generally reaches a maximum for those of around 3 nm [43,44]. Here, only a size effect on activity was observed for the case of **CYD**. The fact that the hydrogenation of **CYD** is faster with larger NPs can be related to two factors:

(1) Larger NPs present the appropriate number of neighbouring surface sites to facilitate the π-bond activation of the conjugated system [45].
(2) Through this π-bonding activation similar to benzene, 1,3-cyclohexadiene would lose part of its resonance energy and react more readily [41].

Table 3
Conversion, selectivity, turnover number and turnover frequency for the hydrogenation of CYD at 30 °C. Experiments 1–3 using 1.2 bar H_2. Experiments 4 and 5 using 4 bar H_2.

Experiment number	Catalyst (nm)	Pressure H_2 (bar)	Conversion at 90 min (%)	Selectivity CYE (%)	TON	TOF (h^{-1})	Size after catalysis (nm)
1	**Ru_0** (1.1)	1.2	66 ± 5	97	70 ± 5	46 ± 3	1.3 ± 0.4
2	**Ru_{25}** (2.3)	1.2	75 ± 5	86	79 ± 5	53 ± 3	2.1 ± 0.5
3	**Ru_{50}** (2.9)	1.2	83 ± 5	80	87 ± 5	58 ± 3	2.7 ± 0.5
4	**Ru_0** (1.1)	4.0	57 ± 5	92	59 ± 5	40 ± 3	–
5	**Ru_{50}** (2.9)	4.0	73 ± 5	80	77 ± 5	51 ± 3	–

Table 4
Conversion, turnover number and turnover frequency for the hydrogenation of CYE at 30 °C under 1.2 bar H_2.

Experiment number	Catalyst (nm)	Conversion at 90 min (%)	TON	TOF (h^{-1})
6	**Ru_0** (1.1)	61 ± 5	64 ± 5	43 ± 3
7	**Ru_{25}** (2.3)	64 ± 5	67 ± 5	45 ± 3
8	**Ru_{50}** (2.9)	67 ± 5	70 ± 5	47 ± 3

The coordination of monoenes such as **CYE** does not necessitate large surfaces, explaining the less pronounced size effect in this case.

3.8. Catalytic selectivity

In the hydrogenation of **CYD**, **CYE** is obtained as the major product. Interestingly, the selectivity for **CYE** diminishes with increasing NP size. Indeed, for **Ru_0**, selectivity for **CYE** is 100% at low conversion and only slightly diminishes at high conversion (97%). In contrast, for **Ru_{50}**, the hydrogenation is unselective even at low conversion, Fig. 5.

Assuming highly crystalline particles with hcp structure, a particle of diameter 1.1 nm would have the vast majority of catalytic surface atoms occupying vertex or edge positions. Such vertex ruthenium atoms **Ru_v**, which under H_2 atmosphere are ligated by hydrides, may coordinate one C=C double bond of **CYD**. The product of the subsequent hydrogenation is **CYE**, which must undergo a second coordination to give the fully hydrogenated **CYA**. Similarly, for a larger particle of average diameter 2.9 nm assuming high crystallinity and an hcp structure, it is evident that most of the catalytically active surface ruthenium atoms are found in facial positions, **Ru_f**. Indeed, here, such crystallinity has already been observed by HREM, Fig. 1. **Ru_f** may hydrogenate the olefin using the mechanism previously discussed, but due to the planar arrangement of **Ru_f**, another mechanism may be envisaged involving the double coordination of the diene, as generally found during the hydrogenation of 1,3-cyclohexadiene on metallic surfaces [46,47], and thus, rapid consecutive hydrogenation of both double bonds leading to the fully hydrogenated **CYA** may be envisaged. In Fig. 6 are represented simplified SYBYL models of **CYD** molecules coordinating to the surface of perfectly crystalline RuNPs of calculated average diameter 1.3 nm and 2.8 nm. This illustrates nicely the greater facility of planar coordination to faces of the larger NPs and could explain the lower selectivity of the larger RuNPs despite identical reaction conditions. Likewise, in the hydrogenation of 1,3-butadiene or 1-hexyne, the selectivity of small NPs towards 1-butene or 1-hexene versus butane or hexane is still higher than that of larger NPs [45–48]. In this work, in the hydrogenation of **CYD**, the selectivity in **CYE** versus **CYA** drops from 97% to 80% when the RuNP size increases from 1.1 to 2.9 nm.

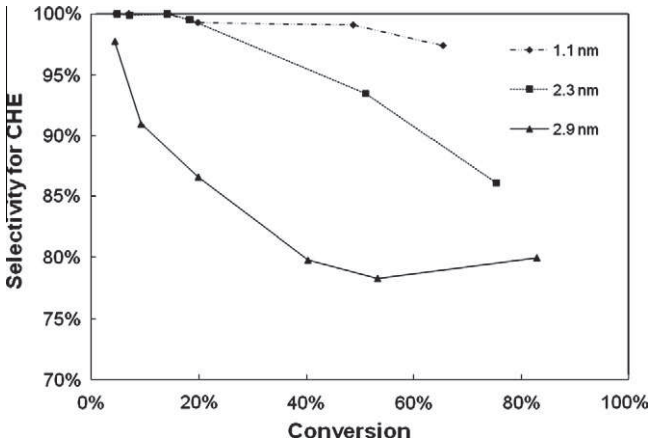

Fig. 5. Selectivity for cyclohexene as a function of conversion for the three different sizes of RuNPs.

Our hypothesis is based on idealised particle shape, which is not likely to exist in reality. Nonetheless, it is widely accepted that large NPs are more likely to present larger open facets where planar π-coordination of diene substrates can occur, whereas small NPs are often reported to be amorphous, therefore presenting no open facets, making this planar coordination even less likely [41].

In studies of CO hydrogenation on RhNPs, the difference in reactivity with size was related to the increasing probability of finding step sites with increasing NP size [49–51]. However, for RuNPs of less than 3 nm, as reported here, calculations have shown that such step sites are not likely to exist [52].

The highly selective hydrogenation of 1,3-cyclohexadiene to cyclohexene has also been performed with PdNPs in organic and IL media [33,53,54]. The high selectivity results from the intrinsic properties of Pd metal and its small NP size [55].

3.9. Hydrogen effect

According to the literature, the hydrogenation of olefins in ILs is often biphasic in its nature [56–59], due to the poor solubility of hydrogen and olefins in these media [60–63]. Therefore, the diffusion process of the substrate or H_2 may limit the rate of hydrogenation.

To find out whether H_2 is in fact a rate-limiting reagent, experiments varying the H_2 pressure are performed. Increasing H_2 pressure to 4 bars in the case of **Ru_0** and **Ru_{50}** is seen to affect neither the activity nor selectivity in a substantial manner, Table 3, Experiments 4 and 5. This is similar to results reported by Dupont's group who observed that the reaction rate **does not** depend on the H_2 pressures in $C_1C_4ImBF_4$ [64].

In parallel, it is generally reported that a higher H_2 concentration should influence the activity of the large rather than small particles, as the H_2 storage capacity is related to the particle volume; therefore, large particles may experience an increase in the availability of subsurface hydrogen [44].

In reality, little difference in activity is observed in either case. This proves that the rate is not dictated by the availability and adsorption of H_2, in agreement with observations of labile surface hydrides on the NP surface [17], but by the mobility and absorption of the substrate [26]. Indeed, it is highly likely that the surface of the NPs is already saturated with adsorbed H_2 at the temperature of the reaction [17].

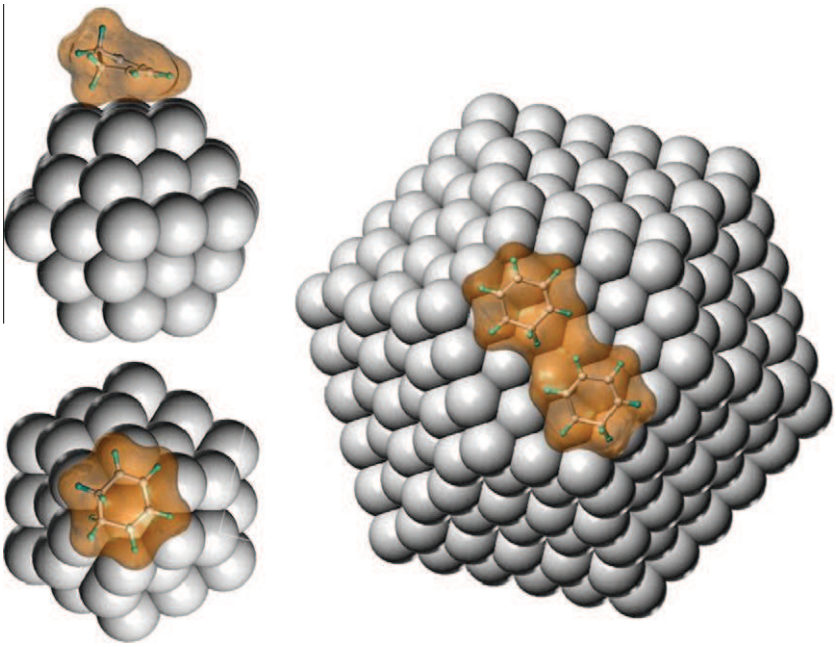

Fig. 6. SYBYL representations of CYD coordinated to the face of highly crystalline RuNPs of mean diameter 1.3 nm (left) and 2.8 nm (right).

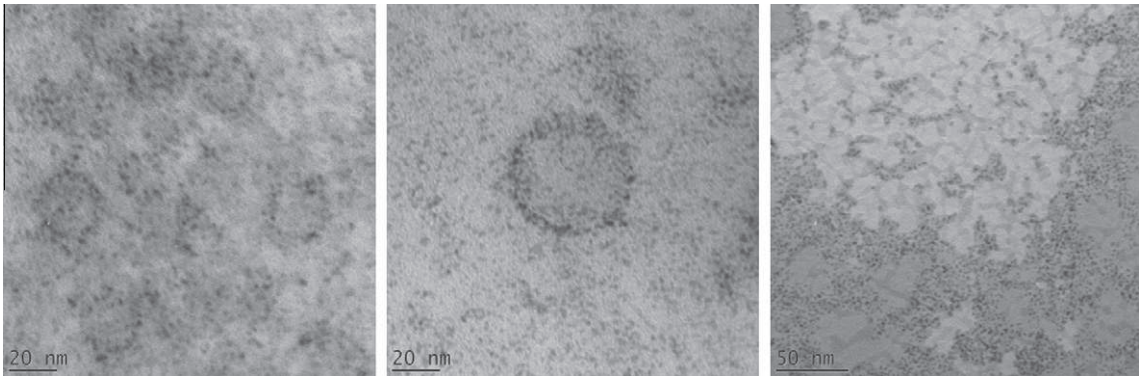

Fig. 7. Transition electron micrographs of RuNPs after CYD hydrogenation for Ru_0 (left), Ru_{25} (middle) and Ru_{50} (right).

Table 5
Recycling of the catalyst **Ru_0**. Conversion, selectivity, turnover number and turnover frequency for the hydrogenation of CYD at 30 °C under 1.2 bar H_2. Products removed under vacuum after each run and analysed by GC.

Experiment number	Cycle	Conversion at 90 min (%)	Selectivity CYE (%)	TON	TOF (h^{-1})	Size after catalysis (nm)
1	1st	66	97	70	46	1.3 ± 0.4
9	2nd	73	95	76	51	–
10	3rd	69	94	73	49	–
11	4th	68	89	71	47	–
12	5th	64	86	67	45	–
13	6th	65	86	68	45	1.8 ± 0.5

3.10. Recycling

TEM images of the reaction medium after hydrogenation, Fig. 7, show that the average size measured (Table 3) does not differ greatly from the original size, in accordance with the stability of RuNPs in ILs under molecular hydrogen [17]; however, the size distribution is larger, probably as an effect of stirring [65].

The apparent resistance to coalescence of the NPs means that they may be tested for their recyclability. Consequently, using the most selective catalyst, **Ru_0**, recycling experiments are performed, by extracting *in vacuo* and quantifying the volatiles after each 90-min run. More **CYD** is then added for hydrogenation. From the results, Table 5 and Fig. 8, it can be seen that both the activity and selectivity remain high after five recycles, diminishing only slightly with each run. This small decrease of course is attributable to the gradual coalescence of the NPs, leading to a diminution in the number of active surface sites and larger, less selective NPs. Indeed, TEM images obtained of the NPs after all recycling

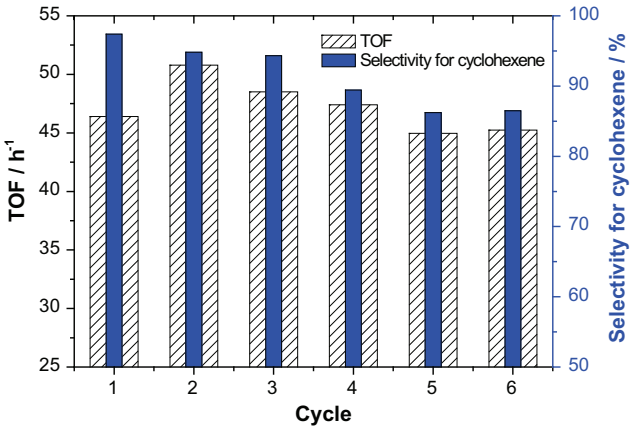

Fig. 8. Evolution of TOF and selectivity with catalyst recycling.

experiments showed that the NPs undergo coalescence to attain an average diameter of 1.8 ± 0.5 nm, approaching the size of **Ru_{25}** and of course presenting a similar selectivity.

4. Conclusion

In this work, the catalytic hydrogenation of 1,3-cyclohexadiene, **CYD**, and cyclohexene, **CYE**, in $C_1C_4ImNTf_2$, was used as a probe for the relationship between size and catalytic performance of RuNPs.

Firstly, tailor-made, size-controlled and zero-valent RuNPs (1–3 nm) were generated from the decomposition of [Ru(COD)(COT)] under H_2 in $C_1C_4ImNTf_2$, by varying the experimental conditions. RuNPs were fully characterised *in situ* by TEM and HREM to determine their sizes and demonstrate their degree of crystallinity and *ex situ* by XPS to verify their zero oxidation state.

Secondly, all catalytic reaction compositions were carefully calculated in order that all parameters except particle size were maintained constant, i.e. **Ru_s** concentration, **CYD/Ru_s** ratio and **CYD/IL** ratio, the latter governing solvation phenomena and mass transfer factors (viscosity and diffusivity). It was found that for catalytic hydrogenations of **CYD** and **CYE**, the activity of catalyst increases with the NP size in agreement with the literature results on heterogeneous catalysts. In contrast to activity, in the hydrogenation of **CYD**, the selectivity for **CYE** versus **CYA** drops from 97% to 80% when the RuNP size increases from 1.1 to 2.9 nm.

Both results, activity and selectivity, are in agreement with a mechanism involving a π-bond activation and a double coordination of diene substrates, necessitating several neighbouring surface atoms only found in facial positions on the larger NPs. Furthermore, these RuNPs show a high level of recyclability with neither loss of activity nor significant agglomeration.

To conclude, in olefin hydrogenation by ruthenium nanoparticles in ionic liquid media, both reactivity and selectivity are significantly dependent on the nanoparticle size.

Acknowledgments

P.S.C. acknowledges the Ph.D. grant attributed by the Ministère de l'Enseignement Supérieur et de la Recherche, France, and the EU transnational access programme. A.P. thanks the post-doctoral grant by the project ANR CALIST. This work has been funded by CNRS and ANR (ANR Project CALIST, ANR-07-CP2D-02-03).

Appendix A. Supplementary data

Supplementary data associated with this article can be found, in the online version, at doi:10.1016/j.jcat.2010.07.018.

References

[1] M. Valden, X. Lai, D.W. Goodman, Science 281 (1998) 1647.
[2] A.T. Bell, Science 299 (2003) 1688–1691.
[3] G. Schmid, Nanoparticles: From Theory to Application, Wiley-VCH, Weinheim, 2004.
[4] K. Lee, M. Kim, H. Kim, J. Mater. Chem. 20 (2010) 3791–3798.
[5] A.Z. Moshfegh, J. Phys. D: Appl. Phys. 42 (2009) 233001. 233032.
[6] G.A. Somorjai, J.Y. Park, Top. Catal. 49 (2008) 126–135.
[7] H. Boennemann, K.S. Nagabhushana, in: B. Corain, G. Schmid, N. Toshima (Eds.), Metal Nanoclusters in Catalysis and Materials Science: The Issue of Size Control, Elsevier B.V., Amsterdam, pp. 21–48.
[8] H. Bönnemann, K.S. Nagabhushana, R.M. Richards, in: D. Astruc (Ed.), Nanoparticles and Catalysis, Wiley-VCH, Weinheim, 2008, pp. 49–92.
[9] H. Tada, T. Kiyonaga, S. Naya, Chem. Soc. Rev. 38 (2009) 1849.
[10] D. Astruc, Nanoparticles and Catalysis, Wiley-VCH, Weinheim, 2008.
[11] J. Dupont, J.D. Scholten, Chem. Soc. Rev. 39 (2010) 1780–1804.
[12] J. Dupont, Nanoparticles and Catalysis, Wiley-VCH, Weinheim.
[13] T. Gutel, C.C. Santini, K. Philippot, A. Padua, K. Pelzer, B. Chaudret, Y. Chauvin, J.-M. Basset, J. Mater. Chem. 19 (2009) 3624–3631.
[14] A.A.H. Padua, M.F. Costa Gomes, J.N.A. Canongia Lopes, Acc. Chem. Res. 40 (2007) 1087–1096.
[15] J.N. Canongia Lopes, M.F. Costa Gomes, A.A.H. Padua, J. Phys. Chem. B 110 (2006) 16816–16818.
[16] T. Gutel, J. Garcia-Anton, K. Pelzer, K. Philippot, C.C. Santini, Y. Chauvin, B. Chaudret, J.-M. Basset, J. Mater. Chem. 17 (2007) 3290–3292.
[17] P.S. Campbell, C.C. Santini, D. Bouchu, B. Fenet, K. Philippot, B. Chaudret, A.A.H. Padua, Y. Chauvin, Phys. Chem. Chem. Phys. 12 (2010) 4217–4223.
[18] C. Vollmer, E. Redel, K. Abu-Shandi, R. Thomann, H. Manyar, C. Hardacre, C. Janiak, Chem. Eur. J. 16 (2010) 3849–3858. S3849/3841-S3849/3834.
[19] E. Redel, J. Kraemer, R. Thomann, C. Janiak, J. Organometal. Chem. 694 (2009) 1069–1075.
[20] M.H.G. Prechtl, J.D. Scholten, J. Dupont, J. Mol. Catal. A 313 (2009) 74–78.
[21] B. Leger, A. Denicourt-Nowicki, H. Olivier-Bourbigou, A. Roucoux, Inorg. Chem. 47 (2008) 9090–9096.
[22] P. Wasserscheid, T. Welton, Ionic Liquids in Synthesis, Wiley-VCH, Weinheim, 2008.
[23] H. Olivier-Bourbigou, C. Vallee, Multiphase Homogeneous Catalysis, Wiley-VCH, Weinheim, pp. 413–431.
[24] J. Dupont, P.A.Z. Suarez, R.F. De Souza, R.A. Burrow, J.-P. Kintzinger, Chem. Eur. J. 6 (2000) 2377–2381.
[25] J. Lachwa, I. Bento, M.T. Duarte, J.N.C. Lopes, L.P.N. Rebelo, Chem. Commun. (2006) 2445–2447.
[26] T. Gutel, C.C. Santini, A.A.H. Padua, B. Fenet, Y. Chauvin, J.N. Canongia Lopes, F. Bayard, M.F. Costa Gomes, A.S. Pensado, J. Phys. Chem. B 113 (2009) 170–177.
[27] P.S. Campbell, A. Podgorsek, T. Gutel, C.C. Santini, A.A.H. Padua, M.F. Costa Gomes, F. Bayard, B. Fenet, Y. Chauvin, J. Phys. Chem. B 114 (2010) 8156–8165.
[28] A. Mele, G. Romano, M. Giannone, E. Ragg, G. Fronza, G. Raos, V. Marcon, Angew. Chem. Int. Ed. 45 (2006) 1123–1126.
[29] A. Triolo, O. Russina, H.-J. Bleif, E. Di Cola, J. Phys. Chem. B 111 (2007) 4641–4644.
[30] L. Magna, Y. Chauvin, G.P. Niccolai, J.-M. Basset, Organometallics 22 (2003) 4418–4425.
[31] P. Pertici, G. Vitulli, Inorg. Synth. 22 (1983) 176–181.
[32] Y. Chauvin, S. Einloft, B.H. Olivier, Ind. Eng. Chem. Res. 34 (1995) 1149–1155.
[33] J. Huang, T. Jiang, B. Han, H. Gao, Y. Chang, G. Zhao, W. Wu, Chem. Commun. (2003) 1654–1655.
[34] A.P. Umpierre, G. Machado, G.H. Fecher, J. Morais, J. Dupont, Adv. Synth. Catal. 347 (2005) 1404–1412.
[35] E.T. Silveira, A.P. Umpierre, L.M. Rossi, G. Machado, J. Morais, G.V. Soares, I.J.R. Baumvol, S.R. Teixeira, P.F.P. Fichtner, J. Dupont, Chem. Eur. J. 10 (2004) 3734–3740.
[36] K. Philippot, B. Chaudret, C.R. Chimie 6 (2003) 1019–1034.
[37] N. Bedford, C. Dablemont, G. Viau, P. Chupas, V. Petkov, J. Phys. Chem. C 111 (2007) 18214–18219.
[38] R. Nyholm, N. Martensson, J. Phys. Chem. 13 (1980) L279.
[39] J.A. Van Bokhoven, J.T. Miller, J. Phys. Chem. C 111 (2007) 9245.
[40] V.A. Finkel, M.I. Palatnik, G.P. Kovtun, Phys. Met. Metall. 32 (1971) 231.
[41] R.A. Van Santen, Acc. Chem. Res. 42 (2009) 57–66.
[42] A. Denicourt-Nowicki, A. Ponchel, E. Monflier, A. Roucoux, Dalton Trans. 48 (2007) 5714–5719.
[43] D.Y. Murzin, Chem. Eng. Sci. 64 (2009) 1046–1052.
[44] A. Binder, M. Seipenbusch, M. Muhler, G. Kasper, J. Catal. 268 (2009) 150–155.
[45] N. Semagina, A. Renken, L. Kiwi-Minsker, J. Phys. Chem. C 111 (2007) 13933–13937.
[46] M. Saeys, M.-F. Reyniers, M. Neurock, G.B. Marin, Surf. Sci. 600 (2006) 3121–3134.
[47] W.L. Manner, G.S. Girolami, R.G. Nuzzo, J. Phys. Chem. B 102 (1998) 10295–10306.
[48] J. Silvestre-Albero, G. Rupprechter, H.-J. Freund, J. Catal. 240 (2006) 58–65.
[49] H. Arakawa, K. Takeuchi, T. Matsuzaki, Y. Sugi, Chem. Lett. 13 (1984) 1607.
[50] T. Hanaoka, H. Arakawa, T. Matsuzaki, Y. Sugi, K. Kanno, Y. Abe, Catal. Today 58 (2000) 271.
[51] S. Zhou, H. Zhao, D. Ma, S. Miao, M. Cheng, X. Bao, Z. Phys. Chem. 219 (2005) 949.
[52] J. Gavnholt, J. Schiotz, Phys. Rev. B 77 (2008) 035404/035401–035404/035410.
[53] M.V. Seregina, L.M. Bronstein, O.A. Platonova, D.M. Chernyshov, P.M. Valetsky, J.r. Hartmann, E. Wenz, M. Antonietti, Chem. Mater. 9 (1997) 923.

[54] J. Huang, T. Jiang, H. Gao, B. Han, Z. Liu, W. Wu, Y. Chang, G. Zhao, Angew. Chem. Int. Ed. 43 (2004) 1397–1399.
[55] G. Ertl, H. Knozinger, J. Weitkamp (Eds.), Handbook of Heterogeneous Catalysis, Wiley-VCH, Weinheim, 1997.
[56] J. Dupont, G.S. Fonseca, A.P. Umpierre, P.F.P. Fichtner, S.R. Teixeira, J. Am. Chem. Soc. 124 (2002) 4228–4229.
[57] P.J. Dyson, Appl. Organomet. Chem. 16 (2002) 495–500.
[58] P.J. Dyson, in: a.M.T.J. Mc Cleverty (Ed.), Comprehensive Coordination Chemistry II, Elsevier, Amsterdam, pp. 557–566.
[59] P.J. Dyson, D. Zhao, Multiphase Homogeneous Catalysis, Wiley-VCH, Weinheim, pp. 494–511.
[60] P.J. Dyson, G. Laurenczy, C.A. Ohlin, J. Vallance, T. Welton, Chem. Commun. (2003) 2418–2419.
[61] J. Jacquemin, M.F. Costa Gomes, P. Husson, V. Majer, J. Chem. Thermodyn. 38 (2006) 490–502.
[62] J. Jacquemin, P. Husson, V. Majer, M.F. Costa Gomes, Fluid Phase Equilib. 240 (2006) 87.
[63] J. Jacquemin, P. Husson, V. Majer, M.F. Costa Gomes, J. Solution Chem. 36 (2007) 967–979.
[64] P. Migowski, D. Zanchet, G. Machado, M.A. Gelesky, S.r.R. Teixeira, J. Dupont, Phys. Chem. Chem. Phys. 12 (2010) 6826–6833.
[65] D. Li, R.B. Kaner, J. Am. Chem. Soc. 128 (2006) 968–975.

Imidazolium ionic liquids as promoters and stabilising agents for the preparation of metal(0) nanoparticles by reduction and decomposition of organometallic complexes

Martin H. G. Prechtl,†*[a] Paul S. Campbell,[b] Jackson D. Scholten,[a] Georgina B. Fraser,[b] Giovanna Machado,[c] Catherine C. Santini,*[b] Jairton Dupont*[a] and Yves Chauvin[b]

Received 9th August 2010, Accepted 1st September 2010
DOI: 10.1039/c0nr00574f

The organometallic complexes ([Ru(COD)(2-methylallyl)$_2$] and [Ni(COD)$_2$] (COD = 1,5-cyclooctadiene) dissolved in imidazolium ionic liquids (ILs) undergo reduction and decomposition, respectively, to afford stable ruthenium and nickel metal(0) nanoparticles (Ru(0)-NPs and Ni(0)-NPs) in the absence of classical reducing agents. Depending on the case, the reduction/auto-decomposition is promoted by either the cation and/or anion of the neat imidazolium ILs.

Introduction

In recent years, ILs have proven their versatility in synthetic and catalytic applications, provoking ever-growing interest in both academic and industrial research. One particularly intriguing field is the synthesis of nanoscale metal catalysts of controlled size and shape, namely metal(0) nanoparticles (M-NPs).[1–4] ILs have unique and tuneable properties useful in the synthesis of M-NPs *via* chemical routes. This can be controlled simply by incorporating coordinating groups,[5–7] varying the coordination strength of the anion,[8,9] or changing the length of the alkyl-chain in the cation.[10–15] In general, appropriate metal complexes or metal salts are dispersed/dissolved in the IL and subsequently reduced to the corresponding M-NPs, in the ubiquitous presence of reducing reagents such as molecular hydrogen gas, complex hydrides ($NaBH_4$ and $LiAlH_4$), hydrazine,[1–4] alcohols,[16] and thiols.[17] In some cases, the IL itself can carry the reducing agent, *e.g.* hydroxylated imidazolium salts,[18,19] and depending on the redox potential of the metal precursor, the imidazolium cation may even undergo oxidation. For example, in the case of Au(III), the imidazolium cation itself can act as a reducing agent to yield prismatic gold particles in BMI·PF_6.[20]

The preparation of M-NPs in ILs by simple decomposition of organometallic compounds in their formal zero oxidation states is invariably performed in the presence of hydrogen[11,21,22] or under thermal[8,15,23] or photolytic[9] conditions.

In this work, we report a novel approach for the synthesis of Ru(0)- and Ni(0)-NPs in imidazolium ILs, which act as incommensurably mild reducing/decomposing reagents for the organometallic complexes [Ru(COD)(2-methylallyl)$_2$] (COD = 1,5-cyclooctadiene) and [Ni(COD)$_2$] under very mild conditions. In these studies the role of both anion and cation is addressed and reaction pathways for the reduction/decomposition processes are proposed.

Results and discussion

The formation of Ru(0)-NPs using standard protocol with [Ru(COD)(2-methylallyl)$_2$] in IL (*i.e.* under 4 bar hydrogen at 50 °C)[7,14] was accompanied by the evolution of small amounts of odorous by-products (characteristic of ammonia/amines). This odour was particularly intense in the ILs BMI·NTf_2 and HM_2I·NTf_2 (Fig. 1).

The volatiles were thus analysed online in the gas phase with a mass gas-analyser. Indeed, compounds were detected with masses that could be assigned to small molecules formed due to the fragmentation of the imidazolium ring, such as acetonitrile/isocyanomethane ($M^+ = 41$), methylamine ($M^+ = 29$, MeN), ethylene ($M^+ = 28$) and hydrogen cyanide ($M^+ = 27$). Moreover, the observed C_4-fragment signals ($M^+ = 56$–58) provide strong evidence for the decomposition of the ruthenium complex [Ru(COD)(2-methylallyl)$_2$] involving the formation of isobutene/isobutane from the 2-methylallyl-ligand in the Ru(II) complex. Interestingly, the fragmentation of the IL seems to occur only during the reduction of Ru complex, but it is not promoted by the Ru(0)-NPs. The gaseous by-products were exclusively detected during the NP synthesis, but not when Ru(0)-NPs were stirred in BMI·NTf_2 and HM_2I·NTf_2 for a prolonged duration (several days) under identical conditions. A similar observation for the imidazolium ring fragmentation has previously been made, during the ultrasonic irradiation of imidazolium chloride

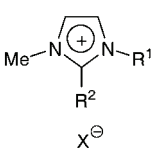

BMI.NTf_2, R^1= ^{n}Bu, R^2= H, X= $N(SO_2CF_3)_2$
$HM_2I.NTf_2$, R^1= ^{n}Hex, R^2= Me, X= $N(SO_2CF_3)_2$
BMI.BF_4, R^1= ^{n}Bu, R^2= H, X= BF_4
EMI.$B(CN)_4$, R^1= Et, R^2= H, X= $B(CN)_4$
BMI.$N(CN)_2$, R^1= ^{n}Bu, R^2= H, X= $N(CN)_2$
EMI.NTf_2, R^1= Et, R^2= H, X= $N(SO_2CF_3)_2$
$BM_2I.NTf_2$, R^1= ^{n}Bu, R^2= Me, X= $N(SO_2CF_3)_2$

Fig. 1 Structure of the ILs used in this study.

[a]*Laboratory of Molecular Catalysis, Institute of Chemistry, Universidade Federal do Rio Grande do Sul, Av. Bento Gonçalves 9500, 91501-970 Porto Alegre, RS, Brazil. E-mail: jairton.dupont@ufrgs.br; Fax: +55 51 33087304; Tel: +55 51 33086321*
[b]*Université de Lyon, Institut de Chimie de Lyon, C2P2, UMR 5265 CNRS—ESCPE Lyon, 43 bd du 11 Novembre 1918, F-69626 Villeurbanne Cedex, France. E-mail: santini@cpe.fr*
[c]*Centro de Tecnologias Estratégicas do Nordeste—CETENE, 50740-540 Recife, PE, Brazil*
† Present address: Humboldt University Berlin, Brook-Taylor-Strasse 2, 12489 Berlin, Germany. E-mail: . E-mail: martin.prechtl@hu-berlin.de

at 135 °C, causing degradation of ILs.[24–26] However, herein the observed decomposition of the imidazolium ring is not clearly understood.

More interestingly, further investigations of the Ru(II)/IL reaction system revealed a more important result: the presence of hydrogen gas as a reducing reagent for the Ru complex seems to be obsolete. Stirring a mixture of the complex in $HM_2I \cdot NTf_2$ under argon atmosphere at 50 °C for a prolonged period (2 days) resulted in a dark brown/black colloidal solution. Samples for TEM analysis were prepared by placing a small amount of the Ru(0)-NPs dispersed in $HM_2I \cdot NTf_2$ onto a holey carbon film supported by a copper grid. The diameters of the particles in the micrographs were measured using the software Sigma Scan Pro 5. Size distribution histograms of the NPs were obtained by measuring the diameter of randomly selected particles, resulting in the particle size of 2.0 ± 0.3 nm (see Fig. 2) with a monomodal distribution.

The crystalline structure of the particles was confirmed by HR-TEM micrographs, analysed using *Gatan Digital Micrograph Software*. By means of HR-TEM measurements it was possible to obtain the Fourier transform images from which lattice spacings of 2.04 Å and 2.13 Å were measured. These lattice spacings correspond to the interplanar distances (1 0 1) and (0 0 2), respectively, of hcp Ru(0). Isolation of the Ru(0)-NPs for analysis by XRD was not possible, corroborating previous reports.[14,22] The size and size distribution of the ruthenium NPs were similar to those of Ru(0)-NPs previously generated using hydrogen gas as a reducing agent for the reduction of [Ru(COD)(2-methylallyl)$_2$] or decomposition of [Ru(COD)(COT)] (COT = 1,3,5-cyclooctatriene).[7,11,14,22]

The Ru(0)-NP formation led us to propose a reaction pathway in which the imidazolium ILs $BMI \cdot NTf_2$ and $HM_2I \cdot NTf_2$ might act as reducing agents for [Ru(COD)(2-methylallyl)$_2$]. Here the NTf_2 anion would act as a nucleophile[27,28] and attack the allylic-ligand of the complex (Schemes 1 and 2).

This stoichiometric reaction would cause the concomitant reduction of the Ru(II) complex and subsequent decomposition of the IL. Consequently, the ruthenium would lose its ligand-sphere and be reduced to ruthenium(0) atoms that coalesce generating the Ru(0)-NPs. It is proposed that during the reduction process of the Ru(II) complex, the first step involves a ligand exchange between the COD and a stronger coordinating ligand, occurring readily under the given reaction conditions.[29] A stronger coordinating ligand is easily provided in *neat* imidazolium ionic liquid as solvent, where classical and abnormal *N*-heterocyclic carbenes (NHCs) formed *in situ* might act as a ligand.[30,31] As a consequence, the NTf_2 anion would "lose" its counterion, thus enhancing its nucleophilicity. And this would favour its subsequent attack on the allylic species of the Ru(II) complex. The resulting ruthenium(0) metal atoms in the IL go on to generate the M-NPs. The isobutene by-product was detected by MS analysis of the gas phase (see above). However, attempts to detect the hypothesised by-product *N*-isobutene *N*-triflate in the liquid-phase by NMR were unsuccessful, presumably due to the very low concentration.

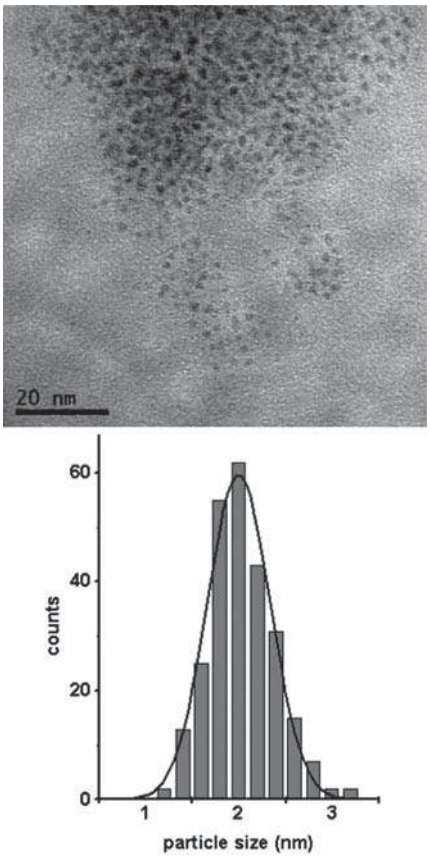

Fig. 2 Selected TEM image of Ru(0)-NPs (2.0 ± 0.3 nm) in $HM_2I \cdot NTf_2$ and the histogram of the NPs size distribution.

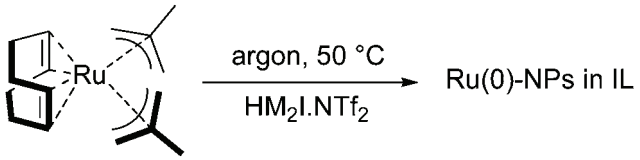

Scheme 1 Formation of Ru(0)-NPs in $HM_2I \cdot NTf_2$.

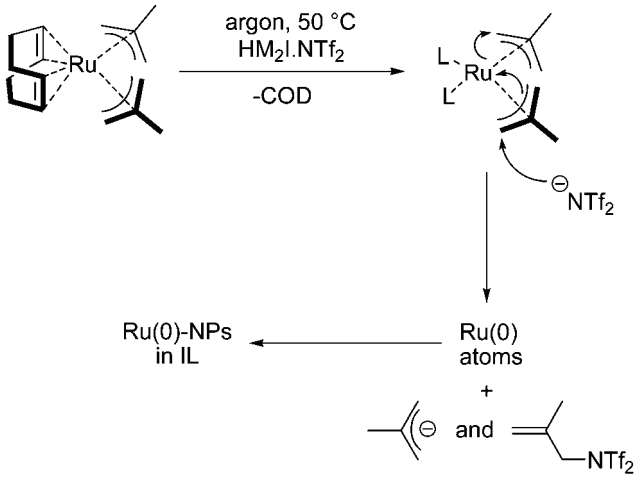

Scheme 2 Proposed reductive elimination of the allyl-ligand induced by the NTf_2 anion (L = ligand/solvent-IL).

To prove this pathway, the anion-effect in different imidazolium ILs was therefore investigated. When using the IL BMI·BF_4 (BF_4 = tetrafluoroborate), for example, a green suspension that showed no indication of IL decomposition or Ru(0)-NPs formation was obtained. Also, using EMI·$B(CN)_4$ and BMI·$N(CN)_2$, the strongly coordinating nature of the anions prevented the reduction of the Ru(II) complex and the reaction solution remained clear and colourless, even when subjected to a longer reaction time (5 days). Furthermore, the typical catalytic properties of nanoscale ruthenium catalysts in arene hydrogenation were tested with these Ru/IL-systems.[14] Indeed, the Ru(0)-NPs produced in HM_2I·NTf_2 showed the highest activity in toluene hydrogenation, resulting in conversions above 95% (4 bar H_2 at 75 °C, 18 h), similar to results previously reported.[14] The Ru(0)-NPs in BMI·NTf_2 were also active in toluene hydrogenation, but with a poorer conversion (55%) under the same conditions. In addition, the systems using the ILs BMI·BF_4, EMI·$B(CN)_4$ and BMI·$N(CN)_2$ were subjected to identical conditions, to gauge whether Ru(0)-NPs would form *in situ* during toluene hydrogenation. Indeed, the green suspension in BMI·BF_4 turned dark brown and the toluene was hydrogenated, albeit with low conversion (<20%), indicating the formation of Ru(0)-NPs. In contrast, the clear solutions in EMI·$B(CN)_4$ and BMI·$N(CN)_2$ turned slightly yellow, but no hydrogenation of toluene was observed.

The stability of [Ni(COD)$_2$] in imidazolium ILs was also investigated. This complex can be easily decomposed affording Ni(0)-NPs under hydrogen in organic solvents such as THF, in the presence of hexadecylamine (HDA) as the stabilising ligand or polyvinylpyrrolidone (PVP) as the polymer support.[32,33] In this case, cyclooctane is produced as a side product. Moreover, Ni(0)-NPs from the decomposition of [Ni(COD)$_2$] under hydrogen in imidazolium-based ILs have also been reported.[12,34] However, it is worth noting that in this previous work a substantial amount of benzene was used to aid the dissolution of [Ni(COD)$_2$] (6 mL of benzene for 2 mL of IL), and although effort was made to remove the volatiles before decomposition, it is not possible to be sure of the complete removal of benzene and therefore the media in which the decomposition actually occurred.[12,34]

In this work, spontaneous decomposition of [Ni(COD)$_2$] occurred upon dissolution at 25 °C, in both EMI·NTf_2 and BMI·NTf_2, in the absence of hydrogen. TEM was performed on the resulting black solutions and revealed in each case a mixture of Ni(0)-NPs (<10 nm) and sponge-like agglomerates of larger particles (Fig. 3). It can be seen from the TEM image that these sponge-like structures clearly consist of agglomerates of individual particles. This is completely different from previous findings, highlighting the important role of co-solvents.[12,34]

Notably ^{1}H NMR spectroscopy and gas chromatography performed on the resulting solution showed only a trace of cyclooctane, resulting from the hydrogenation of 1,5-COD ligand, the by-product of decomposition reported in the literature.[32,33] Instead, the presence of both 1,5-COD and its isomer 1,3-cyclooctadiene (1,3-COD) was detected by both gas chromatography and ^{1}H/^{13}C NMR spectroscopy. 1,3-COD must be a result of the isomerisation of 1,5-COD, which could only take place at a metal centre in the presence of Ni–H bond (Scheme 3).

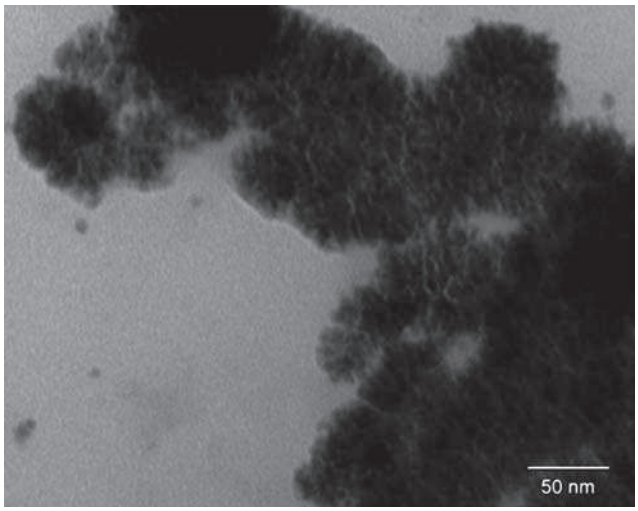

Fig. 3 Sponge-like agglomerates of Ni(0)-NPs formed by auto-decomposition of [Ni(COD)$_2$] in BMI·NTf_2.

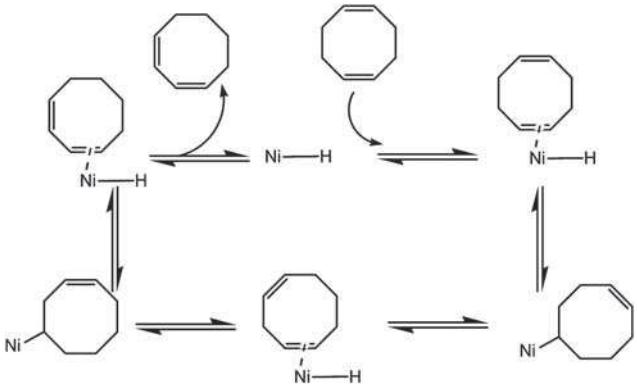

Scheme 3 Mechanism for the isomerisation of COD necessitating a Ni–H specie.

With Ru(0)-NPs, the presence of surface hydrides has been proven by hydrogenation of ethylene without the addition of H_2 by a solution of Ru(0)-NPs in IL.[35] This experiment was repeated for the Ni(0)-NPs formed by auto-decomposition of [Ni(COD)$_2$] in BMI·NTf_2. After treatment under ethylene atmosphere (4 bars, 100 °C, 24 h) no ethane was detected by GC as a result of ethylene hydrogenation, however, significant amounts of butenes and hexenes were detected, probably a result of oligomerisation of the ethylene. Interestingly, the formation of an ethyl substituted IL BMEI·NTf_2 (BMEI = 1-*n*-butyl-2-ethyl-3-methylimidazolium) was also observed by NMR spectroscopies (COSY, HETCOR and DOSY) and confirmed by electrospray mass spectrometry where cations at m/z = 139 and 167 were observed with similar abundances, corresponding to $[BMI]^+$ and $[BMEI]^+$, respectively. A small amount of the cation $[B_2MI]^+$ (B_2MI = 1,2-di-*n*-butyl-3-methylimidazolium) was also observed by mass spectrometry, m/z = 195, probably a result of oligomerisation of ethylene to 1-butene before reaction with the imidazolium cycle. The evidence gathered suggests that the observed decomposition could be due to the cleavage of the very acidic C2–H bond and the consequent *in situ* generation of NHC

species, as already reported in the case of Ir(0)-NP preparation in ILs,[36–40] and with homogeneous complexes of Ni,[41] Pd,[42–44] Rh,[30,45] and Ir.[45] Cavell and co-workers have proposed a mechanism for the possible catalytic cycle for the imidazolium/alkene coupling reaction where the organometallic starting material was $[Ni(OAc)_2]$.[46] The same phenomenon has also been observed in work by Lecocq and Olivier-Bourbigou who were investigating the oligomerisation behaviour of Ni in imidazolium ILs.[41] At this point it is impossible to determine whether the observed reactions (isomerisation of COD and formation of $BMEI \cdot NTf_2$) occur on molecular or colloidal species. However, these results do prove that the cleavage of the C2–H bond occurs during the spontaneous decomposition on dissolution. The proposed mechanism of the reaction of imidazolium salts with low valent M(0) (M = Pd and Ni) hypothesises the formation of a molecular carbene–M–H species, as also proposed in the catalytic cycle for oligomerisation and formation of trialkylimidazolium species.[47,48] The presence of bis(imidazolylidene)nickel complexes $[(NHC)_2NiH]^+$ was also detected by mass spectrometry, implying that a molecular intermediate is in fact present as proposed. This may act as a transient species and could be the active species for the above mentioned reactions. Similar bis-carbene iodide nickel complexes have already been prepared in imidazolium ILs and isolated by Wasserscheid's group.[46] These were indeed found to be active in the dimerisation of butene carried out in ILs, although no production of Ni(0)-NPs was noted here, perhaps due to the presence of the strongly coordinating iodides. Although the exact mechanism remains unclear, from our investigations it is certain that the spontaneous decomposition of $[Ni(COD)_2]$ on dissolution into the ILs with short alkyl chains involves attack on the acidic C2–H (Scheme 4).

To achieve the controlled generation of small-size Ni(0)-NPs, we must find a way of inhibiting this auto-decomposition in imidazolium ILs with short alkyl chains. Another strategy attempted in order to circumvent the problem was to use an IL which does not contain the most acidic C2–H proton such as $BM_2I \cdot NTf_2$. Surprisingly, the $[Ni(COD)_2]$ still decomposed on stirring, but this time afforded well dispersed Ni(0)-NPs (7.0 ± 2.0 nm, Fig. 4). This can only be explained by attack on the two less acidic protons C4–H, C5–H of the imidazolium ring and generation of transient non-classical NHC ligands.[31]

In another attempt to avoid auto-decomposition the NTf_2-anion was exchanged for the more strongly coordinating BF_4-anion, yielding important results. In this case, similarly to the case of $[Ru(COD)(2\text{-methylallyl})_2]$ the decomposition of $[Ni(COD)_2]$ in $BMI \cdot BF_4$ occurred not spontaneously but very slowly at 25 °C only under 4 bar of H_2, once again highlighting the importance of the NTf_2-anion. Therefore, as the auto-decomposition of $[Ni(COD)_2]$ to Ni(0)-NPs was also observed uniquely in NTf_2-ILs, it is possible that the NTf_2 anion intervenes in the Ni(0)-NP formation through interaction with the COD ligands, similarly to the case of the Ru(II) complex.

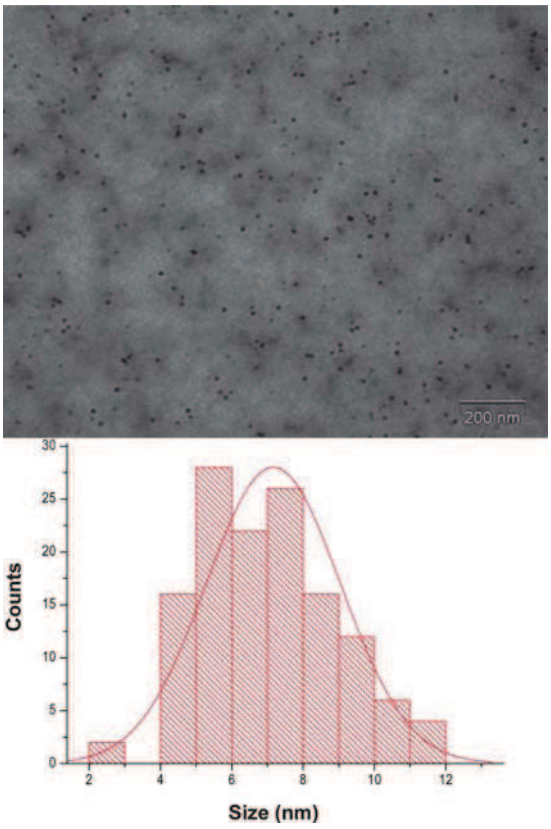

Fig. 4 TEM image of Ni(0)-NPs (7.0 ± 2.0 nm) formed by auto-decomposition of $[Ni(COD)_2]$ in $BM_2I \cdot NTf_2$ and size distribution histogram.

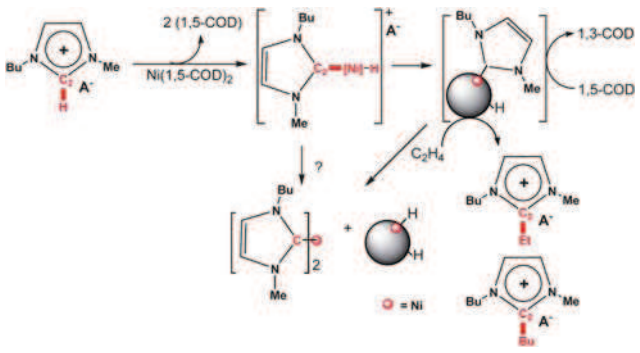

Scheme 4 Reactions occurring during the auto-decomposition of $[Ni(COD)_2]$ in imidazolium ILs.

Conclusions

In summary, IL decomposition and simultaneous Ru(0)-NP formation are limited to imidazolium salts containing the NTf_2 anion. These results may explain how the Ru(0)-NPs formation is induced by imidazolium *N*-triflate ILs, but cannot explain the exact mechanism for the imidazolium ring fragmentation in small quantities. Most importantly, the formation of small-sized active ruthenium nanoscale hydrogenation catalysts is possible at low temperature and atmospheric pressure in the absence of classical and potentially dangerous reducing agents such as hydrogen gas (under elevated pressure), pyrophoric $LiAlH_4$ or hazardous hydrazine. Moreover, an unexpected spontaneous decomposition of $[Ni(COD)_2]$ occurred without the addition of hydrogen for imidazolium ILs with short alkyl chains: ILs $BMI \cdot NTf_2$, $EMI \cdot NTf_2$ and $BM_2I \cdot NTf_2$. In the case of ILs $BMI \cdot NTf_2$ and $EMI \cdot NTf_2$, TEM micrographs showed that Ni(0)-NPs of fairly large diameter were formed as well as sponge-like super

agglomerates. However, for IL $BM_2I \cdot NTf_2$ well dispersed Ni(0)-NPs are formed. An explanation for the activation of the acidic protons on the imidazolium ring and the subsequent NHC formation that led to a rapid decomposition of the complex has been proposed. The additional interaction between the NTf_2 anion and the COD ligands on the Ni complex, which also may support the Ni(0)-NPs formation, cannot be excluded nonetheless. It is conceivable that this novel approach may be extended as a general access to M-NPs in imidazolium NTf_2-ILs, starting from organometallic complexes bearing only COD, allylic and/or olefinic ligands, such as $[Co(COD)_2]$, [Ru(COD)(COT)], $[Rh(allyl)_3]$, $[Pd(COD)_2]$, $[Pt(COD)_2]$ or [Pt(norbornene)$_3$].

Experimental

General

All manipulations were carried out under argon atmosphere. The organometallic complexes [Ru(COD)(2-methylallyl)$_2$] and $[Ni(COD)_2]$ were purchased from Sigma-Aldrich and Strem Chemicals, respectively. For the ruthenium experiments, a Hiden QIC20 MS-QTOF gas-analyser was used for the gas phase analysis after the synthesis of Ru(0)-NPs. TEM analyses were performed in a JEOL-JEM 2010 microscope operating at 200 kV (*UFRGS-CME*, Brazil) and EDS, and used for catalytic experiments as previously described.[14] The HR-TEM was performed at the *"Centro de Tecnologias Estratégicas do Nordeste" (CETENE)*, Recife/Brazil. The ILs were synthesised as previously reported,[49] and ILs $EMI \cdot B(CN)_4$ and $BMI \cdot N(CN)_2$ were purchased from *Merck KGaA*, Germany.

In the case of nickel experiments, conventional TEM micrographs were obtained at the *"Centre Technologique des Microstructures"*, France, using a Philips 120 CX electron microscope operating at 120 kV. Size distribution histograms were constructed from the measurement of at least 200 different NPs assuming a near spherical shape and random orientation. Solution NMR spectra were recorded on Bruker Avance 300 MHz spectrometer for ^{1}H and ^{13}C. DRX 500 MHz for ^{2}H. Gas phase ^{1}H NMR spectra were obtained on a Bruker DRX 500 instrument at 298 K (nominal). Mass spectra were acquired on a ThermoFinnigan LCQ Advantage ion trap instrument, detecting positive (+) and negative (−) ions in the ESI mode. Samples (1 to 10 μg mL^{-1} in acetonitrile) were infused directly into the source (5 μL min^{-1}) using a syringe pump. The following source parameters were applied: spray voltage 3.0–3.5 kV, nitrogen sheath gas flow 5–20 arbitrary units. The heated capillary was held at 200 °C. MS spectra were obtained by applying a relative collision energy of 25 to 40% of the instrumental maximum. The products were quantitatively analysed by gas chromatography on a P6890 chromatograph equipped with a flame ionisation detector (FID) and an Al_2O_3/KCl column (*L*: 50 m, diameter: 0.32 mm, and film thickness: 5 μm). The injector and detector temperature was 230 °C, and the injection volume was 1 μL. The temperature was fixed at 190 °C. The synthesis of ILs was carried out as previously reported.[43]

Synthesis of Ru(0)-NPs

In a typical experiment, a Fischer–Porter bottle was loaded with [Ru(COD)(2-methylallyl)$_2$] (30 mg, 0.094 mmol) under argon. Then, the IL $HM_2I \cdot NTf_2$ (1.5 mL) was added *via* syringe under an argon flow. The mixture was stirred at room temperature for 60 min, resulting in a turbid dispersion. The system was heated to 50 °C, and stirred under argon for two days resulting in a black suspension. The Fischer–Porter bottle was connected to a mass gas-analyser in order to evaluate the gas phase. After analysis the Fischer–Porter bottle was then kept under reduced pressure to eliminate the organic volatiles formed. An aliquot of the Ru(0)-NPs embedded in the IL was analysed by TEM.

Synthesis of Ni(0)-NPs

$[Ni(COD)_2]$ (50 mg, 0.14 mmol) was stirred under argon in the ILs $BMI \cdot NTf_2$, $EMI \cdot NTf_2$ and $BM_2I \cdot NTf_2$ (10 mL) producing a pale yellow solution at 25 °C. After 1 h the solution had turned green and after a further hour a black solution resulted. Samples for TEM observations were prepared by placing a thin film of the Ni(0)-NPs dispersed in ILs on a copper grid coated with holey carbon film.

Oligomerisation of ethylene by Ni(0)-NPs in IL

A 2 mL sample of the Ni(0)-NPs solution in the IL was introduced under argon into a Schlenk of known volume. The sample was treated under flow of argon for 18 h. The argon atmosphere was replaced with a known pressure of ethylene using a vacuum line and the system was stirred. A decrease of the internal pressure was observed, and the composition of the gas phase was monitored by gas chromatography. After 12 h, the atmosphere was replaced by a H_2 atmosphere and the system was heated and stirred for 12 h. The composition of the gas phase was again monitored by gas chromatography.

Acknowledgements

This work was funded by ANR project CALIST (ANR-07-CP2D-02-03), the "Ministère de l'enseignement supérieur et de la recherche" (P.S.C.), CNPq, CAPES, INCT-Catal. and the Alexander-von-Humboldt Foundation (M. H. G. Prechtl). G.B.F. acknowledges the grant attributed by the Erasmus programme.

References

1 J. Dupont and J. D. Scholten, *Chem. Soc. Rev.*, 2010, **39**, 1780–1804.
2 P. Migowski and J. Dupont, *Chem.–Eur. J.*, 2007, **13**, 32–39.
3 H. Boennemann and K. S. Nagabhushana, *Nanoclusters in Catalysis and Materials Science: the Issue of Size Control*, ed. B. Corain, G. Schmid and N. Toshima, Elsevier B.V., Amsterdam, 2008, pp. 21–48.
4 H. Boennemann, K. S. Nagabhushana and R. M. Richards, *Nanoparticles and Catalysis*, Wiley-VCH, Weinheim, 2008.
5 Y. G. Cui, I. Biondi, M. Chaubey, X. Yang, Z. F. Fei, R. Scopelliti, C. G. Hartinger, Y. D. Li, C. Chiappe and P. J. Dyson, *Phys. Chem. Chem. Phys.*, 2010, **12**, 1834–1841.
6 Z. F. Fei, D. B. Zhao, D. Pieraccini, W. H. Ang, T. J. Geldbach, R. Scopelliti, C. Chiappe and P. J. Dyson, *Organometallics*, 2007, **26**, 1588–1598.
7 M. H. G. Prechtl, J. D. Scholten and J. Dupont, *J. Mol. Catal. A: Chem.*, 2009, **313**, 74–78.
8 E. Redel, R. Thomann and C. Janiak, *Inorg. Chem.*, 2008, **47**, 14–16.
9 E. Redel, R. Thomann and C. Janiak, *Chem. Commun.*, 2008, 1789–1791.

10 P. S. Campbell, C. C. Santini, F. Bayard, Y. Chauvin, V. Collière, A. Podgorsek, M. F. Costa Gomes and J. Sá, *J. Catal.*, 2010, **257**, 99–107.
11 T. Gutel, C. C. Santini, K. Philippot, A. Padua, K. Pelzer, B. Chaudret, Y. Chauvin and J. M. Basset, *J. Mater. Chem.*, 2009, **19**, 3624–3631.
12 P. Migowski, G. Machado, S. R. Texeira, M. C. M. Alves, J. Morais, A. Traverse and J. Dupont, *Phys. Chem. Chem. Phys.*, 2007, **9**, 4814–4821.
13 P. Migowski, D. Zanchet, G. Machado, M. A. Gelesky, S. R. Teixeira and J. Dupont, *Phys. Chem. Chem. Phys.*, 2010, **12**, 6826–6833.
14 M. H. G. Prechtl, M. Scariot, J. D. Scholten, G. Machado, S. R. Teixeira and J. Dupont, *Inorg. Chem.*, 2008, **47**, 8995–9001.
15 M. Scariot, D. O. Silva, J. D. Scholten, G. Machado, S. R. Teixeira, M. A. Novak, G. Ebeling and J. Dupont, *Angew. Chem., Int. Ed.*, 2008, **47**, 9075–9078.
16 H. J. Ryu, L. Sanchez, H. A. Keul, A. Raj and M. R. Bockstaller, *Angew. Chem., Int. Ed.*, 2008, **47**, 7639–7643.
17 L. Zhao, C. Y. Zhang, L. Zhuo, Y. G. Zhang and J. Y. Ying, *J. Am. Chem. Soc.*, 2008, **130**, 12586–12587.
18 S. Choi, K. S. Kim, S. H. Yeon, J. H. Cha, H. Lee, C. J. Kim and I. D. Yoo, *Korean J. Chem. Eng.*, 2007, **24**, 856–859.
19 K. S. Kim, S. Choi, J. H. Cha, S. H. Yeon and H. Lee, *J. Mater. Chem.*, 2006, **16**, 1315–1317.
20 Y. Gao, A. Voigt, M. Zhou and K. Sundmacher, *Eur. J. Inorg. Chem.*, 2008, 3769–3775.
21 E. T. Silveira, A. P. Umpierre, L. M. Rossi, G. Machado, J. Morais, G. V. Soares, I. L. R. Baumvol, S. R. Teixeira, P. F. P. Fichtner and J. Dupont, *Chem.–Eur. J.*, 2004, **10**, 3734–3740.
22 T. Gutel, J. Garcia-Anton, K. Pelzer, K. Philippot, C. C. Santini, Y. Chauvin, B. Chaudret and J. M. Basset, *J. Mater. Chem.*, 2007, **17**, 3290–3292.
23 D. O. Silva, J. D. Scholten, M. A. Gelesky, S. R. Teixeira, A. C. B. Dos Santos, E. F. Souza-Aguiar and J. Dupont, *ChemSusChem*, 2008, **1**, 291–294.
24 D. J. Flannigan, S. D. Hopkins and K. S. Suslick, *J. Organomet. Chem.*, 2005, **690**, 3513–3517.
25 J. D. Oxley, T. Prozorov and K. S. Suslick, *J. Am. Chem. Soc.*, 2003, **125**, 11138–11139.
26 S. Sowmiah, V. Srinivasadesikan, M. C. Tseng and Y. H. Chu, *Molecules*, 2009, **14**, 3780–3813.
27 S. Chowdhury, R. S. Mohan and J. L. Scott, *Tetrahedron*, 2007, **63**, 2363–2389.
28 R. Bini, C. Chiappe, E. Marmugi and D. Pieraccini, *Chem. Commun.*, 2006, 897–899.
29 J. P. Genet, S. Mallart, C. Pinel, S. Juge and J. A. Laffitte, *Tetrahedron: Asymmetry*, 1991, **2**, 43–46.
30 J. D. Scholten and J. Dupont, *Organometallics*, 2008, **27**, 4439–4442.
31 S. Grundemann, A. Kovacevic, M. Albrecht, J. W. Faller and R. H. Crabtree, *Chem. Commun.*, 2001, 2274–2275.
32 N. Cordente, C. Amiens, B. Chaudret, M. Respaud, F. Senocq and M. J. Casanove, *J. Appl. Phys.*, 2003, **94**, 6358–6365.
33 N. Cordente, M. Respaud, F. Senocq, M. J. Casanove, C. Amiens and B. Chaudret, *Nano Lett.*, 2001, **1**, 565–568.
34 P. Migowski, S. R. Teixeira, G. Machado, M. C. M. Alves, J. Geshev and J. Dupont, *J. Electron Spectrosc. Relat. Phenom.*, 2007, **156**, 195–199.
35 P. S. Campbell, C. C. Santini, D. Bouchu, B. Fenet, K. Philippot, B. Chaudret, A. A. H. Padua and Y. Chauvin, *Phys. Chem. Chem. Phys.*, 2010, **12**, 4217–4223.
36 L. S. Ott, S. Campbell, K. R. Seddon and R. G. Finke, *Inorg. Chem.*, 2007, **46**, 10335–10344.
37 L. S. Ott, M. L. Cline, M. Deetlefs, K. R. Seddon and R. G. Finke, *J. Am. Chem. Soc.*, 2005, **127**, 5758–5759.
38 L. S. Ott and R. G. Finke, *Inorg. Chem.*, 2006, **45**, 8382–8393.
39 J. D. Scholten, G. Ebeling and J. Dupont, *Dalton Trans.*, 2007, 5554–5560.
40 J. D. Scholten and J. Dupont, in *Iridium Complexes in Organic Synthesis*, ed. L. A. Oro and C. Claver, Wiley-VCH Verlag GmbH & Co. KGaA, Weinheim, 2009, pp. 369–389.
41 V. Lecocq and H. Olivier-Bourbigou, *Oil Gas Sci. Technol.*, 2007, **62**, 761–773.
42 C. M. Crudden and D. P. Allen, *Coord. Chem. Rev.*, 2004, **248**, 2247–2273.
43 L. Magna, Y. Chauvin, G. P. Niccolai and J. M. Basset, *Organometallics*, 2003, **22**, 4418–4425.
44 M. H. G. Prechtl, J. D. Scholten and J. Dupont, *Molecules*, 2010, **15**, 3441–3461.
45 U. Hintermair, T. Gutel, A. M. Z. Slawin, D. J. Cole-Hamilton, C. C. Santini and Y. Chauvin, *J. Organomet. Chem.*, 2008, **693**, 2407–2414.
46 D. S. McGuinness, W. Mueller, P. Wasserscheid, K. J. Cavell, B. W. Skelton, A. H. White and U. Englert, *Organometallics*, 2002, **21**, 175–181.
47 N. D. Clement, K. J. Cavell, C. Jones and C. J. Elsevier, *Angew. Chem., Int. Ed.*, 2004, **43**, 1277–1279.
48 D. C. Graham, K. J. Cavell and B. F. Yates, *Dalton Trans.*, 2007, 4650–4658.
49 C. C. Cassol, G. Ebeling, B. Ferrera and J. Dupont, *Adv. Synth. Catal.*, 2006, **348**, 243–248.

iii

Appendix 3

Separation of Hafnium from Zirconium in Ionic Liquids

Separation of Zirconium from Hafnium in Ionic Liquids

The issue

Zirconium and hafnium occur naturally together, the most common ore being "zircon". As their chemical properties are very similar, extracting and separating highly pure metals is a difficult challenge. In nuclear applications zirconium has a low neutron absorption cross-section and is therefore a useful cladding material ("zircaloy"). Hafnium, on the other hand, has a high neutron absorption cross-section (nearly 600 times that of zirconium). Therefore, for nuclear applications, zirconium metal must contain less than 100 ppm hafnium. Three main processes are in current use for the separation of zirconium from hafnium: multiple crystallization of potassium zirconium fluoride; solvent extraction of the chlorides using methyl isobutyl ketone and water; extractive distillation of the chlorides using a $KCl/AlCl_3$ molten salt bath at high temperature.[1-11] These three processes present several severe drawbacks, e.g. recovery of oxide products, corrosion problems, high running temperatures, etc. Hf/Zr separation is still a economic and technical challenge (more than 60 papers published during the last decade, of which 25 % as patents and from more than 20 different countries).[12]

Strategies

As part of this work, two strategies were attempted using ionic liquids with the ultimate goal of achieving Zr/Hf separation with reduced hazards and process costs, as ILs are considered as "green solvents", due to some specific features such as non-flammability, high thermal stability and non-volatility.[13]

1) Firstly, a novel range of imidazolium chlorometallate ionic liquids based on hafnium and zirconium were synthesised and fully characterised. A difference in chemical or physical properties of the resulting materials may have been exploited in their extraction. The full characterisation of the new materials obtained is described in the *Dalton Transactions* paper attached.
2) Secondly, it is reported in the literature that $ZrCl_4$ and $HfCl_4$ display a different reactivity towards methyl-substituted aromatics; $ZrCl_4$ produces a molecular complex,[14] while reaction with $HfCl_4$ results in an ionic species.[15, 16] Thus the approach was to use this difference in reactivity to undertake a subsequent liquid-liquid extraction, based on

the potential high solubility of the ionic complex in an ionic liquid compared to an organic solvent. The preliminary positive results, for which a patent application has been submitted, are described in the *Chimica Oggi* paper, also included in this appendix.

References

[1] B. Prakash, C. V. Sundaram, *Met. Mater. Proc.* **2009**, *21*, 21.

[2] V. Ogarev, A. Skotnicki, B. Ninham, ,, *Patent AU. 20080527.* **2009**, 12pp.

[3] L. A. Niselson, E. A. Egorov, E. L. Chuvilina, O. A. Arzhatkina, V. D. Fedorov, *J. Chem. Eng.*, **2009**, *54*, 726.

[4] M. Smolik, A. Jakobik-Kolon, M. Poranski, *Hydrometallurgy*, **2009**, *95*, 350.

[5] K. Saberyan, A. H. Meysami, F. Rashchi, E. Zolfonoun, *Chin. J. Chem.*, **2008**, *26*, 2067.

[6] M. Taghizadeh, R. Ghasemzadeh, S. N. Ashrafizadeh, K. Saberyan, M. G. Maragheh, *Hydrometallurgy*, **2008**, *90*, 115.

[7] L. Delons, G. Picard, D. Tigreat, *Compagnie Europeenne Du Zirconium Cezus, WO 20020412.* **2002**, 20 pp.

[8] L. Delons, S. Lagarde, A. Favre Reguillon, S. Pellet Rostaing, M. Lemaire, L. Poriel, *Compagnie Europeenne du Zirconium-Cezus, Fr. Fr 2004-7721* **2006**, 40.

[9] J. A. Sommers, J. G. Perrine, *US, ATI Properties, Inc., USA, 20020129.* **2003**, 8 pp.

[10] N. Ozanne, M. L. Lemaire, A. Guy, J. Foos, S. Pellet-Rostaing, F. Chitry, *WO, Compagnie Europeenne du Zirconium Cezus, Fr., 20010910.* **2002**, 23 pp.

[11] A. Da Silva, E. El-Ammouri, P. A. Distin, *Can. Metall. Q.* **2000**, *39*, 37.

[12] R. H. Nielsen, in *KIRK OTHMER ENCYCLOPEDIA OF CHEMICAL TECHNOLOGY* John Wiley & Sons, New York, **2004**.

[13] P. Wasserscheid, T. Welton, *Ionic liquids in synthesis*, Wiley-VCH, Weinheim, **2008**.

[14] F. Musso, E. Solari, C. Floriani, K. Schenk, *Organometallics* **1997**, *16*, 4889.

[15] F. Calderazzo, I. Ferri, G. Pampaloni, S. Troyanov, *J. Organomet. Chem.*, **1996**, *518*, 189.

[16] F. Calderazzo, P. Pallavicini, G. Pampaloni, P. F. Zanazzi, *J. Chem. Soc., Dalton Trans.*, **1990**, 2743.

Synthesis and characterisation of ionic liquids based on 1-butyl-3-methylimidazolium chloride and MCl_4, M = Hf and Zr†

Paul S. Campbell,[a] Catherine C. Santini,*[a] Denis Bouchu,[b] Bernard Fenet,[c] Leszek Rycerz,[d] Yves Chauvin,[a] Marcelle Gaune-Escard,[e] Catherine Bessada[f] and Anne-Laure Rollet[f,g]

Received 15th September 2009, Accepted 26th October 2009
First published as an Advance Article on the web 1st December 2009
DOI: 10.1039/b919094e

Dialkylimidazolium chlorometallate molten salts resulting from the combination of zirconium or hafnium tetrachloride and 1-butyl-3-methylimidazolium chloride, $[C_1C_4Im][Cl]$, have been prepared with a molar fraction of MCl_4, $R = n_{MCl4}/n_{MCl4} + n_{[C1C4IM][Cl]}$ equal to 0, 0.1, 0.2, 0.33, 0.5, 0.67. The structure and composition were studied by Differential Scanning Calorimetry (DSC), ^{35}Cl (263 to 333 K), ^{1}H and ^{13}C solid state and solution NMR spectroscopy, and electrospray ionisation (ESI) mass spectrometry. The primary anions of the MCl_4-based ILs were $[MCl_5]$, $[MCl_6]$ and $[M_2Cl_9]$, whose relative abundances varied with R. For $R = 0.33$, pure solid $[C_1C_4Im]_2[MCl_6]$, for both M = Zr and Hf are formed (m.p. = 366 and 385 K, respectively). For $R = 0.67$ pure ionic liquids $[C_1C_4Im][M_2Cl_9]$ for both M = Zr and Hf are formed (T_g = 224 and 220 K, respectively). The thermal dissociation has been attempted of $[C_1C_4Im]_2[HfCl_6]$, and $[C_1C_4Im]_2[ZrCl_6]$ monitored by ^{35}Cl and ^{91}Zr solid NMR (high temperature up to 551 K).

Introduction

During the past couple of decades, ionic liquids have undergone fast development for use in industrial chemical procedures, driven by a need for more environmentally friendly solvents. From a chemical engineering point of view, there are certain advantages offered by the properties of ionic liquids, notably the large range of temperatures, high thermal conductivity and negligible vapour pressure. This means that they are completely non-volatile right up to their temperature of decomposition (typically above 573 K) and therefore the risk of solvent vapours escaping into the atmosphere is considerably reduced.

The development of acidic ionic liquids, derived from metal halides, as replacement for traditional acids has received significant attention.[1-6] Since the first chloroaluminate of N-butylpyridinium,[7] similar results have been obtained with salts of the N-alkylimidazolium cation. Chloroaluminate anions have been widely characterised by NMR spectroscopy (^{27}Al, ^{31}P and ^{1}H),[5,8-12] Raman scattering, UV and IR spectroscopies and electrochemical methods,[11-15] showing the accessibility of the mono-, di- and trinuclear anions, $AlCl_4^-$, $Al_2Cl_7^-$ and $Al_3Cl_{10}^-$ with no more than two different species coexisting at any given organochloride/$AlCl_3$ ratio. Their utility in catalysis has been proven in a number of recent publications.[16-20]

In the literature, several imidazolium salts of less hydrolysable chlorides, based on iron,[21-23] tin,[22,24] zinc,[19,22,24-27] copper,[22] indium, gold,[24,28,29] nickel,[30] platinum,[31] cobalt,[30] manganese[22] and vanadium,[32] have been reported.

In group 4, imidazolium salts derived from Ti(IV) have recently been reported.[33] However, only one imidazolium chlorozirconate, $[C_1C_4Im]_2[ZrCl_6]$, is described,[22] although these chlorometallates may be studied for the separation Hf/Zr which is still an economic and technical challenge.[34]

This paper describes the synthesis and full characterisation [DSC, thermogravimetric analysis (TGA), ^{1}H, ^{13}C and ^{35}Cl NMR spectroscopy, electrospray mass spectrometry] of a range of imidazolium salts based on $ZrCl_4$ and $HfCl_4$ and the study of their thermal stability by high temperature ^{35}Cl and ^{91}Zr NMR experiments.

Results and discussion

The ionic liquids were prepared by a slow addition of solid anhydrous MCl_4 into molten $[C_1C_4Im][Cl]$ (338 K), and the mixture was kept at 338 K for 12 h under argon, Scheme 1, with R, the molar fraction, *i.e.* the ratio of the number of moles of MCl_4 divided by the sum of the number of moles of $[C_1C_4Im][Cl]$ and MCl_4 $R = n_{MCl4}/n_{MCl4} + n_{[C1C4IM][Cl]}$ with R = 0.1 ; 0.2 ; 0.33 ; 0.5 and 0.67. As generally observed for all chlorometallates, for R = 0.33, 0.5 and 0.67 stoichiometric compounds have been obtained and fully characterised.

[a]*Université de Lyon, Institut de Chimie de Lyon, UMR 5265 CNRS-Université de Lyon-ESCPE Lyon, LC2P2, Equipe COMS, ESCPE 43 Boulevard du 11 Novembre 1918, 69616, Villeurbanne, France. E-mail: santini@cpe.fr; Fax: +33(0)472431795; Tel: +33(0)472431794*
[b]*Centre Commun de Spectrométrie de Masse, Université de Lyon, ESCPE, 43 Boulevard du 11 Novembre 1918, F-69616 Villeurbanne, France*
[c]*Centre Commun de RMN, Université de Lyon, ESCPE, 43 Boulevard du 11 Novembre 1918, F-69616 Villeurbanne, France*
[d]*Chemical Metallurgy Group, Faculty of Chemistry, Wrocław University of Technology, Wybreze Wyspianskiego 27, 50-370, Wrocław, Poland*
[e]*Ecole Polytechnique, CNRS UMR 6595 Technopole de Chateau-Gombert 5 Rue Enrico Fermi, 13453, Marseille cedex 13, France*
[f]*Université d'Orléans CEMHTI - CNRS UPR 3079, Orléans, France*
[g]*Université Paris 06, UMR 7196, PECSA Paris, France*
† Electronic supplementary information (ESI) available: Experimental details. See DOI: 10.1039/b919094e

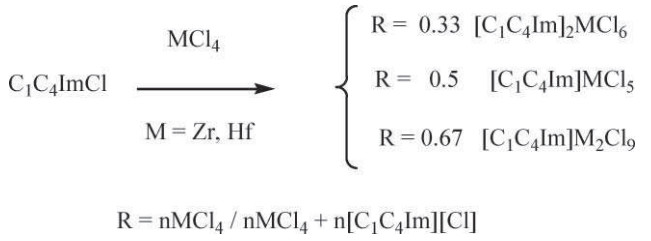

$$R = nMCl_4 / nMCl_4 + n[C_1C_4Im][Cl]$$

Scheme 1 The preparation of imidazolium chlorometallates.

DSC (differential scanning calorimetry)

This analysis was performed on the stoichiometric compounds. Analytical samples (30–50 mg) were sealed in Pyrex® ampoules under reduced pressure of argon.

For $R = 0.33$, the results for $[C_1C_4Im]_2[ZrCl_6]$ and $[C_1C_4Im]_2[HfCl_6]$, obtained with a heating and cooling rate of 5 K min^{-1}, are presented and compared to pure $[C_1C_4Im]Cl$ in Fig. 1. The values of temperature and enthalpy were determined from measurements performed on three different samples for each compound. A significant supercooling effect was observed during cooling. The following data were determined from DSC heating curves. It was found that $[C_1C_4Im]Cl$ melts congruently at 340 ± 1 K with a corresponding enthalpy $\Delta_{fus}H_m = 22.9 \pm 0.6$ kJ mol^{-1}. It should be pointed out that due to the supercooling effect, crystallisation was not observed in the DSC cooling curve up to 330 K, at which temperature the measurements were stopped (Fig. 1a). $[C_1C_4Im]_2[HfCl_6]$, melts congruently at 385 ± 1 K with enthalpy $\Delta_{fus}H_m = 48.1 \pm 1.1$ kJ mol^{-1}. Due to supercooling, crystallisation takes place at a lower temperature of about 362 K.

It is very likely that the analogous Zr compound, *i.e.* $[C_1C_4Im]_2[ZrCl_6]$ also melts congruently at $T_{fus} = 366 \pm 1$ K with a molar enthalpy $\Delta_{fus}H_m = 21.5 \pm 0.3$ kJ mol^{-1}. However a small additional endothermic effect at 391 K is observed in the heating DSC curves (Fig. 1c). This could be indicative of a small deviation from stoichiometry or the more complicated behaviour of this compound (for example incongruent melting). Additional measurements performed on this compound and mixtures with molar fractions of $[C_1C_4Im][Cl]$ larger and smaller in comparison with $[C_1C_4Im]_2[ZrCl_6]$ planned in the near future, would help to explain the phenomena connected with melting of the $[C_1C_4Im]_2[ZrCl_6]$ compound.

For $R = 0.67$, DSC measurements performed on the samples $[C_1C_4Im][Hf_2Cl_9]$ and $[C_1C_4Im][Zr_2Cl_9]$, showed only one thermal effect corresponding to the glass transition. This transition appears at $T_g = 225$ K with $\Delta c_p = 0.098$ J g^{-1} K^{-1} on heating, Fig. 2a, and at $T_g = 220$ K with $\Delta c_p = -0.081$ J g^{-1} K^{-1} on cooling for the hafnium compound. In the case of the zirconium compound, glass transition takes place at $T_g = 224$ K with $\Delta c_p = 0.131$ J g^{-1} K^{-1} on heating, Fig. 2b, and at $T_g = 219$ K with $\Delta c_p = -0.117$ J g^{-1} K^{-1} on cooling.

An interesting phenomenon was observed during the DSC measurements of the compounds formed at $R = 0.5$, stoichiometrically $[C_1C_4Im][MCl_5]$. Both products appeared to consist of "wet crystals", and on cooling, glass transitions were found of around 225 K, similar to the values found for $[C_1C_4Im][M_2Cl_9]$. For both metals, an exothermic peak appeared at around 340 K on heating, indicating the occurrence of a reaction in the system before a large endothermic peak due to melting at around 380 K. Subsequent

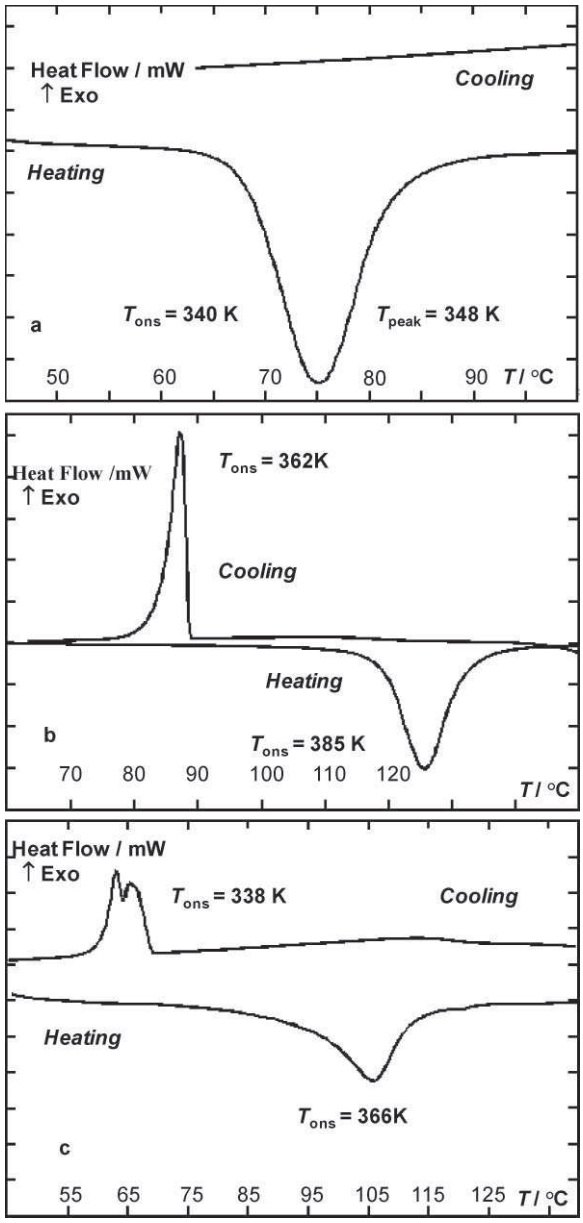

Fig. 1 DSC curves of (a) $[C_1C_4Im]Cl$, (b) $[C_1C_4Im]_2[HfCl_6]$, (c) $[C_1C_4Im]_2[ZrCl_6]$: heating/cooling rate = 5 K min^{-1}.

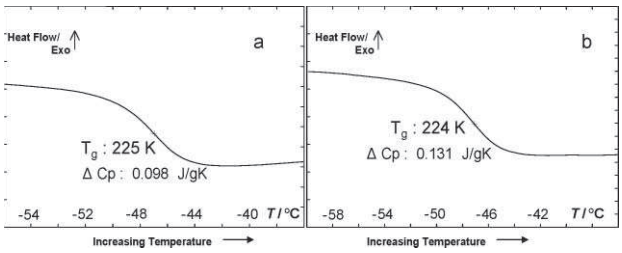

Fig. 2 Low temperature DSC curves of (a) $[C_1C_4Im]Hf_2Cl_9$ and (b) $[C_1C_4Im]Zr_2Cl_9$ on heating (heating rate 5 K min^{-1}).

runs produced different DSC profiles with endothermic peaks present at around 360 K and 380 K for Zr and Hf derivatives, respectively. However no T_g was detected on further DSC analyses of the same products. Removing the products from the system, it

became clear that a reaction had occurred as the products were coloured solids, (pale green Hf, and red Zr). Deliberate formation of this red Zr product by heating first to 473 K for 30 min gave DSC profiles with distinct endothermic peaks at 351 K and 374 K. One hypothesis is that at room temperature there is formation of a mixture of $[C_1C_4Im][M_2Cl_9]$ (liquid) and $[C_1C_4Im]_2[MCl_6]$ (solid), the "kinetic products" as wet crystals, which on heating to 340 K undergo a partial comproportionation reaction to give a eutectic mixture, possibly containing $M_2Cl_{10}^{2-}$ anions already reported.[35,36]

DSC results showed firstly a variation in the melting point of the salts produced, that was almost identical in the case of Hf and Zr. Also interestingly, the complexes $[C_1C_4Im][M_2Cl_9]$ at $R = 0.67$ were still liquid at sub zero temperatures. The appearance of the DSC profiles themselves indicated that pure complexes $[C_1C_4Im]_2[MCl_6]$, were achieved in the case of $R = 0.33$, as these gave the sharpest most precise peak for the phase change. For $R = 0.5$, the DSC data would support the formation of $[M_2Cl_{10}][C_1C_4Im]_2$ during the acquisition.

ESI mass spectrometry

Electrospray ionisation mass spectrometry is used to investigate the nature of ILs in both the gas and solution phase and to determine the nature of the ionic species present within.[37-39]

In the positive-ion mode mass spectra of the ionic liquids studied at concentrations of ~10^{-6} M in acetonitrile, for all ionic liquids, the peak at $m/z = 139.1$ corresponding to the $[C_1C_4Im]^+$ ion is present. The peak of the ion $[2(C_1C_4Im)Cl]^+$ at $m/z \sim 313$, which decreased when R increased, was absent in each case when $R = 0.67$. Larger clusters of $[n(C_1C_4Im)(n\text{-}1)Cl]^+$ were not observed. When $R = 0.33$ larger metal containing clusters were observed as follows : $[3(C_1C_4Im)\ MCl_6]^+$ and $m/z = 720.7$ for Zr, and $m/z = 808.7$ for Hf, Fig. 3. At $R = 0.5$ clusters of $[2(C_1C_4Im)MCl_5]^+$ at 544.5 and 693.8 were observed for Zr and Hf, respectively. For $R = 0.67$ clusters of $[2(C_1C_4Im)MCl_5]^+$ at 544.5, $[3(C_1C_4Im)\ MCl_6]^+$ at 720.7 (major) and of $[2(C_1C_4Im)M_2Cl_9)]^+$ at 776.1 were observed for Zr. In the case of Hf only the band $[3(C_1C_4Im)MCl_6)]^+$ at $m/z = 808.7$ was present.

Negatively charged clusters due to the presence of Cl^- and $M_xCl_y^-$ anions appear in the ESI^- spectra. For $R = 0.33$, the isotopic patterns corresponding to MCl_5^- ($m/z = 266.9$ (Zr) and 356.96 (Hf)) and the cluster $[5(C_1C_4Im)_3(HfCl_6)]^-$, $m/z = 1867$ were present. For $R = 0.5$ only the isotopic patterns corresponding to $[MCl_5]^-$ {($m/z = 266.9$ (Zr) and 356.9 (Hf)} were observed, Fig. 4. These data for $R = 0.5$ agree with the structure $[C_1C_4Im][MCl_5]$ and not $[C_1C_4Im]_2[M_2Cl_{10}]$, as previously reported.[35,36]

For $R = 0.67$, as well as the isotopic pattern corresponding to $[MCl_5]^-$ ($m/z = 266.9$ (Zr) and 356.9 (Hf), the isotopic pattern corresponding to $[M_2Cl_9]^-$ $m/z = 500.3$ for Zr, and $m/z = 676.5$ for Hf, and the cluster corresponding to $[C_1C_4Im][Zr_2Cl_9]$ at 1141.0 were apparent, Fig. 5. These results are consistent with findings by FTICR-MS, IR, and Raman spectra proving that $[(C_4C_4ImCl)2(TiCl_4)]$ contained a large amount of $[Ti_2Cl_9]^-$ ions and a small amount of $[TiCl_6]^{2-}$ ions.[33]

NMR experiments

The cation $[C_1C_4Im]^+$ can be used as a probe to study the nature of the ionic liquid. For this purpose, solutions of the different ionic liquids in the same solvent (CD_3CN) and at the same concentration and temperature (0.1 mol L^{-1}, 278 K), were analysed by ^1H, ^{13}C NMR. Also, solid state ^1H, ^{13}C, NMR analyses have been run on neat derivatives. The assignment of the nuclei is depicted in Scheme 2.

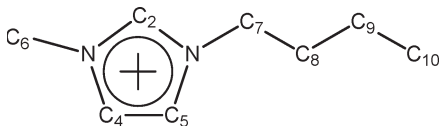

Scheme 2 Assignments of the C and H in the Imidazolium cation.

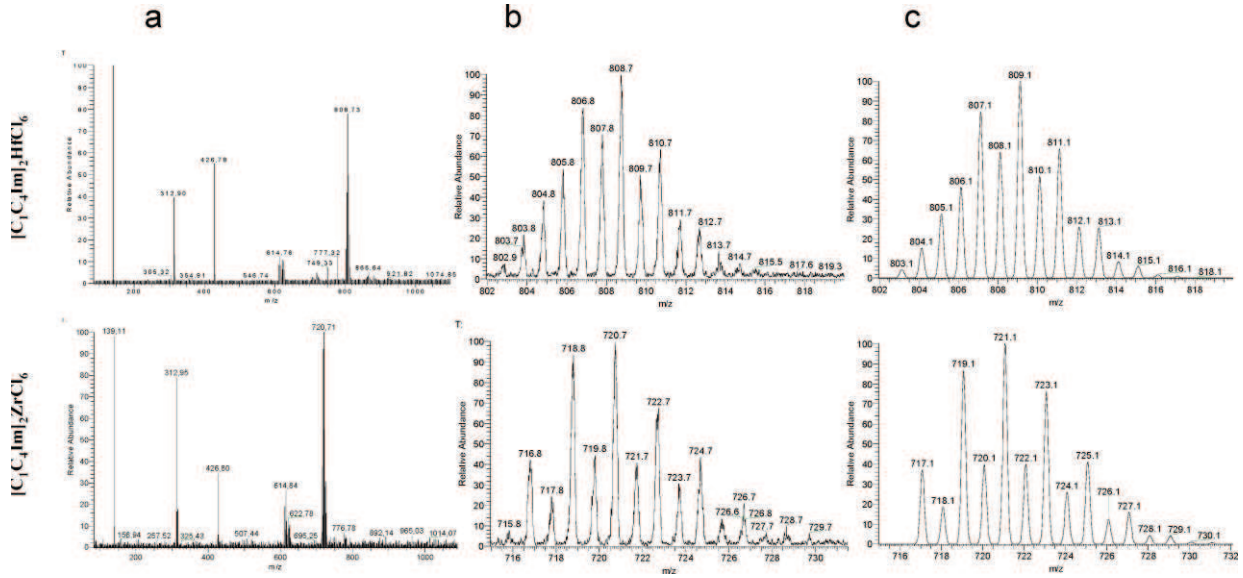

Fig. 3 (a) Full ESI^+ mass spectra of products for $R = 0.33$ $[C_1C_4Im]_2[HfCl_6]$ (upper) and $[C_1C_4Im]_2$ $[ZrCl_6]$ (lower), (b) zoom on the $[(C_1C_4Im)_3MCl_6]^+$ region showing isotopic peaks, (c) theoretical simulation of $[C_1C_4Im]_3[MCl_6]^+$ isotopic peaks for comparison.

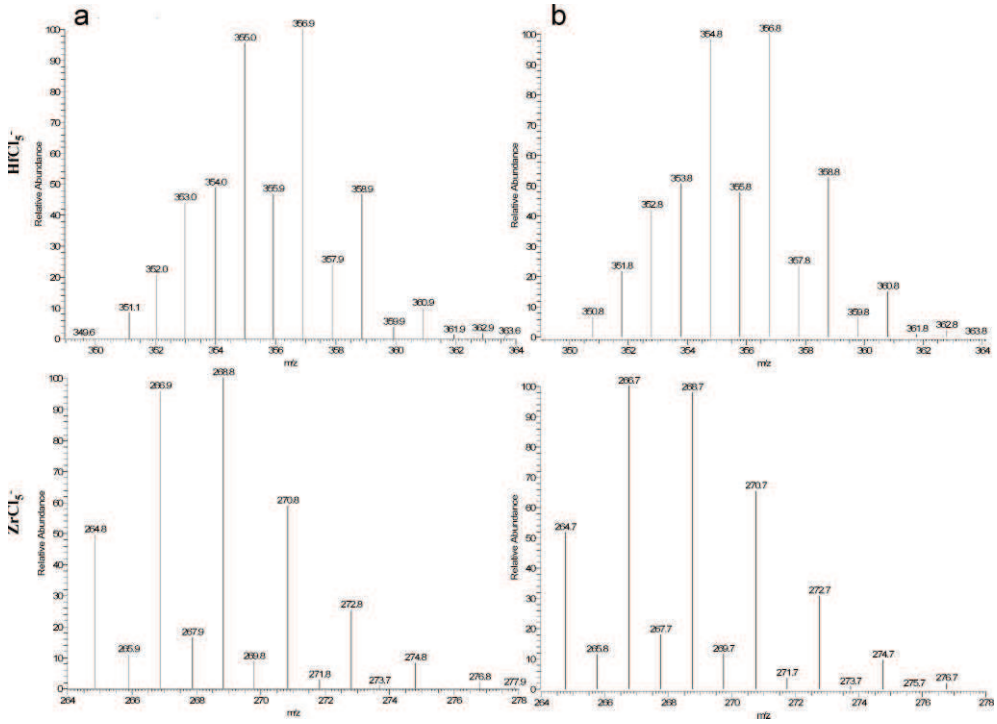

Fig. 4 (a) Zoom ESI⁻ mass spectra of products for $R = 0.5$; Hf (upper) and Zr (lower), in $[MCl_5]^-$ region showing isotopic peaks, (b) theoretical simulation of $[MCl_5]^-$ isotopic peaks for comparison.

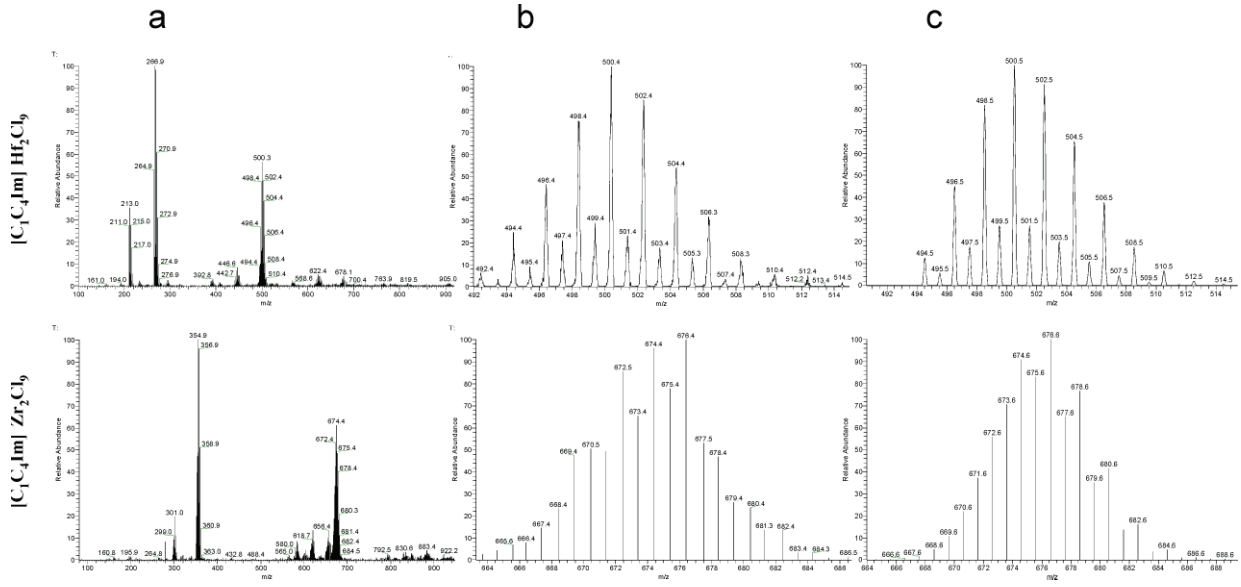

Fig. 5 (a) Full ESI-mass spectra of $R = 0.67$ *i.e.* $[C_1C_4Im][Hf_2Cl_9]$ (upper) and $[C_1C_4Im][Zr_2Cl_9]$ (lower), (b) zoom on the $[M_2Cl_9]^-$ region showing isotopic peaks, (c) theoretical simulation of $[M_2Cl_9]^-$ isotopic peaks for comparison.

^{1}H solution NMR

In ^{1}H NMR spectra of $[C_1C_4Im]^+$, the chemical shift of C_2–H proton (δ_{H2}) as well as ethylenic hydrogens C_4–H (δ_{H4}) and C_5–H (δ_{H5}), although less markedly, exhibit a monotonous decrease with increasing R, Fig. 6a and 6b. This evolution could be due to the decreasing hydrogen bond interactions between C_n–H and the anion as R increases.

^{13}C solution NMR

Besides the chemical shift of carbon C_2 (δC_2) which shifts towards high field with increasing R, Fig. 6c, the evolution of the ^{13}C NMR spectra is not significant ($\Delta\delta < 0.1$, Experimental part).

The solution NMR analyses of both ^{1}H and ^{13}C of the imidazolium moiety, show clearly a linear displacement of chemical shifts with increasing MCl_4 concentration. The addition

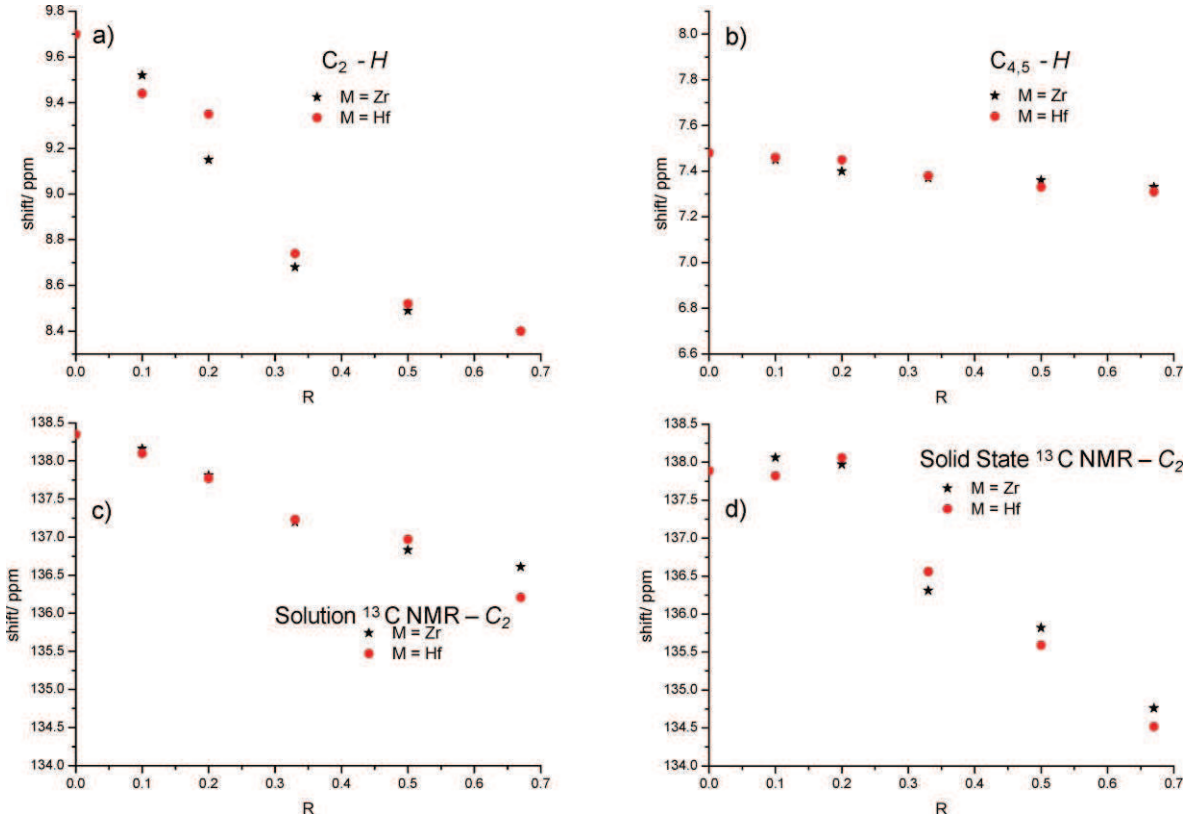

Fig. 6 (Upper) Variation of the chemical shift in ^{1}H NMR (CD_3CN, 298 K, 0.1 mol L^{-1}, δ ppm) of (a) δ_{H2} as a function of R (b) δ_{H4} and δ_{H5} as a function of R. (Lower) Variation of the chemical shift of δ_{C2} in (c) ^{13}C solution NMR (CD_3CN, 0.1 mol L^{-1}, δ ppm). (d) ^{13}C Solid state NMR, as a function of R.

Table 1 Evolution of the chemical shift δ_{C2}–H in ^{1}H solution NMR and of the melting point for the ratios 0.33, 0.5 and 0.67

R	$TiCl_4$ m.p. or T_g/K (δ_{C2}–H ppm)[33]	$Zr\ Cl_4$ m.p. or T_g/K (δ_{C2}–H ppm)[a]	$Hf\ Cl_4$ m.p. or T_g/K (δ_{C2}–H ppm)[a]	$AlCl_3$ m.p or T_g/K (δ_{C2}–H ppm)[40,41]
0.33	377.96 (n.d)	363 (8.68)	391 (8.74)	213 (6.72)
0.5	337.5 (n.d)	~ 357 (8.49)	~ 370 (8.52)	(6.5)
0.67	233.65 (n.d)	228 (8.40)	228 (8.40)	177 (6.2.5)

[a] This work.

of MCl_4 clearly has an effect on the electron density of the ring. Ionic interactions in the MCl_4 : ImCl system led to the formation of hydrogen-bonded aggregates of anions and cations, mainly through a C_2–H–anion interaction. The nature and extent of these depend on the susceptibility of the anion population towards hydrogen bond formation with Im^+. In general, the stronger C_2–H–anion hydrogen-bond induced, the more δ_{C2}–H is shifted to lower field, and the higher the melting point, Table 1.

^{13}C solid state NMR of IL in pure form at 298 K

In the ^{13}C solid state NMR (of neat IL), when the R value is increased all peaks are clearly affected, Table 2, particularly δ_{C7}, δ_{C8} and δ_{C10}, which are eventually completely replaced by three new peaks. However, there is no clear trend between their δ values and R unlike for δC_2, which is shifted monotonously towards high field with increasing R, Fig. 6d. NMR analysis performed in neat IL can reveal information, on the internal structure and ionic association of these media. It could be proposed that the C_2H–anion H-bond is thus a significant factor in the tuning of the physical properties of the resulting salt, Table 2.

^{35}Cl liquid NMR (variable temperature)

In the ^{35}Cl NMR spectra of $[C_1C_4Im]_2[HfCl_6]$, and $[C_1C_4Im]_2$-$[ZrCl_6]$, at 398 K, there is only one broad peak centred at 300 ppm, which persists upon cooling to 378 K.

The variable temperature ^{35}Cl solution NMR (CD_3CN) spectra $[C_1C_4Im]\ Zr_2Cl_9$ showed two peaks at 450 and 350 ppm in a ratio of around 1 : 2 which became sharper but did not shift when the temperature varied from 278 to 333 K. Similarly for $[C_1C_4Im]\ Hf_2Cl_9$, peaks at 350 and 300 ppm are observed although the smaller is a shoulder possibly due to their proximity, Fig. 7. In the literature, the anion $[M_2Cl_9]^-$ in complexes $[M_2Cl_9]^-[C]^+$ M = Zr, Hf presents the same structure of $Cl_3M(\mu^2\text{-}Cl_3)MCl_3$, *i.e.* six terminal chloride atoms and three bridging chloride atoms.[42-45] Consequently, by analogy with the structure of published $[M_2Cl_9]^-[C]^+$, the peaks at 350 ppm (Hf) and 450 ppm (Zr) were assigned to the three bridging chloride atoms and the peak at 300 ppm (Hf) and 350 ppm (Zr) to the six terminal chloride atoms. The ^{35}Cl NMR and ESI^- findings are consistent regarding the structure of these anions.

Table 2 ^{13}C Solid-state NMR of neat compounds obtained by reaction of MCl_4 with $[C_1C_4Im][Cl]$ in ratios $R = n_{MCl4}/n_{MCl4} + n_{[C1C4IM][Cl]}$ equal to 0, 0.33, 0.5 and 0.67

Compound	δ_{C2} ($\Delta\delta$)	$\delta_{C4,5}$	δ_{C7}	δ_{C6}	δ_{C8}	δ_{C9}	δ_{C10}
$[C_1C_4Im]Cl$	137.89	125.23	48.34	38.57	35.70	20.17	12.96
	(0)	124.28					
$[C_1C_4Im]_2[ZrCl_6]$,	136.31	124.19	49.90	38.10	31.91	19.28	15.09
	(−1.58)	122.71		36.86			13.36
$[C_1C_4Im]_2Zr_2Cl_{10}$	135.82	124.46	49.68	39.11	32.50	20.08	13.40
	(−2.07)	123.15		37.52			10.83
$[C_1C_4Im]\ Zr_2Cl_9$	134.76	124.84	51.05	37.50	32.18	19.58	14.03
	(−3.13)	123.39					
$[C_1C_4Im]_2[HfCl_6]$,	136.56	124.46	50.72	38.10	32.66	20.04	15.09
	(−1.33)	123.47		36.62			13.36
$[C_1C_4Im]_2Hf_2Cl_{10}$	135.59	123.22	49.73	39.34	32.41	20.04	13.36
	(−2.30)						10.88
$[C_1C_4Im]\ Hf_2Cl_9$	134.52	124.61	51.03	37.16	32.20	19.57	13.87
	(−3.37)	123.37					

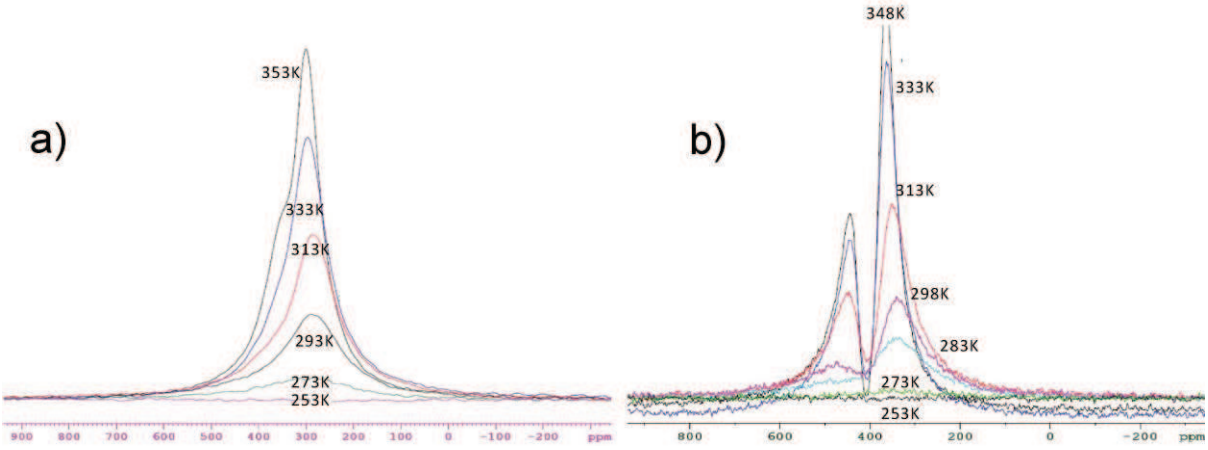

Fig. 7 Variable temperature NMR spectra; (a) ^{35}Cl of $[C_1C_4Im][Hf_2Cl_9]$, (b) ^{35}Cl of $[C_1C_4Im][Zr_2Cl_9]$.

Thermal dissociation by ^{35}Cl and ^{91}Zr solid NMR (high temperature) of $[C_1C_4Im]_2HfCl_6$, and $[C_1C_4Im]_2ZrCl_6$

In the case of 1-butyl-2,3-dimethylimidazolium trichlorozincate $[C_1C_1C_4Im][ZnCl_3]$ and 1-butyl-3-methylimidazolium trichlorozincate $[C_1C_4Im][ZnCl_3]$, the results of variable temperature ^{35}Cl and ^{13}C NMR analyses indicated that the species are dissociated to give ImCl and $ZnCl_2$, at temperatures superior to 373 K and 338 K, respectively.[46] The reverse process was observed on cooling. This dissociation could be used for the recovery and/or separation of a metal chloride from a mixture. Such dissociation in the case of zirconium and/or hafnium chloride would be of crucial interest for their separation which is still an economic challenge.[34] Furthermore, in the literature MCl_4 compounds are described as typical Lewis acids that readily react with chloride ions to produce the hexachlorometallate ion, either with alkali metals:

$$2M'Cl + ZrCl_4 \rightarrow M'_2\,[ZrCl_6]^{47,48}$$

or with bases such as pyridine or quinoline (B) in the presence of HCl:

$$2B + 2HCl + ZrCl_4 \rightarrow (BH)_2[ZrCl_6].^{49}$$

All these compounds undergo thermal dissociation at 622 K for KCl and above 522 K for (BHCl):

$$M'_2\,[ZrCl_6] \rightarrow 2M'Cl + ZrCl_4.$$

Due to the presence of a strong hydrogen bond B–H···Cl the thermal dissociation, with BHCl, is total only in the presence of oxygen affording ZrO_2 instead of $ZrCl_4$ which is economically unavailable for the Zr/Hf separation process.

The thermogravimetric analysis (TGA) of $[C_1C_4Im]_2[ZrCl_6]$, and $[C_1C_4Im]_2[HfCl_6]$, indicated also that the weight losses began at 528 K and 538 K, respectively, instead of 493 K for $[C_1C_4Im]Cl$. This shows firstly, the presence of the chlorometallate increases significantly the thermal stability, and secondly no significant difference is apparent between the Zr and Hf compounds.

Due to these findings, ^{35}Cl and ^{91}Zr solid NMR spectra could be run at high temperatures ranging from 513 K to 551 K, Fig. 8. The spectra were recorded both with increasing and decreasing temperature. For ^{35}Cl, the peak width decreases with temperature corresponding to a decrease in viscosity. A small displacement combined with a decrease of the peak width is observed at low temperature. This may be due to an increase of ^{35}Cl mobility towards the C_1C_4Im cation. No such phenomenon is observed in the ^{91}Zr spectrum, whose peak remains sharp at all the temperatures. Consequently, no dissociation was observed and so no decomposition occurred. This result for $[C_1C_4Im]_2[ZrCl_6]$, could be explained by the presence of a close interaction between

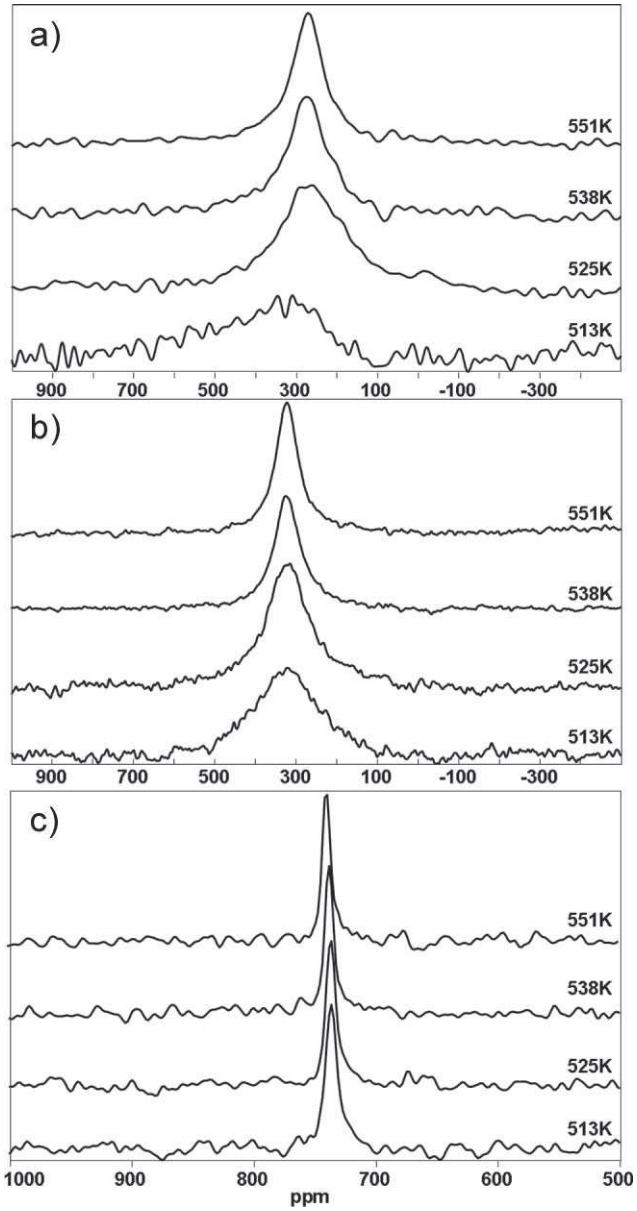

Fig. 8 Variable temperature NMR spectra; (a) ^{35}Cl of $[C_1C_4Im]_2HfCl_6$, (b) ^{35}Cl of $[C_1C_4Im]_2ZrCl_6$, (c) ^{91}Zr of $[C_1C_4Im]_2ZrCl_6$.

the acidic ring protons and the chlorine of the anion indicated by the crystallographic data.[22]

Conclusion

1-Butyl-3-methylimidazolium chlorometallates were prepared by the combination of MCl_4 (M = Zr, Hf) with $[C_1C_4Im][Cl]$. The molar percentage of MCl_4 was varied as follows; $R = n_{MCl4}/n_{MCl4} + n_{[C1C4IM][Cl]}$ equal to 0, 0.1, 0.2, 0.33, 0.5, 0.67. Pure compounds $[C_1C_4Im]_2[MCl_6]$, $[C_1C_4Im][M_2Cl_9]$ have been fully characterised by DSC, ^1H and ^{13}C solid state and solution NMR spectroscopy, and ESI mass spectrometry. The primary anions of the MCl_4-based ILs were $[MCl_5]$, $[MCl_6]$ and $[M_2Cl_9]$, whose abundances varied with R. The variable temperature ^{35}Cl solution NMR spectra $[C_1C_4Im][M_2Cl_9]$ allowed us to identify the bridging and terminal chlorine atoms. $[C_1C_4Im][M_2Cl_9]$ constitute new ionic liquids whose catalytic properties are currently under study. The high temperature ^{35}Cl and ^{91}Zr solid state NMR experiments show that there is no dissociation of $[C_1C_4Im]_2MCl_6$ in $[C_1C_4Im][Cl]$ and MCl_4 up to 551 K. This result could be explained by the presence of a close interaction between the acidic ring protons and the chlorine of the anion.

Experimental

All operations were performed in the strict absence of oxygen and water under a purified argon atmosphere using glovebox (Jacomex or MBraun) or vacuum-line techniques. Under argon, solvents were distilled using the appropriate drying agents: pyridine from CaH_2, acetonitrile and acetonitrile-d_3 (99% de deuterium) from P_2O_5 and stored over molecular sieves. 1-chlorobutane and 1,2-dimethylimidazole were obtained from Aldrich, and were freshly distilled before use. 1-Butyl-3-methylimidazolium chloride $[C_1C_4Im][Cl]$ was synthesised as described in the literature.[1]

^1H and ^{13}C and ^{35}Cl liquid NMR

Solution NMR spectra were recorded on a Bruker Avance 300 MHz spectrometer for ^1H and ^{13}C and a DRX 500 MHz spectrometer for ^{35}Cl. Chemical shifts were measured relative to $SiMe_4$ as internal standard for ^1H and ^{13}C and relative to external HCl (0.1 mol L^{-1} in H_2O) for ^{35}Cl. The sample for ^{35}Cl NMR was prepared as follows : the sample was introduced in an NMR tube (5 mm) in a glovebox. Then, the NMR tube was put inside a Schlenk tube, which was heated, under argon, until compounds were liquefied and put under vacuum for 1 h. Then, a capillary of DMSO-d_6 was introduced under argon into the molten solid.

^1H and ^{13}C solid NMR

Solid state NMR spectra were recorded on a Bruker DSX-300 spectrometer equipped with a standard 4 mm double-bearing probe head and operating at 75.47, and 300.18 MHz for ^{13}C, and ^1H, respectively. ^{13}C NMR spectra were recorded as follows : 30° pulse on ^{13}C nuclei, and acquisition under a 80 kHz decoupling field on protons, with 1 s recycle delay and 5 kHz spinning speed unless otherwise specified.

^{35}Cl, ^{91}Zr high temperature NMR

The High Temperature NMR (HT NMR) spectra were recorded using a Bruker Avance WB 400 MHz spectrometer, operating at 9.40 T. *In situ* HT NMR spectra were obtained by using the CO_2 laser heating system developed at CRMHT-CNRS in Orléans (France) and previously described.[50,51] To prevent sample contamination by air, the samples were put in a BN (HIP grade) crucible inside a glovebox under argon. The HT NMR spectra were acquired using a single pulse sequence. For ^{35}Cl and ^{91}Zr, the parameters were a recycle delay of 0.3 s, $\pi/2$ pulses of 35 μs with 1024 accumulations. The chemical shifts were referred to NaCl 1 mol L^{-1} solution for ^{35}Cl and to a saturated solution of $(\eta^5\text{-}C_5H_5)_2ZrCl_2$ in CH_2Cl_2 for ^{91}Zr.

DSC procedure[52]

Compounds were investigated with a Setaram DSC 121 differential scanning calorimeter. Experimental samples (30–50 mg) were

contained in vacuum-sealed Pyrex™ cells (7 mm diameter and 15 mm long). In order to avoid compound decomposition during sealing under reduced pressure of argon, the ampoule containing the compound was cooled down to liquid nitrogen temperature just before sealing. The side walls and bottom of the ampoules were grounded in order to make these cells fit snugly into the heat flow detector. This consists of two thermopiles, connected in electrical opposition, accommodating both the previous experimental cell with the sample and another empty and identical cell, which acts as a reference. This experimental DSC set up is characterised both by a high sensitivity and an excellent integration of the thermal heat flow since the sensing thermocouples in each thermopile are evenly distributed all over the cell surface. Experiments were conducted at heating and cooling rates ranging up to 5 K min^{-1}.

As the differential scanning calorimeter works in a wide temperature range, knowledge of the calorimeter constant dependence on temperature is crucial in measurements with this apparatus. Such a dependence for Setaram DSC 121 was determined during calorimeter calibration by the " Joule effect". This calibration was carried out at defined temperatures by the so-called "step method" ($\Delta T = 5$ K) over the entire temperature range of the calorimeter work. As a result the calibration curve, *i.e.* calorimeter constant dependence on temperature, $K(\mu V\ mW^{-1}) = f(T)$, was obtained. This dependence was automatically used during data treatment by the original Setaram software. The measurement of sample temperature was performed through a platinum probe located in the calorimetric block. The fusion of standard materials was studied at various scanning rates and temperature correction coefficients were determined and introduced into the calorimeter software. The maximum relative error of enthalpy of phase transition determination did not exceed 1%. It was checked by measurements of temperature and enthalpy of phase transitions of standard substances. Results obtained (differences in fusion temperatures less than 1 K, differences in enthalpies of fusion less than 0.5%) confirmed the correct working of the calorimeter.

Mass spectrometry

Mass spectra were acquired on a ThermoFinnigan LCQ Advantage ion trap instrument, detecting positive (+) and negative (–) ions in the ESI mode. Samples (1 to 10 μg ml^{-1} in acetonitrile) were infused directly into the source (5 μl min^{-1}) using a syringe pump. The following source parameters were applied: spray voltage 3.0–3.5 kV, nitrogen sheath gas flow 5–20 arbitrary units. The heated capillary was held at 473 K. MS spectra were obtained by applying a relative collision energy of 25 to 40% of the instrumental maximum.

Preparation of ionic liquid

Under argon in glovebox, the solid reactants are weighed and mixed together thoroughly using a mortar and pestle. For each experiment, 0.5 ± 0.005 g (2.86×10^{-3} mol) of the ionic liquid C_1C_4ImCl (relative molecular mass 174.7 g mol^{-1}, white solid at room temperature) is weighed into each tube and the according amounts of MCl_4 are added.

This is then heated to 343 K, (m.p. $C_1C_4ImCl = 339$ K), under constant stirring. This produces a homogenous solution except for in the cases of $R = 0.33$ and $R = 0.5$, where extra heating is necessary with use of a heat gun, in order to obtain a homogenous solution. The products are left stirring for 2 h and then cooled down to room temperature. A solid is obtained for $R = 0.2$, 0.33, a semi-solid for $R = 0.5$, and liquids obtained for $R = 0.1$, 0.7.

Example of the synthesis of 1-butyl-3-methylimidazolium zirconium pentachloride: *{[C_1C_4Im][$ZrCl_5$], with $R = 0.5$}*: Anhydrous zirconium tetrachloride (0.667 g, 2.86 mmol) was mixed under argon with solid 1-butyl-3-methylimidazolium chloride (0.5 g, 2.86 mmol). The mixture was heated to 70 °C and stirred over 2 h until a homogenous mixture formed.

^{1}H NMR (CD_3CN, δ) : 8.49 (1H, s, C_2H), 7.38 and 7.34 (2H, d, $C_{4,5}H$), 4.20 (2H, t, C_7H_2), 3.83 (3H, s, C_6H_3), 1.80 (2H, qn, C_8H_2), 1.31 (2H, sx, C_9H_2), 0.95 (3H, t, $C_{10}H_3$).^{13}C NMR (CD_3CN, δ) : 136.83 (s, C_2), 124.59 and 123.21 (d, $C_{4,5}$), 50.30 (s, C_7), 36.98 (s, C_6), 32.56 (s, C_8), 19.91 (s, C_9), 13.65 (s, C_{10}).^{13}C Solid-state NMR (δ) : 135.82 (C_2), 124.46 and 123.15 ($C_{4,5}$), 49.68 (C_7), 39.11 and 37.52 (C_6), 32.50 (C_8), 20.08 and 19.02 (C_9), 13.47 and 10.83 (C_{10}). ESI$^+$: 139.1 [$C_1C_4Im^+$], 312.8 [2($C_1C_4Im^+$) Cl^-], 544.5 [2($C_1C_4Im^+$)$ZrCl_5^-$], 721.0 [3($C_1C_4Im^+$) $ZrCl_6^{2-}$], 1302.8 [5($C_1C_4Im^+$) 2$ZrCl_6^{2-}$] ESI$^-$: 266.9 [$ZrCl_5^-$]

[$C_1C_4Im^+$][Cl^-] ($R = 0$). ^{1}H NMR (CD_3CN, δ) : 9.70 (1H, s, C_2H), 7.49 and 7.46 (2H, d, $C_{4,5}H$), 4.20 (2H, t, C_7H_2), 3.88 (3H, s, C_6H_3), 1.81 (2H, qn, C_8H_2), 1.30 (2H, sx, C_9H_2), 0.91 (3H, t, $C_{10}H_3$). ^{13}C NMR (CD_3CN, δ) : 138.35 (s, C_2), 124.38 and 123.13 (d, $C_{4,5}$), 49.80 (s, C_7), 36.56 (s, C_6), 32.58 (s, C_8), 19.83 (s, C_9), 13.63 (s, C_{10}). ^{13}C Solid-state NMR (δ) : 137.89 (C_2), 125.23 and 124.28 ($C_{4,5}$), 48.34 (C_7), 38.57 (C_6), 35.70 (C_8), 20.17 (C_9), 12.96 (C_{10}).

M = Zr $R = 0.1$; [C_1C_4Im][Cl] (0.5 g, 2.86 mmol); $ZrCl_4$ (7.40×10^{-2} g, 3.17×10^{-4} mol) ^{1}H NMR (CD_3CN, δ) : 9.52 (1H, s, C_2H), 7.47 and 7.43 (2H, d, $C_{4,5}H$), 4.19 (2H, t, C_7H_2), 3.88 (3H, s, C_6H_3), 1.81 (2H, qn, C_8H_2), 1.30 (2H, sx, C_9H_2), 0.91 (3H, t, $C_{10}H_3$). ^{13}C NMR (CD_3CN, δ) : 138.16 (s, C_2), 124.41 and 123.10 (d, $C_{4,5}$), 49.98 (s, C_7), 36.67 (s, C_6), 32.60 (s, C_8), 19.88 (s, C_9), 13.63 (s, C_{10}). ^{13}C Solid-state NMR (δ) : 138.06 (C_2), 125.45 and 124.21 ($C_{4,5}$), 48.49 (C_7), 38.60 (C_6), 35.88 (C_8), 20.04 (C_9), 13.36 (C_{10}). ESI$^+$: 139.1 ($C_1C_4Im^+$), 312.8 ([$2C_1C_4Im$,^{35}Cl]$^+$) ESI$^-$: 384.8 ([$2C_1C_4Im^+$,$3^{35}Cl^-$]), 556.8 ([$3C_1C_4Im^+$,$4^{35}Cl^-$]), 734.8 ([$4C_1C_4Im^+$,$5^{35}Cl^-$])

$R = 0.2$; [C_1C_4Im][Cl] (0.5 g, 2.86 mmol); $ZrCl_4$ (0.167 g, 7.15×10^{-4} mol) ^{1}H NMR (CD_3CN, δ) : 9.15 (1H, s, C_2H), 7.42 and 7.39 (2H, d, $C_{4,5}H$), 4.20 (2H, t, C_7H_2), 3.87 (3H, s, C_6H_3), 1.81 (2H, qn, C_8H_2), 1.30 (2H, sx, C_9H_2), 0.92 (3H, t, $C_{10}H_3$). ^{13}C NMR (CD_3CN, δ) : 137.81 (s, C_2), 124.42 and 123.09 (d, $C_{4,5}$), 49.99 (s, C_7), 36.74 (s, C_6), 32.59 (s, C_8), 19.85 (s, C_9), 13.62 (s, C_{10}). ^{13}C Solid-state NMR (δ) : 137.97 (C_2), 125.16 and 124.18 ($C_{4,5}$), 50.75 and 48.49 (C_7), 38.59 (C_6), 35.68 (C_8), 20.35 (C_9), 13.95 (C_{10}). ESI$^+$: 139.1 ($C_1C_4Im^+$), 312.8 ([$2C_1C_4Im$,^{35}Cl]$^+$) ESI$^-$: 268.8 ($ZrCl_5^-$), 384.8 ([$2C_1C_4Im^+$,$3^{35}Cl^-$]), 556.8 ([$3C_1C_4Im^+$,$4^{35}Cl^-$]), 734.8 ([$4C_1C_4Im^+$,$5^{35}Cl^-$]).

$R = 0.33$; [C_1C_4Im][Cl] (0.5 g, 2.86 mmol); $ZrCl_4$ (0.333 g, 1.43×10^{-3} mol) ^{1}H NMR (CD_3CN, δ) : 8.68 (1H, s, C_2H), 7.38 and 7.36 (2H, d, $C_{4,5}H$), 4.20 (2H, t, C_7H_2), 3.86 (3H, s, C_6H_3), 1.81 (2H, qn, C_8H_2), 1.32 (2H, sx, C_9H_2), 0.94 (3H, t, $C_{10}H_3$). ^{13}C NMR (CD_3CN, δ) : 137.20 (s, C_2), 124.54 and 123.13 (d, $C_{4,5}$), 50.24 (s, C_7), 36.97 (s, C_6), 32.66 (s, C_8), 19.92 (s, C_9), 13.65 (s, C_{10}). ^{13}C Solid-state NMR (δ) : 136.31 (C_2), 124.19 and 122.71 ($C_{4,5}$), 49.97 (C_7), 38.10 and 36.86 (C_6), 31.91 (C_8), 19.28 (C_9), 15.09, 13.36 and 11.63 (C_{10}). ESI$^+$: 139.1 [$C_1C_4Im^+$], 313.0 [2($C_1C_4Im^+$) Cl^-], 720.7

[3($C_1C_4Im^+$) $ZrCl_6^{2-}$], 1302.8 [5($C_1C_4Im^+$) $2ZrCl_6^{2-}$] ESI^-: 266.9 [$ZrCl_5^-$]

***R* = 0.67**; [C_1C_4Im][Cl] (0.5 g, 2.86 mmol); $ZrCl_4$ (1.56 g, 6.67 mmol) ^1H NMR (CD_3CN, δ) : 8.40 (1H, s, C_2H), 7.35 and 7.31 (2H, d, $C_{4,5}H$), 4.12 (2H, t, C_7H_2), 3.80 (3H, s, C_6H_3), 1.78 (2H, qn, C_8H_2), 1.27 (2H, sx, C_9H_2), 0.88 (3H, t, $C_{10}H_3$). ^{13}C NMR (CD_3CN, δ) : 136.61 (s, C_2), 124.57 and 123.20 (d, $C_{4,5}$), 50.31 (s, C_7), 37.01 (s, C_6), 32.49 (s, C_8), 19.90 (s, C_9), 13.69(s, C_{10}). ^{13}C Solid-state NMR (δ) : 134.76 (C_2), 124.84 and 123.39 ($C_{4,5}$), 51.05 (C_7), 37.50 (C_6), 32.18 (C_8), 19.58 (C_9), 14.03 (C_{10}). ESI^+: 139.1 [$C_1C_4Im^+$], 544.5 [2($C_1C_4Im^+$)$ZrCl_4^-$], 720.7 [3($C_1C_4Im^+$)$ZrCl_6^{2-}$], 776.1 [2($C_1C_4Im^+$)$Zr_2Cl_9^-$]ESI^-: 266.9 [$ZrCl_5^-$], 500.3 [$Zr_2Cl_9^-$], 1141.0 [$C_1C_4Im^+$ $2Zr_2Cl_9^-$]

M = Hf *R* = 0.1; [C_1C_4Im][Cl] (0.5 g, 2.86 mmol); $HfCl_4$ (0.102 g, 3.17×10^{-4} mol) ^1H NMR (CD_3CN, δ): 9.44 (1H, s, C_2H), 7.46 and 7.43 (2H, d, $C_{4,5}H$), 4.19 (2H, t, C_7H_2), 3.87 (3H, s, C_6H_3), 1.78 (2H, qn, C_8H_2), 1.32 (2H, sx, C_9H_2), 0.91 (3H, t, $C_{10}H_3$). ^{13}C NMR (CD_3CN, δ) : 138.10 (s, C_2), 124.37 and 123.07 (d, $C_{4,5}$), 49.89 (s, C_7), 36.64 (s, C_6), 32.57 (s, C_8), 19.86 (s, C_9), 13.60 (s, C_{10}). ^{13}C Solid-state NMR (δ) : 137.82 (C_2), 125.44 and 124.21 ($C_{4,5}$), 48.50 (C_7), 38.84 (C_6), 35.88 (C_8), 20.28 (C_9), 13.11 (C_{10}). ESI^+: 139.1 [$C_1C_4Im^+$], 312.8 [2($C_1C_4Im^+$) Cl^-] ESI^-:

***R* = 0.2**; [C_1C_4Im][Cl] (0.5 g, 2.86 mmol); $HfCl_4$ (0.229 g, 7.15×10^{-4} mol) ^1H NMR (CD_3CN, δ) : 9.35 (1H, s, C_2H), 7.47 and 7.43 (2H, d, $C_{4,5}H$), 4.18 (2H, t, C_7H_2), 3.91 (3H, s, C_6H_3), 1.81 (2H, qn, C_8H_2), 1.28 (2H, sx, C_9H_2), 0.90 (3H, t, $C_{10}H_3$). ^{13}C NMR (CD_3CN, δ) : 137.77 (s, C_2), 124.38 and 123.06 (d, $C_{4,5}$), 49.92 (s, C_7), 36.71 (s, C_6), 32.56 (s, C_8), 19.80 (s, C_9), 13.59 (s, C_{10}). ^{13}C Solid-state NMR (δ) : 138.06 (C_2), 125.69 and 124.21 ($C_{4,5}$), 49.98 and 48.50 (C_7), 38.84 (C_6), 35.88 (C_8), 20.29 (C_9), 13.11 (C_{10}). ESI^+: 139.1 ($C_1C_4Im^+$), 312.8 ([2 C_1C_4Im,^{35}Cl]$^+$) ESI^-: 354.9 [$HfCl_5^-$]

***R* = 0.33**; [C_1C_4Im][Cl] (0.5 g, 2.86 mmol); $HfCl_4$ (0.458 g, 1.43 mmol) ^1H NMR (CD_3CN, δ) : 8.74 (1H, s, C_2H), 7.40 and 7.37 (2H, d, $C_{4,5}H$), 4.17 (2H, t, C_7H_2), 3.87 (3H, s, C_6H_3), 1.80 (2H, qn, C_8H_2), 1.30 (2H, sx, C_9H_2), 0.91 (3H, t, $C_{10}H_3$). ^{13}C NMR (CD_3CN, δ) : 137.23 (s, C_2), 124.51 and 123.12 (d, $C_{4,5}$), 50.19 (s, C_7), 36.96 (s, C_6), 32.65 (s, C_8), 19.89 (s, C_9), 13.64 (s, C_{10}). ^{13}C Solid-state NMR (δ) : 136.56 (C_2), 124.46 and 123.47 ($C_{4,5}$), 50.72 (C_7), 38.10 and 36.62 (C_6), 32.66 (C_8), 20.04 (C_9), 15.09 and 13.36 (C_{10}). ESI^+: 139.1 [$C_1C_4Im^+$], 312.9 [2($C_1C_4Im^+$) Cl^-], 808.7 [3($C_1C_4Im^+$) $HfCl_6^{2-}$], 1447.6 [5(C_1C_4Im+) $2HfCl_6^{2-}$)] ESI^-: 356.9 [$HfCl_5^-$], 1867.4 [5($C_1C_4Im^+$) $3HfCl_6^{2-}$]

***R* = 0.5**; [C_1C_4Im][Cl] (0.5 g, 2.86 mmol); $HfCl_4$ (0.916 g, 2.86 mmol) ^1H NMR (CD_3CN, δ) : 8.52 (1H, s, C_2H), 7.36 and 7.31 (2H, d, $C_{4,5}H$), 4.14 (2H, t, C_7H_2), 3.81 (3H, s, C_6H_3), 1.80 (2H, qn, C_8H_2), 1.29 (2H, sx, C_9H_2), 0.90 (3H, t, $C_{10}H_3$). ^{13}C NMR (CD_3CN, δ) : 136.97 (s, C_2), 124.46 and 123.06 (d, $C_{4,5}$), 50.14 (s, C_7), 36.92 (s, C_6), 32.53 (s, C_8), 19.80 (s, C_9), 13.57 (s, C_{10}). ^{13}C Solid-state NMR (δ) : 135.59 (C_2), 123.22 ($C_{4,5}$), 49.73 (C_7), 39.34 (C_6), 32.41 (C_8), 20.04 (C_9), 13.36 and 10.88 (C_{10}). ESI^+: 139.1 [$C_1C_4Im^+$], 313.0 [2($C_1C_4Im^+$) Cl^-], 693.8[2($C_1C_4Im^+$) $HfCl_5^-$], 809.0 [3($C_1C_4Im^+$) $HfCl_6^{2-}$], 1447.8 [5($C_1C_4Im^+$) $2HfCl_6^{2-}$] ESI^-: 356.9 [$HfCl_5^-$]

***R* = 0.67**; [C_1C_4Im][Cl] (0.5 g, 2.86 mmol); $HfCl_4$ (2.13 g, 6.67 mmol) ^1H NMR (CD_3CN, δ) : 8.40 (1H, s, C_2H), 7.33 and 7.29 (2H, d, $C_{4,5}H$), 4.07(2H, t, C_7H_2), 3.78 (3H, s, C_6H_3), 1.75 (2H, qn, C_8H_2), 1.25 (2H, sx, C_9H_2), 0.84 (3H, t, $C_{10}H_3$). ^{13}C NMR (CD_3CN, δ) : 136.21 (s, C_2), 125.62 and 124.18 (d, $C_{4,5}$), 49.91 (s, C_7), 36.63 (s, C_6), 32.10 (s, C_8), 19.51 (s, C_9), 13.32(s, C_{10}). ^{13}C Solid-state NMR (δ) : 134.52 (C_2), 124.61 and 123.37 ($C_{4,5}$), 51.03 (C_7), 37.16 (C_6), 32.20 (C_8), 19.57 (C_9), 13.87 (C_{10}). ESI^+: 139.1 [$C_1C_4Im^+$], 808.7 [3($C_1C_4Im^+$) $HfCl_6^{2-}$] ESI^-: 356.9 [$HfCl_5^-$], 676.5 [$Hf_2Cl_9^-$]

Acknowledgements

We would like to thank Areva Cezus for financing this work, Anne Baudouin for solid state NMR and also undergraduate students Céline Chong, Thibault Alphazan and Sandra Garcia for their participation.

Notes and references

1 P. Wasserscheid and T. Welton, *Ionic Liquids in Synthesis*, Wiley-VCH, Weinheim, 2003.
2 A. P. Abbott, G. Capper, D. L. Davies and R. K. Rasheed, *Chem.–Eur. J.*, 2004, **10**, 3769–3774.
3 R. T. Carlin and R. A. Osteryoung, *J. Mol. Catal.*, 1990, **63**, 125–129.
4 Y. Chauvin, S. Einloft and B. H. Olivier, *Ind. Eng. Chem. Res.*, 1995, **34**, 1149–1155.
5 K. Yoo, V. V. Namboodiri, R. S. Varma and P. G. Smirniotis, *J. Catal.*, 2004, **222**, 511–519.
6 Y. Gu, F. Shi and Y. Deng, *J. Mol. Catal. A: Chem.*, 2004, **212**, 71–75.
7 R. A. Osteryoung, *Molten Salt Chemistry*, Reidel Publishing, Dordrecht, Holland, 1987.
8 R. T. Carlin and R. A. Osteryoung, *J. Electroanal. Chem.*, 1988, **252**, 81.
9 A. A. Fannin, L. A. King, J. A. Levisky and J. S. Wilkes, *J. Phys. Chem.*, 1984, **88**, 2609–2614.
10 C. Woodcock and D. F. Shriver, *Inorg. Chem.*, 1986, **25**, 2137.
11 J. T. A. Zawodzinski and R. A. Osteryoung, *Inorg. Chem.*, 1989, **28**, 1710.
12 Y. Chauvin, F. Di Marco-Van Tiggelen and H. Olivier, *J. Chem. Soc., Dalton Trans.*, 1993, 1009–1011.
13 C. A. Angell and P. D. Bennett, *J. Am. Chem. Soc.*, 1982, **104**, 6304.
14 B. Gilbert, Y. Chauvin and I. Guibard, *Vib. Spectrosc.*, 1991, **1**, 299–304.
15 Y. Chauvin, B. H. Olivier, C. Wyrvalski, L. C. Simon and R. F. de Souza, *J. Catal.*, 1997, **165**, 275–278.
16 X. Liu, L. Xiao, H. Wu, Z. Li, J. Chen and C. Xia, *Catal. Commun.*, 2009, **10**, 424–427.
17 J. Zhang, C. Hunang, B. Chen, P. Ren and M. Pu, *J. Catal.*, 2007, **249**, 261–268.
18 X. Liang, G. Gong, H. Wu and J. Yang, *Fuel*, 2009, **88**, 613–616.
19 Q.-G. Zhang and Y. Wei, *J. Chem. Thermodyn.*, 2008, **40**, 640–644.
20 X.-w. Zhang and Q.-h. Ai, *Huaxue Shiji*, 2008, **30**, 121–124.
21 M. S. Sitze, E. R. Schreiter, E. V. Patterson and R. G. Freeman, *Inorg. Chem.*, 2001, **40**, 2298–2304.
22 C. Zhong, T. Sasaki, A. Jimbo-Kobayashi, E. Fujiwara, A. Kobayashi, M. Tada and Y. Iwasawa, *Bull. Chem. Soc. Jpn.*, 2007, **80**, 2365–2374.
23 X. Chen and Y. Peng, *Catal. Lett.*, 2008, **122**, 310–313.
24 A. P. Abbott, *ChemPhysChem*, 2004, **5**, 1242–1246.
25 D. Ballivet-Tkatchenko, M. Picquet, M. Solinas, G. Francio, P. Wasserscheid and W. Leitner, *Green Chem.*, 2003, **5**, 232–235.
26 T. J. Bell, A. P. Abbott, S. Handa and B. Stoddart, *Abstracts of Papers, 231st ACS National Meeting*, *Atlanta*, 2006.
27 V. Lecocq, A. Graille, C. C. Santini, A. Baudouin, Y. Chauvin, J.-M. Basset, D. Bouchu and B. Fenet, *New J. Chem.*, 2005, **29**, 700–706.
28 J. L. Anthony, J. F. Brennecke, J. D. Holbrey, E. J. Maginn, R. A. Mantz, R. D. Rogers, P. C. Trulove, A. E. Visser and T. Welton, in *Ionic Liquids in Synthesis*, Ed. P. Wasserscheid, T. Welton, Wiley-VCH, Weinheim, 2003, pp. 41-55.
29 G. D. Allen, M. C. Buzzeo, I. G. Davies, C. Villagran, C. Hardacre and R. G. Compton, *J. Phys. Chem. B*, 2004, **108**, 16322–16327.
30 P. B. Hitchcock, K. R. Seddon and T. Welton, *J. Chem. Soc., Dalton Trans.*, 1993, 2639.
31 M. Hasan, I. V. Kozhevnikov, M. Siddiqui, C. Femoni, A. Steiner and N. Winterton, *Inorg. Chem.*, 2001, **40**, 795–800.

32 P. B. Hitchcock, R. J. Lewis and T. Welton, *Polyhedron*, 1993, **12**, 2039.
33 L. Gao, L. Wang, T. Qi, J. Chu and J. Qua, *J. Electrochem. Soc.*, 2009, **156**, 49–55.
34 R. H. Nielsen, in *Kirk Othmer Encyclopedia of Chemical Technology*, Wiley, New York, 2004.
35 B. Neumueller and K. Dehnicke, *Z. Anorg. Allg. Chem.*, 2004, **630**, 2576–2578.
36 E. Robe, S. Maria, P. Richard and R. Poli, *Eur. J. Inorg. Chem.*, 2007, 2434–2442.
37 F. C. Gozzo, L. S. Santos, R. Augusti, C. S. Consorti, J. Dupont and M. N. Eberlin, *Chem.–Eur. J.*, 2004, **10**, 6187–6193.
38 P. J. Dyson, I. Khalaila, S. Luettgen, J. S. McIndoe and D. Zhao, *Chem. Commun.*, 2004, (19), 2204–2205.
39 D. F. Kennedy and C. J. Drummond, *J. Phys. Chem. B*, 2009, **113**, 5690–5693.
40 C. Scordilis-Kelley, K. D. Robinson, K. A. Belmore, J. L. Atwood and R. T. Carlin, *J. Crystallogr. Spectrosc. Res.*, 1993, **23**, 601–606.
41 D. Bankmann and R. Giernoth, *Prog. Nucl. Magn. Reson. Spectrosc.*, 2007, **51**, 63–90.
42 F. Calderazzo, I. Ferri, G. Pampaloni and S. Troyanov, *J. Organomet. Chem.*, 1996, **518**, 189–196.
43 F. Musso, E. Solari, C. Floriani and K. Schenk, *Organometallics*, 1997, **16**, 4889–4895.
44 M. Schormann, S. Garratt, D. L. Hughes, J. C. Green and M. Bochmann, *J. Am. Chem. Soc.*, 2002, **124**, 11266–11267.
45 M. Schormann, S. Garratt and M. Bochmann, *Organometallics*, 2005, **24**, 1718–1724.
46 C. C. Cassol, G. Ebeling, B. Ferrera and J. Dupont, *Adv. Synth. Catal.*, 2006, **348**, 243–248.
47 J. E. Drake and G. W. A. Fowles, *J. Inorg. Nucl. Chem.*, 1961, **18**, 136.
48 P. Gelbman and A. D. Westland, *J. Chem. Soc., Dalton Trans.*, 1975, 1598.
49 H. V. Thanh, L. Gruzdiewa, J. Rak and J. Blazejowski, *Thermochim. Acta*, 1993, **230**, 269–292.
50 V. Lacassagne, C. Bessada, B. Ollivier, D. Massiot and J.-P. Coutures, *C. R. Acad. Sci. IIb*, 1997, **325**, 91–98.
51 D. Massiot, C. Bessada, P. Echegut, J. P. Coutures and F. Taullele, *Solid State Ionics*, 1990, **37**, 223.
52 (*a*) M. Gaune-Escard, Calorimetric methods, in *Molten Salt Techniques*, Eds. R.J. Gale and D. G. Lovering, Vol. 4, Plenum Press, New York, pp. 151-192 (1991); (*b*) E. Ingier-Stocka, L. Rycerz, M. Berkani and M. Gaune-Escard, *J. Mol. Liq.*, 2009, **148**, 40–44 and references therein.

Exploiting the solvation properties of Ionic Liquids

A novel approach for the separation of zirconium from hafnium

S. PAUL CAMPBELL, C. SANTINI CATHERINE, CHAUVIN YVES

Université de Lyon, Institut de Chimie de Lyon, UMR 5265 CNRS-Université de Lyon 1 -ESCPE Lyon,C2P2
Equipe Chimie Organométallique de Surface, ESCPE, 43 bd du 11 novembre 1918, Villeurbanne cedex, F-69626, France

KEYWORDS: Separation, hafnium, zirconium, ionic liquids.

ABSTRACT: Hexamethylbenzene reacts differently with zirconium and hafnium tetrachloride, affording, for the former, a binuclear *molecular* complex $Zr(\eta^6\text{-}Me_6C_6)Cl_2(\mu\text{-}Cl)_3ZrCl_3$ and for the latter a binuclear *ionic* complex $[Hf(\eta^6\text{-}Me_6C_6)Cl_3]^+[Hf_2Cl_9]^-$. This difference in reactivity is exploited to carry out a two-phase extraction using 1-butyl-3-methylimidazolium tetrachloroaluminate as the ionic liquid phase and a toluene/pentane mixture as the organic phase. This technique presents the potential advantage of recovering of pure zirconium chloride without the formation of highly inert oxides.

GRAPHICAL ABSTRACT: Organic solvents selectively extract the zirconium complex from a mixture of neutral $Zr(\eta6\text{-}Me6C6)Zr(\eta^6\text{-}Me_6C_6)Cl_2(\mu\text{-}Cl)_3ZrCl_3$ and ionic $[Hf(\eta^6\text{-}Me_6C_6)Cl_3]^+[Hf_2Cl_9]^-$ in ionic liquid solution.

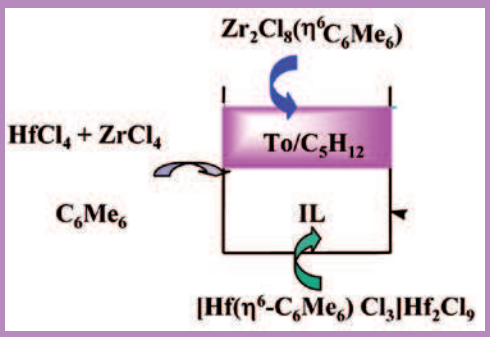

INTRODUCTION

Zirconium and hafnium occur naturally together, the most common ore being "zircon". As their chemical properties are very similar, extracting and separating highly pure metals is a difficult challenge. In nuclear applications zirconium has a low neutron absorption cross-section and is therefore a useful cladding material ("zircaloy"). Hafnium, on the other hand, has a high neutron absorption cross-section (nearly 600 times that of zirconium). Therefore, for nuclear applications, zirconium metal must contain less than 100 ppm hafnium. Three main processes are in current use for the separation of zirconium from hafnium: multiple crystallization of potassium zirconium fluoride; solvent extraction of the chlorides using methyl isobutyl ketone and water; extractive distillation of the chlorides using a $KCl/AlCl_3$ molten salt bath at high temperature (1-11). These three processes present several severe drawbacks, e.g. recovery of oxide products, corrosion problems, high running temperatures, etc. Hf/Zr separation is still a economic and technical challenge (more than 60 papers published during the last decade, of which 25 percent as patents and from more than 20 different countries) (12). Here we describe a new ionic liquid-based extraction system.

Ionic liquids (ILs) as a new generation of solvents, are considered as "green solvents", due to some specific features such as non-flammability, high thermal stability and non-volatility. Therefore considerable attention has recently been devoted to their application in separations, often as replacements for the conventional organic solvents employed in traditional liquid–liquid (L–L) or membrane-based systems for the separation of metal ions or organic solutes (13-15). Furthermore, ILs are generally considered as highly polar and weakly coordinating solvents in which ionic complexes tend to be more soluble then neutral complexes (16). This behavior has had a huge impact in biphasic catalysis (IL/Organic solvent) preventing catalyst leaching (17, 18), and also in the extraction or separation of metals (16, 19).

For two different complexes, one ionic and one neutral, it could therefore be expected that their solubility be dependent on the nature of the solvent, i.e. IL vs. organic. Indeed, the reaction of hexamethylbenzene and other methyl- substituted aromatics with $ZrCl_4$ affording a binuclear *neutral* complex $Zr(\eta^6\text{-}Me_6C_6)Cl_2(\mu\text{-}Cl)_3ZrCl_3$ (20), whereas under the same conditions, $HfCl_4$ affords a binuclear *ionic* complex $[Hf(\eta^6\text{-}Me_6C_6)Cl_3]^+[Hf_2Cl_9]^-$ (21, 22) This chemical difference in the nature of complexes Zr and Hf, could be useful for their separation.

The ionic liquid used is a "neutral" imidazolium chloroaluminate prepared from a 1:1 ratio of 1-butyl-2-methylimidazolium chloride and aluminium trichloride as an "acidic" medium (excess of aluminium trichloride) could react with hexamethylbenzene and a more "basic" medium (excess of imidazolium chloride) could react with with Hf and Zr chloride complexes (23).

The association toluene/ILs is often used in extractive metal

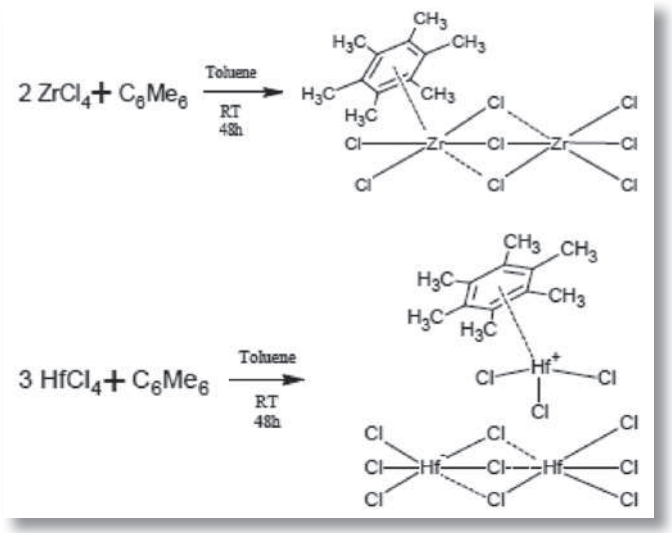

Figure 1.

removal from chloride liquors (24). However, the high miscibility of toluene in ionic liquids (wt. ~ 40 percent) (25-27) can be sharply decreased in the presence of aliphatic hydrocarbon (28, 29). Consequently, for the extractions a mixture of toluene and pentane was chosen. This study has opened the way to a potential new process for the separation of Zr and Hf, under mild conditions using an ionic liquid/organic solvent system.

RESULTS AND DISCUSSION

The complexes $Zr(\eta^6\text{-}Me_6C_6)Cl_2(\mu\text{-}Cl)_3ZrCl_3$ and $[Hf(\eta^6\text{-}Me_6C_6)Cl_3]^+[Hf_2Cl_9]^-$ were synthesized as reported in the literature (20-22) (Figure 1).

Their ^{13}C solid state NMR spectra indicate that the chemical shifts of hexamethylbenzene ligand are higher than in the free aromatic proving that the arene is coordinated to the metals. The deshielding is higher in the case of $[Hf(\eta^6\text{-}Me_6C_6)Cl_3]^+[Hf_2Cl_9]^-$ than for $Zr(\eta^6\text{-}Me_6C_6)Cl_2(\mu\text{-}Cl)_3ZrCl_3$; Me : $\Delta\delta$(+5.2 ppm) versus (+0,7ppm) and C_{Ar} : $\Delta\delta$(+16 ppm) versus (~ 0ppm). Moreover, in the negative ESI mass spectra the highest intensive massif for Zr is at 658.5 corresponding to $[Zr_2(\eta^6\text{-}Me_6C_6)Cl_9]^-$ and for Hf the massif at 676.4 assigned to $[Hf_2Cl_9]^-$.

All the solubilities are evaluated by X-ray fluorescence. The method is rapid, sensitive, accurate and almost universally applicable. When a sample that contains element A is irradiated by the incident X-ray source, fluorescent X-ray radiation of element A is generated, [Hf (Lα) 0.5476 and Zr (Kα) 0.3731] where the intensity of this fluorescence is directly proportional to the amount of element A in the sample. Taking this into account, if the fluorescent X-ray intensity and concentration of an element contained in a sample is known [ZrO_2 and HfO_2] then we can go in reverse and find how much element A contained in another sample by its fluorescent X-ray intensity.[30] Suitable procedures have been developed for the determination of microgram amounts.

Solubility is also tested in $C_1C_4ImAlCl_4$. The complex is added to ionic liquid and stirred overnight. The following quantities of complex are dissolved: 50 mg (8.5µmol) of $Zr(\eta6\text{-}Me_6C_6)Cl_2(\mu\text{-}Cl)_3ZrCl_3$ in $C_1C_4ImAlCl_4$ (2 ml) and 47 mg (4.9 µmol) of of $[Hf(\eta^6\text{-}Me_6C_6)Cl_3]^+[Hf_2Cl_9]^-$ in $C_1C_4ImAlCl_4$ (1 ml). The X-ray intensity of both Zr and Hf in these solutions was measured (Table1).

Then, toluene was added (3 ml for Zr solution; 1.5 ml for Hf solution]; the mixtures were stirred during one day to extract the complex. After the decantation, only one phase was observed. Pentane was used to extract the toluene from the ionic liquid (2 ml for Zr solution; 1 ml for Hf solution]. The quantity of extracted complexes by the toluene/pentane mixture from the ionic liquid was analyzed by fluorescent X-ray of element Zr and Hf. In order to have double control of the measurements, the quantities of Zr and Hf were calibrated with respect to a standard ZrO2 and HfO2 and also to the chlorine Cl X-ray peak intensity. Both determinations indicate that in the Zr solution about 13 ± 5 percent of the Zr complex is extracted from IL media into the organic phase, whereas only a trace amount the Hf complex is recovered in the organic phase (Table 1)

All constituents of the organic phase could be easily recovered (under vacuum at 25°C for organic solvents, 10^{-2} mm Hg) and by heating to 100°C under 10^{-5} mm Hg, the coordination of the aromatic ligand is reversible and $ZrCl_4$ is recovered. The development of a multistage process for the separation and recovery of pure $ZrCl_4$ is currently under investigation.

CONCLUSION

These preliminary results demonstrate that when reacted with methyl substituted arenes, different reactivity presented by $ZrCl_4$ and $HfCl_4$ may be exploited in their separation. This process may be further optimized by testing various ionic liquids (altering the cation), the solvents in the organic phase or the ligand and the development of a multistage process for the separation and recovery of pure $ZrCl_4$ may therefore be envisaged.

Experimental section

All operations were carried out under an atmosphere of purified argon in a glove box or using standard Schlenk techniques. Solvents were dried and distilled by conventional methods. Synthesis of the ionic liquid $C_1C_4ImAlCl_4$, $Hf(\eta^6\text{-}Me_6C_6)Cl_3]^+[Hf_2Cl_9]^-$, and $Zr(\eta^6\text{-}Me_6C_6)Cl_2(\mu\text{-}Cl)_3ZrCl_3$ were synthesized as reported in the literature (14, 20-22).

X-ray fluorescence: Samples were analyzed on Shimadzu EDX 800HS spectrometer. Plastic films used for the analyses are polypropylene for the ionic liquid and polyethylene- terephtalate for the organic phases.

Solution NMR spectra ^1H and ^{13}C: were recorded on Bruker Avance 300 MHz spectrometer for ^1H and ^{13}C. Chemical shifts were measured relative to $SiMe_4$ as internal standard for ^1H and ^{13}C.

^{13}C Solid state NMR spectra were recorded on a Bruker DSX-300 spectrometer equipped with a standard 4 mm double-bearing probe head and operating at 75.47, and 300.18 MHz for 13C, and 1H, respectively. 13C NMR spectra were recorded as follows: 30° pulse on 13C nuclei, and acquisition under an 80 KHz decoupling field on protons, with 1s recycle delay and 5 KHz spinning speed unless otherwise specified.

Mass Spectrometry: was realized on a ThermoFinnigan LCQ Advantage ion trap instrument, detecting positive (+) an negative (-) ions in the ESI mode. Samples (1 to 10 µg ml-1 in acetonitrile) were infused directly into the source (5 µl min-1) using a syringe pump. The following source parameters were applied: spray voltage 3.0-3.5 kV, nitrogen sheath gas flow -520 arbitrary units. The heated capillary was held at 473 K. MS

	Zr (Kα)Int.	Hf (Lα)Int	extraction efficiency	
Ionic liquid before extraction	22. 5912	4.6839	Zr %	Hf %
Ionic liquid after extraction	17.1616	4.4281	87 ± 5	98 ± 2
Organic phase after extraction	0.7214	0.0923	13 ± 5	≈ 1

Table 1. Intensities of Kα ray for Zr and Lα ray for Hf in ionic liquid and organic phase and extraction efficiency for Zr and Hf.

spectra were obtained by applying a relative collision energy of 25 to 40 percent of the instrumental maximum.

Solubility tests and extractions: All solubilities were evaluated by X-ray fluorescence. Intensity: Hf (La) 0.5476 and Zr (Ka) 0.3731. Complexes were added to the ionic liquid and stirred overnight. Then toluene was added and stirred during one day. Only one phase was observed. Pentane was then added to extract the toluene from the ionic liquid (Table 1).

ACKNOWLEDGMENTS

We thank undergraduate students Lucie Caumette and Fabien Foissac for their experimental contribution. Anne Baudouin, Pr. Denis Bouchu and Pr. Robert Chareyron for their help in NMR, Mass Spectrometry and X-ray fluorescence experiments and Dr. Ronga (Cezus Society) for the gift of pure $HfCl_4$ sample.

REFERENCES AND NOTES

1. B. Prakash, C.V. Sundaram, *Met. Mater. Proc.*, **21**, p. 21 (2009).
2. V. Ogarev, A. Skotnicki et al., *Patent AU. 20080527*. p. 12 (2009).
3. L.A. Niselson, E.A. Egorov et al., *J. Chem. Eng.*, 54, p. 726 (2009).
4. M. Smolik, A. Jakobik-Kolon et al., *Hydrometallurgy*, **95**, p. 350 (2009).
5. K. Saberyan, A.H. Meysami et al., *Chin. J. Chem.*, **26**, p. 2067 (2008).
6. M. Taghizadeh, R. Ghasemzadeh et al., *Hydrometallurgy*, **90**, p. 115 (2008).
7. L. Delons, G. Picard et al., *Compagnie Europeenne Du Zirconium Cezus, WO 20020412*. p. 20 (2002).
8. L. Delons, S. Lagarde et al., *Compagnie Europeenne du Zirconium-Cezus, Fr.) Fr 2004-7721*, p. 40 (2006).
9. J.A. Sommers, J.G. Perrine, *US, ATI Properties, Inc., USA, 20020129.*, p. 8 (2003).
10. N. Ozanne, M.L. Lemaire et al., *WO, Compagnie Europeenne du Zirconium Cezus, Fr., 20010910*, **23**, (2002).
11. A. Da Silva, E. El-Ammouri et al., *Can. Metall. Q.*, **39**, p. 37 (2000).
12. R.H. Nielsen, in *Kirk othmer encyclopedia of chemical technology John Wiley & Sons,*, New York (2004).
13. L. Huimin, D. Sheng, *Ionic Liquids in Chemical Analysis* (Ed.: M. Koel), CRC Presss Boca Raton, p. 269 (2009).
14. P. Wasserscheid, T. Welton, *Ionic liquids in synthesis*, Wiley-VCH, Weinheim (2008).
15. M.L. Dietz, *Sep. Sci. Techol.*, **41**, p. 2047 (2006).
16. V.A. Cocalia, A.E. Visser et al., *Ionic liquids in Synthesis,* **1**, 2d ed. (Ed.: P. Wasserscheid, Welton, T., Eds.;), Wiley -VCH, Weinheim (2008).
17. D.J. Cole-Hamilton, R.P. Tooze, *Catalyst separation, recovery and recycling: Chemistry and Process Design*, Springer, Dordrecht (2006).
18. T. Gutel, P. Campbell et al., *Chimica Oggi/Chemistry Today*, **27**, p. 48 (2009).
19. V.A. Cocalia, K.E. Gutowski et al., *Coord. Chem. Rev.*, **250**, p. 755 (2006).
20. F. Musso, E. Solari et al., *Organometallics*, **16**, p. 4889 (1997).
21. F. Calderazzo, I. Ferri et al., *J. Organomet. Chem.*, **518**, p. 189 (1996).
22. F. Calderazzo, P. Pallavicini et al., *J. Chem. Soc., Dalton Trans.*, p. 2743 (1990).
23. P.S. Campbell, C.C. Santini et al., *Dalton Trans*, **39**, p. 1379 (2010).
24. M. Regel-Rosocka, *Sep. Purif. Technol.*, **66**, p. 19 (2009).
25. H.-T. Shang, J.-S. Wu et al., *J. Chem. Eng. Data*, **51**, p. 1286 (2006).
26. G. Wytze Meindersma, A. Podt et al., *Fuel Processing Technology*, **87**, p. 59 (2005).
27. U. Domanska, A. Marciniak, *J. Chem. Therm.*, **37**, p. 577 (2005).
28. J.S. Torrecilla, M. Deetlefs et al., *Phys. Chem. Chem. Phys.*, **10**, p. 5114 (2008).
29. L. Yansheng, Z. Zhongxin et al., *Petroleum Science*, **3**, p. 73 (2006).
30. B. Beckhoff, B. Kanngießer et al., (Eds.), *Handbook of Practical X-Ray Fluorescence Analysis,* Springer-Verlag, Berlin (2006).